Alma Mater Studiorum · University of Bologna

**School of Science**
**Department of Physics and Astronomy**
**Master Degree in Physics**

# Theory and phenomelogy of dark matter models for the 511 keV galactic photons

**Supervisor:**

**Prof. Filippo Sala**

**Submitted by:**

**Michael Mancini**

Academic Year 2024/2025

# ABSTRACT

The origin of the 511 keV gamma-ray line from the Galactic Center has been one of the biggest misteries and most enduring puzzles in astrophysics since its discovery. While conventional astrophysical explanations struggle to account for both the intensity and morphology of the signal, models involving light dark matter have emerged as promising candidates over the past decades.

In this thesis we investigate dark matter models that are able to consistently explain the 511 keV line from the Galactic Center, going through their theoretical foundation and analyzing their phenomenological consequences.
The core of this work focuses on two specific frameworks: one involving $p$-wave annihilation of dark matter particles and another dealing with coannihilation between nearly-degenerate dark matter states. We examine the compatibility of these models with experimental and observational constraints, such as those from direct detection experiments and collider searches, along with bounds from the Cosmic Microwave Background (CMB), Supernova 1987A (SN 1987A) and observations of the Bullet Cluster.

The results obtained in this master thesis show that viable dark matter scenarios can explain the 511 keV line and reproduce the observed dark matter relic abundance, while remaining compatible with current experimental limits. Our analysis also identifies clear strategies to test these potential dark matter explanations of the 511 keV line in the near future, using upcoming experiments with enhanced sensitivity to sub-GeV dark matter.

# Contents

# 1

# Introduction

Despite decades of intense research, the nature of dark matter (DM) remains one of the most profound mysteries in modern physics and its nature still elusive. Although the Standard Model successfully describes a vast array of phenomena, it does not contain any viable dark matter candidates within it[1]. This limitation has led to the proposal of numerous BSM theories aimed at explaining the observed properties of dark matter (see Sec. 2.2).

One of the most intriguing astrophysical misteries, which could find an answer in dark matter models, is the 511 keV gamma-ray line observed from the Galactic Center of the Milky Way. Initially detected by balloon-borne experiments[2] and later confirmed with greater precision by space-based missions such as INTEGRAL[3–5], this line is widely interpreted as arising from the annihilation of non-relativistic electron-positron pairs via para-positronium formation[6]. However, the astrophysical origin of the positrons remains elusive. This motivates the attempt to explain the spatial morphology and intensity of the lines with positrons produced by dark matter.

This master thesis aims to investigate theoretical dark matter models, that can account for the 511 keV gamma-ray line observed from the Galactic Center, while matching the observed DM relic abundance.
The morphology of the 511 keV signal from the Galactic Center favours dark matter annihilations into final states that eventually give rise to positrons, rather than DM decays, as the latter would typically result in a broader spatial distribution of the resulting 511 keV emission[7, 8]. However, the intensity of the signal requires DM annihilation cross sections that are significantly smaller than the canonical thermal relic value $\langle \sigma v \rangle \simeq 10^{-26}\text{cm}^3/\text{s}$. This is to avoid an overproduction of positrons, which could lead to an excess of 511 keV photons beyond what is observed by instruments such as INTEGRAL/SPI[9]. This motivates scenarios where the annihilation cross section is large enough in the early universe to generate the correct relic abundance, but it is suppressed at late cosmological times. Two well-motivated classes of models that naturally realize this behaviour are:

- $p$-wave annihilating dark matter models, where the annihilation cross section depends on the relative velocity between DM particles and is therefore suppressed at late times (see Chapter 4);
- coannihilation models, which involve nearly degenerate DM states with a mass splitting

$\delta \equiv m_{\chi_2} - m_{\chi_1}$. This class of models is naturally late-time suppressed, as the number density of the heavier DM component $\chi_2$ is Boltzmann suppressed relative to that of the lighter state $\chi_1$, namely $n_{\chi_2} \simeq n_{\chi_1} e^{-\delta/T}$.

Moreover, to avoid an overproduction of 511 keV photons from the Galactic Center, the injected positrons must be non-relativistic or mildly relativistic. This constrains their injection energy to a few MeV or less[8, 9], which, in turn, implies that the mass of DM annihilating into $e^-e^+$ pairs must satisfy $M_{\rm DM} \lesssim 3$ MeV. However, such light dark matter is severely constrained by cosmological data and therefore a potential MeV dark matter interpretation of the 511 keV signal observed from the Galactic bulge had been claimed excluded[10].
Recent progress has changed this picture. In particular, it has been shown that the positron injection rate required to explain the 511 keV line can be enhanced by astrophysical features such as dark matter density spikes near the supermassive black hole at the Galactic Center, allowing the signal to be matched even for DM masses above 10 MeV[11, 12]. This opens up novel avenues for testing dark matter explanations of the 511 keV line, which this thesis begins to investigate.

In Chapter 2 we discuss the astrophysical evidence for dark matter and outline the key properties that viable candidates must satisfy, in order to be consistent with observations. We also give a general overview of the experimental and observational limits on dark matter models. We then continue the discussion with Chapter 3, which introduces the 511 keV line and its observational features, providing the astrophysical motivation for the models explored. We also derived new best-fit values of the thermally-averaged DM annihilation cross sections, needed to reproduce the 511 keV line. In addition, Chapters 4 and 5 are dedicated respectively to the detailed construction and phenomenological analysis of the $p$-wave annihilation and coannihilation models. In these two final chapters we show that that these two dark matter scenarios can explain the 511 keV line and reproduce the observed DM relic abundance, while remaining compatible with current experimental and observational limits. Finally, we present new strategies to test these dark matter scenarios with upcoming experiments.

Furthermore, in App. A we review the thermal history of the early universe and the formalism used to compute relic abundances, starting from the Boltzmann equation, while in App. B we present some computations of cross sections and decay rates, relevant for this thesis. Concluding, in App. C we analyze resonant enhancements of the dark matter annihilation cross section, focusing on the velocity dependence near the resonance condition and its implications for thermal freeze-out and positron injection rates.

# 2

# Dark matter

DM remains one of the most intriguing and persistent mysteries in modern physics. Although it does not emit, absorb, or reflect light, its presence is evident through its gravitational influence on the Universe. We see its effects in the rotation curves of galaxies, the bending of light through gravitational lensing, and the temperature fluctuations of the CMB. Yet, despite decades of effort, we still do not know what DM is made of.
The Standard Model of particle physics, despite its empirical success, lacks a viable dark matter candidate, strongly suggesting the need for new physics.
Numerous theoretical extensions have been proposed to explain dark matter, including axions [13], sterile neutrinos [14], models involving dark sectors [15], weakly interacting massive particles (WIMPs)[16] and primordial black holes[17].
These frameworks offer a variety of potential experimental signatures, which have guided the development of both direct and indirect detection strategies.

In this chapter, we present an in-depth study of dark matter evidence and its properties, also giving a general overview of current experimental and observational constraints on dark matter models, as in the following chapters we will explore the possibility that dark matter could provide explain one the most puzzling astrophysical anomalies, which is the 511 keV gamma-ray signal from the GC.

## 2.1 Dark matter evidence

Currently, discrepancies between the visible matter content and the gravitational behaviour of large-scale structure strongly support the existence of DM. These observational evidence for dark matter span a wide range of spatial scales, from rotation curves in spiral and dwarf spheroidal galaxies, to cluster-scale phenomena like gravitational lensing in systems such as the Bullet Cluster, extending eventually the analysis to cosmological scales, as revealed by precise measurements of the Cosmic Microwave Background (CMB) anisotropies.

In the following, we present a brief overview of key observational pillars supporting the dark matter hypothesis, hoping to convey to the reader the consistency of the evidence accumulated over decades.

### 2.1.1 Galactic rotational curves

An historically strong evidence for the existence of DM comes from the study of galactic rotational curves.
We can define the mean rotational velocity of the components of a gravitationally bound system, as a function of the distance r from the Galactic Center (GC), as

$$v(r) = \sqrt{\frac{GM(r)}{r}}, \tag{2.1}$$

where $G$ is the Newtonian gravitational constant, while $M(r)$ is the mass enclosed within a sphere of radius $r$. Eq. (2.1) comes from balancing gravitational and centrifugal forces.
If all the mass of a certain galaxy were accounted for by luminous matter like dust, stars and gas, distribuited as an hard shell core of uniform density, then we would expect that within a core of radius $R$, the mean rotational velocity increaseas linearly with radius as $v(r) \propto r$, since the mass inside a sphere of radius $r$ and uniform density is $M(r) \propto r^3$. Outside the core, instead, and thus for $r > R$, the mass would be $M(R) \approx$ const and therefore the mean rotational velocity would go as $v(r) \propto r^{-1/2}$.
This suggests that any deviation from this behaviour is an indicator of the fact that luminous matter does not actually constitute all the mass present in a galaxy.

In the early 1970s Vera Rubin, Kent Ford and collaborators showed that the rotational velocities of stars and gas in spiral galaxies do not decrease at large radii, whereas they tend to level off and remain roughly constant far beyond the region occupied by most of the visible matter[18].
These so-called *flat rotational curves* have been observed in a wide range of galaxies of different type and sizes, becoming particularly pronounced in galaxies with little luminous mass[19, 20].
The persistent presence of flat rotational curves in different galaxies strongly suggests that we also have a dominant component of non-luminous matter that does not follow the distribution of visible matter and this is a peculiar characteristic of galaxy dynamics and not rather confined to individual cases.

In Fig. 2.1 we illustrate how a DM halo can allow to fit properly the observational data.

#### Dwarf spheroidal galaxies

Dwarf spheroidal galaxies (dSph) are among the most dark matter-dominated systems known in the Universe. They are low-luminous galaxies with around 10-1000 stars and they are distant 20-200 kpc from us, so they are gravitationally linked to the Milky Way.
These galaxies have a mass $M_{\mathrm{dSph}} \gtrsim 10^7 M_{\odot}$ and a radius $R_{\mathrm{dSph}} \gtrsim 1$kpc.
Typically DM velocity dispersion[1] in dwarf spheroidal galaxies is $v_{\mathrm{DM}} \approx 3 \cdot 10^{-5}$, so significantly smaller compared to the one in larger galaxies like the Milky Way, where instead $v_{\mathrm{DM}} \approx 10^{-3}$.

### 2.1.2 Gravitational lensing and the Bullet Cluster

Gravitational lensing, a phenomenon predicted by Einstein's theory of General Relativity, arises due to the deflection of light by massive objects under the influence of gravity. In particular,

[1] In astrophysics velocity dispersion is a measure of how fast particles are moving relative to each other.

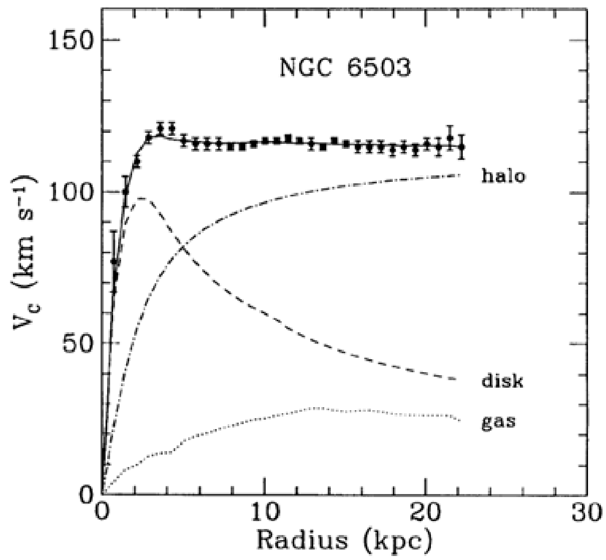


Figure 2.1: Galactic rotational curve for NGC 6503 which shows disk and gas contribution in addition to a DM halo component needed to match the observational data.
***Reprinted from "Review of Observational Evidence for Dark Matter in the Universe and in upcoming searches for Dark stars", by Katherine Freese, Michigan Center for Theoretical Physics, University of Michigan***[21]

.

we can have three different types of gravitational lensing[22]:

- *strong lensing*, which results in pronounced distortions such as multiple images, arcs, and Einstein rings, typically observed in galaxy clusters.
- *weak lensing*, which, differently from the strong lensing, is just able to modify and stretch images.
- *microlensing*, which causes distortions too small to be detected, but the image may appear brighter.

Over the past years, gravitational lensing has become a powerful observational tool in astrophysics and cosmology, because it allows to infer the total mass of a gravitationally bound system, and then, comparing it with the distribution of visible matter, it is possible to find the abundance of non-luminous matter. This makes it possible to study systems, where luminous and dark matter could be spatially displaced. One of the most studied examples of such a system comes from the Bullet Cluster, which consists of two galaxy clusters that have recently collided, providing the opportunity to study rigorously the distribution of visible and invisible matter[23].
During the merger, the hot gas plasma decelerates due to the frequent interactions, while the galaxies themselves pass through undisturbed. Since most of the baryonic mass is in the plasma, one might naively think that the gravitational potential is centered there, however this is not the case. Indeed, one can study the distribution of the hot gas plasma by analyzing

the X-ray emissions due to the significant interactions during the merger. In particular, weak lensing analysis show that these X-ray emitting gas do not constitute the majority of the Bullet Cluster's mass, but rather coincide with the distribution of collisionless galactic components. This implies that the majority of the mass is in regions associated to low X-ray emissions, as it is depicted in Fig. 2.2.

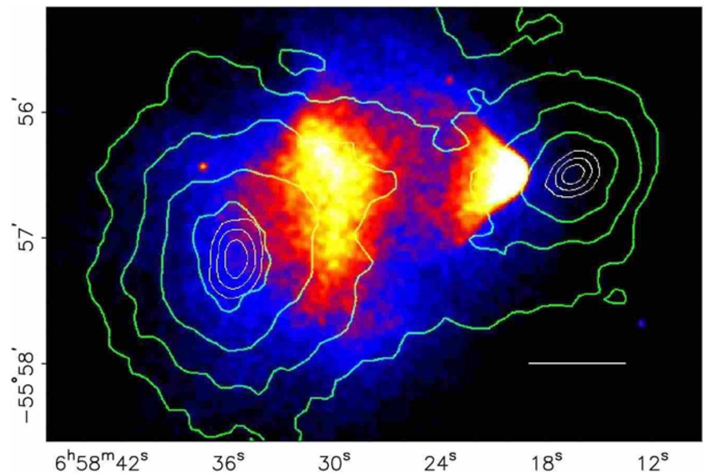


Figure 2.2: A composite image of the Bullet Cluster obtained by the Chandra X-ray Observatory, showing the X-ray emission from the hot gas and the gravitational mass distribution, traced by weak lensing, in green. The spatial separation of the gas and the mass distribution supports the presence of dark matter in the cluster.
***Reprinted from "A direct empirical proof of the existence of dark matter", by Douglas Clowe et al., Steward Observatory, University of Arizona***[23].

The spatial separation between the baryonic mass and the gravitational potential in the Bullet Cluster strongly suggests that most of the mass is non-luminous, non-baryonic and it interacts gravitationally but not electromagnetically.
Importantly, the Bullet Cluster is not an isolated case. Similar spatial offsets between luminous matter and gravitational mass have been observed in several other merging clusters, such as the Musket Ball Cluster[24] and Abell 520[25]. These observations further support the dark matter hypothesis and highlight the need for a component of mass that interacts primarily through gravity[1].

On galaxy cluster scales, evidence for dark matter arises not only from gravitational lensing and merging clusters, but also from the application of the virial theorem, which shows that the mass required to gravitationally bind the system, inferred from galaxy velocity dispersions, significantly exceeds the mass of visible matter [26]. In this subection, however, we have focused on a specific well-studied example of dark matter evidence at these scales, which is the Bullet Cluster.

### 2.1.3 Cosmological evidence: the CMB

Observations of the CMB provide some of the most precise evidence for the existence of dark matter on cosmological scales.
The CMB is relic radiation from the early universe, emitted approximately 380,000 years after the Big Bang during the epoch of recombination, when electrons combined with protons to form neutral hydrogen, allowing photons to propagate freely across space.

From the Planck satellite[27] and earlier missions, like WMAP[28], we can infer that the Universe is spatially flat, which means that its total density parameter satisfies $\Omega_{\text{TOT}} \equiv \frac{\rho}{\rho_c} \sim 1$. Here, $\rho$ is the energy density of the Universe, including all possible contributions, such as those from matter, radiation and vacuum energy. On the other hand, $\rho_c = \frac{3H_0^2}{8\pi G}$ is the critical density, where $H_0$ is the present-day value of the Hubble parameter, while $G$ is the Newton's gravitational constant (see App. A for more details).
Moreover, detailed analysis of the CMB power spectrum reveals how the total energy content of the Universe is partitioned among its constituents:

- 5% accounted for by baryonic matter $\implies \Omega_{\text{B}} \sim 0.05$.
- 26% accounted for by dark matter $\implies \Omega_{\text{DM}} \sim 0.26$.
- 69% accounted for by dark energy $\implies \Omega_{\Lambda} \sim 0.69$.

The CMB is not perfectly uniform, but it exhibits tiny temperature fluctuations of the order of $\frac{\delta T}{T} \sim 10^{-5}$, which are the fuel that drives the formation of all cosmic structure we see today, such as galaxies and galaxy clusters. Their properties are encoded in the CMB angular power spectrum, which displays acoustic peaks, reflecting oscillations in the baryon-photon plasma before recombination. The height and spacing of these peaks, shown in Fig. 2.3, are sensitive to the total matter density and the baryonic-to-dark matter ratio.

The temperature fluctuations in the Universe can be analysed as a function of the angular separation between different points on the CMB sky map, and to accomplish this idea, we can expand these fluctuations in terms of spherical harmonics:

$$\frac{\delta T(\theta, \phi)}{T} = \sum_{\ell=1}^{\infty} \sum_{m=-\ell}^{\ell} a_{\ell m} Y_{\ell m}(\theta, \phi), \tag{2.2}$$

where $\ell$ denotes the multipole moment.
We can notice that in Eq. (2.2), we do not consider the $\ell = 0$ term, which represents the monopole moment, because it constitutes the average CMB temperature, corresponding to $\sim 2.725$ K. It is essentially a constant offset and, for this reason, we exclude it, since we are interested in the analysis of temperature fluctuations as an indicator of CMB anisotropies. The $\ell = 1$ term, which represents the dipole anisotropy, reflects, instead, the local motion of the Solar System relative to the CMB rest frame. Therefore, it is dominated by the Doppler shift caused by this kinematic effect, which overwhelms any intrinsic dipole anisotropy in the CMB itself. As a consequence, the observed dipole is typically removed from the data and one can consider in the analysis of the CMB anisotropies just the $\ell \geq 2$ terms.

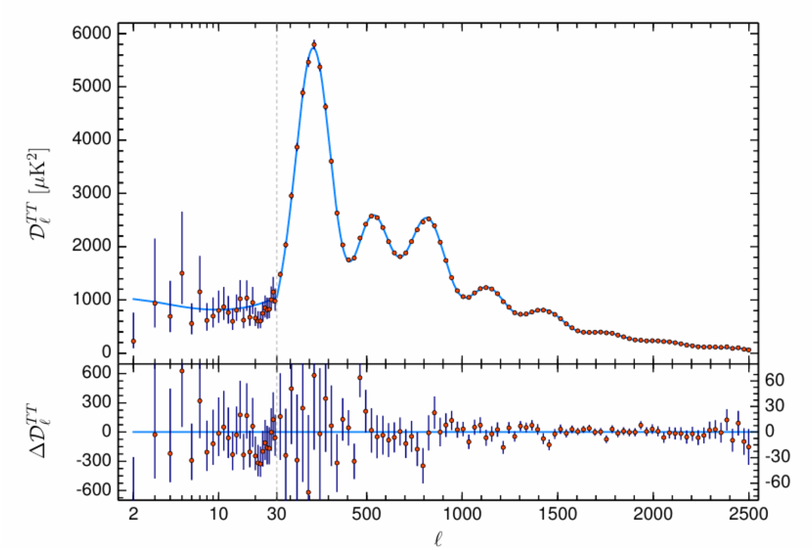


Figure 2.3: CMB angular power spectrum, as measured by the Planck satellite. The quantity plotted is $D_\ell^{TT} = \frac{\ell(\ell+1)}{2\pi} C_\ell^{TT}$, which represents the variance of temperature fluctuations at multipole moment $\ell$. The distinct acoustic peaks reflect oscillations in the early universe's baryon-photon plasma and are highly sensitive to cosmological parameters such as the total matter density and the baryon-to-dark matter ratio.
***Reprinted from "Planck 2018 results. VI. Cosmological parameters", by Planck Collaboration***[27].

It is possible to quantify the variance of temperature fluctuations in the CMB by defining the temperature-temperature angular power spectrum, which is given by

$$C_\ell^{TT} = \frac{1}{2\ell+1} \sum_{m=-\ell}^{\ell} \langle |a_{\ell m}|^2 \rangle. \tag{2.3}$$

However, usually the analised quantity is

$$D_\ell^{TT} = \frac{\ell(\ell+1)}{2\pi} C_\ell^{TT}, \tag{2.4}$$

which flattens the steep decay of $C_\ell^{TT}$ in Eq. (2.3) and make the acoustic peaks clearly visible and easier to interpret. For this reason, in Fig. 2.3 we plot $D_\ell^{TT}$.
As already said, each peak in the CMB angular power spectrum in Fig. 2.3 reveals some important cosmological information. In particular:

- The first peak reflects the total gravitational potential and gives us information about the geometry of the Universe, confirming that it is spatially flat.
- The second peak, which is sensitive to the baryon-to-dark matter ratio and its height relative to the first peak, reveals how much baryonic matter is present in the Universe.
- The third peak indicates, instead, the amount of dark matter in the Universe.

In this sense, the CMB acoustic peak structure is a direct consequence of dark matter's gravitational role in shaping the primordial density fluctuations.
In addition, dark matter annihilation injects energy into the intergalactic medium, affecting thus the ionization history of the universe and leaving detectable imprints on the CMB. These signatures places significant constraints, relevant for light dark matter candidates capable of producing positrons, such as those considered in explaining the 511 keV signal from the Galactic Center. These constraints are discussed more in detail in Sec. 2.4.4.

On cosmological scales, DM leaves imprints not only in the CMB, but also in the formation and statistical distribution of large-scale structures, as revealed by observations of galaxy clustering and baryon acoustic oscillations (BAO)[27, 29, 30]. However, in this subsection we have focused on the CMB, as it provides the most direct probe of the matter content in the early universe. In particular, its angular power spectrum strongly supports the existence of cold, non-baryonic DM.[27, 31].

All the evidence for dark matter presented so far is compelling. Nevertheless, it is important to acknowledge that alternative frameworks have been proposed to explain the observed phenomena without invoking dark matter. One such example is Modified Newtonian Dynamics (MOND), which will be discussed in the next subsection.

### 2.1.4 Modified Newtonian Dynamics (MOND)

The discrepancies between the visible matter content and the gravitational behaviour of large-scale structure, discussed previously, arise if we assume Newtonian gravity to hold. We can thus wisely think to solve these observational inconsistencies, not anymore by adding a non-luminous matter component, as suggested earlier, but by modifying the gravitational framework in which we work.
Therefore, we now briefly discuss how Modified Newtonian Dynamics (MOND) could provide an alternative explanation for flat rotational curves in galaxies.

In Newtonian mechanics, given a star of mass $m$ moving in a galaxy, its centripetal force is given by

$$F = \frac{GM(r)m}{r^2}, \tag{2.5}$$

where again $G$ is the Newtonian gravitational constant and $M(r)$ is the mass enclosed within a sphere of radius $r$ centered on the GC.
MOND, instead, as suggested by M. Milgrom in Ref. [32], propose that the Newton's second law $\vec{F} = m\vec{a}$ should be replaced by

$$\vec{F} = m\mu\left(\frac{a}{a_0}\right)\vec{a}, \tag{2.6}$$

where $m$ is the mass of a body, like a star, moving in a static field force $\vec{F}$ with acceleration $\vec{a}$, $a_0 \sim 1.2 \cdot 10^{-10} \frac{m}{s^2}$ is a constant and $\mu(x)$ is a function defined such that

$$\begin{cases} \mu(x \gg 1) \approx 1 \\ \mu(x \ll 1) \approx x \end{cases} . \tag{2.7}$$

Moreover, we have defined $a \equiv |\vec{a}|$. We thus notice from Eq. (2.6) that for accelearations much larger than $a_0$, we get that $\mu\left(\frac{a}{a_0}\right) \approx 1$ and, therefore, we recover the Newtonian dynamics, while in the regime where $a \ll a_0$, MOND predicts flat rotational curves in outer galactic regions without the need of considering the presence of dark matter[33].

While MOND was originally proposed as a phenomenological modification of Newtonian gravity[32], aimed at explaining the observed flat rotation curves of galaxies without dark matter, it is important to note that MOND itself is not a complete relativistic theory. Rather, it just provides a phenomenological relation between the gravitational acceleration $a$ and the Newtonian potential $\phi_N$, through the function $\mu\left(\frac{a}{a_0}\right)$.

In order to extend MOND to a consistent framework capable of addressing cosmological phenomena, such as the CMB, a relativistic completion is required. One of the most developed proposals is TeVeS (Tensor-Vector-Scalar gravity), introduced by Bekenstein[34], which generalizes MOND into a relativistic theory involving additional gravitational fields. More recent studies by Skordis and collaborators have explored refinements of such frameworks[35]. These relativistic extensions attempt to provide a more fundamental basis for MOND-like behaviour and allow for cosmological predictions.

However, despite these efforts, current relativistic MOND models still face challenges in reproducing the detailed structure of the CMB power spectrum, unlike the standard ΛCDM paradigm[23, 36, 37].

In the next section we present a general overview of DM properties, inferred from experiments and observations.

## 2.2 Dark matter properties

The evidence for dark matter presented in Sec. 2.1 strongly supports its existence across a wide range of astrophysical and cosmological scales. Understanding the nature of DM requires identifying the key physical properties that any viable candidate must possess in order to be consistent with current experimental observations. While the precise identity of DM remains unknown, decades of data constrain its behaviour in both the early and late universe. Below we summarize the main properties of DM inferred from observations:

- *Cold and non-relativistic at structure formation*: cosmological structure formation strongly supports cold dark matter (CDM), which is DM that was non-relativistic when structure began to form. Hot dark matter, such as neutrinos with eV-scale masses, suppresses small-scale structures via free-streaming, leading to a top-down structure formation scenario[2] that is inconsistent with the observed galaxy clustering and the matter power spectrum[38–40]. Cold dark matter, in contrast, allows hierarchical formation, with small structures forming first and merging into larger halos, in agreement with N-body simulations and large-scale surveys[27, 41].

[2]In top-down structure formation, predicted by hot dark matter, large structures form first and fragment into smaller ones. This scenario is inconsistent with observations showing early formation of small-scale structures.

- *Gravitationally interacting*: DM must inetract gravitationally, as it dominates the matter content of the Universe and drives the growth of structure. Its gravitational effects are evident from a wide range of phenomena, such as flat rotation curves at galactic scales[19], virial mass discrepancy and gravitational lensing at cluster scales[23, 26] and CMB anisotropies and large-scale structure formation at cosmological scales[27] (see Sec. 2.1 for a more detailed discussion on DM evidence).

- *Electromagnetically neutral and dark*: DM must be non-luminous and electrically neutral, as it does not emit, absorb, or reflect light. Observations of the CMB and galaxy surveys impose tight constraints on any charged or interacting DM component, as it would lead to spectral distortions, excess radiation, or deviations from standard structure formation[42].

- *Stable on cosmological timescales*: to account for the observed matter density today, DM must be stable on cosmological timescales. Some models allow for decaying dark matter, provided the decay rate is slow enough to be consistent with bounds from gamma-ray, neutrino, and positron backgrounds[43, 44].

- *Non-baryonic*: Big Bang Nucleosynthesis (BBN) and the CMB tightly constrain the total baryonic content of the Universe, which accounts for only $\sim 5\%$ of the total energy density. The other 26% of the Universe's matter density must be non-baryonic, ruling out MACHOs and standard astrophysical objects as the dominant DM component[45, 46].

- *Weakly coupled to the Standard Model*: current bounds from direct detection, collider experiments, and indirect searches, such as gamma-ray or cosmic-ray telescopes, imply that DM either interacts very weakly with Standard Model particles or lies in a hidden sector with suppressed couplings to the Standard Model sector[47].

- *Broad mass range*: there are several dark matter candidates spanning a broad mass range. In particular, a thermal relic must have a mass roughly in the range 1 keV $\lesssim M_{\rm DM} \lesssim$ 100 TeV to satisfy structure formation and unitarity bounds[48, 49].

- *Self-interacting*: even though it is not a general DM's feature, some models allow for self-interacting dark matter, which could alleviate small-scale structure issues such as the core-cusp and missing satellites problems. However, astrophysical observations, particularly from merging galaxy clusters like the Bullet Cluster, constrain the DM self-interaction cross section to be $\frac{\sigma_{\rm self}}{M_{\rm DM}} \lesssim 1\frac{\rm cm^2}{\rm g}$[50, 51] (see Sec. 2.2.1 for a more detailed analysis of self-interacting DM).

- *Large-scale dominance*: in large disk galaxies like the Milky Way, dark matter is sub-dominant in the inner regions, that is within a few kiloparsecs of the GC, where baryonic matter dominates the gravitational potential. However, at radii beyond $\simeq 5-10$ kpc, DM becomes the dominant mass component, as indicated by flat rotation curves (see Sec. 2.1). In contrast, dSph galaxies are dark matter dominated even at small radii, with a significant contribution already within $\sim 100$ pc of the GC[52, 53].

To conclude the discussion on DM properties, DM could have been produced in the early universe in two different ways, which are

- *Thermal production*: DM was in thermal equilibrium with the SM plasma and then froze-out, becoming a relic[54].

- *Non-thermal production*: in this case, DM was not originally in thermal equilibrium with the SM plasma and, therefore, it was produced in other ways. An example is the freeze-in mechanism[55].

In this thesis we focus on DM as a thermal candidate.

In the following section, we provide a general overview of self-interacting dark matter (SIDM) models and discuss how they may help address some of the small-scale challenges associated with the cold dark matter paradigm, such as the core-cusp problem and the missing satellite problem.

### 2.2.1 SIDM models

The ΛCDM model succesfully explains large-scale structure formation, however, it faces significant challenges at smaller scales, regime that it is nowadays investigated through N-body simulations. In particular, over the decades, some discrepancies between CDM predictions and observations have arisen, such as[56]

- *Core-Cusp problem*: according to Ref. [57–59], the mass density profile for CDM halos scale approximately as $\rho_{\text{DM}} \propto r^{-1}$, increasing thus toward the center. However, many observed rotation curves of disk galaxies prefer a constant "cored" density profile, that is $\rho_{\text{DM}} \propto r^0$[60–62]. This behaviour is prevalent in DM-dominated envinronments, such as dSph galaxies, which, therefore, represent promising targets to test CDM predictions.

- *Diversity problem*: in CDM models the formation of structures, like galaxies and their DM halos, is self-similar, meaning that halos with the same total mass are predicted to have very similar internal structures[59, 63]. However, nature seems to be inconsistent with observations. Indeed, if we look at disk galaxies with the same maximum circular velocity, which is an indicator of the total mass, they exhibit rotation curves that differ more than expected[64].

- *Missing satellites problem*: from CDM predictions, structures in the Universe form hierarchically, which means that smaller halos form first and then merge in order to create larger ones. The former often survive as subhalos within the latter, which implies that, for example, a halo with the dimension of the Milky Way is predicted to contain many smaller subhalos orbiting within it[65]. However, again, CDM predictions do not seem to match observations, since if we look at the Local Group[3] we see far fewer small galaxies than expected.

- *Too-big-to-fail problem*: in recent years, CDM simulations have suggested that the brightest satellite galaxies around the Milky Way are expected to live inside the most massive DM subhalos, which should be large enough to form stars and create visible galaxies. This expectation gave origin to the term *too-big-to-fail*. Once again, observations reveal discrepancies with CDM predictions. Indeed, the most massive simulated subhalos are too dense in the central region compared to what is inferred from the motion of stars in the observed brightest dSph galaxies[66, 67].

[3]The Local Group is a collection of more than 20 galaxies, including the Milky Way and Andromeda.

These discrepancies between observations and predictions, though, are not limited to the Milky Way, but studies of dSph galaxies within Andromeda[68] and the Local Group[69] have found similar behaviours.

These issues, however, which arise in DM-only simulations, can be alleviated in the ΛCDM framework if we include baryonic processes, such as gas cooling and star formation[70, 71].

Another possible solution to these issues is to consider warm DM particles, which are quasi-relativistic during kinetic decoupling from the thermal bath in the early universe[38, 72]. In particular, recent simulations showed that warm DM may lead to a suppression of satellite galaxies, providing a solution for the missing satellite and the too-big-to-fail problems[73–75]. However, it should be noted that the mass range of warm DM is strongly constrained by Lyman-$\alpha$ forest observations[48, 76] and, as a consequence, warm DM core are too small to solve the core-cusp problem[77].

A valid alternative to collisionless CDM is self-interacting DM (SIDM), which was proposed as possible solution to the core-cusp and the missing satellites problems[50].

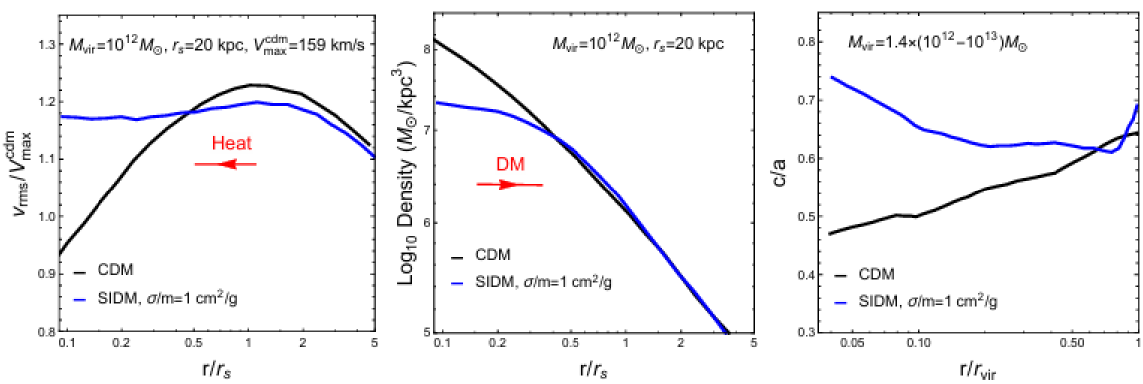


Figure 2.4: Comparison of the density profiles (left panel), velocity dispersion profiles (central panel) and minor-to-major axis ratio $\frac{c}{a}$ for SIDM with $\frac{\sigma}{m} = 1\ \mathrm{cm}^2/\mathrm{g}$ and its CDM counterpart (right panel).
***Reprinted from "Dark Matter Self-interactions and Small Scale Structure", by Sean Tulin and Hai-Bo Yu***[56].

DM self-interactions introduce significant deviations from CDM predictions, in particular:

- In CDM halos the DM velocity dispersion decreases toward the center and thus it is not constant. On the other hand, self-interactions transfer heat from the hotter outer to the cooler inner region of a DM halo, resulting in a thermalization of the inner halo and, therefore, in a *isothermal velocity dispersion*, as it is illustrated in the left panel of Fig. 2.4[78].

- When we consider CDM, hierarchical structure formation produces halos with a universal and cuspy density profile[58, 59]. In the SIDM framework, instead, collisions between DM particles in the dense inner regions heat low-entropy particles. This redistributes energy and flattens the central density, producing, thus, a core-like structure, rather than a cusp, as shown in the central panel of Fig. 2.4

- According to Ref. [57], CDM halos are triaxial[4], while self-interactions between DM particles tend to isotropize their velocities and, as a consequence, the minor-to-major axis ratio $\frac{c}{a}$ is closer to unity toward the center of SIDM halos, compared to CDM halos, as we can see in the right panel of Fig. 2.4

Let us now consider two colliding galaxy clusters; the probability that DM in a cluster 1 collides with DM in a cluster 2 is given by

$$\frac{dP_1}{dt} = \sigma_{\rm self}\ \phi_2^{\rm DM} = \sigma_{\rm self}\ \frac{\rho_2}{M_{\rm DM}} v_{\rm rel}, \tag{2.8}$$

where $\phi_2^{\rm DM}$ is the flux of incoming DM, while $\rho_2$ is the DM mass density.
Using that $x = v_{\rm rel} \cdot t$, we can now write that

$$\frac{dP_1}{dx} = \frac{1}{v_{\rm rel}} \frac{dP_1}{dt} = \sigma_{\rm self} \frac{\rho_2}{M_{\rm DM}}. \tag{2.9}$$

Therefore, we obtain that [79]

$$P_1 = \int_0^{L_{\rm cluster}} \frac{dP_1}{dx} dx = \frac{\sigma_{\rm self}}{M_{\rm DM}} \int_0^{L_{\rm cluster}} \rho_2 dx \simeq \frac{\sigma_{\rm self}}{M_{\rm DM}} 0.3 \frac{\rm gr}{\rm cm^2}. \tag{2.10}$$

In order to avoid any offset in the observations, we should satisfy that $P_1 \lesssim 0.3 \implies \frac{\sigma_{\rm self}}{M_{\rm DM}} \lesssim 1 \frac{\rm cm^2}{\rm gr}$.

## 2.3 Dark Matter candidates

In this section we want to give a general overview of DM candidates, presenting briefly the WIMP scenario as it has been extensively studied in recent years.

Despite decades of research, no particle within the Standard Model satisfies all the criteria required of a dark matter candidate[1]. As a consequence, numerous extension to the SM have been proposed, in order to include new particles and new mediators able to explain the unsolved mistery of DM, remaining though consistent with experimental and observational constraints. While its exact nature remains still unknown, numerous well-motivated candidates have been proposed across a significant mass range, reflecting the diversity of theoretical models proposed to explain its nature. Some of the main BSM candidates for DM are:

- Axions, which are extremely light particles originally introduced to solve the strong CP problem in QCD and they also represent a viable non-thermal DM candidate, with a mass $M_{\rm DM} \ll 1$ eV[13].

- Sterile neutrinos, which are SM singlets and a possible DM candidate, with a mass in the range 1 keV $\lesssim M_{\rm DM} \lesssim$ 100 keV. Sterile neutrinos are an example of WARM DM.[14]

[4] A triaxial object is a three-dimensional structure with three axes of different lengths.

- Sub-GeV DM, which are particles with a mass $M_{\rm DM} \lesssim 1$ GeV, interacting with the SM through new mediators like dark photons[80].
- WIMPs, which interact through the weak force and they are among the most well-studied DM candidates. Even though they have not been detected yet, they remain a viable and highly-motivated possibility. Their mass range is 1 GeV $\lesssim M_{\rm DM} \lesssim 100$ TeV[81].
- There are also heavier non-thermal DM candidate, an example are PBH[17].

After a brief overview of the potential DM candidates, which can be found in the literature, we present in the next chapter the computation to derive the DM abundance.

### 2.3.1 Dark matter abundance

In this subection we want to derive the dark matter abundance, taking into acccount the impact of the SM thermodynamics.
As already found in App. A.3, the DM number density evolves according to the Boltzmann equation

$$\frac{dn_{\rm DM}}{dt} + 3Hn_{\rm DM} = -\langle \sigma v \rangle (n_{\rm DM}^2 - n_{\rm DM,eq}^2). \tag{2.11}$$

In particulars, if $M_{\rm DM} \lesssim 10$ MeV, the DM annihilation after the neutrino decoupling modifies the temperatures of the neutrinos and the photons. This leads to the shift of the effective neutrino number $\Delta N_{\rm eff}$ and affects the DM abundance estimation.[82–85]The results proposed here, as indicated by the authors of Ref. [54], are obtained neglecting this effect for simplicity. The Boltzmann equation (2.11) can also be rewritten in terms of the DM yield, $Y_{\rm DM} \equiv \frac{n_{\rm DM}}{s}$, and the mass-to-temperature ratio $x = \frac{M_{\rm DM}}{T}$, as

$$\frac{dY_{\rm DM}}{dx} = -\frac{\lambda}{x^2} \langle \sigma v \rangle [Y_{\rm DM}^2 - (Y_{\rm DM}^{\rm eq})^2], \tag{2.12}$$

where $\lambda = \frac{x^3 s}{H(M_{\rm DM})} = \left(\frac{45}{8\pi^2}\right)^{-1/2} g_*^{1/2} M_{\rm DM} M_{\rm p}$[5] is taken approximately constant and $\langle \sigma v \rangle \simeq a_s + b_p \langle v_{\rm rel}^2 \rangle$ is the thermally-averaged DM annihilation cross section. Indeed, the only temperature-dependent term inside $\lambda$ is $g_*^{1/2}$, which is defined as in Eq. (A.27) and its behaviour with temperature is shown in Fig. A.4. However, we can treat it as approximately constant, even though around the QCD phase transition we need to be more cautious.
Moreover, since $Y_{\rm DM}^{\rm eq}$ is exponentially suppressed at later times, in first approximation we can write the Boltzmann equation as

$$\frac{dY_{\rm DM}}{Y_{\rm DM}^2} = -\left(\frac{45}{8\pi^2}\right)^{-1/2} \frac{g_*^{1/2} M_{\rm DM} M_{\rm p}}{x^2} dx \tag{2.13}$$

and, integrating both sides of the equation from FO until a temperature of $T = 1$ eV, we find that

$$\frac{1}{Y_{\rm DM}^{\rm FO}} - \frac{1}{Y_{\rm DM}^{\infty}} \simeq -\left(\frac{45}{8\pi^2}\right)^{-1/2} \frac{g_\rho^{1/2} M_{\rm DM} M_{\rm p}}{x_{\rm fo}} \left(a_s + 3\frac{b_p}{x_{\rm fo}}\right), \tag{2.14}$$

[5] $M_{\rm p} = \frac{M_{\rm pl}}{\sqrt{8\pi}}$ is the *reduced* Planck mass, where $M_{\rm pl} = 1.2 \cdot 10^{19}$ GeV.

where we have used that $1/x_\infty \simeq 0$ and we have approximated $g_*^{1/2} \approx g_\rho^{1/2}(T_{\rm fo})$ since we are treating it as constant. Here, $g_\rho(T)$ is defined as in Eq. (A.17).

We note that $Y_{\rm DM}^{\rm FO} \equiv Y_{\rm DM}^{\rm eq}(x = x_{\rm fo})$ and, as done typically in the literature, we can neglect $\frac{1}{Y_{\rm DM}^{\rm FO}}$, obtaining that

$$Y_{\rm DM}^{\infty} \simeq \left(\frac{45}{8\pi^2}\right)^{1/2} \frac{x_{\rm fo}}{g_\rho^{1/2} M_{\rm DM} M_{\rm p}} \frac{1}{a_s + \frac{3b_p}{x_{\rm fo}}}. \tag{2.15}$$

At this point, the DM abundance is approximately given by

$$\Omega_{\rm DM}{\rm h}^2 = \frac{s_0 h^2 M_{\rm DM} Y_{\rm DM}^{\infty}}{\rho_c} \sim \frac{s_0 h^2}{\rho_c} \left[\frac{45}{8\pi^2 g_\rho(T_{\rm fo})}\right]^{1/2} \frac{M_{\rm DM}}{T_{\rm fo} M_{\rm p}\left(a_s + 3\frac{b_p}{x_{\rm FO}}\right)}, \tag{2.16}$$

where $s_0$ is the entropy density after the neutrino decoupling, $\rho_c$ is the critical density at the present time and $T_{\rm fo}$ is the freeze-out (FO) temperature.
In the instantaneous FO scenario, the FO temperature, $T_{\rm fo}$, is fixed by

$$\Gamma(T_{\rm fo}) = H(T_{\rm fo}), \tag{2.17}$$

where $\Gamma(T_{\rm fo})$ is the DM interaction rate and $H(T_{\rm fo})$ is the Hubble parameter, both evaluated at $T = T_{\rm fo}$ and given by

$$\begin{aligned} \Gamma(T_{\rm fo}) &= n_{\rm DM}\langle\sigma v\rangle = g_{\rm DM}\left(\frac{M_{\rm DM}T}{2\pi}\right)^{3/2} e^{-M_{\rm DM}/T}\langle\sigma v\rangle \\ H(T_{\rm fo}) &= \sqrt{\frac{\pi^2 g_\rho(T_{\rm fo})}{90}}\frac{T_{\rm fo}^2}{M_{\rm p}} \end{aligned}. \tag{2.18}$$

Here, $g_{\rm DM}$ counts the internal degrees of freedom of the WIMP particle under consideration. Moreover, we have used the non-relativistic expression of the number density in Eq. (A.13), under the well-motivated assumption that dark matter decoupled while non-relativistic.
Requiring that $\frac{\Gamma(T_{\rm fo})}{H(T_{\rm fo})} \simeq 1$, we find that[6]

$$\frac{g_{\rm DM}}{g_\rho^{1/2}(T_{\rm fo})} \frac{3}{(2\pi)^{3/2}} M_{\rm p} M_{\rm DM} x_{\rm fo}^{1/2} e^{-x_{\rm fo}} \langle\sigma v\rangle \simeq 1, \tag{2.19}$$

which defines $T_{\rm fo}$

### 2.3.2 $s$- and $p$-wave annihilations

The annihilation rate of dark matter particles in the early universe plays a critical role in determining their present-day abundance.

[6] Here $\langle\sigma v\rangle$ has an implicit dependence on $x_{\rm fo}$. For example, for an $s$-wave dominated process we have $\langle\sigma v\rangle = a_s$, while for a $p$-wave dominated process we can write $\langle\sigma v\rangle = 6\frac{b_p}{x_{\rm fo}}$. Therefore, depending on the process we are considering, the overall power of $x_{\rm fo}$ changes.

In the non-relativistic limit, where the relative velocity between DM particles satisfy that $v_{\rm rel} \ll 1$, it is possible to expand the DM annihilation cross section times velocity as

$$\sigma v_{\rm rel} \simeq a_s + b_p v_{\rm rel}^2, \tag{2.20}$$

where $a_s$ takes into account the $s$-wave contribution, independent of velocity, while $b_p$ captures the $p$-wave contribution.
By taking the thermal average of the annihilation cross section, we obtain

$$\langle \sigma v_{\rm rel} \rangle \simeq a_s + b_p \frac{6T}{M_{\rm DM}} \tag{2.21}$$

and, solving the Boltzmann equation 2.11, up to 1 eV, which corresponds to the CMB era, we can compute $\Omega_{\rm DM} h^2$.
By assuming to work with Majorana DM, which means that $g_{\rm DM} = 2$, and requiring to match the observed relic DM abundance, that is $\Omega_{\rm DM} h^2 = 0.120 \pm 0.001$[27], we can find the predicted cross section for $s$- and $p$-wave annihilating DM necessary to be consistent with observations in Fig. 2.5.

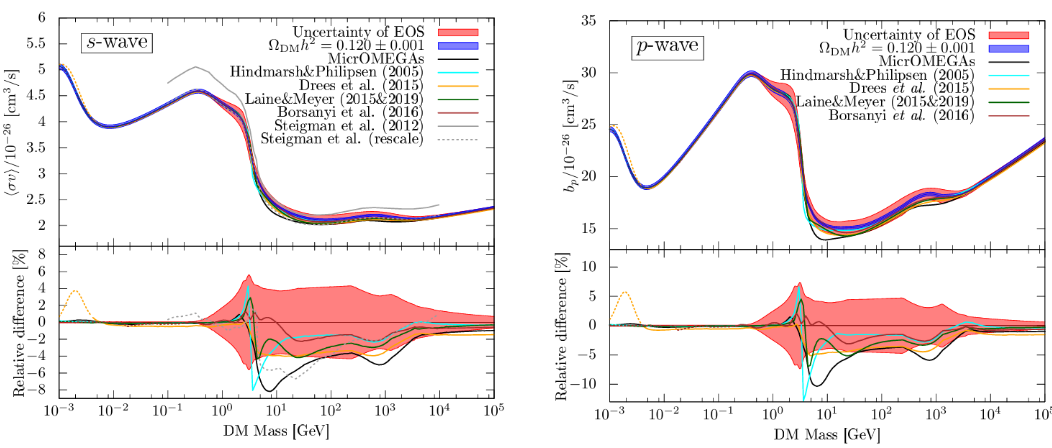


Figure 2.5: On the left we have the thermal average of the annihilation cross section times velocity for an $s$-wave process and on the right the p-wave term $b_p$, defined as in Eq. (2.20), necessary to realize the observed DM relic abundance $\Omega_{\rm DM} h^2 = 0.120 \pm 0.001$[27], for respectively an $s$-wave and a $p$-wave annihilating Majorana fermion DM. The red shaded region shows the uncertainty from the thermodynamics of the SM, and the blue shows uncertainty of the DM abundance measurement. In the figure there are also shown the results from Refs. [86–91]. ***Reprinted from "Precise WIMP Dark Matter Abundance and Standard Model Thermodynamics", by Ken'ichi Saikawa and Satoshi Shirai***[54].

The expansion of the thermally-averaged cross section in Eq. (2.21) gives good results only for small relative velocities $v_{\rm rel}$, where the dark matter particles are non-relativistic and their velocity distribution is well-approximated by a Maxwell-Boltzmann form. Near a resonance, however, this expansion becomes inappropriate, as the annihilation cross section varies rapidly with energy and cannot be accurately captured by a low-velocity Taylor series. In such cases, the full relativistic thermal average must be used to avoid unphysical results, such as incorrect

suppression of the relic density[92].
This will be important for the models studied in this thesis, specifically in Chapters. 4 and 5. We will provide more details about this resonant regime in App. C.

Finally, we close this chapter by reviewing the current experimental and observational constraints on dark matter models.

## 2.4 Experimental constraints

Numerous experiments have been conducted in the search for direct signs of interactions between dark and ordinary matter, focusing on a range of theoretical candidates, from heavy particles like WIMPs to lighter alternatives like axions. The quest to uncover its true nature continues to drive much of today's research in particle physics and cosmology.
Experimental constraints on DM come from multiple fronts:

- *Direct detection experiments*: these aim to observe the scattering of DM particles off atomic nuclei or electrons in ultra-sensitive underground detectors. Leading experiments, such as XENON1T[93, 94], SENSEI[95, 96] and DarkSide-50[97], search for nuclear recoils or electron recoils caused by incident DM particles.
- *Indirect detection experiments*: these are sensitive to SM particles, such as gamma rays[98], neutrinos[99, 100], or cosmic rays[101], which are produced by DM annihilation or decay in regions of high DM density, like the GC.
- *Collider searches*: high-energy particle colliders such as the Large Hadron Collider (LHC) can probe DM production through missing energy signatures. In particular, experiments like NA64[102, 103] and LDMX[104] target light DM and dark sector particles, including dark photons.
- *Cosmological and astrophysical measurements*: observations of the CMB[27], BBN[105, 106], large-scale structure formation[107], and stellar cooling mechanisms[108, 109] impose stringent constraints on the properties of DM, especially on its mass and interaction cross-sections. For instance, strong bounds exist on MeV-scale DM due to its potential impact on BBN and recombination processes.

In the following subsections, we present a more detailed discussion of each class of constraints.

### 2.4.1 Direct detection constraints

Direct detection experiments aim to observe interactions between DM particles and ordinary matter by measuring the recoil energy transferred to target particles, which are typically nuclei or electrons, within ultra-sensitive detectors. The energy deposits from WIMP-nucleus scattering, for WIMPs in the GeV-TeV mass range, are expected to be of the order of $E_{\text{recoil}} \sim$ keV. Experiments such as XENON1T[110], LUX[111], and PandaX[112] have placed extremely stringent bounds on the DM-nucleon scattering cross section, excluding spin-independent interactions with $\sigma_{\text{SI}} \gtrsim 10^{-47}$ cm$^2$ for DM masses around $20 - 60$ GeV.

However, the direct detection of DM becomes more challenging as the DM mass decreases, indeed for sub-GeV DM, the nuclear recoil energies fall below current detection thresholds. As a result, attention has shifted toward DM-electron scattering, where sub-GeV DM can deposit sufficient energy to ionize electrons. Therefore, a new generation of experiments with ultra-low thresholds has emerged, designed specifically to probe sub-GeV DM candidates. Experiments such as SENSEI, DAMIC, SuperCDMS, and EDELWEISS have pioneered the use of low-noise silicon and germanium to search for DM-induced electron recoils. Both SENSEI[95] and DAMIC[113] employ Skipper-CCD technology, which enables the detection of single-electron events with exceptional precision.
The XENON10 experiment provided the first bounds on DM-electron scattering using ionization-only events[114], later refined by XENON100 and XENON1T, which extended sensitivity to higher-mass regimes and lower cross sections[93]. Complementary searches from EDELWEISS have probed similar parameter space with cryogenic Ge detectors[115].

In the context of sub-GeV DM models that aim to explain the 511 keV gamma-ray line observed by INTEGRAL in the GC, direct detection constraints provide essential bounds. Numerous models suggest that DM particles annihilate into low-energy positrons, which, subsequently interacting with the electrons in the interstellar medium, produce the observed 511 keV gamma-ray line observed in the GC. If DM couples to electrons with sufficient strength to explain this signal, the same interactions could, in principle, be probed by direct detection experiments. This creates the opportunity to test in the laboratory DM models that explain the 511 keV line signal, which we will explore in Chapters 4 and 5. Consequently, direct detection experiments play a crucial role in evaluating the viability of models aimed at explaining indirect astrophysical signals such as the 511 keV line, also providing essential constraints on sub-GeV DM parameter space.

### 2.4.2 Indirect detection constraints

Indirect detection experiments aim to identify signatures of DM through its annihilation or decay products in astrophysical environments. Unlike direct detection, which searches for DM interactions with detectors on Earth, indirect detection experiments search for an excess in the flux of cosmic particles, such as gamma rays, positrons, antiprotons or neutrinos, that may originate from DM interactions in regions with high DM density, like the GC, dSph galaxies or galaxy clusters[116, 117].
In the standard WIMP framework, DM particles with masses in the GeV-TeV range can annihilate into SM particles, leading to detectable fluxes of gamma rays and charged cosmic rays. This approach has led to numerous constraints from instruments like Fermi-LAT[118, 119], AMS-02[120, 121], H.E.S.S.[122, 123], and IceCube[99, 124]. However, the absence of signals that can be clearly attributed to DM, rather than known astrophysical sources, has driven increasing interest in light or sub-GeV DM, which may produce distinct indirect signatures, particularly in the MeV energy range, which for now remains relatively unexplored[101].

As already mentioned, one of the most intriguing observations, possibly linked to light DM, is the 511 keV gamma-ray line, detected by INTEGRAL/SPI from the GC, interpreted as evidence of positron annihilation. Injecting too many positrons would lead to an excess in the observed flux; consequently, stringent bounds on the DM annihilation cross section have been placed over the years, using approximately 16 years of INTEGRAL/SPI data[125].

Additional constraints on sub-GeV DM come from soft gamma-ray and X-ray observations. When DM particles annihilate or decay into $e^-e^+$ pairs, the resulting electrons and positrons can upscatter[7] photons from the interstellar radiation field and the CMB via inverse Compton scattering, leading to potentially observable X-ray emission. A reanalysis of INTEGRAL data that includes this effect has placed stringent limits on DM models, particularly for particle masses $M_{\rm DM} \gtrsim 20$ MeV[126, 127].

Cosmic-ray measurements also contribute to indirect detection constraints. In particular, by analyzing the scattering of cosmic rays off DM particles, one can place bounds on the DM-electron and DM-proton scattering cross sections, for DM masses below 1 GeV[128, 129]. In the near future, next-generation gamma-ray telescopes, such as AMEGO and e-ASTROGAM, will significantly increase the sensitivity to MeV-scale gamma rays, particularly those originating from DM annihilation into light mesons or leptons[130, 131]. These missions are expected to probe cross-sections well below current limits, significantly improving our ability to test light DM models relevant to the 511 keV line[132].

### 2.4.3 Collider constraints

Collider experiments offer a complementary strategy for probing DM, independent of astrophysical assumptions such as halo density profiles or cosmic-ray rays propagation models.
At high-energy facilities such as the LHC, it is possible to search for dark matter by looking for missing transverse energy signals, associated with visible particles, recoiling against invisible states. These searches include mono-jet, mono-photon, mono-Z/W, and mono-Higgs final states[8], as well as signatures involving long-lived particles or displaced vertices[9] when DM interacts via a light mediator.
In the conventional WIMP framework, where dark matter has masses in the GeV-TeV range, collider experiments can probe dark matter interactions by searching for signals of its production, either through effective contact operators or via explicit mediators, such as dark photons or scalar portals. Limits on the strength of the interaction, derived by these experiments, are often expressed in terms of the cutoff scale $\Lambda$ or the mediator mass.
The LHC has placed stringent bounds on the production cross-section of such DM candidates, excluding significant portions of parameter space, particularly when the mediator is accessible on-shell.

When considering sub-GeV DM, instead, collider searches face kinematic limitations due

[7] When a high-energy electron or positron collides with a low-energy photon, from the CMB or interstellar radiation, it can transfer part of its energy to the photon. This phenomenon is called inverse Compton scattering, because it is the reverse of the standard Compton scattering, where a high-energy photon transfers part of its energy to an electron.

[8] Mono-X searches are events where one visible particle X is detected and the rest of the event shows missing transverse energy (MET), which could indicate particles that are invisible to the detector, such as dark matter. For example, in a mono-jet event we have a single energetic jet, from a quark or gluon, recoiling against missing energy.

[9] Displaced vertices refer to particle decay points that occur significantly away from the primary collision vertex, often indicating the presence of long-lived particles.

to its relatively small mass and suppressed couplings to visible states. However, dedicated low-energy experiments and fixed-target setups, such as NA64[102, 103], BaBar[133], Belle II[134, 135], and future electron-positron colliders, play a crucial role in probing this regime. These experiments look for missing energy signals or displaced decays of long-lived particles, particularly in scenarios with light mediators, like dark photons or scalars coupled to electrons.
The NA64 experiment, in particular, utilizes a fixed-target setup at CERN to actively search for dark sector particles, including dark photons and axion-like particles, by detecting signatures of missing energy in the detector. It provides strong sensitivity to sub-GeV DM models and light mediators by exploiting the high-intensity SPS[10] beam, offering potential complementary constraints on DM models.[136].

In the context of the 511 keV line observed by INTEGRAL, models involving sub-GeV DM annihilation into $e^- e^+$ pairs have gained attention and collider constraints are essential to test such models, since the required annihilation cross sections are typically small. Experiments such as BaBar and Belle II constrain the dark photon $V$ parameter space through visible and invisible decay searches, limiting the kinetic mixing parameter $\epsilon$ and the mediator mass. These bounds are particularly relevant for DM masses $M_{\mathrm{DM}} \lesssim 100$ MeV, because they directly constrain models that aim to explain the 511 keV gamma-ray signal through annihilation into electron-positron pairs.

### 2.4.4 Cosmological and astrophysical constraints

Cosmological and astrophysical observations provide some of the most stringent constraints on the properties of DM, particularly in the sub-GeV mass range. These constraints come from a variety of probes, including the CMB[27], BBN[105, 106], structure formation[107], and stellar cooling mechanisms[108, 109].
These comsological processes are highly sensitive to the thermal history and energy injection mechanisms in the early universe, therefore, they allow to exclude wide regions of DM parameter space that are difficult to access with terrestrial experiments. Indeed, energy injection from DM annihilation can affect both the abundance of light elements produced during BBN and the ionization history of the universe probed by the CMB. In particular, DM annihilation into electromagnetically interacting final states, such as $e^- e^+$ or photons, can increase the ionization fraction[11] at recombination and modify the CMB anisotropy spectrum. Consequently, measurements from *Planck* have been used to set strong bounds on the annihilation cross-section of light DM[27, 137]. Similarly, light DM particles that remain in thermal equilibrium with the SM plasma during BBN can alter the expansion rate or change the neutron-to-proton ratio $\frac{n_n}{n_p}$, thus affecting the primordial helium and deuterium abundances. This limits both the mass and interaction strength of thermal sub-GeV DM candidates[105, 138].

The matter power spectrum, inferred from galaxy surveys and Lyman-$\alpha$ forest observations,

[10] SPS stands for *Super Proton Synchrotron*, which is one of the major particle accelerators at CERN.

[11] The ionization fraction refers to the proportion of atoms or molecules in a gas that are ionized. In the context of cosmology and dark matter studies, particularly around the time of recombination, the ionization fraction usually denotes the fraction of free electrons relative to the total number of baryons in the early universe, indicated as $x_e = \frac{n_e}{n_{\mathrm{H}}}$.

is sensitive to the free-streaming length of dark matter[12]. Models of warm or semi-relativistic dark matter, which have longer free-streaming lengths, lead to a suppression of small-scale structure, in contrast to the CDM predictions, which, instead, supports structure formation on all scales. Sub-GeV DM models with non-negligible thermal velocities or late kinetic decoupling can thus be constrained by requiring consistency with observed large-scale structure[107]. For example, models with dark matter-photon or dark matter-neutrino scattering may delay structure formation in ways that are now testable with high-redshift galaxy observations[139–141].

DM particles with significant couplings to electrons or nucleons can be produced inside stellar interiors or supernova cores, carrying away energy and modifying standard cooling rates. Furthermore, observations of white dwarfs, red giants, and supernova SN 1987A constrain the production and escape of such particles[108, 142, 143]. These constraints typically limit the coupling strength of sub-GeV DM to SM particles, particularly in the MeV-GeV mass range.

Overall, cosmological and astrophysical data impose powerful and often model-independent constraints on the properties of sub-GeV dark matter. These bounds are especially relevant for scenarios aiming to explain astrophysical anomalies, such as the 511 keV line from the GC, where annihilation into electrons is a key feature.
An in-depth study of supernova cooling mechanisms, discussed below, is worthwhile, since it plays a central role in constraining the *p*-wave dark matter model discussed in Chapter. 4.

### 2.4.5 Supernova cooling constraints

The search for new physics beyond the Standard Model has been a driving force in modern particle physics and cosmology. Among the various proposed extension, light scalar particles play a central role, because they can act as mediators of interactions between DM particles and the SM[144, 145], they can be DM themselves[146, 147], they can contribute in the generation of neutrino masses[148] and they may also solve the electroweak hierarchy problem[149, 150].

Supernovae, and in particular SN 1987A, are a useful tool to constrain these hypothetical scalar particles. Indeed, when a massive star's core collapses, it releases an enormous amount of energy primarily in the form of neutrinos, whose emission from SN 1987A lasted about 10 seconds. This is consistent with the leading theoretical model of core-collapse supernovae based on the delayed neutrino mechanism[151]. Therefore, it is clear that any additional energy loss, due to the emission of BSM particles, may potentially alter the observed neutrino signal.
Indeed, neutrinos interact only weakly with SM particles and this allows them to escape from supernovae, contributing to the cooling of the core; for the same mechanism, if there were BSM particles with sufficiently weak couplings with SM particles, then they may be able to escape the core contributing to the supernovae cooling, too.
In order to preserve agreement with observations, the Raffelt criterion constrains the emission rate of BSM particles from the supernova core, thus stating that new particles cannot carry away more energy than neutrinos do. Therefore, we have an upper bound on the average

[12] The free-streaming length of dark matter corresponds to the distance over which dark matter particles can travel before remaining gravitationally bound.

luminosity of the protoneutron star (PNS) in the form of BSM particles of[109]

$$L_{\mathrm{BSM}} \lesssim (2-3)\cdot 10^{52}\ \mathrm{erg}/s^{13} \tag{2.22}$$

We can observe that Eq. (2.22) is satisfied for sufficiently strong couplings to the SM sector. This is because, in this regime, called *trapping regime*, BSM particles interact frequently with the dense stellar plasma inside the PNS, preventing them from escaping freely. As a result, these particles remain confined within the star, behaving similarly to neutrinos, which are confined to the inner regions and only emitted from the surface, too. Consequently, their contribution to the total energy loss is reduced, because they are not emitted anymore from the bulk, as it happens for sufficiently weak couplings, and this leads to a decrease in $L_{\mathrm{BSM}}$, which thus satisfy the Raffelt criterion.
On the other hand, for sufficiently weak couplings to the SM sector, BSM particles do not interact significantly with the interior of PNS and thus they can free-stream leading to an increase of $L_{\mathrm{BSM}}$. Indeed, in this regime, called *free-streaming regime*, BSM particles would be emitted directly from the interior of PNS, while it is known that neutrinos are emitted solely from the surface.

Following Ref. [109], we can see that BSM scalar particles $\phi$ can be generated through

- continuum production;
- resonant production, which is dominant if $m_\phi < \omega_p{}^{14} \simeq \mathcal{O}(10\ \mathrm{MeV})$.

Let us consider lepthophilic BSM scalars, namely particles that couple only to leptons through an interaction term $y_e\phi\bar{e}e$. From Ref. [109] it is clear that the production rate of $\phi$ depends on the square of the coupling $y_e^2$, so that the smaller the value of $y_e$ is, the fewer scalar particles are produced, resulting in a decrease of the luminosity $L_{\mathrm{BSM}}$. Therefore, there exists a minimum coupling $y_e$, below which the production rate is so low that the energy loss through BSM particles is completely negligible compared to the one due to neutrinos.
This implies that SN 1987A constrains only a band in the mass-coupling parameter space of a given candidate BSM particle and, as already said, couplings $y_e$ corresponding to the lower region of such a band lead to the *free-streaming regime*, while those corresponding to the upper part lead to the *trapping regime*.

In Ref. [109], authors calculate the rate of resonant production of leptophilic scalars with an interaction $y_e\phi\bar{e}e$, as already mentioned, and they plot the resulting constraints, as shown in Fig. 2.6. It is possible to see that in this case couplings $y_e$ are sufficiently weak that if $\phi$ decays only to SM particles, then for $m_\phi \gtrsim 2\tilde{m}_e$, where $\tilde{m}_e$ is the effective in-medium electron mass[15], we have no bounds due to the Raffelt criterion, because decays to electrons are sufficiently fast.

[13] 1 erg $= 10^{-7}$ J.

[14] $\omega_p$ is the plasma frequency, which is defined as $\omega_p^2 = \frac{4\alpha_e}{3\pi}\left(\mu_e^2 + \frac{1}{3}\pi^2T^2\right)$, where $\alpha_e$ is the fine structure constant, while $\mu_e$ is the electron chemical potential[152].

[15] The thermal effective mass $\tilde{m}_e$ is defined as $\tilde{m}_e = \frac{m_e}{2} + \sqrt{\frac{m_e^2}{4} + m_{\mathrm{eff}}^2}$, where $m_{\mathrm{eff}}^2 = \frac{\pi\alpha}{2}\left(T^2 + \frac{\mu_e^2}{\pi^2}\right)$[153]

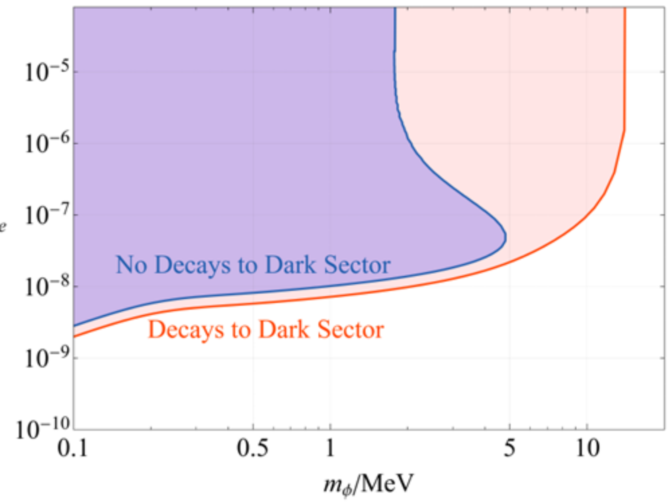


Figure 2.6: SN 1987A constraints for a lepthophilic scalar $\phi$ with a $y_e \phi \bar{e} e$ interaction term. The red area corresponds to theories in which $\phi$ decays quickly to some additional dark sector particles that do not interact with the SM, while the blue area refer to theories in which we do not have such decays.
***Reprinted from "Supernova bounds on new scalars from resonant and soft emission", by Edward Hardy, Anton Sokolov and Henry Stubbs, Rudolf Peierls Centre for Theoretical Physics, University of Oxford, Parks Road, Oxford OX1 3PU, UK***[109].

Building on the previous discussion of dark matter and its experimental constraints, the following chapter focuses on the 511 keV gamma-ray line from the GC and examines the potential of dark matter to account for this as-yet unexplained astrophysical anomaly.

# 3

# Dark matter models for the 511 keV line

In this chapter we aim at building the necessary framework to analyze more in detail two different dark matter models, which are the $p$-wave annihilation and the coannihilation models, discussed respectively in Chapters 4 and 5, proposed to explain the origin of the 511 keV gamma-ray line observed in the GC. This particular phenomenon, first detected some decades ago, remains one of the most intriguing astrophysical anomalies, and its persistence continues to motivate theoretical interpretations beyond standard astrophysical sources, see Ref. [154] for a recent review.
Ref. [155] was the first to propose sub-GeV dark matter as dominant source of positrons responsible for the 511 keV line emission, suggesting thus that DM may not only play a centrale role in the large-scale structure formation but also leave imprints at sub-galactic scales, through indirect signals like the 511 keV line.

Specifically, in this chapter we start discussing the morphology and intensity of the 511 keV line emission from the Galactic Center and we conclude focusing on the concept of dark matter density enhancements, so called spikes, induced by the presence of the supermassive black hole at the center of our galaxy, Sgr $A^*$. These spikes can significantly boost the annihilation rate of dark matter particles even for small annihilation cross sections, making them a key ingredient in models aiming to explain the 511 keV line.
At the end of this chapter, we also present some original plots concerning the thermally-averaged cross section for DM annihilating into $e^-e^+$, needed to explain the 511 keV gamma-ray signal, for different DM density profiles, discussed in the following.

## 3.1 The 511 keV line

One of the most puzzling problems in astrophysics over the last 50 years is certainly the 511 keV line, observed from the inner regions of our Galaxy.

The 511 keV line was discovered by Ref. [2] in a balloon flight in 1970 and it was confirmed over the years by space-based missions, such as the one related to the INTEGRAL (International Gamma-Ray Astrophysics Laboratory) satellite[3–5].

### 3.1.1 Morphology and intensity of the signal

The entire flux of 511 keV photons in the Milky Way was recently estimated to be $(2.74 \pm 0.25) \cdot 10^{-3}$ photons cm$^{-2}$ s$^{-1}$[156, 157]. This signal, observed by the INTEGRAL/SPI experiment, is due to the annihilation of $\simeq 2.5 \cdot 10^{42}$ $e^+$ $s^{-1}$ in a region within $\sim$ 4 kpc of the GC[11]. The line emission is mostly attributed to para-positronium annihilation of thermal or near-thermal positrons[158, 159].

#### Para-positronium annihilation

We define positronium as a bound system composed of an electron and a positron, whose annihilation produces two photons, which result in a single gamma-ray line at 511 keV. If the electron and positron form instead positronium, their subsequent annihilation results in two or more photons depending on the quantum numbers of the positronium bound state, and give rise overall to a lower energy photon continuum and a 511 keV line[6, 160]. According to Ref. [161], in the conditions of the interstellar medium, most positrons would annihilate after positronium formation.

Electrons and positrons are spin-$\frac{1}{2}$ fermions, one the antiparticle of the other. Therefore, from quantum mechanics principles, we know that the total spin $S$ of positronium would be

$$|s_1 - s_2| \leq S \leq s_1 + s_2, \tag{3.1}$$

where $s_1 = s_2 = \frac{1}{2}$ are the spins of electron and positron. It is thus straightforward to notice that, depending on the relative orientations of the spins of electron and positron, the ground state of positronium can have as total spin $S = 0, 1$. In particular, we denote the singlet state, namely the one with total spin $S = 0$, as $^1S_0$ and we call it *para-positronium.* On the other hand, we denote the triplet state, namely the one with total spin $S = 1$, as $^3S_1$ and we call it *ortho-positronium.*
Since we have a $2S + 1$ degeneracy associated to each state, we can understand easily that positronium will be $\frac{1}{4}$ of the times in the singlet state and $\frac{3}{4}$ of the times in the triplet state.

We now aim to determine the number of photons produced in the decay of each positronium state.
For a system of free particles, the C-parity[16] is defined as the product of the C-parities of each single particle.
The C-parity of a bound system, composed by a fermion $f$ and its antiparticle $\bar{f}$, is defined as

$$\mathcal{C}\,|f\bar{f}\rangle = (-1)^{L+S}\,|f\bar{f}\rangle\,, \tag{3.2}$$

where $L$ takes into account the orbital angular momentum of the pair, while $S$ the spin part of the wave function.
Let us consider the decay of $^1S_0$ into photons. We analyze the process in the rest frame of para-positronium, where its total orbital angular momentum is $L_{\text{in}} = 0$. Moreover, we have already said that $^1S_0$ has total spin $S_{\text{in}} = 0$, therefore para-positronium has C-parity equal to

[16]Charge conjugation parity (C-parity) is a quantum number describing how the wave function of an electrically neutral system transforms under charge conjugation, which is the operation that replaces all particles with their corresponding antiparticles.

$(-1)^{L_{\text{in}}+S_{\text{in}}} = (-1)^0 = 1$. Since electromagnetic interactions, like the one analyzed, preserve C-parity, we should have a final state with total C-parity equal to 1, in order to have a consistent process. In particular, we know that photons have intrinsic C-parity equal to $\eta_C = -1$ and, therefore, this allows to conclude that para-positronium decays into two photons, that is ${}^1S_0 \to \gamma\gamma$, in such a way that the total final C-parity is $(\eta_C)^2 = (-1)^2 = 1$.
We can repeat the same procedure with ${}^3S_1$, which has total spin $S_{\text{in}} = 1$ and, for the same reason as before, analyzing the process in the rest frame of ortho-positronium, the total orbital angular momentum is equal to $L_{\text{in}} = 0$, which implies that its C-parity is $(-1)^{L_{\text{in}}+S_{\text{in}}} = (-1)^1 = -1$. Therefore, from this follows that, in order to have an electromagnetically consistent process, ortho-positronium decays into three photons, that is ${}^3S_1 \to \gamma\gamma\gamma$, in such a way that the total final C-parity is $(\eta_C)^3 = (-1)^3 = -1$.
Recalling that the electron's rest mass is $m_e \simeq 0.511$ MeV $= 511$ keV and that we are looking for 511 keV photons, we can now conclude that the bright line emission coming from the GC is due to the para-positronium decay into two photons.

One of the most intriguing aspects of the so called "positron line puzzle" is that observations clearly show that the 511 keV line emission is highly concentrated in the Galactic bulge, with only a small component coming from the Galactic disk, as we can see from Fig. 3.1. However, most of the known sources of positrons, such as core-collapse supernovae or massive stars, are primarily found in the Galactic disk. This phenomenon obviously raises several questions:

- Where do all these positrons come from?
- Why is the GC so different from other regions of the Milky Way?
- What mechanism could produce such large quantities of positrons?

These questions will be examined in the upcoming sections.

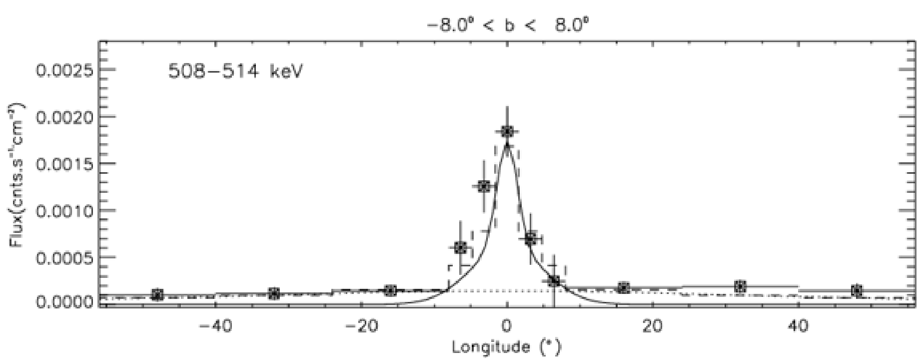


Figure 3.1: Longitude profile of the photon flux from electron-positron annihilation emission in the energy range 508.25-513.75 keV, as measured by SPI/INTEGRAL. The plot shows the distribution along the Galactic longitude $l$ for Galactic latitudes $|b| < 8^{\text{o}}$, where $b$ denotes the angle above or below the Galactic plane.
***Reprinted from "On the morphology of the electron-positron annihilation emission as seen by SPI/INTEGRAL", by L. Bouchet, J.P. Roques and E. Jourdain, CESR-UPS/CNRS, 9 Avenue du Colonel Roche, 31028 Toulouse Cedex 04, France***[162].

### 3.1.2 Known potential sources of positrons for the 511 keV line

If we want to consistently model the 511 keV line originating from DM annihilation, we should account for all potential sources of positrons that could contribute to the observed 511 keV emission in the GC.
There are several different sources that can explain the emission from the Galactic disk, like cosmic rays (CR) interactions, pulsars injecting $e^{\pm}$ or sources able to synthetize radioactive elements which then produce positrons via $\beta^{+}$ decay. Examples are $^{56}$Ni, produced in supernovae 1A, $^{26}$Al, produced in massive stars and eventually $^{24}$Ti, produced in core-collapse supernovae[163]. Since these positron sources are closely linked to stellar populations, it is reasonable to conclude that they contribute predominantly to the disk component of the observed signal, and much less to the bulge component.
In particular, it is easier to keep track of the positrons produced from the $^{26}$Al decay, rather than $^{44}$Ti or $^{56}$Ni. Indeed, from $^{26}$Al decay we produce $^{26}$Mg$^{*}$, via

$$^{26}\mathrm{Al} \to {}^{26}\mathrm{Mg}^{*} + e^{+} + \nu_e, \tag{3.3}$$

which then de-excites producing a 1809 keV $\gamma$-ray through

$$^{26}\mathrm{Mg}^{*} \to {}^{26}\mathrm{Mg} + \gamma. \tag{3.4}$$

The morphology of this signal has been mapped by the INTEGRAL/SPI experiment[164]. Moreover, it is relatively easy to calculate the fraction of 511 keV photons originated by $^{26}$Al, because each decay produces a positron and a 1809 keV $\gamma$-ray. Ref. [3] showed that $^{26}$Al accounts for half of the disk component of the 511 keV signal. It is, instead, more complicated to model the 511 keV signal coming from $^{44}$Ti and $^{56}$Ni, because of their shorter lifetime.

In the following, we investigate how dark matter might account for the 511 keV line.

## 3.2 511 keV line from dark matter annihilations

As we have said previously, there are several astrophysical sources that may account for the emission observed from the Galactic disk. However, no known astrophysical sources located near the Galactic Center are capable of accounting for the high positron injection rate observed in the inner regions of the Milky Way[3, 6, 157, 165].
This motivates the development of quantum field theory models of dark matter that could explain the 511 keV line emission from the Galactic Center and reproduce the required positron injection rate in the central regions of the Galaxy.

The morphology of the 511 keV gamma-ray signal is not compatible with DM decays unless the DM density profile scales as $\rho(r) \propto r^{-1.8}$ or in a steeper way toward the Galactic Center, as shown for example in Refs. [166] and [167]. However, such steep profiles are not supported by any N-body simulation, which instead find inner slopes no steeper than $r^{-1.3}$[168]. This tension disfavors decay scenarios and motivates consideration of dark matter signals that scale as $\rho(r)^2$. Proposals realizing this idea are for example:

- Annihilation of light DM particles into $e^{\pm}$[155];

- Excited DM models (XDM) in which we have excited states of heavy DM $\chi$, denoted as $\chi^*$, which are produced in $\chi - \chi$ collisions and subsequently decay into the ground state, with the formation of an $e^\pm$ pair[169, 170];
- Coannihilation models, where we have two DM particles $\chi_1$ and $\chi_2$, separated by a small mass splitting $\delta$, which coannihilate to produce an $e^\pm$ pair[171].

In the following subsection, we will focus on the formation of dark matter density spikes around the supermassive black hole at the center of the Milky Way. These analysis will serve as the foundation for building dark matter models, presented in Chapters 4 and 5, which may provide an explantion for the 511 keV line.

### 3.2.1 Dark matter density profiles and spikes

The supermassive black hole (SMBH) Sgr A$^*$ at the center of the Milky Way plays a central role in the evolution and cosmological history of DM within our Galaxy, dramatically increasing its density profile over the years.
In particular, following Ref. [11], we can parametrise the DM density profile in the Milky Way as

$$\rho(r) = \left(1 - \frac{2R_S}{r}\right)^{3/2} \begin{cases} 0 & r < 2R_S \\ \rho_{\rm sat}\left(\dfrac{r}{R_{\rm sat}}\right)^{-0.5} & 2R_S \leq r < R_{\rm sat} \\ \rho_{\rm spike}(r) & R_{\rm sat} \leq r \leq R_{\rm sp} \\ \rho_{\rm halo}(r) & r \geq R_{\rm sp} \end{cases}, \tag{3.5}$$

where

- $r$ is the distance from Sgr A$^*$, which in the analysis is assumed to be exactly at the center of the Milky way;
- $\rho_{\rm halo}(r)$ is the halo DM mass density;
- $R_{\rm sp}$ and $\rho_{\rm spike}$ are respectively the radial extension and the mass density profile for the DM spike;
- $R_{\rm sat}$ and $\rho_{\rm sat}$ are respectively the saturation radius and mass density of the spike due to DM annihilation;
- $R_S = \frac{2GM_{\rm BH}}{c^2} = 2.95\left(\frac{M_{\rm BH}}{M_\odot}\right)$ is the Schwarzschild radius for a BH of mass $M_{\rm BH}$.

Moreover, by defining $\rho_{\rm sat}$ as

$$\rho_{\rm sat} = \frac{m_\chi}{\langle\sigma v\rangle t_{\rm BH}} \simeq 3.17 \cdot 10^{11}\ \text{GeV cm}^{-3} \frac{m_\chi}{10\ \text{TeV}} \frac{10^{25}\text{cm}^3 s^{-1}}{\langle\sigma v\rangle} \frac{10^{10}\ \text{yr}}{t_{\rm BH}}, \tag{3.6}$$

where the lifetime of Sgr A$^*$ is $t_{\rm BH} = 10^{10}$ yr, we can compute $R_{\rm sat}$ by imposing that $\rho_{\rm sat} = \rho_{\rm spike}(R_{\rm sat})$, in such a way that we have continuity of the DM density profile, in Eq. (3.5), in correspondence of $r = R_{\rm sat}$.
Since DM particles' orbit are non-circular, the DM density profile continues to grow at $r < R_{\rm sat}$,

too. Furthermore, the slope $\sim r^{-0.5}$ in Eq. (3.5), for $2R_S \leq r < R_{\rm sat}$, is found by assuming $s$-wave DM annihilations[172, 173]. The spike density profile, instead, can be modeled as

$$\rho_{\rm spike}(r) = \rho_{\rm halo}(R_{\rm sp})\left(\frac{r}{R_{\rm sp}}\right)^{-\gamma_{\rm sp}(r)}, \tag{3.7}$$

where $\gamma_{\rm sp}(r)$ is the spike's slope.
The halo distribution can be written as the usual NFW profile[58]

$$\rho^{\rm NFW}_{\rm halo}(r) = \rho_s\left(\frac{r}{r_s}\right)^{-1}\left(1+\frac{r}{r_s}\right)^{-2}, \tag{3.8}$$

with $r_s = 18.6$ kpc and $\rho_s = \rho_\odot\left(\frac{R_\odot}{r_s}\right)\left(1+\frac{R_\odot}{r_s}\right)^2$, where $R_\odot = 8.2$ kpc is the Sun position and $\rho_\odot = 0.42$ GeV/cm$^3$ is the local DM mass density[174].
Finally, the prefactor $\left(1-\frac{2R_S}{r}\right)^{3/2}$ accounts for DM capture by the BH[175].
It is possible to find the radius at which the spike begins to grow, following Refs. [176, 177], according to which $R_{\rm sp} = 0.2R_{\rm h}$. Here, $R_{\rm h} = \frac{GM_{\rm BH}}{v_0^2}$ is the radius of gravitational influence of the SMBH that we are considering, which in this case is Sgr A$^*$ and $v_0$ is the dispersion in velocity of the stars populating the inner halo. Therefore, by using $M_{\rm BH} = 4.3\cdot 10^6 {\rm M}_\odot$, as mass of Sgr A$^*$[178] and $v_0 = (105 \pm 20)$ km s$^{-1}$ [179], then we can find that $R_{\rm sp} \simeq 0.34$ pc.

We now examine various benchmark DM density profiles in the vicinity of Sgr A$^*$

**Gondolo-Silk spike configuration**

Under the assumption of adiabatic growth of a peaked DM halo density around a central SMBH, neglecting all possible interactions with stars surrounding the BH, the value of $\gamma_{\rm sp}$ is predicted to be

$$\gamma^{\rm GS}_{\rm sp}(\gamma > 0) = \frac{9-2\gamma}{4-\gamma}, \tag{3.9}$$

which is valid for inner slopes in the range $1.5 \geq \gamma > 0$[175, 180].
Using the usual NFW density profile in Eq. (3.8), which corresponds to

$$\rho^{\rm NFW}_{\rm halo}(r) = \rho_\odot\left(\frac{R_\odot}{r_s}\right)^{\gamma}\left(1+\frac{R_\odot}{r_s}\right)^{3-\gamma}\left(\frac{r}{r_s}\right)^{-\gamma}\left(1+\frac{r}{r_s}\right)^{\gamma-3}\Bigg|_{\gamma=1}, \tag{3.10}$$

we find out that, in the Gondolo-Silk (GS) case, we have a spike slope of $\gamma_{\rm sp} = \frac{9-2\gamma}{4-\gamma}\Big|_{\gamma=1} = \frac{7}{3}$.

**Maximal stellar heating ($_*$MAX) spike configuration**

If we account for the presence of baryonic matter, such as stars, close to Sgr A$^*$, the gravitational interactions between DM and baryons tend to soften the spike density. According to Refs. [176, 181, 182] we can have a spike configuration with

$$\gamma^{*\rm MAX}_{\rm sp} = 1.5, \tag{3.11}$$

which essentially represents a modification of the GS case, due to the presence of baryonic matter in the vicinity of Sgr A$^*$.

**Minimal stellar heating ($_*$MIN) spike configuration**

According to Refs. [183, 184], since the mean separation between nuclear cluster stars is about 0.01 pc. Therefore, in this region we have minimal scattering between DM and stars, which allows to preserve the DM spike. This scenario of minimal stellar heating scenario is denoted as $_*$MIN, with

$$\gamma_{\rm sp}^{*\rm MIN} = \begin{cases} \dfrac{7}{3} & r < 0.01 \text{ pc} \\ 1.5 & r \geq 0.01 \text{ pc} \end{cases} , \tag{3.12}$$

Based on this framework, we can compute the expected positron injcetion rate within a sphere of radius $r$ arounf the GC.

### 3.2.2 Positron injection and propagation

According to Refs. [11, 185], we can find that the rate of positrons injected by DM in a sphere of radius $r$ and originated by annihilating self-conjugate DM, is given by the volume integral of the following source term

$$Q_e(\vec{x}, E_e) = \frac{\langle \sigma v \rangle}{2} \left( \frac{\rho_\chi(\vec{x})}{m_\chi} \right)^2 \frac{dN_e^{\rm ann}}{dE_e}, \tag{3.13}$$

where $\rho_\chi(\vec{x})$ is the DM density at the position $\vec{x}$, while $\frac{dN_e^{\rm ann}}{dE_e} = \delta(E - m_\chi)$ is the positron injection yield in the direct $\chi\bar{\chi} \to e^+e^-$ channel.
Using now Eqs. 3.5 and 3.13, it is possible to plot the DM density as a function of radial positions from the GC and the rate of positrons injected by DM within a sphere of radius $r$, as shown in Fig. 3.2.

It is now possible to repeat the same procedure as before, by choosing, however, a more peaked NFW density profile toward the GC, which can be obtained just by modifying the inner slope $\gamma$.
In particular, by adopting a generalized NFW density profile

$$\rho_{\rm halo}^{\rm NFW}(r) = \rho_\odot \left( \frac{R_\odot}{r_s} \right)^\gamma \left( 1 + \frac{R_\odot}{r_s} \right)^{3-\gamma} \left( \frac{r}{r_s} \right)^{-\gamma} \left( 1 + \frac{r}{r_s} \right)^{\gamma-3}, \tag{3.14}$$

with $\gamma > 1$, we basically enhances the central density of DM compared to the standard NFW case, whose inner slope is $\gamma = 1$. For instance, choosing $\gamma = 1.2$ results in a steeper inner profile, which significantly increases the DM density at small radii near the GC.
Recalling that the DM density profile is defined as in Eq. (3.5) and the spike configuration is defined as in Eq. (3.7), it is clear that, by using the generalized NFW density profile in Eq. (3.14), we end up with a different positron injection in the GC.
Specifically, the GS spike in Eq. (3.9) depends on the NFW's inner slope $\gamma$, so that for the generalized NFW density profile that we will consider in the following (with slope $\gamma = 1.2$), we get for GS that

$$\gamma_{\rm sp}^{\rm GS} = \frac{9 - 2\gamma}{4 - \gamma} \bigg|_{\gamma=1.2} = 2.357. \tag{3.15}$$

The $_*$MAX scenario, instead, represents a modification of the GS spike configuration, due to the gravitational heating caused by the nuclear star cluster and, therefore, due essentially to

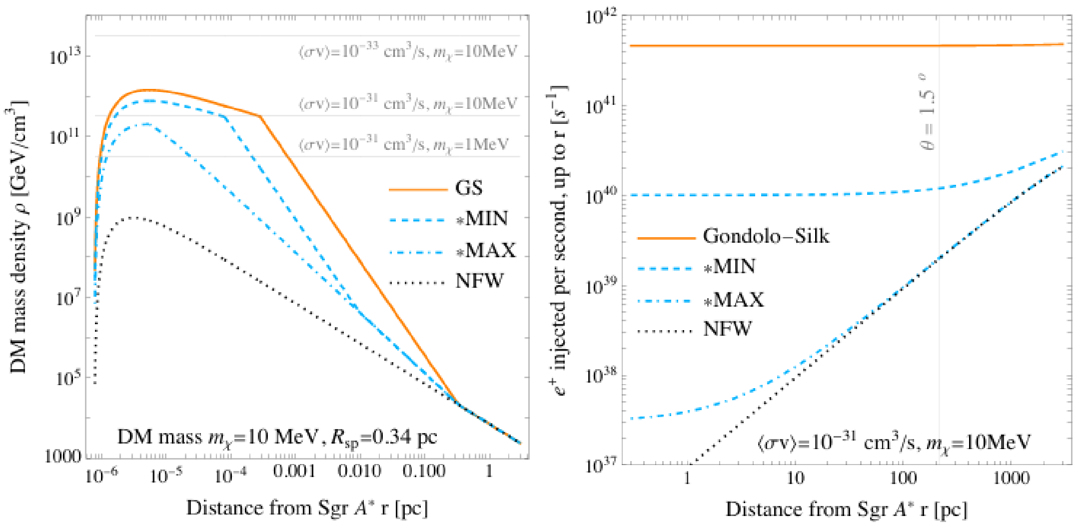


Figure 3.2: On the left, there is plotted the DM density as a function of radial positions from the GC and on the right, there is, instead, the rate of positrons injected by DM within a sphere of radius $r$, obtained by using an NFW halo density profile with $\gamma = 1$. In both figures, there are displayed the GS density profile in orange, the NFW density profile in black dotted, the $_*$MIN density profile in dashed blue and the $_*$MAX density profile in dash-dotted blue. Moreover, we take a DM mass $m_\chi = 10$ MeV and an annihilation cross section $\langle\sigma v\rangle = 10^{-31}$ cm$^3$/s. Eventually, in the left-hand plot the gray lines represent the saturation of DM density induced by different choices of $m_\chi$ and $\langle\sigma v\rangle$.
***Reprinted from "511 keV Galactic Photons from a Dark Matter Spike", by Pedro De la Torre Luque, Shyam Balaji, Malcom Fairbairn, Filippo Sala and Joseph Silk***[11].

the presence of baryonic matter surrounding Sgr A$^*$. This implies that, even by exploting a generalized NFW density profile with slope $\gamma = 1.2$, the $_*$MAX slope will remain as low as $\gamma = 1.5$.

Eventually, the $_*$MIN slope will be modified within a sphere of radius $r \simeq 0.01$ pc of the GC. In particular, we will have that

$$\gamma_{\rm sp}^{*\rm MIN} = \begin{cases} \left.\dfrac{9-2\gamma}{4-\gamma}\right|_{\gamma=1.2} & r < 0.01 \text{ pc} \\ 1.5 & r \geq 0.01 \text{ pc} \end{cases} . \tag{3.16}$$

By using again Eqs. 3.5 and 3.13, we can plot the DM density as a function of radial positions from the GC and the rate of positrons injected by DM within a sphere of radius $r$, by using a steeper NFW density profile ($\gamma = 1.2$), as shown in Fig. 3.3.

In the following subsection we will see that, fixing the positron injection rate within a sphere of radius $r$ around the GC to be $\simeq 2.5 \cdot 10^{42}$ s$^{-1}$[11], we can find the best-fit values of the thermally-averaged DM annihilation cross section, needed to explain the 511 keV line.

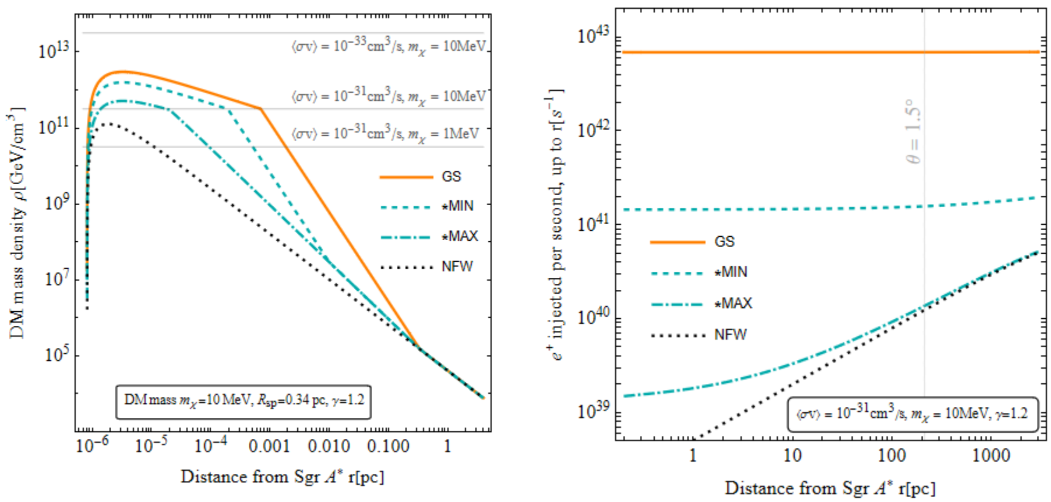


Figure 3.3: On the left, there is plotted the DM density as a function of radial positions from the GC and on the right, there is, instead, the rate of positrons injected by DM in a sphere of radius $r$, obtained by using a generalized NFW halo density profile with $\gamma = 1.2$. In both figures, there are displayed the GS density profile in orange, the NFW density profile in black dotted, the $_*$MIN density profile in dashed blue and the $_*$MAX density profile in dash-dotted blue. Moreover, we take a DM mass $m_\chi = 10$ MeV and an annihilation cross section $\langle\sigma v\rangle = 10^{-31}$ cm$^3$/s. Eventually, in the left-hand plot the gray lines represent the saturation of DM density induced by different choices of $m_\chi$ and $\langle\sigma v\rangle$.

### 3.2.3 DM annihilation cross sections for the 511 keV line

We now fix the thermally-averaged DM annihilation cross section $\langle\sigma v\rangle$, for self-conjugate DM annihilating into $e^-e^+$, to reproduce the 511 keV line for each of the DM profiles and spikes discussed in Sec. 3.2.1. This is achieved by requiring that the positron injection rate within a sphere of radius $r \lesssim 4$ kpc around the GC satisfies[11]

$$\int d^3x\, Q_e(\vec{x}, E_e)\Big|_{r \lesssim 4\ \mathrm{kpc}} \simeq 2.5 \cdot 10^{42}\ \mathrm{s}^{-1}, \tag{3.17}$$

where $Q_e(\vec{x}_e, E_e)$ is the source term defined in Eq. (3.13). Due to significant astrophysical uncertainties, we also compute the best-fit values of the thermally-averaged DM annihilation cross section $\langle\sigma v\rangle$ under the assumption that the positron injection rate within the same region is

$$\int d^3x\, Q_e(\vec{x}, E_e)\Big|_{r \lesssim 4\ \mathrm{kpc}} \simeq 10^{43}\ \mathrm{s}^{-1}. \tag{3.18}$$

The results are plotted in Fig. 3.4.

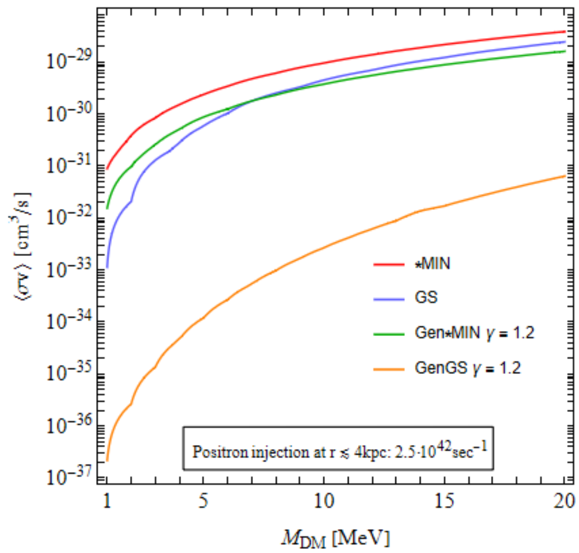


Figure 3.4: Thermally-averaged cross section $\langle\sigma v\rangle$ for DM annihilating into $e^-e^+$, needed to reproduce the 511 keV line, as a function of $M_{\rm DM}$ and for different density profiles. We present $\langle\sigma v\rangle$ for the standard (with NFW's inner slope $\gamma = 1$) $_*$MIN density profile in red, the Gondolo-Silk density profile in blue, the generalized $_*$MIN and the generalized Gondolo-Silk density profiles, both based on an NFW halo configuration with inner slope $\gamma = 1.2$, respectively in green and in orange. These results are obtained by requiring that the positron injection rate within a sphere of radius $r$ arounf the GC is $\simeq 2.5 \cdot 10^{42}$ s$^{-1}$. The best-fit values of $\langle\sigma v\rangle$ for a positron injection rate of $\simeq 10^{43}$ s$^{-1}$ within the same region are similar in magnitude and, therefore, we do no present them.

Alternative best-fit values for the dark matter annihilation cross section can be found in the literature. An example can be found in Ref. [167], which focus on two DM density profiles which are the Einasto profile, written as

$$\rho(r) = \rho_s \exp\left( - \left[ \frac{2}{\alpha} \left( \frac{r}{r_s} \right)^{\alpha} - 1 \right] \right) \tag{3.19}$$

and the generalized NFW configuration, written in Eq. (3.14).

In both cases $r$ represents the distance from the GC, while $\rho_s = \rho_\odot \left(\frac{R_\odot}{r_s}\right)^{\gamma} \left(1 + \frac{R_\odot}{r_s}\right)^{3-\gamma}$ is fixed by the requirement to reproduce the local dark matter density $\rho_\odot \simeq 0.4$ GeV/cm$^3$ at the Sun position $R_\odot \simeq 8.5$ kpc. Moreover, to fit the *Via Lactea II* simulation Ref. [167] fixes $\alpha = 0.17$, $r_s = 25.7$ kpc for the Einasto profile and $\gamma = 1.2$, $r_s = 26.2$ kpc for the generalized NFW configuration.

In particular, here we present the results for the the best-fit DM annihilation cross section found by Ref. [167] for the Einasto profile and the generalized NFW configuration, including in both scenarios the disk component from radioactive isotopes:

$$\begin{aligned} \langle\sigma v\rangle_\chi &= 5.1\cdot 10^{-25}\left(\frac{m_\chi}{\mathrm{GeV}}\right)^2 \mathrm{cm}^3/\mathrm{s} \quad \text{for Einasto + Disk contribution} \\ \langle\sigma v\rangle_\chi &= 6.1\cdot 10^{-26}\left(\frac{m_\chi}{\mathrm{GeV}}\right)^2 \mathrm{cm}^3/\mathrm{s} \quad \text{for NFW + Disk contribution} \end{aligned} \quad . \tag{3.20}$$

An alternative present in the literature is the work conducted by Ref. [11]. Here authors compare the predicted in-flight annihilation emission for DM masses of 2 to 50 MeV, with SPI and COMPTEL data in the $|l| < 30^o$ and $|b| < 15^o$ region of the sky, for a Gondolo-Silk and a *MIN DM spike benchmarks, both constructed using Eq. (3.5) and based on an NFW halo configuration with inner slope $\gamma = 1$. For each DM mass, they then perform a $\chi^2$ fit to the 511 keV longitudinal profile and normalize the $\langle\sigma v\rangle$ value to the best-fit, including the astrophysical disk component from stars.

We can summarize in Table 3.1 the best-fit DM annihilation cross section of Refs. [167] and [11] with our results, displayed in Fig. 3.4.

| | 2 MeV | 5 MeV | 10 MeV | 20 MeV | 50 MeV |
|---|---|---|---|---|---|
| Einasto + Disk | $2.0\cdot 10^{-30}$ | $1.3\cdot 10^{-29}$ | $5.1\cdot 10^{-29}$ | $2.0\cdot 10^{-28}$ | $1.3\cdot 10^{-27}$ |
| gNFW + Disk | $2.4\cdot 10^{-31}$ | $1.5\cdot 10^{-30}$ | $6.1\cdot 10^{-30}$ | $2.4\cdot 10^{-29}$ | $1.5\cdot 10^{-28}$ |
| Gondolo-Silk ($\gamma = 1$) | $5.1\cdot 10^{-34}$ | $5.6\cdot 10^{-33}$ | $3.4\cdot 10^{-32}$ | $2.0\cdot 10^{-31}$ | $2.0\cdot 10^{-30}$ |
| $_*$MIN($\gamma = 1$) | $1.5\cdot 10^{-31}$ | $1.4\cdot 10^{-30}$ | $7.5\cdot 10^{-30}$ | $9.6\cdot 10^{-29}$ | $3.3\cdot 10^{-28}$ |
| Gondolo-Silk ($\gamma = 1.2$) | $2.7\cdot 10^{-36}$ | $1.2\cdot 10^{-34}$ | $2.7\cdot 10^{-33}$ | $6.3\cdot 10^{-32}$ | $4.0\cdot 10^{-30}$ |
| $_*$MIN($\gamma = 1.2$) | $9.8\cdot 10^{-32}$ | $8.3\cdot 10^{-31}$ | $3.7\cdot 10^{-30}$ | $1.6\cdot 10^{-29}$ | $1.1\cdot 10^{-28}$ |

Table 3.1: Values of self-conjugate DM thermally-averaged annihilation cross sections $\langle\sigma v\rangle$ in units of $\mathrm{cm}^3\mathrm{s}^{-1}$ for different DM density profiles. Specifically, the first two lines of the table report the values of $\langle\sigma v\rangle$ for the Einasto and the generalized NFW profile with inner slope $\gamma = 1.2$, taken from Ref. [167] and both including the disk component from radioactive isotopes. The third and fourth line of the table report values of $\langle\sigma v\rangle$ for the Gondolo-Silk and the $_*$MIN density profiles, taken from Ref. [11], both based on an NFW halo configuration with inner slope $\gamma = 1$ and including the disk component from stars. Eventually, in the last two lines we present the values of $\langle\sigma v\rangle$ for the Gondolo-Silk and the $_*$MIN density profiles, obtained through the procedure delined in Sec. 3.2.3 and both based on an NFW halo configuration with inner slope $\gamma = 1.2$. Our result represents an extension of the work presented in Ref. [11].

The DM annihilation cross sections presented in Fig. 3.4 are significantly smaller than those required for thermal freeze-out in $s$-wave annihilation models, which are of the order of $\langle\sigma v\rangle \sim 10^{-26}\mathrm{cm}^3/\mathrm{s}$ to reproduce the observed DM relic abundance[54].
This discrepancy implies that either the annihilation mechanism must be velocity-suppressed, like in the case of $p$-wave annihilation model, or that dark matter interacts via more complex mechanisms inducing a late-time suppression of the annihilation rate, such as the one involving coannihilation between nearly-degenerate DM states.
We will explore these possibilities respectively in Chapters 4 and 5, updating and extending the work of Ref. [171].

It is worth noting that other mechanisms could also allow to explain the 511 keV gamma-ray line from the GC while matching the observed DM relic abundance. For instance, $e^-e^+$ annihilation might be only one of the annihilation channels open to dark matter.
Alternatively, as discussed in Ref. [186], a thermally produced light DM candidate may annihilate into axion-like particles, whose subsequent decay produces multiple $e^-e^+$ pairs. This significantly reduced the kinetic energy of the injected positrons, making this scenario compatible with observational constraints. In this framework, DM annihilation proceeds via a $p$-wave channel, $\chi\bar{\chi} \to aa$, which dominates during freeze-out due to a sufficiently high DM relative velocity, and via an $s$-wave channel, $\chi\bar{\chi} \to aaa$, which is relevant at late times.

In the following Chapters we will use the results obtained so far to present two classes of DM models which could explain the 511 keV line from the GC, while simultaneously reproducing the observed DM relic abundance and remaining compatible with current experimental and observational constraints. Specifically, we discuss a $p$-wave annihilation DM model in Chapter 4 and a coannihilation DM model, involving nearly-degenerate DM states in Chapter 5.

# 4

# $p$-wave annihilation model

The persistent observation of the 511 keV gamma-ray line from the GC, nowadays firmly attributed to electron-positron annihilation into photons via para-positronium formation, remains one of the most intriguing and puzzling astrophysical anomalies. In the same way, the nature of DM remains elusive and represents a central open question in physics. Therefore, given these two misteries, it is natural to entertain the possibility that they are somehow interconnected.

According to Refs. [166–168], the morphology of the signal excludes DM decays in favor of annihilations.
Building QFT models, which explain DM annihilation into pairs of electrons and positrons, represents thus an interesting way to explain the signal in the GC. However, $s$-wave annihilation models face strong observational constraints, as they typically lead to an overproduction of low-energy positrons. This would result in a 511 keV flux significantly exceeding what is observed by experiments such as INTEGRAL/SPI, making such models incompatible with current data.
In order to overcome this problem, it is natural to think at models in which DM annihiliation into $e^-e^+$ pairs are late-time suppressed.
For example, we can realize this idea with models where the DM relic abundance is set by $p$-wave annihilations, whose cross section is velocity-dependent, which means that $\langle \sigma v \rangle \propto v^2$. This velocity suppression naturally reduces the annihilation rate at late times, making it consistent with cosmological observations and with the idea that DM models may explain the 511 keV signal in the GC.

## 4.1 $p$-wave dark matter model for the 511 keV Line

In this section, we analyze a $p$-wave annihilation dark matter model capable of simultaneously explaining the measured DM relic density and the 511 keV gamma-ray emission observed from the GC, ensuring consistency with experimental and observational constraints.

### 4.1.1 Relic abundance and 511 keV line

In Sec. 3.1.1 we have said that the observed 511 keV signal in the GC, attributed to $e^-e^+$ annihilation into photons via para-positronium formation, is strongly peaked and corresponds to a flux of $\simeq 10^{-3}$ photons cm$^{-2}$ s$^{-1}$.

In Sec. 3.2.1 we discussed different benchmarks for the DM density profile and their implications for the DM annihilation cross section. In the following, we start discussing the $p$-wave model under consideration employing the same DM density profile of Ref. [171], as later we will update that study with new limits that were not considered there, such as those from supernovae and DM self-interactions, and updating limits that improved in the meantime like those from NA64.
Therefore, using the best-fit provided in Ref. [167] for an NFW DM density profile, it is possible to explain the 511 keV signal in the GC, through self-conjugate DM annihilations into an $e^- e^+$ pair with

$$\langle \sigma v \rangle_{511} \simeq 5 \cdot 10^{-31} \left( \frac{M_{\rm DM}}{3 \text{ MeV}} \right) \frac{\text{cm}^3}{\text{s}}. \tag{4.1}$$

However, as discussed in Sec. 3.2.1, it is also possible to entertain the idea that DM density is accreted by the supermassive black hole at the center of the Milky Way, forming a density spike. In this case, we can parametrize the DM density profile as in Eq. (3.5). As discussed in Sec. 3.2.3 and following Ref. [11], we impose that the positron injection rate within a sphere of radius $r \lesssim 4$ kpc around the GC satisfies Eq. (3.17). For each DM density profile discussed in Sec. 3.2.1, this condition allows to find the best-fit values of the thermally-averaged self-conjugate DM annihilation cross section, needed to reproduce the 511 keV line. The results obtained from this procedure are displayed in Fig. 4.4 and they can be used to extend the discussion of Ref. [171].

For a $p$-wave dominated process we can write the thermally-averaged annihilation cross section as $\langle \sigma v \rangle = b_p \langle v_{\rm rel}^2 \rangle$, where $b_p$ is independent of $v_{\rm rel}$, which is the relative velocity between DM particles. The constant term $b_p$ is fixed by the requirment of realizing the observed DM abundance and its behaviour in terms of $M_{\rm DM}$ is plotted in the right panel of Fig. 2.5.

We can fit both the observed DM abundance and the 511 keV gamma-ray line from the GC by imposing that

$$b_p \langle v_{\rm rel}^2 \rangle = \langle \sigma v \rangle_{511}. \tag{4.2}$$

### 4.1.2 A concrete setup

Let us realize a model in which we consider a Majorana fermion $\chi$ as DM candidate, which interacts with electrons via a real scalar $S$ as described by the following Lagrangian written in 2-component spinor notation[171]:

$$\mathscr{L} = \frac{1}{2} y_D \chi^2 S + g_e e_L e_R^\dagger S + \text{h.c.} \tag{4.3}$$

Following the procedure delined in App. B, we can rewrite this latter Lagrangian in 4-component spinor notation as:

$$\mathscr{L} = \frac{1}{2} y_D \bar{\psi}_{DM} \psi_{DM} S + g_e \bar{e} e S. \tag{4.4}$$

We prefer to make this conversion because it is preferable to work in 4-component spinor notation since calculations of cross sections are clearer.

On the basis the Lagrangian written in Eq. (4.4), we can compute the cross section for the DM annihilation into $e^-e^+$ as

$$\sigma v_{\chi\chi\to e^-e^+} = v_{\rm rel}^2 \frac{(y_D g_e)^2}{8\pi} \frac{M_{\rm DM}^2\left(1-\frac{m_e^2}{M_{\rm DM}^2}\right)^{3/2}}{(m_S^2-4M_{\rm DM}^2)^2+m_S^2\Gamma_S^2}, \tag{4.5}$$

with the decay rate of $S$ which is defined as

$$\Gamma_S = \Gamma_{S\to\chi\chi}+\Gamma_{S\to e^-e^+} = \frac{g_e^2}{8\pi}m_S\left(1-\frac{4m_e^2}{m_s^2}\right)^2+\frac{y_D^2}{16\pi}m_S\left(1-\frac{4m_\chi^2}{m_S^2}\right)^2, \tag{4.6}$$

where we have used Eqs. B.93, B.96 and $m_\chi \equiv M_{\rm DM}$. Moreover, the full computation of Eq. (4.5) can be found in App. B.2.1.

The cross section for the $\chi e^\pm \to \chi e^\pm$ is

$$\sigma_{\chi e^\pm\to\chi e^\pm} = \frac{(y_D g_e)^2}{\pi}\frac{\mu_{\rm eDM}^2}{m_S^4}, \tag{4.7}$$

where $m_S$ is the mass of the new scalar, added in the toy model whose Lagrangian is written in Eq. (4.4), while $\mu_{\rm eDM} = \frac{m_e M_{\rm DM}}{m_e+M_{\rm DM}}$ is the DM $-$ e reduced mass.
The corresponding full computation can be found in App. B.2.1.

We are going to exploit the cross sections written in Eqs. (4.5) and (4.7) to study the phenomenology of the $p$-wave model we are analyzing to explain the 511 keV gamma-ray line from the GC. First, however, we quickly go through the experimental and observational limits that constrain the $p$-wave model we are anlyzing.

### 4.1.3 Accelerator, direct detection, self-interactions and cosmology

In Sec. 2.4, we reviewed the various observational and experimental limits, such as those from direct detection experiments, collider searches and astrophysical observations, that constrain the properties and interaction cross sections of dark matter candidates across a range of masses. Here, we briefly discuss the specific constraints that apply to the $p$-wave annihilation model under consideration.

#### Collider searches

As briefly mentioned in Sec. 2.4.3, the NA64 experiment at the CERN SPS is a powerful fixed-target experiment designed to search for light, weakly interacting particles such as dark photons. By analyzing events with large missing energy, indicative of particles that escape detection, NA64 has set some of the strongest constraints on invisibly decaying dark photons in the MeV-GeV mass range [102]. These limits are particularly relevant for models where dark matter couples to Standard Model particles through a light mediator.

In the context of the $p$-wave annihilation model we are analyzing, the mediator is not a dark photon but a scalar $S$, which decays predominantly into dark matter particles. Since the original NA64 bounds are derived for dark photons, they cannot be directly applied to our scalar case. However, as proposed in Ref. [171], these constraints can be recast for scalar mediators by relating their coupling $g_e$ to the effective dark photon kinetic mixing parameter $\epsilon$.

Specifically, in Ref. [102], an upper bound on the kinetic mixing $\epsilon < \epsilon_{\text{limit}}(m_V)$ is derived as a function of the dark photon mass $m_V$. In analogy, Ref. [171] translates this into a bound on the scalar coupling $g_e$ by imposing

$$g_e(m_S) < C_S \; e \; \epsilon_{\text{limit}}(m_S), \tag{4.8}$$

where $e$ is the elementary electric charge, while $C_S$ is a proper dimensionless coefficient computed in Ref. [171] and set equal to $C_S = 1.6$.

These recast limits are shown in Fig. 4.1, and represent stringent experimental constraints on the scalar coupling $g_e$ in the MeV-scale regime, significantly narrowing the viable parameter space of the $p$-wave annihilation model.

**Direct detection constraints**

The p-wave annihilation model, characterized by a velocity-suppressed cross section, is subject to direct detection constraints primarily from experiments such as XENON1T, SENSEI, and DAMIC-M. These experiments search for dark matter-electron scattering signals and set strong upper limits on the dark matter-electron elastic scattering cross section, particularly in the sub-GeV mass range.

In the following sections we present direct detection limits taken from Ref. [97], along with projected sensitivities for SENSEI[95], DAMIC-M[187], Obscura[188] and JUNO[189].

For a more detailed discussion about direct detection limits refer to Sec. 2.4.1.

**Limits on dark matter self-interactions**

As discussed in Sec. 2.2.1, DM self-interactions may play a central role in solving some astrophysical issues, such as the core-cusp, the diversity, the missing satellites and the too-big-to-fail problems. However, in order to solve those tensions with DM self-interactions and be at the same time consistent with cluster limits, one should have self-interactions which depend on the environment, like for example on the DM velocity[56]. This is not the case in the $p$-wave model we are considering. Therefore, here, we just impose the limit from Bullet Cluster data. In particular, to remain consistent with those observations, we should require that $\frac{\sigma_{\text{self}}}{M_{\text{DM}}} \lesssim 1 \frac{\text{cm}^2}{\text{g}}$, where we recall that $\sigma_{\text{self}}$ and $M_{\text{DM}}$ are respectively the self-interacting DM cross section and its mass. Specifically, we can compute $\sigma_{\text{self}}$, as derived in App. B.2.1

$$\sigma_{\chi\chi\to\chi\chi} = \frac{y_D^4 M_{\text{DM}}^2}{8\pi m_S^4}, \quad \frac{\sigma_{\text{self}}}{M_{\text{DM}}} \lesssim 1 \frac{\text{cm}^2}{\text{g}} \implies y_D^4 \lesssim \frac{8\pi m_S^4}{M_{\text{DM}}} \frac{\text{cm}^2}{\text{g}} \tag{4.9}$$

This allows to obtain further limits which significantly constrain the phenomenology of the $p$-wave model we are analyzing, as we can see from the right panel of Fig. 4.1.

**Supernova bounds**

Moreover, following the analysis in Ref. [109] and in Sec. 2.4.5, it is possible to further constrain the phenomenology of the $p$-wave model under consideration, based on supernova cooling studies.

We recall very quickly that, as discussed in Sec. 2.4.5, supernova cooling limits are derived on the basis of the Raffelt criterion, which constrains the emission rate of BSM particles from the supernova core. Therefore, new BSM particles cannot carry away more energy than neutrinos do.
In the context of models discussing leptophilic scalars $\phi$, which couple only to leptons through an interaction term $y_e \phi \bar{e} e$, Ref. [109] derived bounds on the electrons-to-scalars coupling $y_e$, which are particularly stringent in the resonant production regime, which corresponds to the region of the DM parameter space where the mass of the scalar satisfies $m_\phi < \omega_p \simeq \mathcal{O}(10 \text{ MeV})$.

In the $p$-wave model under consideration we have a scalar $S$, which couples to SM electrons through an interaction term of the form $g_e S \bar{e} e$. Therefore, we can apply to this model SN 1987A constraints, discussed in Sec. 2.4.5 and derived in Ref. [109].

The results of this procedure are displayed in the right panel of Fig. 4.1.

**Non-perturbativity of the dark coupling**

Least but not last, the computation of the cross sections in Eqs. (4.5) and (4.7) relies on the application of Feynman rules within the framework of perturbative quantum field theory. Therefore, it is essential to remain within the perturbative regime to ensure the validity of these calculations. This implies that the coupling constants involved in the interactions must be sufficiently small for the perturbative expansion to converge, and higher-order loop corrections are assumed to be subdominant compared to the leading tree-level contributions. Deviations from this regime could invalidate the perturbative approach and require more advanced treatment beyond the scope of standard Feynman diagram analysis.

To this end, in order to remain safely within the perturbative regime, we impose that the dark coupling satisfies $y_D \lesssim 3$. As we will see in the following sections, the scalar-to-electron coupling $g_e$ is always significantly smaller than $y_D$ and thus easily remains within the perturbative regime.

After this brief introduction, we are now ready to delve into the phenomenology of the $p$-wave dark matter model under consideration.

## 4.2 Phenomenology of the $p$-wave model for the 511 keV line

Having established the theoretical framework of the $p$-wave model introduced in Sec. 4.1.2, we now proceed to analyze its phenomenological implications and confront it with current experimental and observational constraints. This section aims at identifying the viable regions of the parameter space that are consistent with both the observed dark matter relic abundance and the 511 keV gamma-ray line from the GC.

The annihilation cross section in Eq. (4.5) is velocity-dependent and therefore can be written as

$$\langle\sigma v\rangle_{\chi\chi\to e^-e^+} = b_{\chi\chi\to e^-e^+} v_{\rm rel}^2, \tag{4.10}$$

where $v_{\rm rel}$ is the relative velocity between DM particles.
Following the procedure delined in Sec. 4.1.1, we fix the $b_{\chi\chi\to e^-e^+}$ by imposing to match the observed DM relic abundance, see the right panel of Fig. 2.5. Thereafter, we ask to fit the 511 keV signal from the GC by imposing

$$b_{\chi\chi\to e^-e^+} \underbrace{\langle v_{\rm rel}^2\rangle_{\rm bulge}}_{(1.1\cdot 10^{-3})^2} = \langle\sigma v\rangle_{511}, \tag{4.11}$$

where, as in Ref. [171], we have used the value obtained from the velocity dispersion in the bulge, that is $\sigma \simeq 140$ km/s[190].
The requirement of fitting both the DM relic abundance, as in Eq. (4.10), and the 511 keV gamma-ray line from the GC, as in Eq. (4.11), selects a unique value of $M_{\rm DM}$. Specifically, by using $\langle\sigma v\rangle^{(p)}_{\rm relic}(M_{\rm DM} = 2\ {\rm MeV}) \simeq 2.2 \cdot 10^{-25} v_{\rm rel}^2\ {\rm cm}^3/{\rm s}$ from Ref. [54], we get that

$$M_{\rm DM}^{(p)} \simeq 2\ {\rm MeV} \frac{\langle v_{\rm rel}^2\rangle^{1/2}_{\rm bulge}}{1.1\cdot 10^{-3}}, \tag{4.12}$$

where we have normalised $\langle v_{\rm rel}^2\rangle^{1/2}_{\rm bulge}$ to $\sigma \simeq 140$ km/s from Ref. [190].

Once the annihilation cross section $\sigma v_{\chi\chi\to e^-e^+}$ and the DM mass $M_{\rm DM}$ are fixed by the requirement to fit respectively the 511 keV line and the observed DM relic abundance, we only have two left parameters to fix, which we can choose as $g_e$ and $m_S$. The result obtained from Ref. [171] is plotted in the left panel of Fig. 4.1.

Ref. [171] also mentions that the fact to have $M_{\rm DM}$ and $m_S$ of few MeV is not in conflict with cosmological data, provided to have a small injection of neutrinos in the early universe in a proportion $\sim 1 : 10^4$ to the electron injection[84, 85].
As proposed in Ref. [171], this can be obtained by adding a coupling with neutrinos, of the form $g_\nu \bar{\nu}\nu S$ of size $g_\nu \sim 10^{-2} g_e$, where $g_e \sim 10^{-6}$, which is in the region allowed by the variuos limits in Fig. 4.1.
In particular, it is possible to obtain the couplings to neutrinos and electrons through electroweak-invariant completion of the Lagrangian in Eq. (4.4) (see App. B of Ref. [171]).

In this thesis we have introduced some corrections to the previous work presented in Ref. [171]. First of all, we have derived expressions for the cross sections in Eqs. (4.5) and (4.7) that are identical in form to those presented in Ref. [171]. However, in our derivation, we have corrected an inconsistency in the normalization of the DM-S interaction term in Eq. (4.4), where we have included the appropriate factor of $\frac{1}{2}$. This ensures the correct normalization of the Lagrangian and leads to accurate cross section results. In contrast, Ref. [171] uses a Lagrangian without this normalization factor, which introduces an overall error of a factor of 4 in the final expressions for the cross sections.

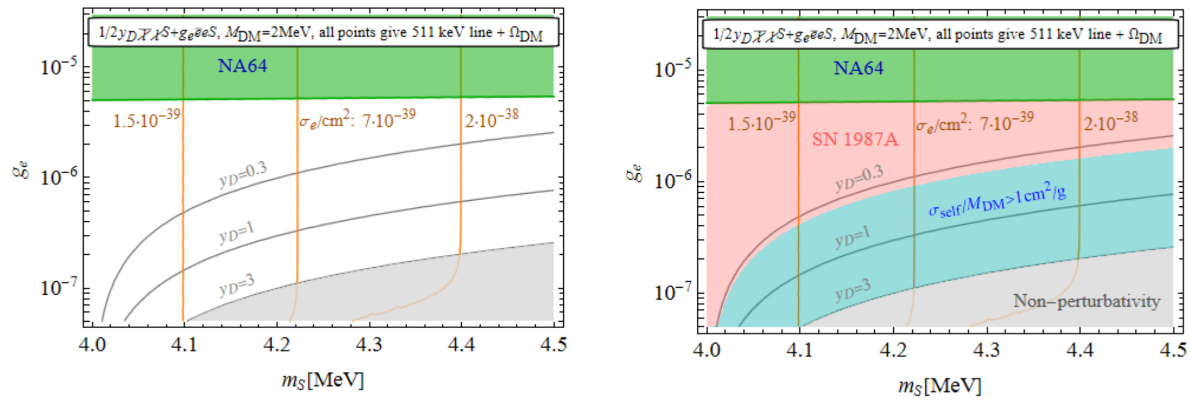


Figure 4.1: The phenomelogy of the model is completely determined by the mass of the scalar $m_S$ and the coupling to electrons $g_e$ once we require to fit both the 511 keV line as in Eq. (4.1) and the observed DM relic abundance as in Eq. (4.12). In the plot there are several constraints: the gray area delimits the region of the parameter space where the dark coupling $y_D$ is no longer perturbative, the green area represents the recast of NA64 dark photon limits[102]. Moreover, orange lines are contours of constant $\sigma_{\chi e^\pm \to \chi e^\pm} \equiv \sigma_e$, while the gray lines are contours of constant dark coupling $y_D$. In these plots, NA64 constraints are updated with respect to the ones used in Ref. [171]. In the right panel we have furter constraints from SN 1987A (pink area) and DM self-interactions (cyan area).

Furthermore, we have updated the results obtained by Ref. [171] by adding further constraints, such as those from SN 1987A and DM self-interactions and updating limits that improved in the meantime, like NA64.
Finally, the plots shown in Fig. 4.1 rely on the cross sections in Eqs. (4.5) and (4.7), which are obtained by performing a Taylor expansion around $v_{\rm rel} \simeq 0$. However, as discussed in Sec. 2.3.2, this procedure is no longer valid near a resonance, like in the scenario depicted in Fig. 4.1.
To address this issue, we provide an updated treatment in Secs. 4.2.2, where we properly account for the DM resonant behaviour, based on the procedure delined in App. C and reported in part in Sec. 4.2.2.

Before delving into the discussion of the dark matter resonant behaviour in Sec. 4.2.2, we first briefly examine the range of dark matter masses that could account for the 511 keV line from the GC within the $p$-wave model under consideration.

### 4.2.1 DM masses predicted by the $p$-wave model

In Sec. 4.1.1 we claimed that the requirement to fit both the observed DM abundance and the 511 keV gamma-ray line from the GC is satisfied by Eq. (4.2), where, as done above, we use $v_{\rm rel} \simeq 1.1 \cdot 10^{-3}$ as relative velocity between DM particles and the coefficient $b_p$ is fixed by the requirement of mathcing the observed DM abundance for a $p$-wave dominated process (see the right panel of Fig. 2.5).
This procedure allows to select a unique value of $M_{\rm DM}$ for each analyzed benchmark of the DM density profile, which realizes consistently the scenario in the non-resonance regime, discussed

more in detail later in Sec. 4.2.2.
Near the resonance, instead, the treatment will be quite different, as we will see more in detail later.

A general lesson that we can take from Ref. [11] is that only DM masses in the range 1 MeV $\lesssim M_{\rm DM} \lesssim$ 20 MeV can account for the 511 keV gamma-ray line from the GC. Indeed, Fig. 6 of Ref. [11] shows the predicted diffuse gamma-ray emission from the DM signals fitted to the 511 keV line profile, compared to experimental measurements by SPI and COMPTEL in the region $|b| < 15^{\rm o}$ and $|l| < 30^{\rm o}$.
It is possible to notice that masses up to $M_{\rm DM} \sim 20$ MeV seem to be well compatible with the current measurements of the diffuse gamma-ray galactic flux, while higher masses will significantly exceed the experimental data, such as those from COMPTEL observations. For this reason, we restrict the DM parameter space to masses 1 MeV $\lesssim M_{\rm DM} \lesssim$ 20 MeV.

We present in Table 4.1 some of the possible DM masses, in the range 1 MeV $\lesssim M_{\rm DM} \lesssim$ 20 MeV, which could succesfully explain the 511 keV line, while matching the observed DM abundance.

| DM density profile | DM mass (MeV) |
|---|---|
| $_*$MIN($\gamma = 1.2$) | 2.90 |
| Gondolo-Silk ($\gamma = 1$) | 3.79 |
| Gondolo-Silk ($\gamma = 1.1$) | 9.62 |
| Gondolo-Silk ($\gamma = 1.17$) | 20.00 |

Table 4.1: Dark matter masses selected to consistently reproduce both the observed DM relic abundance and the 511 keV gamma-ray line from the Galactic Center, for different benchmark dark matter density profiles. These values are obtained in the non-resonant regime by imposing Eq. (4.2), with the relative velocity between DM particles fixed at $v_{\rm rel} \simeq 1.1 \cdot 10^{-3}$, corresponding to the velocity dispersion in the Galactic bulge ($\sigma \simeq 140$ km/s)[190]. Furthermore, the coefficient $b_p$ is fixed by the requirement of matching the observed DM relic abundance for a $p$-wave dominated process (see the right panel of Fig. 2.5). Here, we use the best-fit values of the thermally-averaged DM annihilation cross sections $\langle \sigma v \rangle$ derived by requiring that the positron injection rate within a sphere of radius $r$ around the GC is $\simeq 2.5 \cdot 10^{42}$ s$^{-1}$. These best-fit values of $\langle \sigma v \rangle$ are plotted in Fig. 3.4.

This procedure generalises the study of Ref. [171] by allowing to derive more general lessons from it, that take into account the astrophysical uncertainties.
Moreover, we can notice that for specific choices of DM density profiles, it is possible to select DM masses $M_{\rm DM} > 10$ MeV, which in general do not need an extra injection of neutrinos in the early universe to be consistent with cosmological data, as discussed in Sec. 4.2.

### 4.2.2 Exploring resonant annihilation in dark matter $p$-wave models

In App. C, we discuss resonant enhancements of the dark matter annihilation cross section, focusing on how the velocity dependence near the resonance condition affects thermal freeze-out and positron injection rates. We introduce a small parameter $\epsilon \ll 1$, which parametrizes deviations from unity in the ratio $\frac{m_S}{2M_{\rm DM}}$, such that $\frac{m_S}{2M_{\rm DM}} = 1 + \epsilon$.

Depending on the value of $\epsilon$, different approximations are used to compute the DM thermally-averaged annihilation cross section. Specifically, three main regimes are identified:

- *Large-$\epsilon$ regime ($\epsilon \geq 0.27$)*: for those value of $\epsilon$ the system is far enough that the usual low-velocity expansion around $v_{\rm rel} \simeq 0$ is valid. In this case, the expressions for the cross sections in Eqs. (4.5) and (4.7) can be safely used to match the observed DM relic abundance and explain the 511 keV gamma-ray line from the GC.

- *Intermediate-$\epsilon$ regime ($0.0064 \lesssim \epsilon \leq 0.27$)*: in this region neither the low-velocity nor the resonant approximation works well. A full thermal average of the DM annihilation cross section must be performed numerically without relying on expansions.

- *Small-$\epsilon$ regime ($5.3 \cdot 10^{-5} \lesssim \epsilon \lesssim 0.0064$)*: for those values of $\epsilon$ the system is very close to the resonance region, and the low-velocity expansion breaks down. In this case, the thermally-averaged DM annihilation cross section can be approximated as:

$$\begin{aligned} \langle \sigma v \rangle_{511} &\simeq \frac{y_D^2 g_e^2}{2\pi M_{\rm DM}^2}\left(1-\frac{m_e^2}{M_{\rm DM}^2}\right)^{3/2}\frac{\langle v_{\rm rel}^2\rangle}{64\epsilon^2}, \quad \langle v_{\rm rel}^2\rangle \simeq (1.1\cdot 10^{-3})^2; \\ \langle \sigma v \rangle_{\rm fo} &\simeq \frac{y_D^2 g_e^2}{2\pi M_{\rm DM}^2}\left(1-\frac{m_e^2}{M_{\rm DM}^2}\right)^{3/2}\left\langle \frac{1}{v_{\rm rel}^2}\right\rangle, \quad \left\langle \frac{1}{v_{\rm rel}^2}\right\rangle = \frac{x_{\rm fo}}{2}. \end{aligned} \tag{4.13}$$

  as derived in App. C. Specifically, $\langle \sigma v \rangle_{511}$ and $\langle \sigma v \rangle_{\rm fo}$ are used respectively to fit the 511 keV line today and the observed DM relic abundance.

  We consider $\epsilon \sim 5.3 \cdot 10^{-5}$ as lower limit of the small-$\epsilon$ regimes, because for $\epsilon$ smaller than that value we cannot explain anymore the 511 keV line, while matching the observed DM abundance, as we would have $\langle \sigma v \rangle_{511} \gtrsim \langle \sigma v \rangle_{\rm fo}$, which is not what we desire in this thesis.

In this work we do not focus on the intermediate-$\epsilon$ regime, but rather on the large- and small-$\epsilon$ regime, both discussed in the following paragraphs.

Moreover, as already mentioned in Sec. 4.1.1, assuming that DM form a density spike toward the GC due to Sgr A$^*$ accretion, for each DM density profile discussed in Sec. 3.2.1 we can find the best-fit values of $\langle \sigma v \rangle_{511}$ requiring that the positron injection rate within a sphere of radius $r$ around the GC satisfies Eq. (3.17).
Specifically, for the work presented in the following paragraphs, we adopt as benchmark choices, both in the $5.3 \cdot 10^{-5} \lesssim \epsilon \lesssim 0.0064$ and the $\epsilon \geq 0.27$ regimes, the best-fit values of $\langle \sigma v \rangle_{511}$ obtained for the Gondolo-Silk density profile, which is based on an NFW halo configuration with inner slopes $\gamma = 1.1$ and $\gamma = 1.14$. In particular, we choose these profiles because they allow for larger values of $M_{\rm DM}$ (compared to the $M_{\rm DM} \simeq 2$ MeV scenario discussed in Sec. 4.2), when matching the observed dark matter relic abundance, while still remaining within the preferred mass range 1 MeV $\lesssim M_{\rm DM} \lesssim$ 20 MeV.
Furthermore, DM density profiles based on an NFW halo configuration with inner slope $\gamma > 1.14$ would yield DM parameter spaces which are highly constrained in the small-$\epsilon$ regime, where $5.3 \cdot 10^{-5} \lesssim \epsilon \lesssim 0.0064$. To better analyze the phenomenological implications of these steeper DM density profiles we should go to the $0.0064 \lesssim \epsilon \lesssim 0.27$ regime, which, however,

is not discussed in this thesis. For this reason we present the analysis for Gondolo-Silk density profiles based on an NFW halo configuration with inner slopes $\gamma = 1.1$ and $\gamma = 1.14$ as benchmark choices.

### The non-resonance regime

In this paragraph we focus on the large $\epsilon$ regime ($\epsilon \geq 0.27$), where the system is far enough from the resonance condition and, therefore, we can safely expand the DM annihilation cross section around $v_{\rm rel} \simeq 0$ as it is usually done.

We manage to obtain the observed DM relic abundance and explain the 511 keV gamma-ray line from the GC, by essentially following the procedure delined in Sec. 4.1.1 and in a more detailed way in Sec. 4.2. A difference, though, stays in the fact that instead of adopting the best-fit value of $\langle \sigma v \rangle_{511}$, provided in Ref. [167] and written in Eq. (4.1), we employ the updated values derived using the procedure delined in Sec. 3.2.3, specifically for the Gondolo-Silk density profile based on an NFW configuration with inner slopes $\gamma = 1.1$ and $\gamma = 1.14$, for the reason explained above. The results obtained from this procedure are shown in Fig. 4.2.

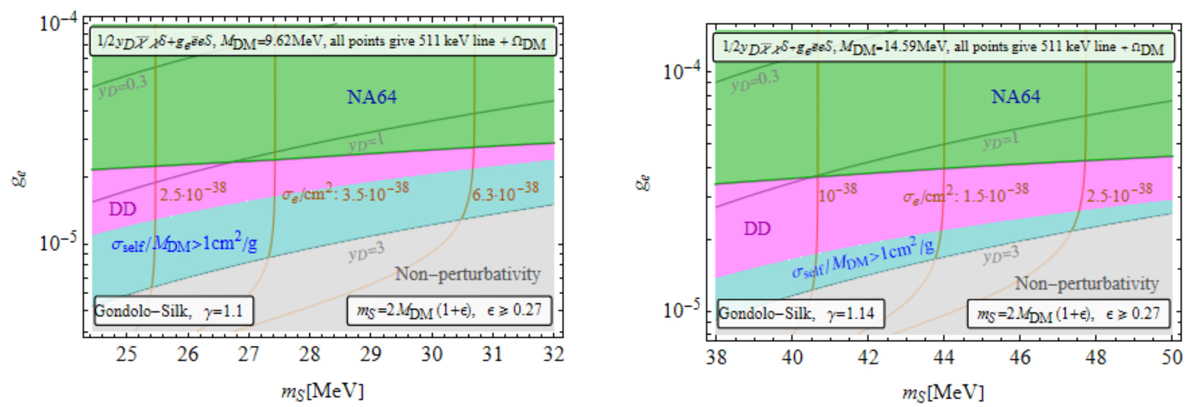


Figure 4.2: The phenomelogy of the model is completely determined by the mass of the scalar $m_S$ and the coupling to electrons $g_e$ once we require to fit both the 511 keV line and the observed DM relic abundance. In the plot there are several constraints: the cyan area represents limits coming from the requirement that the DM self-interacting cross section satisfies $\frac{\sigma_{\rm sel}}{M_{\rm DM}} \lesssim 1 \frac{\rm cm^2}{\rm g}$, the gray area delimits the region of the parameter space where the dark coupling $y_D$ is no longer perturbative, the green area represents the recast of NA64 dark photon limits[102] and the magenta area represents direct detection limits[97]. Moreover, orange lines are contours of constant $\sigma_{\chi e^\pm \to \chi e^\pm} \equiv \sigma_e$, while the gray lines are contours of constant dark coupling $y_D$. We assume that DM follows a Gondolo-Silk density profile based on an NFW halo configuration with inner slope of $\gamma = 1.1$ (left panel) and $\gamma = 1.14$ (right panel). We also assume that the positron injection rate within a sphere of radius $r \lesssim 4$ kpc around the GC is $\simeq 2.5 \cdot 10^{42} {\rm s}^{-1}$. We notice that the p-wave model under consideration is significantly constrained by experimental limits in the large-$\epsilon$ regime. For this reason, we should analyze the model in the small-$\epsilon$ regime to capture physical information.

**The resonance regime**

In this paragraph, we focus on the regime $5.3 \cdot 10^{-5} \lesssim \epsilon \lesssim 0.0064$, where the phenomenological treatment differs significantly from the one used in previous analyses. In this region, the low-velocity expansion around $v_{\rm rel} \simeq 0$ no longer provides reliable results. Consequently, the approximation used so far for the $\chi\chi \to e^- e^+$ cross section should be revised.
Following the procedure outlined in App. C, we instead rely on the thermally-averaged cross sections given in Eq. (4.13) to simultaneously fit the 511 keV gamma-ray line from the Galactic Center and reproduce the observed dark matter relic abundance. However, in contrast to previous analyses that made use of data from Ref. [54], we cannot apply the standard approach based on a Taylor expansion of the cross section in powers of $v_{\rm rel}$, which yields

$$\sigma v \simeq a_s + b_p v_{\rm rel}^2 + \mathcal{O}(v_{\rm rel}^4). \tag{4.14}$$

In particular, as written in Eq. (4.13), the thermally-averaged DM annihilation cross section in the resonance regime is given by

$$\langle \sigma v \rangle_{\rm fo} = c_{\rm fo} \frac{x_{\rm fo}}{2}, \tag{4.15}$$

where $c_{\rm fo} \equiv \frac{y_D^2 g_e^2}{2\pi M_{\rm DM}^2}\left(1 - \frac{m_e^2}{M_{\rm DM}^2}\right)^{3/2}$ is a constant term independent of $v_{\rm rel}$.
Following the computations of the DM relic abundance in Sec. 2.3.1, but using $\langle \sigma v \rangle = c_{\rm fo}\frac{x}{2}$, we find that

$$\Omega_{\rm DM} {\rm h}^2 \simeq \frac{s_0 {\rm h}^2}{\rho_c}\left[\frac{45}{8\pi^2 g_\rho(T_{\rm fo})}\right]^{1/2} \frac{x_{\rm fo}}{M_{\rm p}\frac{c_{\rm fo}}{2} x_{\rm fo} \ln\left(\frac{x_\infty}{x_\infty}\right)}, \tag{4.16}$$

where $x_\infty \equiv \frac{M_{\rm DM}}{1 \text{ eV}}$, as introduced in Ref. [54].
Exploiting the expression for the DM abundance in Eq. (2.16) for an $s$-wave dominated process ($b_p = 0$) and requiring to obtain the observed DM abundance, which means that $\Omega_{\rm DM}{\rm h}^2 \simeq 0.12$[27], we obtain the data presented in the left panel of Fig. 2.5. The same can be done for a $p$-wave dominated process ($a_s = 0$), obtaining the data presented in the right panel of Fig. 2.5.
Analogously, also in the resonance regime we can impose $\Omega_{\rm DM}{\rm h}^2 \simeq 0.12$, where the expression for $\Omega_{\rm DM}{\rm h}^2$ is taken from Eq. (4.16). Therefore, in first approximation we can write that

$$a_s \simeq 3\frac{b_p}{x_{\rm fo}} \simeq \frac{c_{\rm fo}}{2} x_{\rm fo} \ln\left(\frac{x_\infty}{x_{\rm fo}}\right). \tag{4.17}$$

The results obtained for $c_{\rm fo}$ are illustrated in Fig. 4.3.
Defining the thermally-averaged cross section as $\langle \sigma v \rangle = c_{\rm fo}\frac{x_{\rm fo}}{2}$ and, recalling that the FO temperature is defined according to Eq. (2.19), we can finally impose to match the observed DM relic abundance in the resonance regime by writing that

$$\frac{y_D^2 g_e^2}{2\pi M_{\rm DM}^2}\left(1 - \frac{m_e^2}{M_{\rm DM}^2}\right)^{3/2} \equiv c_{\rm fo}. \tag{4.18}$$

Furthermore, we can impose to fit the 511 keV gamma-ray signal from the GC by writing that

$$\frac{y_D^2 g_e^2}{2\pi M_{\rm DM}^2}\left(1 - \frac{m_e^2}{M_{\rm DM}^2}\right)^{3/2} \frac{(1.1 \cdot 10^{-3})^2}{64\epsilon^2} \equiv \langle \sigma v \rangle_{511}, \tag{4.19}$$

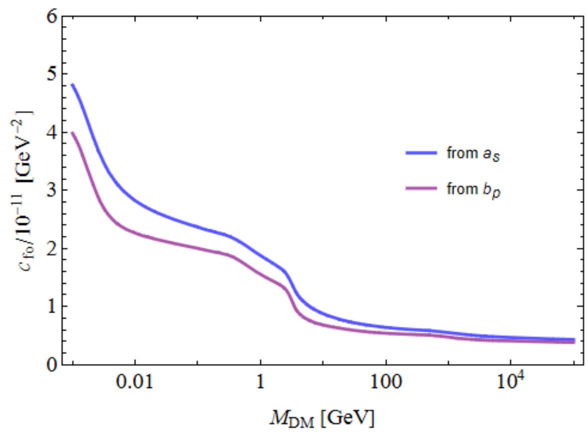


Figure 4.3: Behaviour of the $c_{\rm fo}$ term, defined as in Eq. (4.17), in terms of the DM mass $M_{\rm DM}$. In blue we plot $c_{\rm fo} = \frac{2a_s}{x_{\rm fo}} \frac{1}{\ln\left(\frac{x_\infty}{x_{\rm fo}}\right)}$, while in purple we plot $c_{\rm fo} = \frac{6b_p}{x_{\rm fo}^2} \frac{1}{\ln\left(\frac{x_\infty}{x_{\rm fo}}\right)}$. The two curves are in good agreement across the entire range of $M_{\rm DM}$ values considered, and their difference provides a rough estimate of the uncertainty of our approximate method to derive the freeze-out cross section in the small-$\epsilon$ regime. The $a_s$ and $b_p$ terms, used to define $c_{\rm fo}$, are taken from Fig. 2.5[54].

where, again, $\langle \sigma v \rangle_{511}$ is found by requiring that the positron injection rate within a sphere of radius $r \lesssim 4$ kpc around the GC satisfies Eq. (3.17) for a specific DM density profile. The results obtained from this procedure are displayed in Fig. 4.4. Note that the different $v_{\rm rel}^2$ dependence of the cross section, between freeze-out and the GC, implies that imposing the two requirements to reproduce the 511 keV signal and the DM abundance does not fix any longer the DM mass, as it did in the non-resonant regime.
Note that the region of parameter space shown in Fig. 4.4 is not constrained by either NA64 or direct detection experiments. This is because, in the DM mass range considered here, NA64 and experiments such as SENSEI, DAMIC-M, and XENON1T constrain regions where $g_e \gtrsim 10^{-5}$[102] and $\sigma_e \simeq 10^{-38} - 10^{-39}$ cm$^2$[97], respectively, both of which lie outside the parameter space explored in this work.

In the $5.3 \cdot 10^{-5} \lesssim \epsilon \lesssim 0.0064$ regime just analyzed, we cannot use Eq. (4.9) for the DM self-interacting cross section, since, as already said, the expansion around $v_{\rm rel} \simeq 0$ gives no more reliable results. We should instead write it as

$$\sigma_{\chi\chi\to\chi\chi} = \frac{B f(v_{\rm rel})}{(s - m_S^2)^2 + m_S^2 \Gamma_S^2}, \tag{4.20}$$

where $s$ is the usual Mandelstam variable and $\Gamma_S$ is the decay width of the scalar $S$, defined as in Eq. (4.6). Moreover, $B$ is a constant independent of $v_{\rm rel}$, while, on the contrary, $f(v_{\rm rel})$ is a function of the relative velocity.

To be clear, the DM self-interacting cross section receives contribution from the $s$-,$t$- and $u$-channels but only the $s$-channel is affected by the resonant DM behaviour discussed so far. Near the resonanc, as it occurs in the small-$\epsilon$ regime, the $s$-channel contribution dominates due

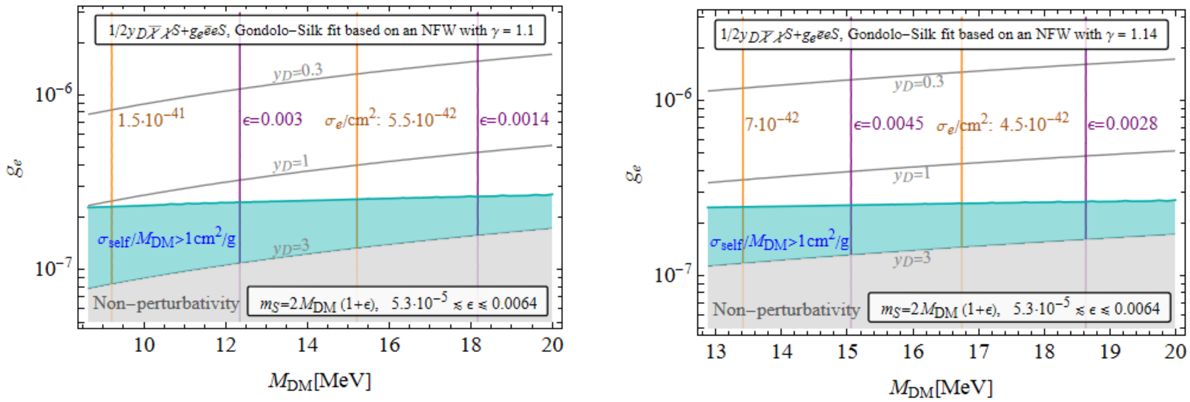


Figure 4.4: The phenomelogy of the model is completely determined by the DM mass $M_{\rm DM}$ and the coupling to electrons $g_e$ once we require to fit both the the observed DM relic abundance, as done in Eq. (4.18), and the 511 keV line, as done in Eq. (4.19). The cyan area represents constraints coming from the requirement that the DM self-interacting cross section satisfies $\frac{\sigma_{\rm sel}}{M_{\rm DM}} \lesssim 1\frac{\rm cm^2}{\rm g}$, while the gray area delimits the region of the parameter space where the dark coupling $y_D$ is no longer perturbative. Moreover, the orange lines are contours of constant $\sigma_{\chi e^\pm \to \chi e^\pm} \equiv \sigma_e$, the gray lines are contours of constant dark coupling $y_D$ and the purple lines are contours of constant $\epsilon$, defined by $\frac{m_S}{2M_{\rm DM}} = 1+\epsilon$. We assume that DM follows a Gondolo-Silk density profile based on an NFW halo configuration with inner slope of $\gamma = 1.1$ (left panel) and $\gamma = 1.14$ (right panel). We also assume that the positron injection rate within a sphere of radius $r \lesssim 4$ kpc around the GC is $\simeq 2.5 \cdot 10^{42}{\rm s}^{-1}$.

to the enhancement of the propagator denominator, which goes as $\propto \frac{1}{(s-m_S^2)^2+m_S^2\Gamma_S^2} \to \infty$ as $s \to m_S^2$. As a result, to a good approximation, we can ignore contributions from the $t$- and $u$-channels to the DM self-interacting cross section in the small-$\epsilon$ regime.

Now, following the same procedure discussed in App. C for the $\chi\chi \to e^-e^+$ cross section, we find that in the resonance regime the DM self-interacting cross section can be rewritten as

$$\sigma_{\chi\chi\to\chi\chi} \simeq \frac{y_D^4}{128\pi M_{\rm DM}^2}. \tag{4.21}$$

Constraints from DM self-interactions in Fig. 4.4 are therefore obtained by requiring that

$$\sigma_{\chi\chi\to\chi\chi} \simeq \frac{y_D^4}{128\pi M_{\rm DM}^2} \lesssim 1\frac{\rm cm^2}{\rm gr}. \tag{4.22}$$

### 4.2.3 Targets for direct detection experiments

So far, we have identified the parameter space of the DM $p$-wave model introduced in Sec. 4.1.2 that explains the 511 keV line, the DM abundance and all the limits on it. We now use this knowledge to derive a benchmark target, motivated by $p$-wave explanations of the 511 keV line, for direct detection experiments looking for DM-electron scatterings. As these experiments are making fast progress, we think that it is a useful exercise to charachterise to what extent they could allow to address a well-defined physics question: Does the 511 keV line originate from

models where DM produces $e^-e^+$ via $p$-wave annihilations?
We therefore proceed as follows: for each DM density profile defined as in Eq. (3.5), we obtain a distinct best-fit value of $\langle\sigma v\rangle_{511}$. Consequently, for each DM density profile, we can construct a corresponding parameter space that incorporates both theoretical and experimental constraints, including:

- recast of exclusion limits from NA64[102];
- constraints from DM self-interactions;
- non-perturbativity requirement on the dark coupling $y_D$;
- compatibility with the 511 keV line in the GC and correct reproduction of the observed DM relic abundance.

From each resulting parameter space, we extract values of the scattering cross section $\sigma_{\chi e^\pm\to\chi e^\pm} = \frac{(y_D g_e)^2}{\pi}\frac{\mu^2_{\rm eDM}}{m_S^4}$ that are compatible with all experimental constraints, both in the $5.3\cdot 10^{-5}\lesssim\epsilon\lesssim 0.0064$ and in the $\epsilon\geq 0.27$ regions. These results are then combined into a single plot, showing existing direct detection limits and future sensitivities on $\sigma_e\equiv\sigma_{\chi e^\pm\to\chi e^\pm}$ as a function of the DM mass $M_{\rm DM}$. In the same plot we display, as a blue shaded area, the cross sections that can be achieved by the $p$-wave model studied so far, compatibly with limits from supernovae, NA64 and continuum photons at energies higher than 511 keV. The results of this procedure are displayed in Fig. 4.5.
In particular, the purple region indicates model-dependent limits arising from our use of the $_*$MIN and the Gondolo-Silk density profiles, both based on an NFW halo configuration with inner slopes in the range $1\leq\gamma\leq 1.2$. We do not consider less steep profiles, as we aim at explaining the presence of a dark matter spike around the supermassive black hole at the GC, and would otherwise result in sub-MeV DM masses, which is not the aim of this work, when imposing Eq. (4.11), with the coefficient $b_{\chi\chi\to e^-e^+}$ that is fixed by the requirement of matching the observed DM abundance. Steeper profiles are also excluded, as they lead to excessively large annihilation signals, making such configurations, in principle both highly testable and and consequently subject to stringent observational constraints.
Exploiting different DM density profiles can shift the boundaries of $\sigma_{\chi e^\pm\to\chi e^\pm}$ upward or downward. In this sense, the purple region represents model limitations due to the dependence on the assumed DM density profile.

In conclusion, the p-wave annihilation model offers a compelling framework for explaining both the observed dark matter relic abundance and the 511 keV gamma-ray line from the GC, while remaining consistent with current experimental constraints. By imposing the requirements of thermal freeze-out and compatibility with the positron injection rate inferred from the 511 keV signal, we have identified the viable parameter space for this scenario across different DM density profiles. Note that the model predicts DM-electron elastic scattering cross sections that are within the reach of upcoming direct detection experiments such as SENSEI[95] and DAMIC-M[187]. Future experiments like Obscura[188] may also offer complementary sensitivity, while JUNO[189] could provide indirect constraints through neutrino observatory techniques.

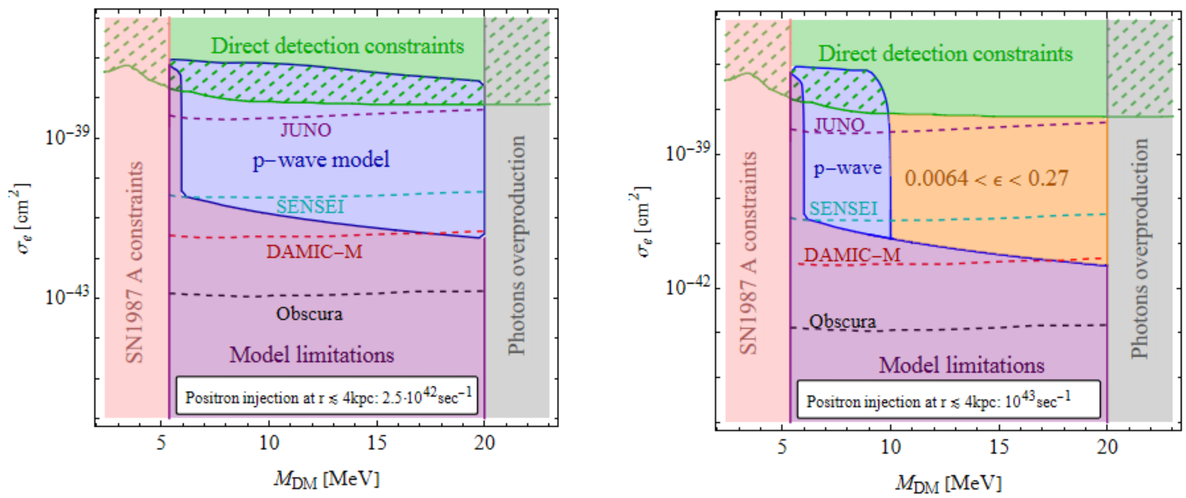


Figure 4.5: $M_{\rm DM} - \sigma_e$ parameter spaces. The blue region delimits the area where the $p$-wave annihilation model introduced in Sec. 4.1.2 successfully reproduces both the observed dark matter relic abundance and the 511 keV gamma-ray line from the GC. The upper and lower boundary of the blue region are obtained by extracting the corresponding values of cross section $\sigma_e$ from the constrained DM parameter spaces and combining the results for the $5.3 \cdot 10^{-5} \lesssim \epsilon \lesssim 0.0064$ and $\epsilon \geq 0.27$ regimes. The gray band excludes $M_{\rm DM} \lesssim 20$ MeV, because these masses lead to an overproduction of photons from the GC, while the pink band represents constraints from SN 1987A[109]. Additionally, the purple region represents model-dependent limits. The orange area in the right panel delimits the region of the parameter space which may succesfully fit both the observed DM relic abundance and the 511 keV line, but this requires to study the regime where $0.0064 \lesssim \epsilon < 0.27$ for a better analysis. Moreover, we present in green direct detection constraints[97], along with projected sensitivities for JUNO (dashed purple)[189], SENSEI (dashed cyan)[95], DAMIC-M (dashed red)[187] and Obscura (dashed black)[188]. The positron injection rate within a sphere of radius $r \lesssim 4$ kpc is $\simeq 2.5 \cdot 10^{42}$ s$^{-1}$ for the left panel and $\simeq 10^{43}$ s$^{-1}$ for the right panel.

These preliminary results suggest that future generations of low-threshold direct detection experiments will be able to probe the entire viable parameter space of the $p$-wave model analyzed so far. This makes them a powerful tool not only for testing light dark matter scenarios but also for potentially uncovering the long-sought connection between dark matter and the 511 keV line.

# 5

# Coannihilation model

We have already said in Chapter 4 that, in order to avoid an overproduction of low-energy positrons, we can study models in which DM annihilation into $e^-e^+$ pairs are late-time suppressed. One way to do that, as already analized, is through models in which DM relic abundance is set by $p$-wave annihilations, where the resulting cross section is velocity-dependent.

Another class of DM models that one can think, in order to realize that kind of setup, are inelastic DM models (iDM). In this framework, the DM relic abundance is determined by coannihilations between a DM particle and a slightly heavier partner. These processes are efficient in the early universe, when thermal energies are sufficient to maintain the heavier dark matter species in thermal equilibrium. However, as the Universe expands and cools, the number density of the heavier state becomes exponentially suppressed by the Boltzmann factor $e^{-\Delta m/T}$, where $\Delta m$ is the mass splitting between the two states. As a result, the efficiency of coannihilation processes diminishes rapidly at late times.
As a result, positron production today is drastically reduced, remaining consistent with cosmological observations.

## 5.1 Coannihilation dark matter model for the 511 keV line

In this section, we present a coannihilation dark matter model capable of simultaneously explaining the measured DM relic density and the 511 keV gamma-ray emission observed from the GC, ensuring consistency with experimental and observational constraints.

### 5.1.1 Model overview

Let us realize a consistent inelastic DM model, by adding to the SM a dark gauge group $U(1)'$, whose dark gauge boson is indicated as $V_\mu$, two-component fermions $\xi$ and $\eta$ of charges 1 and $-1$ respectively and a scalar $\phi$ with charge 2 which spontaneously breaks the symmetry.
The most general low-energy Lagrangian that preserves charge conjugation, which means $\eta \leftrightarrow \xi$, $\phi \leftrightarrow \phi^*$ and $V_\mu \leftrightarrow -V_\mu$, reads as

$$\mathscr{L} = V(|\phi|)+\frac{\varepsilon}{2}V_{\mu\nu}F^{\mu\nu}+(ig_D\chi_2^\dagger\bar{\sigma}_\mu\chi_1 V^\mu+\text{h.c.})-\frac{\bar{m}}{2}(\chi_1^2+\chi_2^2)-\frac{y_\phi}{2}(\phi+\phi^*)(\chi_2^2-\chi_1^2)+\text{h.c.}, \quad (5.1)$$

where $\chi_1 = \frac{i(\eta-\xi)}{\sqrt{2}}$ and $\chi_2 = \frac{\eta+\xi}{\sqrt{2}}$ are the Majorana mass eigenstates, $F_{\mu\nu}$ is the electromagnetic field strength tensor and $V_{\mu\nu}$ is the dark gauge boson field strength.

Furthermore, we can write $\phi$ in polar coordinates as $\phi = |\phi| e^{i\frac{\theta}{v_\phi}}$, where $\theta$ is a Goldstone boson and $|\phi| = \frac{\varphi+v_\phi}{\sqrt{2}}$. In the unitary gauge the Goldstone boson disappears and we remain with $\phi = \phi^* = \frac{\varphi+v_\phi}{\sqrt{2}}$, where both $\varphi$ and $v_\phi$ are real and in particular this latter is the VEV of $\phi$.

Let us now instead consider the potential $V(|\phi|) = \lambda_\phi \left(|\phi|^2 - \frac{v_\phi^2}{2}\right)^2$. We can now expand it considering that $|\phi|^2 = \frac{\varphi^2+2\varphi v_\phi+v_\phi^2}{2}$ and thus we get that

$$V(|\phi|) = \lambda_\phi \left(\frac{\varphi^2}{2} + \varphi v_\phi\right)^2 = \lambda_\phi \frac{\varphi^4}{4} + \lambda_\phi v_\phi \varphi^3 + \lambda_\phi v_\phi^2 \varphi^2 = \lambda_\phi \frac{\varphi^4}{4} + \underbrace{6\lambda_\phi v_\phi}_{\lambda_{\varphi^3}} \frac{\varphi^3}{6} + \lambda_\phi v_\phi^2 \varphi^2. \quad (5.2)$$

Therefore, we can find the masses for all particles appearing in the Lagrangian in Eq. (5.1) through symmetry breaking mediated by $\phi$, as we derive in App. B.4. In particular, the physical vector and fermion masses are given by

$$m_V = 2g_D v_\phi, \quad m_{1,2} = \bar{m} \mp \frac{\delta}{2}, \quad m_\varphi^2 = 2\lambda_\phi v_\phi^2, \quad (5.3)$$

where $\delta = 2\sqrt{2} y_\phi v_\phi \ll m_{1,2}$ is the $U(1)'$ breaking Majorana masses. From Eq. (5.3), it is straightforward that $m_2 = m_1 + \delta$. In particular, it is technical natural to require that $\delta \ll \bar{m}$ since in the $\delta \to 0$ limit we restore the $U(1)'$ symmetry, analogous to the SM lepton number[191][17].

In the following subsection we present the general strategy to explain the 511 keV gamma-ray signal from the GC, while reproducing the observed DM relic abundance.

### 5.1.2 Relic abundance and 511 keV line

In this subsection we aims at building the theoretical framework necessary to explain the 511 keV gamma-ray signal that we observe from the GC, while consistently reproducing the DM relic abundance. Specifically, as already mentioned in the previous chapters, the observed 511 keV signal in the GC, attributed to $e^-e^+$ annihilation into photons via para-positronium formation, is strongly peaked and corresponds to a flux of $\simeq 10^{-3}$ photons cm$^{-2}$ s$^{-1}$.

In Sec. 5.3 we will start discussing the phenomenology of the iDM model introduced in Sec. 5.1, updating the results obtained by Ref. [171] and, therefore, exploiting the best-fit value of the self-conjugate DM annihilation into $e^-e^+$ cross section, provided in Ref. [167] for an NFW DM density profile:

$$\langle \sigma v \rangle_{511} \simeq 5 \cdot 10^{-31} \left(\frac{M_{\rm DM}}{3\ \rm MeV}\right) \frac{\rm cm^3}{\rm s}. \quad (5.4)$$

[17] A physical quantity is said to be technically natural if setting it to zero increases the symmetry of the theory. In this case, any quantum corrections to the quantity must be proportional to its original value, ensuring that if the parameter is small, it remains small under renormalization.

However, as discussed in Sec. 3.2.1, the supermassive black hole at the center of the Galaxy may accrete the DM density, which thus form a spike. In that specific case the DM density profile is parametrized as in Eq. (3.5). Requiring that the positron injection rate within a sphere of radius $r \lesssim 4$ kpc around the GC is $\simeq 2.5 \cdot 10^{42}$ s$^{-1}$[11], we can find for each different benchmark of the DM density profile discussed in Sec. 3.2.1 the best-fit values of the thermally-averaged self-conjugate DM annihilation cross section, needed to reproduce the 511 keV line. The results obtained from this procedure are displayed in Fig. 3.4 and they can be used to extend the discussion in Ref. [171].

As already discussed in Sec. 4.2.1, we restrict the dark matter parameter space to DM masses in the range 1 MeV $\lesssim M_{\rm DM} \lesssim$ 20 MeV. This is motivated by the need to avoid overproduction of gamma-ray photons and to remain consistent with observational constraints, such as those from COMPTEL. Consequently, in the following we focus only on the cross sections that are dominant within this mass range.

We start reporting the cross section relative to the coannihilation process $\chi_1\chi_2 \to$ SM SM, which, in the non-relativistic limit and including all kinematically accessible channels, is[192, 193]

$$\langle \sigma v \rangle_{\rm ann} \simeq \frac{16\pi\alpha_e\alpha_D\epsilon^2 m_1^2}{(4m_1^2 - m_V^2)^2}, \tag{5.5}$$

where $\alpha_e$ is the fine-structure constant and $\alpha_D \equiv \frac{g_D^2}{4\pi}$. In particular, for 1 MeV $\lesssim M_{\rm DM} \lesssim$ 20 MeV, which is the mass range that we consider in the iDM model in Sec. 5.1.1 to explain the 511 keV line, the only kinematically accessible channel is $\chi_2\chi_1 \to e^-e^+$, whose cross section in the limit that $\delta \ll m_{1,2} \simeq M_{\rm DM}$ is

$$\sigma v_{\chi_1\chi_2\to e^+e^-} = 4\alpha_e\epsilon^2 g_D^2 \frac{M_{\rm DM}^2 + m_e^2/2}{(m_V^2 - 4M_{\rm DM}^2)^2}\sqrt{1 - \frac{m_e^2}{M_{\rm DM}^2}}, \tag{5.6}$$

where we have used Eq. (B.61).
This cross section is, indeed, consistent with Eq. (5.5) in the limit that $M_{\rm DM} \gg m_e$.

Moreover, if $m_\varphi < M_{\rm DM}$ and $\varphi$ decays to $e^-e^+$, then another process is kinematically allowed, which is the $\chi_i\chi_i$ annihilation into $\varphi\varphi$, whose cross section, in the limit that $\frac{y_\phi v_\phi}{\lambda_\varphi^3} \ll 1$, is

$$\sigma v_{\chi_i - \chi_i \to \varphi\varphi} = v_{\rm rel}^2 \frac{y_\phi^2 \lambda_{\varphi^3}^2}{64\pi} \frac{1}{(4m_i^2 - m_\varphi^2)^2}\sqrt{1 - \frac{m_\phi^2}{m_i^2}}, \tag{5.7}$$

where we have used Eq. (B.72).
Ref. [171] specifies that $\varphi$'s decay into $e^-e^+$ is guaranteed by an operator $\frac{|\phi|^2(e_L e_R^\dagger + \text{h.c.})}{\Lambda_{\phi e}}$, with $\Lambda_{\phi e} \sim 10^9 - 10^{10} v_\phi$.

If $m_V > m_1 + m_2$, then $\chi_i\chi_i \to VV$ is kinematically forbidden and thus the DM relic abundance is reproduced by imposing that

$$\sigma v_{\chi_1\chi_2\to e^+e^-} + 3\frac{\sigma v_{\chi_i\chi_i\to\varphi\varphi}/v_{\rm rel^2}}{x_{\rm fo}} = \langle \sigma v \rangle_{\rm fo}, \tag{5.8}$$

where we are summing the $s$-wave and $p$-wave contributions and this allows to fix the kinetic mixing parameter $\epsilon$, which appears in the Lagrangian in Eq. (5.1). Moreover, $x_{\text{fo}} \equiv \frac{M_{\text{DM}}}{T_{\text{fo}}}$, where $T_{\text{fo}}$ is the freeze-out temperature and $\langle \sigma v \rangle_{\text{fo}}$ is the value of the thermally-averaged DM annihilation cross section, needed to reproduce the DM relic abundance.

We can, instead, explain the 511 keV signal from the GC by imposing that

$$\sigma v_{\chi_i \chi_i \to \varphi\varphi} = \frac{1}{2} \langle \sigma v \rangle_{511} \frac{v_{\text{rel}}^2}{\langle v_{\text{rel}}^2 \rangle_{\text{bulge}}}, \tag{5.9}$$

where we recall that $\langle v_{\text{rel}}^2 \rangle_{\text{bulge}}^{1/2} \simeq 1.1 \cdot 10^{-3}$. Here, as said, $\langle \sigma v \rangle_{511}$ denotes the best-fit value of the thermally-averaged DM annihilation cross section, needed to reproduce the 511 keV line from the GC. In Sec. 5.3 we will discuss the phenomenological implications of adopting different benchmarks values for $\langle \sigma v \rangle_{511}$.
The factor $\frac{1}{2}$ in Eq. (5.9) is due to the fact that $\chi_i - \chi_i$ annihilation emits two $\varphi$ particles and each of them then decays into an $e^- e^+$ pair, so that for each $\chi_i \chi_i \to \varphi\varphi$ scattering process, we actually produce two electron-positron pairs.

We will see later that in iDM models, such as the one just presented, the heavier DM component $\chi_2$ can play a significant role in direct detection experiments through down-scattering processes, such as $\chi_2 \text{N} \to \chi_1 \text{N}$, where $\chi_2$ scatters off nuclei N, or $\chi_2 e^\pm \to \chi_1 e^\pm$, where $\chi_2$ scatters off electrons or positrons $e^\pm$. These processes can produce detectable nuclear or electron recoils, respectively, offering promising signals in direct detection experiments such as CRESST in the first case and XENON1T in the second case, depending on the nature of the DM interaction.
To that end, in the next section we present a general overview of elastic scattering, up-scattering and down-scattering processes. Specifically, in the iDM model, introduced in Sec. 5.1 and which will be discussed more in detail later, we deal with sufficiently large mass splittings $\delta$, which kinematically forbid up-scattering processes. For this reason, we focus on down-scattering signals in direct detection experiments like XENON1T and CRESST, highlighting their relevance for MeV-scale dark matter models.

### 5.1.3 Elastic scattering, up-scattering and down-scattering

Light inelastic dark matter models predict a wide array of observable signals in direct detection experiments. These scenarios allow for a rough categorization of the DM parameter space into three main regimes:

- Elastic scattering;
- Up-scattering;
- Down-scattering.

In the following sections, we will analize each regime more in detail, focusing mainly on down-scattering limits, as they would be essential for the phenomenology of the coannihilation model under consideration.

### Elastic scattering

If the mass splitting $\delta$ is large enough, the heavier state $\chi_2$ has decayed by the present era, via the decay channels that we will discuss in Sec. 5.2.1. In this case $\chi_1$ up-scattering into $\chi_2$ is not kinematically accessible. This is because the energy required to overcome the mass splitting $\delta \equiv m_2 - m_1$ , exceeds the available kinetic energy of $\chi_1$. Specifically, up-scattering can occur only if $\frac{1}{2}m_1 v^2 \gtrsim \delta$ and for large values of $\delta$, such processes become kinematically forbidden.

In this scenario, the only detectable signals arise from elastic scattering of the lighter DM component $\chi_1$ off nucleons or electrons, which can occur only at loop level. However, in the iDM model introduced in Sec. 5.1.1, we consider a mass splitting $\delta$ that is small enough that $\chi_2$ has not yet decayed by today.

### Up-scattering

In regions where the mass splitting $\delta$ is small compared to the kinetic energy of $\chi_1$, the heavier state $\chi_2$ can be regenerated via up-scattering processes such as $\chi_1 e^\pm \to \chi_2 e^\pm$ or $\chi_1\mathrm{N} \to \chi_2\mathrm{N}$. As mentioned by Ref. [194], the precise kinematic boundary for up-scattering depends on the DM escape velocity, which is taken to be 553 km s$^{-1}$[18]. At higher DM masses, this kinematic boundary also depends on the mass of the target nucleus, with higher-mass target nuclei allowing up-scattering for larger values of $\delta$.

In Fig. 5.1, we present in orange the region of the DM parameter space where up-scattering is possible off lead, which is heavier than any nucleus used in direct detection. All up-scattering exclusions from terrestrial experiments should be contained in this region, even though the actual exclusions from experiments are less stringent, because the expected up-scattering cross sections may exceed the experimental sensitivities.
For a more precise analysis, in Sec. 5.2.3 we will discuss how $\chi_1\chi_1 \to \chi_2\chi_2$ up-scattering processes become kinematically accessible when the local dark matter temperature $T_{\mathrm{DM}}$ satisfies $T_{\mathrm{DM}} \gtrsim \delta$, typically occurring in dense or heated environments like the GC. This class of processes allows for the regeneration of $\chi_2$ long after freeze-out and kinetic decoupling, potentially leading to observable signatures through subsequent down-scattering processes.

However, due to the large expected cross sections, most of the parameter space, where up-scattering processes are kinematically allowed, is strongly excluded by null results from direct detection experiments. These constraints are especially stringent for larger dark matter masses and smaller splittings, where elastic scattering experiments are most sensitive, as shown in Fig. 5.1.

### Down-scattering

A unique and promising direct detection signal arises from the tree-level down-scattering of the sub-dominant heavier dark matter state $\chi_2$ into the lighter state $\chi_1$. Unlike traditional elastic scattering scenarios, this process results in a recoil signal that is nearly mono-energetic. This

[18]The escape velocity $v_{\mathrm{esc}} = 553$ km s$^{-1}$ represents the maximum speed that DM can have in the Galactic halo, while remaining gravitationally bound to the Milky Way.

leads to a sharp peak in the recoil energy spectrum, offering a distinct experimental signature. Even when the abundance of $\chi_2$ is highly suppressed, the kinetic energy released during the scattering enhances the detectability of this process, making it a powerful probe for iDM models.

Following Refs. [194–196], we can write that when the DM kinetic energy dispersion is much smaller than $\delta$, namely in the limit that $v_0 \ll \sqrt{\frac{\delta}{\mu_{\chi_2 \mathrm{N}}}}$, the expected rate for the down-scattering processes of $\chi_2$ off nuclei can be approximated as

$$R_{\mathrm{N}} \simeq \epsilon_{\mathrm{det}} f_{\chi_2}^{\mathrm{det}} \frac{\rho_\chi}{m_2} \frac{\mathrm{N_A}}{\mathrm{A_N}} \sigma_{\chi_2 \mathrm{N}} v. \tag{5.10}$$

Here, we have that $v_0 = 220$ km s$^{-1}$ is the DM velocity dispersion, equal to the Sun's circular rotation velocity and $\mu_{\chi_2 \mathrm{N}} = \frac{m_2 m_{\mathrm{N}}}{m_2 + m_{\mathrm{N}}}$ is the $\chi_2$-nucleus reduced mass. Moreover,

- $\epsilon_{\mathrm{det}}$ accounts for the efficiency of the detector and it thus ranges from 0 to 1.
- $f_{\chi_2}^{\mathrm{det}} = \epsilon_{\mathrm{Earth}} f_{\chi_2}$ accounts for the suppressed abundance of $\chi_2$ relative to the total DM density at the detector, where $\epsilon_{\mathrm{Earth}}$ accounts for the Earth shadowing suppression[19] and $f_{\chi_2} = \frac{\mathrm{Y}_2}{\mathrm{Y_{TOT}}}$ is the fractional abundance of $\chi_2$.
- $\frac{\rho_\chi}{m_2}$ is the DM number density, where $\rho_\chi \sim 0.4$ GeV cm$^{-3}$ is the DM mass density at the Sun's position and $m_2$ is the $\chi_2$'s mass.
- $\mathrm{N_A} \sim 6.022 \cdot 10^{23}$ mol$^{-1}$ is the Avogadro's number and $\mathrm{A_N}$ is the atomic mass of the target nucleus, measured in g/mol. Therefore, $\frac{\mathrm{N_A}}{\mathrm{A_N}}$ measures the number of atoms per grams.
- $\sigma_{\chi_2 \mathrm{N}} v = \frac{\sqrt{2}\; 16\pi\alpha_e\alpha_D\epsilon^2\mu_{\chi_2\mathrm{N}}^{3/2}\delta^{1/2}\mathrm{Z_N^2}}{m_V^4}|\mathrm{F(E_R)}|^2$ is the cross section for DM-nucleus scattering, where $\alpha_D = \frac{g_D^2}{4\pi}$ and $g_D$ is the dark coupling, while $\mathrm{Z_N}$ is the atomic number of the nucleus N and $|\mathrm{F(E_R)}|^2$ is the nuclear form factor. The form factor is $\mathcal{O}(1)$ as long as the transferred momentum $q = \sqrt{2\mu_{\chi\mathrm{N}}\delta}$ is small compared to the size of the nucleus, which is true in most of the DM parameter space.

The expected rate for $\chi_2$ down-scattering off electrons is instead defined as

$$R_e \simeq \epsilon_{\mathrm{det}} f_{\chi_2}^{\mathrm{det}} \frac{\rho_\chi}{m_2} \frac{\mathrm{N_A}}{\mathrm{A_N}} \mathrm{Z_{exc}} \sigma_{\chi_2 \mathrm{e}} v, \tag{5.11}$$

where

- $\mathrm{Z_{exc}}$ is the number of electrons associated with each atom that can be excited by this transition.
- $\sigma_{\chi_2 e} v = \frac{\sqrt{2}\; 16\pi\alpha\alpha_D\epsilon^2\mu_{\chi_2 e}^{3/2}\delta^{1/2}}{m_V^4}$ is the $\chi_2$-e down-scattering cross section.

[19] $\epsilon_{\mathrm{Earth}}$ accounts for the suppression of the signal in direct detection experiments due to Earth shadowing, which means that if $\chi_2 - \mathrm{N}$ interactions are stronger $\epsilon_{\mathrm{Earth}}$ will be smaller. Indeed, $\chi_2$ DM particles may scatter off nuclei in the Earth before reaching detectors, converting into the lighter state $\chi_1$ and therefore reducing the detectable down-scattering flux.

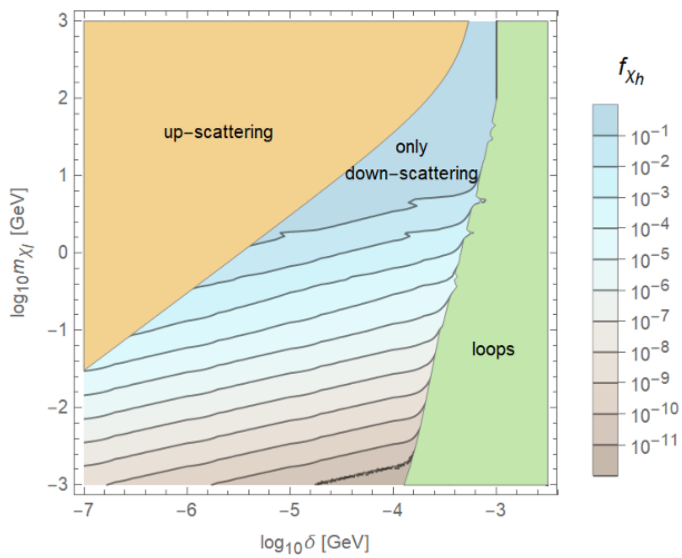


Figure 5.1: The orange area delimits the region where up-scattering processes are kinematically accessible. For larger values of $M_{\mathrm{DM}}$ the kinematic boundary also depends on the target nucleus, with higher-mass target nuclei allowing up-scattering for larger values of $\delta$. Here it is shown the kinematic boundary for up-scattering off lead to show the largest possible region in which up-scattering processes are kinematically allowed. The portion named *only down-scattering* delimits, instead, the area where down-scattering are the only tree-level processes that can occur. Within this region, contours of the relative abundance of the excited state at the recombination temperature $T^{\mathrm{rec}}$, obtained for the benchmarks values $m_V = 3(m_1 + \frac{\delta}{2})$ and $\alpha_D = 0.5$, are also displayed, defined as $f_2 = \frac{Y_2}{Y_{\mathrm{TOT}}}$, where Y represents the relic yield. Eventually, the green area represents the region of the parameter space where $\chi_2$ decays have strongly depleted the heavier DM component and only loop-level elastic scatterings of $\chi_1$ off nuclei and electrons are possible.
***Reprinted from "Cosmology and Signals of Light Pseudo-Dirac Dark Matter", by Mariana Carrillo González and Natalia Toro***[194].

Up-scattering and down-scattering limits can significantly constrain iDM models, but they are only applicable if these processes remain active at late cosmological times, that is, if the heavier dark matter component $\chi_2$ has not yet been completely depleted. To that end, in the next section we discuss the various depletion mechanisms that $\chi_2$ can undergo, outlining its cosmological history.

## 5.2 $\chi_2$'s cosmological history

In this section, we want to investigate the cosmological history of the heavier DM component $\chi_2$ within the framework of the coannihilation model. In the following, we will explore how $\chi_2$, which is nearly-degenerate in mass with the lighter DM state $\chi_1$, evolves throughout the thermal history of the Universe. Starting from the freeze-out of coannihilation processes that fix the relic abundance, we analyze the subsequent depletion mechanisms acting on $\chi_2$, such as primarily down-scattering processes, up until the point of kinetic decoupling from the Standard Model particles.

However, in certain dense regions of the Milky Way, such as the Galactic Center, DM can be heated to higher temperatures through virialization, which is a process where particles gain kinetic energy as they settle into a gravitationally bound system. We will see that when the local dark matter temperature $T_{\rm DM}$ becomes comparable to the mass splitting $\delta$ between the two DM states $\chi_2$ and $\chi_1$, the up-scattering processes $\chi_1\chi_1 \to \chi_2\chi_2$ reenter equilibrium. This allows the heavier state $\chi_2$ to be regenerated long after freeze-out, increasing its population in these high-density regions.

The goal of this section is to understand how these dynamics affect the final abundance and distribution of DM in the Universe.

### 5.2.1 $\chi_2$'s lifetime

In this subsection we will discuss possible decay channels for the havier DM component $\chi_2$ into Standard Model particles, based on the Lagrangian in Eq. (5.1), which correctly describes the physics induced by the new gauge group, $U(1)'$, at energy scales much smaller than the electroweak one. A UV complete Lagrangian extending Eq. (5.1) is given by (see for example Refs. [193, 197])

$$\mathscr{L} \supset -\frac{1}{4}B_{\mu\nu}B^{\mu\nu} - \frac{1}{4}V_{\mu\nu}V^{\mu\nu} + \frac{\epsilon}{2\cos\theta_W}V_{\mu\nu}B^{\mu\nu} + \frac{1}{2}\overline{m}_Z^2 Z_\mu Z^\mu + \frac{1}{2}\overline{m}_V^2 V_\mu V^\mu, \tag{5.12}$$

where $\theta_W$ is the Weinberg angle and the $Z$ boson is defined as in the SM. Furthermore, it is important to notice that $\overline{m}_Z$ and $\overline{m}_V$ are the masses in the un unmixed basis and thus correspond to the physical masses only in the limit that $\epsilon \to 0$.

Authors of Ref. [193] mention that $\overline{m}_V$ may arise from an extended $U(1)'$ Higgs sector or the Stueckelberg mechanism for instance. In our coannihilation model in Sec. 5.1.1 the mass of the dark photon arise from the $U(1)'$ symmetry breaking induced by the scalar $\phi$, as it is shown in App. B.4. On the other hand, $\overline{m}_Z$ denotes the mass of the Z boson as defined in the SM, as a consequence of the standard Higgs mechanism and thus before any kinetic or mass mixing effects.

In Eq. (5.12) $\epsilon$ denotes the kinetic mixing parameter between the dark gauge boson field strength $V_{\mu\nu}$ and the hypercharge field strength $B_{\mu\nu}$. We should notice, however, that in the Lagrangian in Eq. (5.1) we have a kinetic mixing between the dark photon field strength $V_{\mu\nu}$ and the electromagnetic field strength $F_{\mu\nu}$, written as $\frac{\epsilon}{2}V_{\mu\nu}F^{\mu\nu}$, which is consistent with $\frac{\epsilon}{2\cos\theta_W}V_{\mu\nu}B^{\mu\nu}$ in the limit that $m_Z \gg m_V$, which is the case in the coannihilation model discussed in Sec. 5.1.1.

Following the computations shown in App. B of Ref. [193], we can finally make the following redefinition:

$$\begin{pmatrix} V \\ Z \\ A \end{pmatrix} = \underbrace{\begin{pmatrix} (\eta/\epsilon)\cos\alpha\cot\theta_W & (\eta/\epsilon)\sin\alpha\cot\theta_W & 0 \\ -(\sin\alpha+\eta\cos\alpha) & \cos\alpha-\eta\sin\alpha & 0 \\ \eta\cos\alpha\cot\theta_W & \eta\sin\alpha\cot\theta_W & 1 \end{pmatrix}}_{C} \begin{pmatrix} V \\ Z \\ A \end{pmatrix}, \tag{5.13}$$

where we have defined

$$\begin{aligned} \eta &\equiv \frac{\epsilon\tan\theta_W}{(1-\epsilon^2/\cos^2\theta_W)^{1/2}} \\ \delta &\equiv \frac{\overline{m}_V/\overline{m}_Z}{(1-\epsilon^2/\cos^2\theta_W)^{1/2}} \end{aligned}. \tag{5.14}$$

Furthermore, the angle $\alpha$, used to diagonalize the $V-Z$ mass matrix, is defined as

$$\tan\alpha = \frac{1}{2\eta}[1-\eta^2-\delta^2-\mathrm{sign}(1-\delta^2)\sqrt{(1-\eta^2-\delta^2)^2+4\eta^2}]. \tag{5.15}$$

Applying this transformation matrix $C$ to the interacting Lagrangian in the $\epsilon\to 0$ limit

$$\mathscr{L}_{\text{int}} = ig_D V_\mu \bar{\chi}_2\gamma^\mu\chi_1 + \sum_f \left[\frac{g}{\cos\theta_W} Z_\mu \bar{f}\gamma^\mu(g_V^f - g_A^f\gamma^5)f + eQ_f A_\mu \bar{f}\gamma^\mu f\right], \tag{5.16}$$

where[20]

$$g_V^f = \frac{1}{2}T_f^3 - Q_f\sin^2\theta_W \quad g_A^f \frac{1}{2}T_f^3 \tag{5.17}$$

we obtain

$$\begin{aligned} \mathscr{L}_{\text{int}} \to & (C_{VV}V_\mu + C_{VZ}Z_\mu) ig_D\bar{\chi}_2\gamma^\mu\chi_1 + \sum_f \Bigg[V_\mu\bar{f}\gamma^\mu\Bigg(\frac{g}{\cos\theta_W}g_V^f C_{ZV} + eQ_f C_{AV} \\ & - \frac{g}{\cos\theta_W}g_A^f C_{ZV}\gamma^5\Bigg)f + Z_\mu\bar{f}\gamma^\mu\Bigg(\frac{g}{\cos\theta_W}g_V^f C_{ZZ} + eQ_f C_{AZ} \\ & - \frac{g}{\cos\theta_W}g_A^f C_{ZZ}\gamma^5\Bigg)f\Bigg] \end{aligned}, \tag{5.18}$$

where $C_{XY}$ with $XY \in A, Z, V$ are the elements of the matrix $C$ defined in Eq. (5.13). Here $ig_D\bar{\chi}_2\gamma^\mu\chi_1$ is the dark current $J^\mu_{\text{DM}}$ as defined in the coannihilation Lagrangian in Eq. (5.1).

The interacting lagrangian in Eq. (5.18) induces new decay modes for $\chi_2$, such as the processes depicted in Fig. 5.2.

We can now thus compute the decay width of $\chi_2$ into $\chi_1$ and two neutrinos, where the tree-level contribution from $V-Z$ mixing dominates over the loop level one from $V-\gamma$ mixing, obtaining that

$$\Gamma_{\chi_2\to\chi_1\bar{\nu}\nu} =\simeq \frac{4\epsilon^2\alpha_e\alpha_D\delta^9}{945\pi m_V^4 m_Z^4\cos^4\theta_W}, \tag{5.19}$$

where $\alpha_e$ is the electromagnetic fine structure constant, while $\alpha_D = \frac{g_D^4}{4\pi}$, with $g_D$ which is the dark coupling[198, 199]. As mentioned by Ref. [199], we can notice that $\Gamma_{\chi_2\to\chi_1\bar{\nu}\nu}$ scales with

[20] $T_f^3$ is the third component of the weak isospin and $Q_f$ denotes the electric charge of the fermion $f$ under consideration.

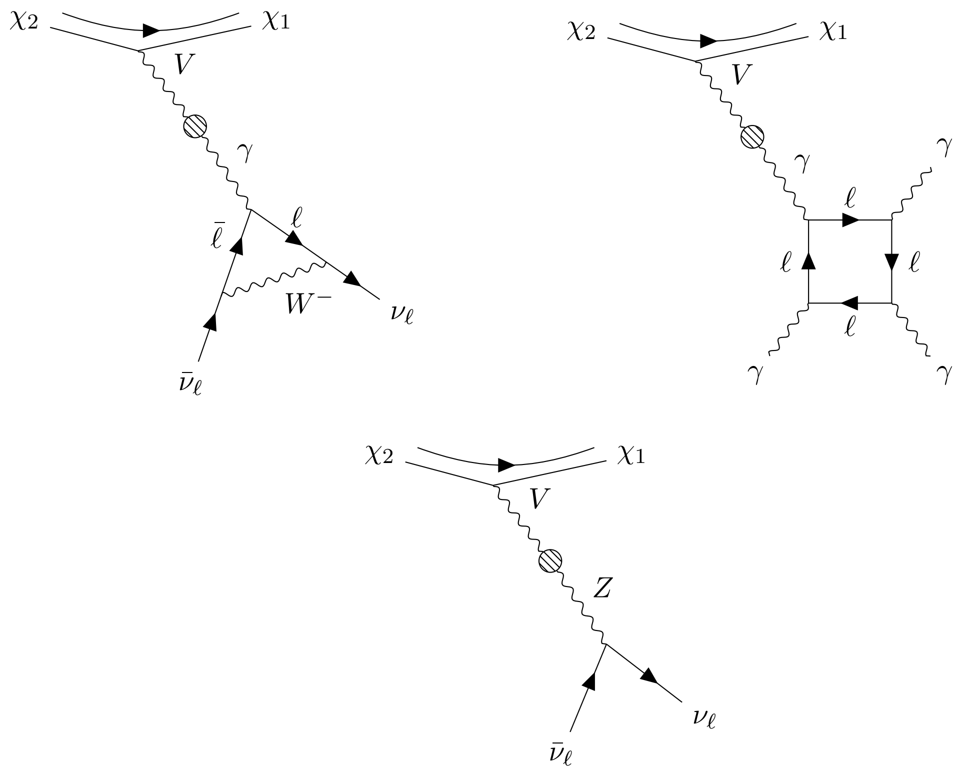


Figure 5.2: $\chi_2$ decay modes induced by the Z-V mixing and $\gamma$-V mixings, in the basis before diagonalization.

the ninth power of the energy released $\delta^9$, even though usually we have a $\delta^5$ scaling in weak decays. This can be understood as follows: in the basis before diagonalization, the $V - Z$ mixing is kinetic and it then implies in the amplitude a factor proportional to the transferred momentum, $q^2$, which is saturated by $\delta^2$.

As it is depicted in Fig. 5.2, another available $\chi_2$ decay channel is $\chi_2 \to \chi_1\gamma\gamma\gamma$, whose decay width is[198]

$$\Gamma_{\chi_2 \to \chi_1\gamma\gamma\gamma} \simeq \frac{17\alpha_e^3\alpha_D^2\epsilon^2\delta^{13}}{2^7 3^6 5^3 \pi^3 m_e^8 m_V^4}. \tag{5.20}$$

If the mass splitting satisfies $\delta > 2m_e$, then we also have another possible $\chi_2$ decay channel, which is the one depicted in Fig. 5.3.

However, in the coannihilation model introduced in Sec. 5.1.1 we always work in the regime where $\delta < m_V, m_e$ and, therefore, $\chi_2 \to \chi_1 V$ and $\chi_2 \to \chi_1 e^- e^+$ are kinematically forbidden decay channels. Hence, we can infer that

$$\frac{1}{\Gamma_{\chi_2}} \simeq \frac{1}{\Gamma_{\chi_2 \to \chi_2\bar{\nu}\nu} + \Gamma_{\chi_2 \to \chi_1\gamma\gamma\gamma}} \gg \tau_{\text{universe}}, \tag{5.21}$$

where $\tau_{\text{universe}}$ denotes the age of the Universe. Therefore, these decay channels are generally sub-dominant when compared to the down-scattering processes, which will be analyzed later, especially in the portion of the DM parameter space that we will consider.

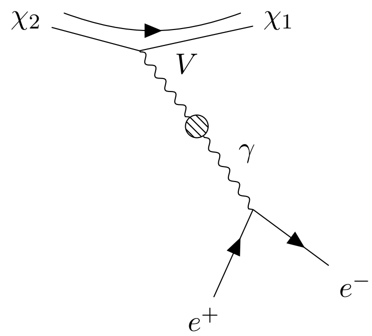


Figure 5.3: $\chi_2 \to \chi_1 e^- e^+$ decay channel.

In outlining the cosmological history of $\chi_2$, we can thus ignore these subdominant decay channels and consider only the effects of down-scattering processes in determining the late-time depletion of $\chi_2$[199].

### 5.2.2 Late-time depletion mechanisms

In the late-time evolution of dark matter models with nearly-degenerate DM states, such as coannihilation scenarios, depletion mechanisms, like down-scattering processes of the heavier DM component $\chi_2$ into the lighter one $\chi_1$, play a crucial role in determining the abundance of $\chi_2$. After kinetic decoupling from Standard Model particles, $\chi_2$ continues to be depleted primarily through efficient down-scattering processes like $\chi_2\chi_2 \to \chi_1\chi_1$. These interactions gradually reduce the $\chi_2$'s population, influencing its fractional abundance at late cosmological times.

In this section we follow the analysis of Ref. [191] to study more in detail these late-time depletion mechanisms and consequently depict the cosmic history of inelastic DM (iDM) as shown in Fig. 5.4.

#### DM-SM kinetic decoupling

After DM-SM chemical decoupling, $\chi_2 e^\pm \to \chi_1 e^\pm$ remains in kinetic equilibrium until a temperature $T_{\rm kd}$. We should notice, however, that we have other similar processes of the form $\chi_2\mathrm{SM} \to \chi_1\mathrm{SM}$, which are though subdominant because the thermal densities of SM particles are exponentially suppressed compared to the electrons' one[21].
These processes do not change the total number of DM particles as, after FO, $N_{\rm DM} \approx$ const, but they guarantee that for $T \gtrsim T_{\rm kd}$ the DM and SM sector share the same temperature, which means that $T_{\rm DM} = T_{\rm SM} \approx g_s^{-1/3} a^{-1}$, where $a$ is the scale factor.
In the limit that $m_V \gg s \gg \delta$ and $m_1 \gg m_e, T$, the differential cross section for $\chi_2 e^\pm \to \chi_1 e^\pm$

[21] For a non-relativistic particle species $X$ with mass $m_X$, the non-relativistic number density, according to Eq. (A.13), is given by $n_X \propto e^{-m_X/T}$, which means that the number density is exponentially suppressed for heavier particles. Since electrons are the lightest SM charged particles that remain unconfined after the QCD phase transition, their thermal number density is significantly larger than that of other SM particles such as hadrons and quarks.

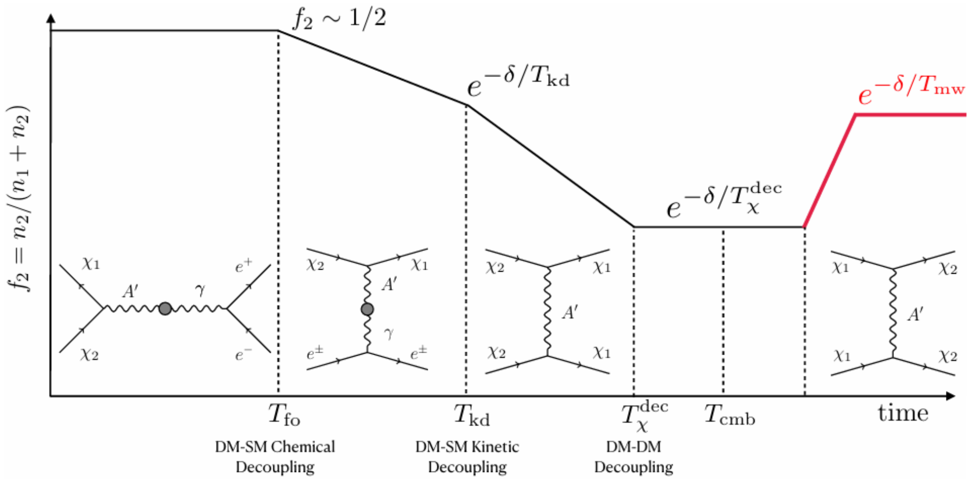


Figure 5.4: Cosmic history of iDM. DM relic abundance is fixed by the coannihilation process $\chi_2\chi_1 \to$ SM SM, which freezes-out at a temperature $T_{\rm fo} \gg \delta$. After FO, the total number of DM particles, denoted as $N_{\rm DM}$, remains roughly constant because the coannihilation processes are no more efficient due to the expansion of the universe. Written differently, we have that $N_{\rm DM} \equiv N_1 + N_2 \approx$ const, however $\chi_2$ continues to be depleted through $\chi_2$SM $\to \chi_1$SM processes until DM-SM kinetic decoupling occurs at a temperature $T_{\rm kd}$. For $T < T_{\rm kd}$ the heavier state $\chi_2$ continues to be depleted more rapidly through $\chi_2\chi_2 \to \chi_1\chi_1$ downscattering processes until DM-DM decoupling occurs at a DM temperature $T_{\rm DM} = T_\chi^{\rm dec}$. As a result, the primordial fraction of $\chi_2$ is exponentially suppressed at the time of recombination and CMB limits on DM annihilation are easily evaded. At much later times, in local regions of the Milky Way where the effective Galactic temperature of DM satisfies $T_{\rm mw} \gtrsim T_\chi^{\rm dec}$, the virialization of DM in the Milky Way increases its velocity, such that $\chi_1\chi_1 \to \chi_2\chi_2$ up-scattering partially restores the $\chi_2$ abundance.
***Reprinted from "Reviving MeV-GeV Indirect Detection with Inelastic Dark Matter", by Asher Berlin, Gordan Krnjaic and Elena Pinetti, University of Chicago***[191].

is given by[191]

$$\frac{d\sigma_{\chi e}}{dt} \simeq \frac{\pi \alpha_e \alpha_D \epsilon^2}{2 m_V^4 m_1^2 p_e^2}[2(s - m_1^2 - m_e^2)^2 + 2st + t^2], \tag{5.22}$$

where $s$ and $t$ are the usual Mandelstam variables and $p_e$ is the electron momentum. The rate for mantaining kinetic equilibrium is then given by[200, 201]

$$\Gamma_{\rm kd} \simeq -\frac{1}{3 m_1 T} \int \frac{d^3 p_e}{(2\pi)^3} f_e (1 - f_e) v_e \int_{-4p_e^2}^{0} dt\, t \frac{d\sigma_{\chi e}}{dt}, \tag{5.23}$$

where $f_e = \frac{1}{e^{E_e/T}+1}$ is the phase-space distribution of electrons with energy $E_e$ and $v_e$ is the electron velocity.
It is possible to compute the interaction rate in Eq. (5.23) both in the relatistic and non-

relativistic limit, finding that

$$\Gamma_{\rm kd} \simeq \frac{8\alpha_e \alpha_D \epsilon^2 T^2}{3m_V^4 m_1} \times \begin{cases} \frac{31}{63}\pi^5 T^4 & T \gg m_e \\ \frac{16}{\pi} m_e^4 e^{-m_e/T} & T \ll m_e \end{cases} . \tag{5.24}$$

In the approximation of instantaneous FO, we can find the kinetic decoupling temperature by imposing that

$$\Gamma_{\rm kd}(T_{\rm kd}) = H(T_{\rm kd}), \tag{5.25}$$

where $H(T_{\rm kd})$ is the Hubble parameter at $T = T_{\rm kd}$, defined as $H(T_{\rm kd}) = \sqrt{\frac{8\pi^3}{90} g_\rho(T_{\rm kd})} \frac{T_{\rm kd}^2}{M_{\rm pl}}$, with $M_{\rm pl} \simeq 1.22 \cdot 10^{19}$ GeV.
After kinetic decoupling the temperature of the DM sector, denoted as $T_{\rm DM}$, starts to deviate from that of the SM sector, indicated instead as $T_{\rm SM}$; in particular $T_{\rm SM} \propto g_s^{-1/3} a^{-1}$, while $T_{\rm DM} \propto \frac{1}{a^2}$. Indeed, the momentum of freely propagating particles redshifts as $p(t) = \frac{p_0}{a(t)} \propto \frac{1}{a}$, hence, the temperature of a decoupled non-relativistic particle redshifts as $T \propto E = \frac{p^2}{2m} \propto \frac{1}{a^2}$.

### DM-DM decoupling

After DM-SM kinetic decoupling, the down-scattering process $\chi_2\chi_2 \to \chi_1\chi_1$, which is unsuppressed by the small coupling $\epsilon$, remains in thermal equilibrium for a longer period compared to the processes already discussed, which are $\chi_2\chi_1 \to e^- e^+$ and $\chi_2 e^\pm \to \chi_1 e^\pm$.
The thermally averaged-rate relative to the $\chi_2\chi_2 \to \chi_1\chi_1$ scattering is[191]

$$\Gamma_\chi \simeq \frac{8\pi\alpha_D^2 m_1^{3/2}}{m_V^4} n_1 e^{-\delta/T_\chi} \max\left(\frac{\delta}{2}, \frac{T_\chi}{\pi}\right)^{1/2}, \tag{5.26}$$

where $n_1$ is the $\chi_1$ number density and $T_\chi \equiv T_{\rm DM}$ is the DM sector's temperature. It is possible to estimate the DM temperature $T_\chi^{\rm dec}$ at which $\chi_1 - \chi_2$ chemical decoupling occurs, by imposing that

$$\Gamma_\chi(T_\chi^{\rm dec}) = H(\bar{T}), \tag{5.27}$$

where $\bar{T}$ is instead the SM temperature when $\chi_1 - \chi_2$ chemical decoupling occurs. As we have already said, indeed, after kinetic decoupling the DM and the SM sectors share no more the same temperature, because $T_{\rm SM} \propto g_s^{-1/3} a^{-1}$, while $T_{\rm DM} \propto \frac{1}{a^2}$, so the DM temperature decreases faster than that of the SM. We can thus write that

$$g_s^{1/3}(\bar{T}) a_\chi^{\rm dec} \bar{T} = g_s^{1/3}(T_{\rm kd}) a_{\rm kd} T_{\rm kd} \implies \bar{T} = \left[\frac{g_s(T_{\rm kd})}{g_s(\bar{T})}\right]^{1/3} \frac{a_{\rm kd}}{a_\chi^{\rm dec}} T_{\rm kd}, \tag{5.28}$$

where $a_\chi^{\rm dec}$ corresponds to the scale factor when $\chi_1 - \chi_2$ chemical decoupling occurs.
Meanwhile, we can also write that

$$T_{\rm kd}(a_{kd})^2 = T_\chi^{\rm dec}(a_\chi^{\rm dec})^2 \implies \frac{a_{\rm kd}}{a_\chi^{\rm dec}} = \sqrt{\frac{T_\chi^{\rm dec}}{T_{\rm kd}}}, \tag{5.29}$$

where $a_{\rm kd}$ refers to the scale factor when the DM-SM kinetic decoupling occurs. Using Eqs. 5.28 and 5.29, the final relation between $\bar{T}$ and $T_\chi^{\rm dec}$ is

$$\bar{T} = \left[\frac{g_s(T_{\rm kd})}{g_s(\bar{T})}\right]^{1/3} \sqrt{\frac{T_\chi^{\rm dec}}{T_{\rm kd}}} T_{\rm kd} = \left[\frac{g_s(T_{\rm kd})}{g_s(\bar{T})}\right]^{1/3} \sqrt{T_\chi^{\rm dec} T_{\rm kd}}. \tag{5.30}$$

**Computation of the $\chi_2$'s fractional abundance**

After DM-SM chemical decoupling, which occurs at a temperature $T_{\mathrm{fo}}$, the number of DM particles remains roughly constant, so we can write that

$$n_{\mathrm{DM}}(a_\chi^{\mathrm{dec}})(a_\chi^{\mathrm{dec}})^3 = n_{\mathrm{DM}}(a_{\mathrm{eq}})(a_{\mathrm{eq}})^3 \implies n_{\mathrm{DM}}(a_\chi^{\mathrm{dec}}) = n_{\mathrm{DM}}(a_{\mathrm{eq}})\left(\frac{a_{\mathrm{eq}}}{a_\chi^{\mathrm{dec}}}\right)^3, \tag{5.31}$$

where $a_{\mathrm{eq}}$ denotes the scale factor at matter-radiation equality, which happens at a temperature $T = T_{\mathrm{eq}} \simeq 0.8$ eV.
Recalling Eqs. A.12 and A.14, we can write that at matter-radiation equality

$$\rho_m = m n_m = \rho_r = \frac{\pi^2}{30} g_\rho T^4, \tag{5.32}$$

where $\rho_m$ takes into account both baryonic and DM contributions. From observations of CMB anisotropies we know that $\Omega_{\mathrm{DM},0} \simeq 5\Omega_{\mathrm{B},0}$, where $\Omega_{\mathrm{DM},0}$ and $\Omega_{\mathrm{B},0}$ indicate respectively the DM and baryonic abundance observed today. Using the definition $\Omega_X = \frac{\rho_X}{\rho_c}$ for a generic component $X$, then we can write that

$$\frac{\rho_{\mathrm{DM}}}{\rho_c} \simeq 5\frac{\rho_{\mathrm{B}}}{\rho_c} \implies \rho_{\mathrm{DM}} \simeq 5\rho_{\mathrm{B}} \implies \rho_m = \rho_{\mathrm{DM}} + \rho_{\mathrm{B}} = \frac{6}{5}\rho_{\mathrm{DM}}. \tag{5.33}$$

To be more precise, in the limit that DM does not interact significantly with baryons and it is cosmologically stable, which are well-motivated assumptions, we can write that

$$\frac{\Omega_{\mathrm{DM}}}{\Omega_{\mathrm{B}}} = \frac{\rho_{\mathrm{DM}}}{\rho_{\mathrm{B}}} = \frac{\rho_{\mathrm{DM},0}(1+z)^3}{\rho_{\mathrm{B},0}(1+z)^3} = \frac{\Omega_{\mathrm{DM},0}}{\Omega_{\mathrm{B},0}} \simeq 5, \tag{5.34}$$

where $z$ denotes the redshift.
At matter-radiation equality, Eq. (5.32) can thus be rewritten as

$$\frac{6}{5} M_{\mathrm{DM}} n_{\mathrm{DM}}(a_{\mathrm{eq}}) = \frac{\pi^2}{30} g_\rho(T_{\mathrm{eq}}) T_{\mathrm{eq}}^4 \implies n_{\mathrm{DM}}(a_{\mathrm{eq}}) = \frac{\pi^2}{30}\frac{5}{6} g_\rho(T_{\mathrm{eq}}) \frac{T_{\mathrm{eq}}^4}{M_{\mathrm{DM}}}, \tag{5.35}$$

where $g_\rho(T_{\mathrm{eq}}) \simeq 3.36$, according to App. A.2.2.
Furthermore, recalling that $T_{\mathrm{SM}} \propto g_s^{-1/3} a^{-1}$, we can write that

$$T_{\mathrm{eq}} a_{\mathrm{eq}} g_s(T_{\mathrm{eq}})^{1/3} = \bar{T} a_\chi^{\mathrm{dec}} g_s(\bar{T})^{1/3} \implies \left(\frac{a_{\mathrm{eq}}}{a_\chi^{\mathrm{dec}}}\right)^3 = \frac{g_s(\bar{T})}{g_s(T_{\mathrm{eq}})}\left(\frac{\bar{T}}{T_{\mathrm{eq}}}\right)^3. \tag{5.36}$$

Using Eqs. 5.35 and 5.36, we can rewrite Eq. (5.31) as

$$n_{\mathrm{DM}}(a_\chi^{\mathrm{dec}}) = \frac{\pi^2}{30}\frac{5}{6} g_\rho(T_{\mathrm{eq}}) \frac{T_{\mathrm{eq}}^4}{M_{\mathrm{DM}}} \frac{g_s(\bar{T})}{g_s(T_{\mathrm{eq}})}\left(\frac{\bar{T}}{T_{\mathrm{eq}}}\right)^3. \tag{5.37}$$

Recalling that $m_2 = m_1 + \delta$, we have that the $\chi_2$ number density, denoted as $n_2$, is Boltzmann suppressed compared to $n_1$, which means that $n_2 = n_1 e^{-\delta/T_{\mathrm{DM}}}$. Therefore, exploiting Eqs.

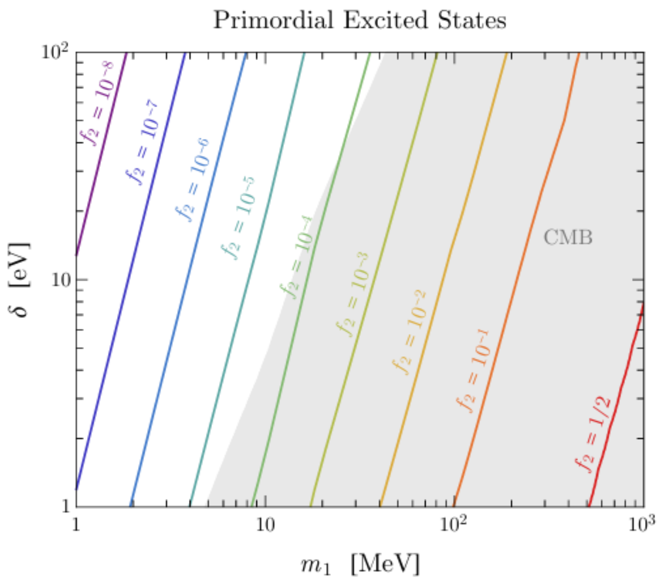


Figure 5.5: Contours of fractional $\chi_2$ abundance, denoted as $f_2$, set by $\chi_1 - \chi_2$ chemical decoupling in the early universe and for the particular choice of parameters $m_V = 3m_1$, $\alpha_D = 0.5$ and $\epsilon$ such that the FO abundance $\chi_{1,2}$ agrees with the observed DM density[202]. The gray shaded region corresponds to CMB limits as imposed by Eq. (5.43). We have reproduced this plot both in the relativistic ($T_{\rm kd} \gg m_e$) and in the non-relativistic ($T_{\rm kd} \ll m_e$) regime, using the corresponding scattering rates given in Eq. (5.24).
***Reprinted from "Reviving MeV-GeV Indirect Detection with Inelastic Dark Matter", by Asher Berlin, Gordan Krnjaic and Elena Pinetti, University of Chicago.***[191]

5.30, 5.37 and using that $n_{\rm DM}(a_\chi^{\rm dec}) \equiv n_1(a_\chi^{\rm dec}) + n_2(a_\chi^{\rm dec}) = n_1(1 + e^{-\delta/T_\chi^{\rm dec}})$, we can write the $\chi_1$ number density at $\chi_1 - \chi_2$ chemical decoupling as

$$n_1(a_\chi^{\rm dec}) = \frac{\pi^2}{30}\frac{5}{6} g_\rho(T_{\rm eq}) \frac{T_{\rm eq}}{M_{\rm DM}} \frac{g_s(T_{\rm kd})}{g_s(T_{\rm eq})} (T_\chi^{\rm dec} T_{\rm kd})^{3/2} \frac{1}{1 + e^{-\delta/T_\chi^{\rm dec}}}. \tag{5.38}$$

At this point, we can estimate the DM temperature $T_\chi^{\rm dec}$ at which $\chi_1 - \chi_2$ chemical decoupling occurs using Eqs. 5.27 and 5.38. Consequently, we can estimate the primordial abundance of $\chi_2$ as

$$f_2 = \frac{n_2}{n_1 + n_2} \simeq \frac{e^{-\delta/T_\chi^{\rm dec}}}{1 + e^{-\delta/T_\chi^{\rm dec}}}. \tag{5.39}$$

In particular, in Fig. 5.5 there are plotted contours of the $\chi_2$'s primordial abundance in the $m_1 - \delta$ parameter space for the particular choice of parameters $m_V = 3m_1$, $\alpha_D = 0.5$ and $\epsilon$ such that the FO abundance of $\chi_{1,2}$ agrees with the observed DM density[191, 202].

**CMB limits**

A big portion of the $m_1 - \delta$ parameter space in Fig. 5.5 is constrained by CMB limits[27]. Indeed, the CMB places strong constraints on the thermally-averaged dark matter annihilation cross section $\langle \sigma v \rangle$ through its sensitivity to energy injection in the early universe. Dark matter annihilation deposits energy into the intergalactic medium during and after recombination, altering the ionization history and leaving imprints on the CMB anisotropies. The *Planck* 2018 data constrain the effective parameter $p_{\text{ann}} = f_{\text{eff}} \frac{\langle \sigma v \rangle}{m_\chi}$, where $f_{\text{eff}}$[22] is the fraction of the energy released by the annihilation process that is transferred to the intergalactic medium (IGM) around the redshifts to which the CMB anisotropy data are most sensitive, namely $z \simeq 600$ and $m_\chi$ is the dark matter mass. Assuming $s$-wave annihilation, *Planck* finds

$$p_{\text{ann}} < 3.2 \cdot 10^{-28} \text{cm}^3 \text{s}^{-1} \text{GeV}^{-1}, \tag{5.40}$$

which translates into upper bounds on $\langle \sigma v \rangle$ that depend on the annihilation channel and DM mass. To interpret correctly CMB limits in Ref. [27], we require that the reaction rates[23] relative to $\chi_2 \chi_1 \to e^- e^+$ and $\chi \chi \to e^- e^+$ are equivalent and, therefore,

$$n_1 n_2 \langle \sigma v \rangle_{\chi_2 \chi_1 \to e^+ e^+} = \frac{n_\chi^2}{2} \langle \sigma v \rangle_{\chi \chi \to e^- e^+}, \tag{5.41}$$

where the factor of 2 on the right-hand side of Eq. (5.41) accounts for the fact that CMB limits in Ref. [27] assumed annihilation of self-conjugate DM particles, whereas $\chi_1 - \chi_2$ coannihilation involve distinct species. Renaming $n_\chi \equiv n_{\text{DM}}$, we can write that

$$\langle \sigma v \rangle_{\chi \chi \to e^- e^+} = 2 \underbrace{\frac{n_1}{n_1 + n_2}}_{f_1} \underbrace{\frac{n_2}{n_1 + n_2}}_{f_2} \underbrace{\left( \frac{n_1 + n_2}{n_{\text{DM}}} \right)^2}_{f_\chi^2} \langle \sigma v \rangle_{\chi_1 \chi_2 \to e^- e^+}, \tag{5.42}$$

where $f_\chi$ represents the fractional abundance of DM that $\chi_1$ and $\chi_2$ jointly constitute, which in our case is $f_\chi = 1$, because we are assuming that all the DM observed in the Universe is accounted for by $\chi_1$ and $\chi_2$.
We can thus reinterpret the CMB limits in Ref. [27] relative to the $e^- e^+$ annihilation channel as

$$\langle \sigma v \rangle_{\chi \chi \to e^- e^+} = 2 f_1 f_2 f_\chi^2 \langle \sigma v \rangle_{\chi_1 \chi_2 \to e^- e^+} \lesssim 2 \cdot 10^{-26} \text{cm}^3 \text{s}^{-1} \left( \frac{m_1}{30 \text{ GeV}} \right). \tag{5.43}$$

Eq.(5.43) is violated in the excluded gray area of Fig. 5.5.

In this section we have analyzed late-time depletion mechanisms that gradually reduce the population of the heavier DM component $\chi_2$. However, at late cosmological times, it may happen that in overdense regions of the Universe, such as those where galactic structures form, the virialization of DM increases its velocity, such that the $\chi_1 \chi_1 \to \chi_2 \chi_2$ up-scattering processes reenter equilibrium. In local regions of the Milky Way where this particular phenomenon

[22] The efficiency factor $f_{\text{eff}}$ depends on several key aspects of the dark matter annihilation process and how the annihilation products interact with the thermal plasma. Specifically, each annihilation channel produces a different spectrum of secondary particles, leading to different energy deposition histories.

[23] The reaction rate quantifies the number of reactions occurring per unit volme and time. It is therefore measured in units of $\text{cm}^{-3} \text{s}^{-1}$.

occurs, the $\chi_2$ population is efficiently regenerated. It is important to understand these mechanisms, because once $\chi_2$ is regenerated, it can undergo even more down-scattering processes which, as we will discuss more in detail in Sec. 5.3, play a crucial role, as they offer a potential strategy to test iDM models.

### 5.2.3 Late-time evolution and regeneration of $\chi_2$

After $\chi_1 - \chi_2$ chemical decoupling, the average fractional abundance $f_2$ remains fixed, as the DM temperature continues to decrease as $T_{\rm DM} \propto \frac{1}{a^2}$, due to the expansion of the Universe. However, within overdense regions, such as those where galaxies form, DM can be heated to much higher temperatures through virialization. When this local temperature satisfies $T_{\rm DM} \gtrsim \delta$ , the up-scattering process $\chi_1\chi_1 \to \chi_2\chi_2$ becomes active and generates a new population of excited states long after the initial freeze-out.

As described in the toy model of Ref. [191], we assume that DM follows a Maxwell-Boltzmann distribution, with an effective temperature $T_{\rm mw}$, which is defined as

$$T_{\rm mw}(r) = \frac{GM_{\rm enc}(r)}{3r} m_1, \tag{5.44}$$

where $M_{\rm enc}(r)$ is the total mass enclosed within a radius $r$ and it is defined as[24]

$$M_{\rm enc}(r) = M_{\rm B}(r) + M_{\rm DM}(r) = 4\pi \int_0^r (\rho_{\rm B}(r') + \rho_1(r'))r'^2 dr'. \tag{5.45}$$

In defining the total enclosed mass in Eq. (5.45), authors of Ref. [191] used the best-fit, spherically symmetric Hernquist profile model advocated in Refs. [203, 204]

$$\rho_{\rm B}(r) = \frac{\rho_{\rm B0} r_0^4}{r(r + r_0^3)}, \tag{5.46}$$

where $\rho_{\rm B0} = 26$ GeVcm$^{-3}$ and $r_0 = 2.7$ kpc. The initial $\chi_1$ mass density, instead, is modeled as the usual NFW profile

$$\rho_1(r) = \frac{\rho_s}{(r/r_s)(1 + r/r_s)^2}, \tag{5.47}$$

where $r_s = 20$ kpc is the scale radius and $\rho_s$ is fixed by the requirement that the DM mass density at the Sun position is

$$\rho_1(r = r_\odot \simeq 8.5 \text{ kpc}) \simeq 0.4 \text{ GeVcm}^{-3}. \tag{5.48}$$

Following Ref. [191], we can model the time-evolution of the $\chi_2$ population through the Boltzmann equation, which, neglecting gradient and gravitational terms[25], becomes

$$\frac{\partial n_2}{\partial t} = n_1^2 \langle \sigma v \rangle_{1\to 2} - n_2^2 \langle \sigma v \rangle_{2\to 1}, \tag{5.49}$$

[24] Ref. [191] assumes that the gravitational potential is dominated by $\chi_1$ and baryons, as at early times in most of the halo $f_2 \ll 1$.

[25] Neglecting gradient and gravitational terms in the time-evolution of $\chi_2$ population significantly simplifies the problem, because the full spatial and velocity distribution would be too complicate to model and would require N-body simulations for a better analysis.

where

$$\langle\sigma v\rangle_{1\to 2} = e^{-2\delta/T_{\rm mw}}\langle\sigma v\rangle_{2\to 1} = e^{-2\delta/T_{\rm mw}}\frac{8\pi\alpha_D^2 m_1^{3/2}}{m_V^4}\max\left(\frac{\delta}{2},\frac{T_{\rm mw}}{\pi}\right)^{1/2}. \tag{5.50}$$

From the Boltzmann equation 5.49, once $n_2$ evolves to $n_2 \simeq e^{-\delta/T_{\rm mw}}n_1$, it approaches a constant value and $\chi_1 - \chi_2$ chemical equilibrium is restored.
Indicating the number of upscatters per $\chi_1$ particle after a time $t$ as $N_{\rm scatt} = n_1\langle\sigma v\rangle_{1\to 2}t$, we can approximate the solution of Eq. (5.49) as

$$n_2 \simeq n_1 \min\left(N_{\rm scatt}, e^{-\delta/T_{\rm mw}}\right) \tag{5.51}$$

and therefore the $\chi_1 - \chi_2$ chemical equilibrium is restored when $N_{\rm scatt} \sim e^{-\delta/T_{\rm mw}}$, which occurs on a timescale

$$t_{\rm CE} \sim \frac{e^{-\delta}/T_{\rm mw}}{n_1\langle\sigma v\rangle_{1\to 2}} = \frac{e^{-\delta}/T_{\rm mw}}{n_1 e^{-2\delta/T_{\rm mw}}\langle\sigma v\rangle_{2\to 1}} = \frac{e^{\delta}/T_{\rm mw}}{n_1\langle\sigma v\rangle_{2\to 1}}. \tag{5.52}$$

Hence, requiring that $t_{\rm CE} < t_{\rm mw} \simeq 13.5$ Gyr, where $t_{\rm mw}$ denotes the age of the Universe, it is possible to plot the radial regions of the Milky Way, where $\chi_1 - \chi_2$ chemical equilibrium is restored, as shown in Fig. 5.6.

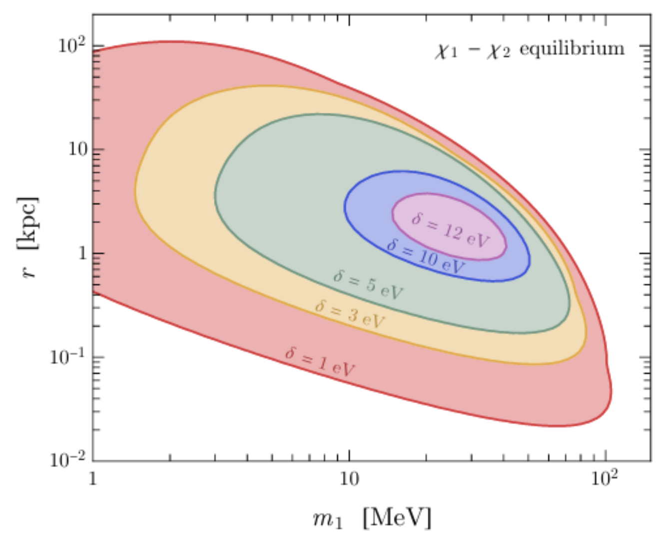


Figure 5.6: Radial regions of the Milky Way where the $\chi_1\chi_1 \to \chi_2\chi_2$ up-scattering processes reenter equilibrium over the age of the Galaxy, which is $t_{\rm mw} \simeq 13.5$ Gyr, in the $m_1 - r$ parameter space, for the particular choice of parameters $m_V = 3m_1$ and $\alpha_D = 0.5$. It is also assumed to have an initial NFW profile for $\chi_1$.
***Reprinted from "Reviving MeV-GeV Indirect Detection with Inelastic Dark Matter", by Asher Berlin, Gordan Krnjaic and Elena Pinetti, University of Chicago***[191].

In the following sections we will see that in the iDM model introduced in Sec. 5.1 we deal with values of mass splittings $\delta \gg 10$ eV, for which the $\chi_1\chi_1 \to \chi_2\chi_2$ up-scattering processes do not reenter equilibrium and, consequently, $\chi_2$'s population is not efficiently regenerated.

In the following, we apply the framework developed so far to study the phenomenology of the iDM model introduced in Sec. 5.1 and derive the corresponding experimental constraints.

## 5.3 Phenomenology of the coannihilation model for the 511 keV line

In this section we proceed to analyze the phenomenological implications of the iDM model introduced in Sec. 5.1 and confront it with experimental and observational constraints. Furthermore, we want to identify the regions of the parameter space which consistently reproduce the observed DM relic abundance and, in the meantime, explain the 511 keV gamma-ray line from the Galactic Center.

We start with a simple analysis, updating the results obtained in Ref. [171]. For that reason, we can exploit the best-fit value of the thermally-averaged DM annihilation cross section, provided in Ref. [167], which is written in Eq. (5.4).
Moreover, we manage to reproduce the observed DM relic abundance and to explain the 511 keV gamma-ray signal from the GC, by imposing respectively Eqs. (5.8) and (5.9). Specifically, authors of Ref. [171] claim that, for simplicity, they use the $s$-wave values at $M_{\rm DM} = 3$ MeV, $\sigma v_{\rm FO}^{(s)} \simeq 8 \cdot 10^{-26} {\rm cm}^3/{\rm s}$ and $x_{\rm fo} \simeq 15$, because their dependence on $M_{\rm DM}$ is very mild[54].
Eqs. (5.8) and (5.9) leave 4 free parameters, two of which are fixed by Ref. [171] to be $m_\varphi = 2$ MeV and $m_V = 15$ MeV.

Following this procedure, authors of Ref. [171] derive the results illustrated in Fig. 5.7, where they also report in orange the contour lines of constant down-scattering cross section $\sigma_{\chi_2 e^\pm \to \chi_1 e^\pm}$, which, from Ref. [171], in the limit that $\delta \to 0$, is given by

$$\sigma_{\chi_2 e^\pm \to \chi_1 e^\pm} = 4\alpha_e g_D^2 \epsilon^2 \frac{\mu_{\rm eDM}^2}{m_V^4}. \tag{5.53}$$

As for the $p$-wave model in Sec. 5.1.1, it is possible to keep these small values of $M_{\rm DM}$ in agreement with CMB and BBN constraints, by adding a coupling to neutrinos $g_\nu V_\mu \bar{\nu}\gamma^\mu \nu$, with $g_\nu \sim 10^{-2} e\epsilon$. The origin of $g_\nu$ is explained in Ref. [171]. This coupling induces the $\chi_2$ decay into neutrinos, which results to be[171]

$$\Gamma_{\chi_2 \to \chi_1 \bar{\nu}\nu} \simeq g_\nu^2 g_D^2 \frac{\delta^5}{40\pi^3 m_V^4}, \tag{5.54}$$

if we ignore the other decay channels of $\chi_2$ into SM particles, discussed in Sec. 5.2.1. Indeed Ref. [171] did not consider them and thus we remain consistent with this procedure if we want to only update their results with recent experimental constraints. In the following, we will move away from this approach. It is possible to see from Fig. 5.7 that for $m_V = 15$ MeV and for $\delta \gtrsim 1$ keV, we obtain that $\tau_2 = \frac{1}{\Gamma_{\chi_2 \to \chi_1 \bar{\nu}\nu}} < 10^9$ years, in such a way that all $\chi_2$'s left after freeze-out have decayed by today.

In this section, we have followed the analysis of Ref. [171], updating the experimental

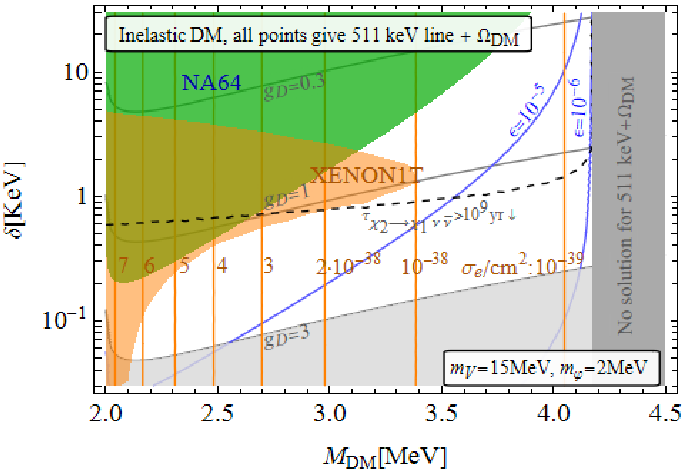


Figure 5.7: After fixing $m_V = 15$ MeV and $m_\varphi = 2$ MeV, the phenomelogy of the model is completely determined by $M_{\rm DM}$ and the mass splitting $\delta$, once we require to fit both the observed DM relic abundance in Eq. (5.8)and the 511 keV line in Eq. (5.9). In the plot there are several constraints: the gray area delimits the region of the parameter space where the dark coupling $g_D$ is no longer perturbative, the green area represents NA64 dark photon limits[102] and in the orange region we present bounds from solar up-scattering, derived by Ref. [171], and based on indicative limits from XENON1T data[205]. The gray band, instead, corresponds to the region of the plot where it is not possible to explain the 511 keV signal in the GC, while matching the observed DM relic abundance. Moreover, orange lines are contours of constant $\sigma_{\chi_2 e^\pm \to \chi_1 e^\pm}$, while the gray lines are contours of constant dark coupling $g_D$. The dashed gray line roughly delimits the region where $\chi_2$ decays into neutrinos are not enough to deplete the primordial $\chi_2$ population and further constraints could arise. This happens only if we follow the procedure of Ref. [171], which does not consider all the additional $\chi_2$ decay channels discussed in Sec. 5.2.1 and, therefore, add the neutrino coupling $g_\nu V_\mu \bar{\nu}\gamma^\mu \nu$ as potential solution to remain consistent with CMB and BBN limits. In the following we will not consider anymore this additional coupling and we will move away from this approach. In this plot, NA64 constraints are updated with respect to the ones derived in Ref. [171].

limits from NA64 in light of recent improvements. We now proceed to extend the work presented in Ref. [171], by using the results obtained in Sec. 3.2.3 as best-fit values of the thermally-averaged DM annihilation cross section. Moreover, in extending the work of Ref. [171], we do not consider anymore the additional coupling to neutrinos, that is $g_\nu V_\mu \bar{\nu}\gamma^\mu \nu$, as in most cases we work with $M_{\rm DM} \gtrsim \mathcal{O}(10\ {\rm MeV})$. Therefore, for those values of DM masses, we do not need an extra-injection of neutrinos in the early universe to be consistent with CMB and BBN limits. Moreover, as we have discussed extensively so far, from now on we consider $\chi_2$ down-scattering processes into $\chi_1$ as the main late-time depletion mechanisms that reduce efficiently $\chi_2$'s population.
Indeed, Ref. [171] did not consider the possibility of having these down-scattering processes that may deplete $\chi_2$ and therefore, they added an additional coupling to neutrinos $g_\nu V_\mu \bar{\nu}\gamma^\mu \nu$, as possible solution for this problem.

**Exploring new alternatives for the coannihilation model**

To extend the work presented in Ref. [171], we adopt two distinct DM density profiles, which are the $_*$MIN and the Gondolo-Silk configurations, both of which are based on a generalized NFW halo density profile with an inner slope $\gamma$ in the range $1 \leq \gamma \leq 1.2$. We do not consider steeper density profiles, because these would lead to very large annihilation signals, which make such profiles strongly testable and consequently also highly constrained.
These DM density profiles are also used in Sec. 3.2.2 to derive the expected positron injection rate from DM annihilations into $e^-e^+$ pairs, as shown in Figs. 3.2 and 3.3, which is directly related to the observed 511 keV gamma-ray line from the GC.

In the following subsections, we will exploit the machinery developed in Secs. 3.2.3 and 5.2 to extend the treatment presented in Ref. [171].

### 5.3.1 Experimental and cosmological constraints for the coannihilation model

In this section we want to give a general overview of the experimental and cosmological limits that may constrain the coannihilation model introduced in Sec. 5.1.1. Specifically, we divide the discussion into three paragraphs:

- In the first one we discuss of cosmological and astrophysical constraints.
- In the second paragraph we briefly discuss of non-perturbativity.
- In the third paragraph we present how we can apply terrestrial limits, some of which already discussed in Sec. 5.1.3, to our specific coannihilation model.

**Cosmological and astrophysical constraints**

We examine cosmological and astrophysical limits relevant to the coannihilation model introduced in Sec. 5.1.1. Key constraints include those derived from the supernova SN 1987A and from CMB observations.

- *CMB bounds*: As already mentioned in Sec. 5.2.2, the CMB places strong constraints on the thermally-averaged DM annihilation cross section $\langle \sigma v \rangle$ through its sensitivity to energy injection in the early universe. According to *Planck 2018* data and, following the discussion delined in Sec. 5.2.2, we can constrain the $e^-e^+$ DM annihilation channel to satisfy Eq. (5.43).
- *SN 1987A*: Following Ref. [142], we can revisit the limits obtained from observations of SN 1987A, which were originally derived under the assumptions $m_V = 3M_{\rm DM}$ and $\alpha_D = 0.5$. In particular, we are interested in the upper boundary of the SN 1987A constraints, which from Eq. 2.14 of Ref. [142], is obtained by requiring that

$$\frac{\epsilon\sqrt{\alpha_D}}{m_V^2} \simeq C\frac{\pi}{2} \implies \epsilon_{\rm limit} \simeq C\frac{\pi}{2}\frac{m_V^2}{\sqrt{\alpha_D}}, \tag{5.55}$$

  where $C$ is a constant. To recast these upper limits in terms of $\epsilon$, we can write that

$$\epsilon'_{\rm limit} \simeq C\frac{\pi}{2}\frac{m_V'^2}{\sqrt{\alpha'_D}} = \epsilon_{\rm limit}\frac{m_V'^2}{m_V^2}\sqrt{\frac{\alpha_D}{\alpha'_D}}, \tag{5.56}$$

where $\alpha'_D \neq \alpha_D = 0.5$ and $m'_V \neq m_V = 3M_{\rm DM}$ in general. However, the whole DM parameter space considered in Fig. 5.9 satisfy that $\epsilon > \epsilon_{\rm limit}$ and thus it remains unconstrained by these limits.

- *Indirect detection constraints*: We do not consider indirect detection bounds to constrain our coannihilation model, because gamma-ray telescopes and cosmic-ray detectors have limited sensitivities to light DM; additionally constraints from CMB and direct dection are stronger for this class of models.

**Non-perturbativity of the dark coupling**

As discussed for the $p$-wave model, the computation of the cross sections in Eqs. (5.6), (5.7) and (5.53) is based on Feynman rules within perturbative quantum field theory. To ensure the validity of these calculations, the coupling constants must be small enough for the perturbative expansion to converge. To that end, to remain safely within the perturbative regime, we impose that the dark coupling satisfies $g_D \lesssim 3$. All the other couplings involved in the coannihilation model introduced in Sec. 5.1.1 easily satisfy that perturbative condition.

**Terrestrial constraints**

In this paragraph we briefly discuss of constraints from NA64. Thereafter, we follow Ref. [194] and, based on what we have already presented in Sec. 5.1.3, we study how DM down-scattering and up-scattering processes can constrain the coannihilation model introduced in Sec. 5.1.1.

- *NA64 constraints*: As already mentioned for the $p$-wave model, the NA64 experiment at CERN SPS, derived some of the most stringent constraints on invisibly decaying dark photons in the MeV-GeV mass range. Specifically, Ref. [102] presents an upper bound on the kinetic mixing parameter $\epsilon < \epsilon_{\rm limit}(m_V)$, as a function of the dark photon mass $m_V$. These limits can thus be applied to our coannihilation model.

- *Up-scattering constraints*: First of all, in the coannihilation model under consideration we deal with values of the mass splittings $\delta \gtrsim \mathcal{O}(100\text{ eV})$. Therefore, from Fig. 5.1 and following the discussion presented in Sec. 5.1.3, we can see that for 1 MeV $\lesssim M_{\rm DM} \lesssim$ 20 MeV, which is the DM mass range under consideration (see Ref. [11]), we are never affected by up-scattering constraints. However, the kinematic boundary for up-scattering in Fig. 5.1 is derived in a very general way by stating that up-scattering can occur only if $\frac{1}{2} m_{\chi_1} v^2 \gtrsim \delta$ in such a way that for large values of $\delta$ these processes become kinematically forbidden.

  For a better analysis we can follow the procedure discussed in Sec. 5.2.3 and taken from Ref. [191]. Therefore, we plot in Fig. 5.8 the radial regions of the Milky Way where $\chi_1\chi_1 \to \chi_2\chi_2$ up-scattering processes reenter equilibirium over the age of the Galaxy for different benchmark values of $m_V$ and $m_\varphi$. We note that these up-scattering processes are kinematically allowed only for small values of $\delta$, which lie below the range considered in our analysis.

- *Down-scattering constraints*: For what concerns down-scattering constraints, following Ref. [194] and the discussion presented in Sec. 5.1.3, we place we place constraints on all regions of the DM parameter space where the expected rate for $\chi_2$ down-scattering off

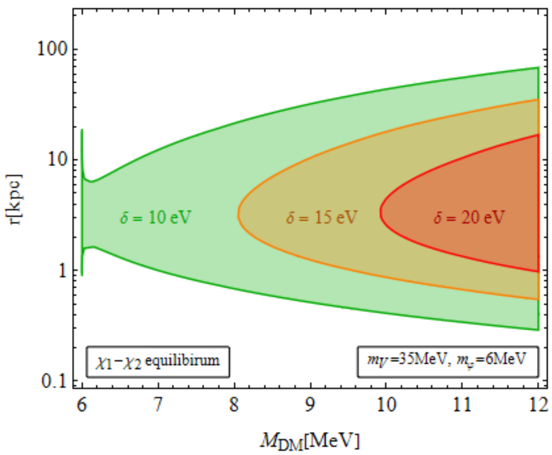


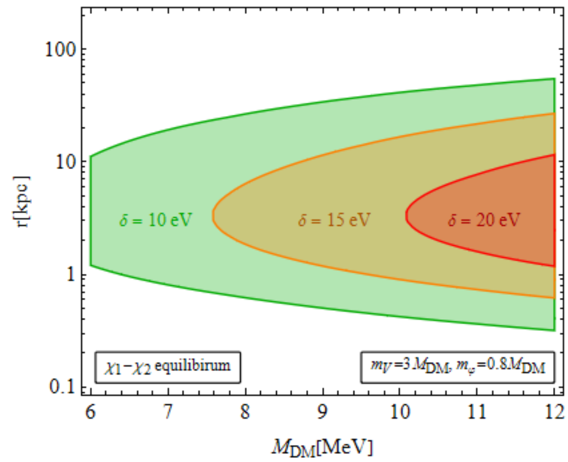


Figure 5.8: Radial regions of the Milky Way where the $\chi_1\chi_1 \to \chi_2\chi_2$ up-scattering processes reenter equilibrium over the age of the Galaxy, which is $t_{\rm mw} \simeq 13.5$ Gyr, in the $M_{\rm DM} - r$ parameters space, for $m_V = 35$ MeV, $m_\varphi = 6$ MeV in the left panel and for $m_V = 3M_{\rm DM}$, $m_\varphi = 0.8M_{\rm DM}$ in the right panel. These results are obtained assuming a positron injection rate within a sphere of radius $r \lesssim 4$ kpc around the GC of $\simeq 2.5 \cdot 10^{42}$ s$^{-1}$.

electrons, $R_e$, and off nuclei, $R_{\rm N}$, exceeds the experimental upper limit set by Xenon1T and CRESST respectively. The down-scattering limits obtained in Ref. [194], however, are valid for $\alpha_D = 0.5$ and $m_V = 3(m_{\chi_1} + \frac{\delta}{2})$ and, therefore, if we want to apply them to the coannihilation model introduced in Sec. 5.1.1, a recasting is necessary.

Since to fit the 511 keV line we focus only on DM masses in the range 1 MeV $\lesssim M_{\rm DM} \lesssim 20$ MeV, we recast only the electron down-scattering constraints, as this channel yields a stronger signal due to the higher recoil energy in this mass range.
Indeed, the characteristic recoil energies are given by $\mathrm{E_R} = \frac{\mu_{\chi_2 e}}{m_e}\delta$ for electrons and $\mathrm{E_R} = \frac{\mu_{\chi_2 \rm N}}{m_{\rm N}}\delta$ for nuclei. Hence, we can notice that for the same values of $\mathrm{M_{DM}} \sim \mathcal{O}(10\ \mathrm{MeV})$ and $\delta \sim \mathcal{O}(1\ \mathrm{keV})$ the recoil energy from scattering off electrons is larger than that from nuclei. In particular, the latter falls below the detection threshold of leading experiments like XENONnT, PandaX and LUX-ZEPLIN.

Looking at the signal rate in Eq. (5.11), we notice that the only model-dependent terms are $f^{\rm det}_{\chi_2}$ and $\sigma_{\chi_2 e}v$. In particular, we recall that $f^{\rm det}_{\chi_2} = \epsilon_{\rm Earth} f_{\chi_2}$, where authors of Ref. [194] claim that $\epsilon_{\rm Earth}$ is always greater than 0.5 and approximately 1 for $M_{\rm DM} \gtrsim 1$ GeV, so we can assume it to remain approximately constant while we change the values of $\alpha_D$ and $m_V$, while $f_{\chi_2}$ is the fractional abundance of the heavier DM state, which can be taken from Fig. 5.1 or computing it directly as $f_{\chi_2} = \frac{Y_2}{Y_{\rm TOT}}$ as done in Ref. [194]. Furthermore, we can write that $\sigma_{\chi_2 e}v \propto \frac{\epsilon^2\alpha_D}{m_V^4}$.
We can thus rewrite the signal rate $R_e$ in first approximation as $R_e \simeq f(M_{\rm DM}, \delta) f_{\chi_2} \frac{\epsilon^2\alpha_D}{m_V^4}$, where $f(M_{\rm DM}, \delta)$ is a generic model-independent function of $M_{\rm DM}$ and $\delta$.

Since we place limits on all regions of the DM parameter space where $R_e > R_{\rm limit}$, with $R_{\rm limit}$ which is the upper experimental bound set by Xenon1T, we can recast the down-scattering constraints in Ref. [194] by writing that

$$R'_e = R_e \frac{f'_{\chi_2}}{f_{\chi_2}} \frac{\epsilon'^2 \alpha'_D}{\epsilon^2 \alpha_D} \frac{m_V^4}{m_V'^4}, \tag{5.57}$$

where the prime denotes the parameters used for the phenomenology of the coannihilation model discussed in Sec. 5.1.1, which are in general different from those chosen by Ref. [194]. In this way, we obtain an approximate recast of down-scattering limits that we can apply to our case, however, a better analysis is needed if we want to find them precisely.

Requiring to match the observed DM relic abundance and explain the 511 keV line, by imposing respectively Eqs. (5.8) and (5.9), we can plot in Fig. 5.9 the $M_{\rm DM} - \delta$ parameter space for different benchmark values of $m_V$ and $m_\varphi$ with all possible experimental constraints for the coannihilation model discussed so far.
From Fig. 5.9 we can observe that down-scattering bounds become less stringent both at small and large values of $\delta$. For smaller $\delta$, this is because the corresponding recoil energy falls below the sensitivity threshold of Xenon1T. For larger $\delta$, instead, the recoil energies exceed the upper end of the experiment's search window, placing them outside the detectable range.
Moreover, to compute the fractional abundance of $\chi_2$ we have followed the procedure discussed in Sec. 5.2.2. In our specific case we can use the non-relativistic interaction rate in Eq. (5.24) to compute the DM-SM kinetic decoupling because all regions of the considered parameter space lie in the non-relativistic regime, where $T_{\rm kd} \ll m_e$.

### 5.3.2 Targets for direct detection experiments

So far, we have identified the regions of the parameter space where the coannihilation model introduced in Sec. 5.1 succesfully explain the 511 keV line, while matching the observed DM relic abundance and in the meantime remaining compatible with experimental and observational limits, expecially those from down-scattering processes of the heavier DM component $\chi_2$ into the lighter one $\chi_1$. We now use this information to derive a benchmark target for direct detection experiments. This serves as a valuable tool to evaluate the extent to which the coannihilation model analyzed in this chapter can account for the 511 keV emission from the Galactic Center.

For each DM density profile under consideration, we can construct the corresponding DM parameter space in the $M_{\rm DM} - \delta$ plane, as shown in Fig. 5.9, under the benchmark assumptions $m_V = 3M_{\rm DM}$ and $m_\varphi = 0.8M_{\rm DM}$, as for these values the DM parameter space seems to be less excluded by down-scattering limits. Each parameter space includes theoretical and experimental constraints such as:

- CMB bounds[27];
- exclusion limits from NA64[102];

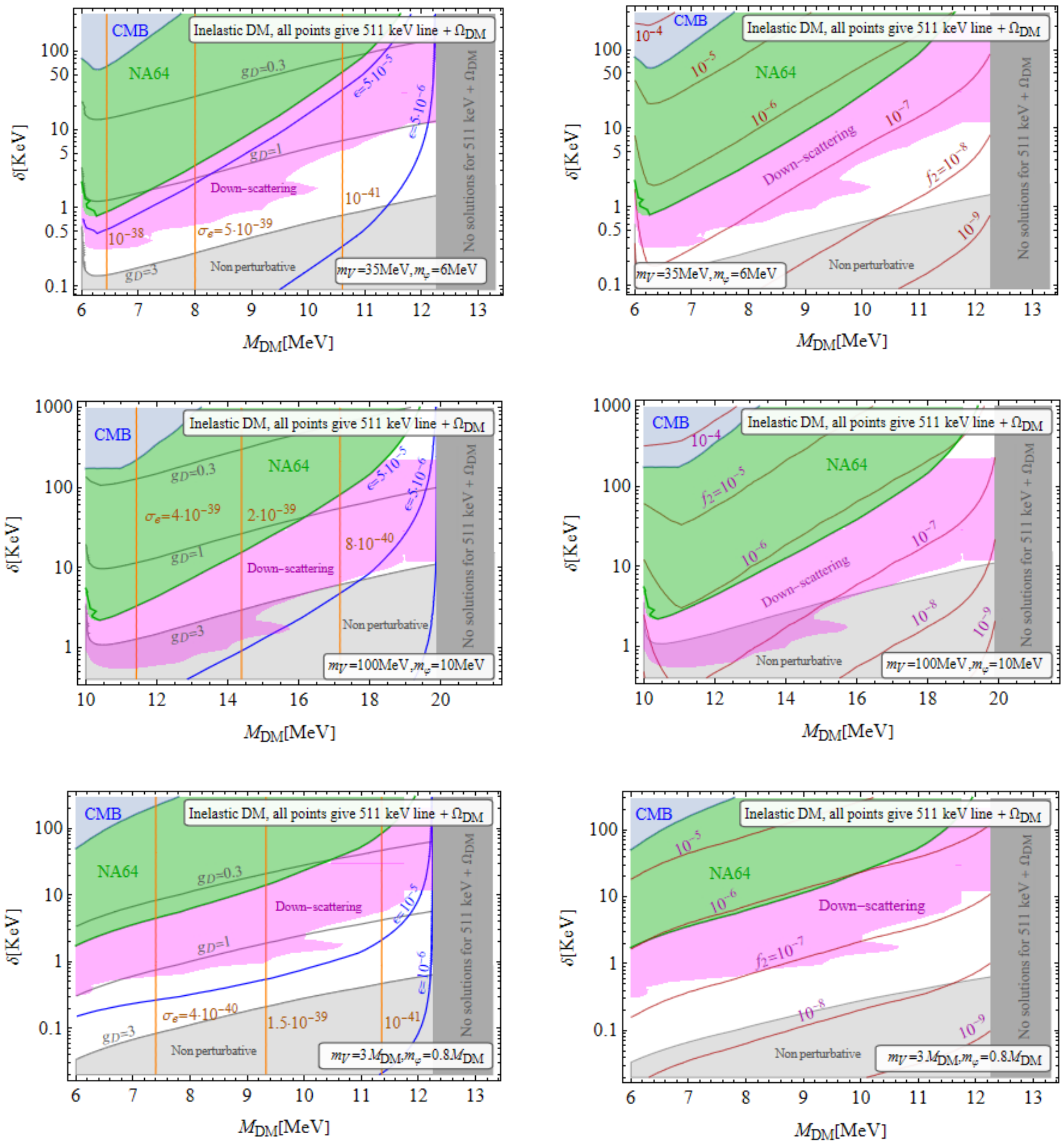


Figure 5.9: $M_{\rm DM} - \delta$ parameter space for different benchmark values of $m_V$ and $m_\varphi$. The 511 keV signal is explained by imposing Eq. (5.9), while the observed dark matter abundance is matched via Eq. (5.8). We present constraints from CMB in blue, NA64 in green, down-scattering in magenta and non-perturbativity of the dark coupling $g_D$ in gray. The dark gray band instead represents the region of the parameter space where it is not possible to explain the 511 keV signal in the GC, while matching the observed DM relic abundance. We also have contour lines of constant $\epsilon$ in blue, dark coupling $g_D$ in gray, down-scattering cross section $\sigma_{\chi_2 e^\pm \to \chi_1 e^\pm}$ in orange and $\chi_2$'s fractional abundance $f_2$ in darker magenta. These results are obtained assuming a positron injection rate within a sphere of radius $r \lesssim 4$ kpc around the GC of $\simeq 2.5 \cdot 10^{42}$ s$^{-1}$.

- constraints from down-scattering cross-sections[194];
- non-perturbativity requirements on the dark coupling $g_D$;
- compatibility with the 511 keV line in the GC and correct reproduction of the observed DM relic abundance.

From each drawn DM parameter space we can extract the values of the scattering cross-section $\sigma_{\chi_2 e^\pm \to \chi_1 e^\pm} = 4\alpha_e g_D^2 \epsilon^2 \frac{\mu_{\rm eDM}^2}{m_V^4}$, that are consistent with all experimental bounds. These values are then combined into a single exclusion plot showing the upper limits on $\sigma_e \equiv \sigma_{\chi_2 e^\pm \to \chi_1 e^\pm}$ as a function of the DM mass $M_{\rm DM}$. The same can be done for the DM scattering cross section off protons, which in the limit that $\delta \to 0$, can be written as

$$\sigma_{\chi_2 p \to \chi_1 p} = 4\alpha_e g_D^2 \epsilon^2 \frac{\mu_{\rm pDM}^2}{m_V^4}, \tag{5.58}$$

where $\mu_{\rm pDM} = \frac{m_p M_{\rm DM}}{m_p + M_{\rm DM}}$ is the DM-proton reduced mass. The results are shown in Fig. 5.10. The parameter space in Fig. 5.10 constitutes a benchmark testable only with direct detection insensitive to our small mass splittings, like cosmic rays up-scattering[206, 207] and DM produced in the atmosphere[208]. We note that $\sigma_p \equiv \sigma_{\chi_2 p \to \chi_1 p}$ reaches larger values in the DM paramater space, compared to $\sigma_e$. This is expected since in the limit that $\delta \to 0$

$$\sigma_p = \sigma_e \left( \frac{\mu_{\rm pDM}}{\mu_{\rm eDM}} \right)^2, \tag{5.59}$$

where, for 1 MeV $\lesssim M_{\rm DM} \lesssim$ 20 MeV, we can write that

$$\mu_{\rm pDM} \simeq M_{\rm DM} \gg \mu_{\rm eDM} \simeq m_e. \tag{5.60}$$

Moreover, in the top panels of Fig. 5.10 the pink band excludes $M_{\rm DM} < 1.875$ MeV. This lower bound arises from kinematic considerations in the coannihilation model. Indeed, positrons are produced via the processes $\chi_2\chi_1 \to e^- e^+$ and $\chi_2\chi_1 \to \varphi\varphi$, followed by $\varphi \to e^- e^+$. For this latter decay to be allowed, we require $m_\varphi > 2m_e$, but choosing $m_\varphi \gtrsim 3m_e$ ensures a prompt decay, which translates into a minimum DM mass $M_{\rm DM} \gtrsim 1.875$ MeV.
In the bottom panels of Fig. 5.10, instead, the pink band excludes $M_{\rm DM} < 1.875$ MeV and $M_{\rm DM} \gtrsim 12.1$ MeV, where the lower bound in $M_{\rm DM}$ has the same origin as for the top panels, while the upper boundary is fixed by Eq. (5.8), using the steepest DM density profile which we have considered in realizing those plots, which is the Gondolo-Silk configuration based on a generalized NFW density profile with an inner slope $\gamma = 1.2$.
In principle, choosing a steeper DM density profile, it is possible to push $M_{\rm DM}$ to values bigger than $\simeq 12.1$ MeV, however, this may result in stronger annihilation signals, which are thus more constrained.

In conclusion, we have shown that the coannihilation model discussed in Sec. 5.1 represents a viable dark matter scenario capable of explaining the 511 keV line from the Galactic Center, while simultaneously reproducing the observed dark matter relic abundance and remaining consistent with current observational and experimental constraints. We also discussed how down-scattering processes of the heavier dark matter component $\chi_2$ into the lighter one

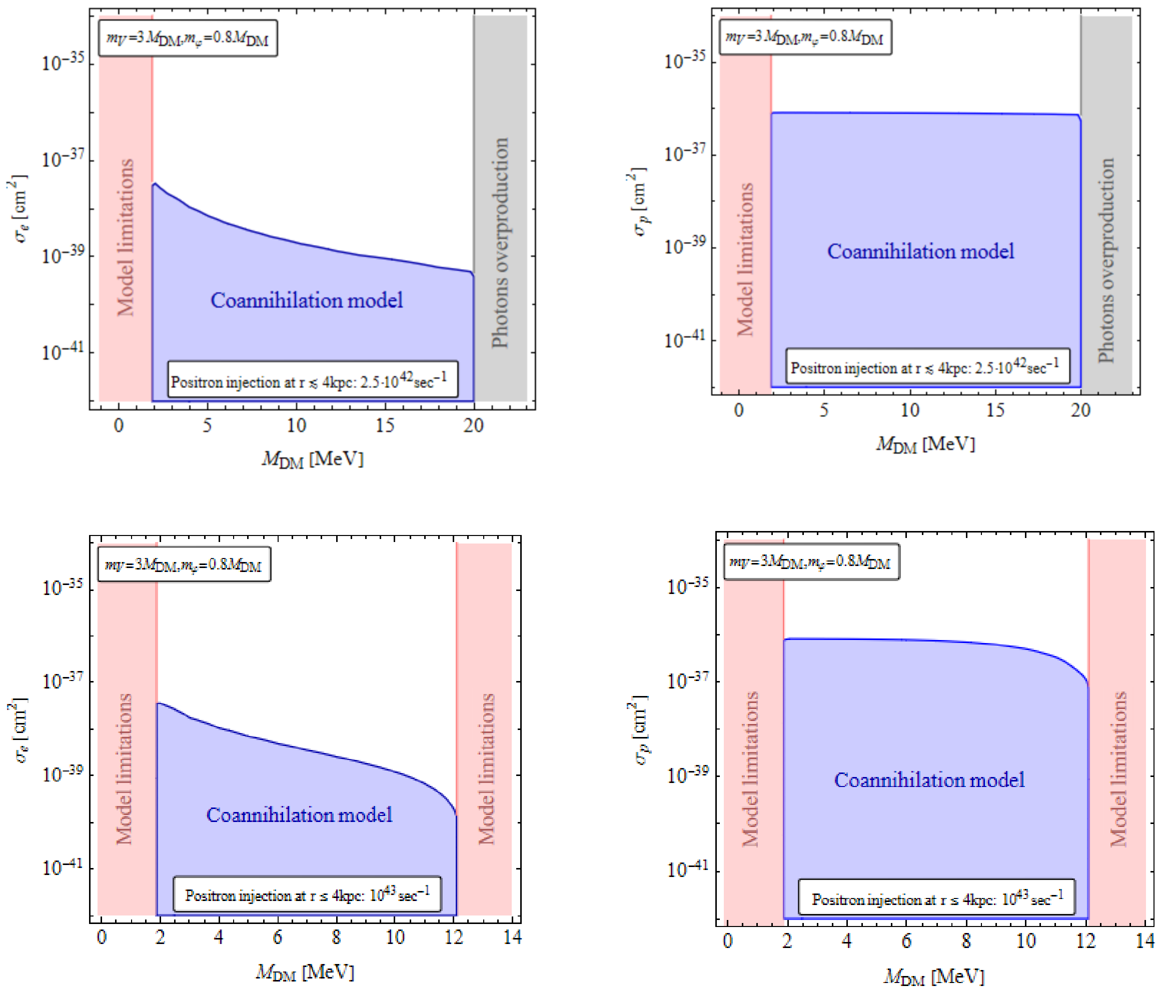


Figure 5.10: $M_{\rm DM} - \sigma_e$ and $M_{\rm DM} - \sigma_p$ parameter spaces for the benchmark choices $m_V = 3M_{\rm DM}$ and $m_\varphi = 0.8M_{\rm DM}$. The blue region delimits the area where the coannihilation model discussed in Sec. 5.1.1 successfully reproduces both the observed dark matter relic abundance and the 511 keV gamma-ray line from the GC. The upper boundary of this blue region is obtained by extracting $\sigma_e$ and $\sigma_p$ values from the constrained $M_{\rm DM} - \delta$ parameter spaces plotted in Fig. 5.9 for each different benchmark of DM density profile. The presented coannihilation model succesfully explains the 511 keV line while matching the observed DM abundance for values of cross sections down to $\sigma_e, \sigma_p \simeq 10^{-48}$ cm$^2$. The gray band excludes $M_{\rm DM} \gtrsim 20$ MeV, since these masses lead to an overproduction of high-energy positrons. As shown in Ref. [11], this results in a broader spatial distribution of the diffuse gamma-ray emission than what is observed by experiments such as COMPTEL, leading to tension with observational data. Additionally, the pink band shows model-dependent limits. These results are obtained assuming a positron injection rate within a sphere of radius $r \lesssim 4$ kpc around the GC of $\simeq 2.5 \cdot 10^{42}$ s$^{-1}$ in the top panels and $\simeq 10^{43}$ s$^{-1}$ in the panels below.

$\chi_1$, can serve as a potential strategy to test this class of models.
In the near future, the increased sensitivity of low-threshold direct detection experiments, such as XENON1T and CRESST, will provide further opportunities to probe the parameter space of the coannihilation model examined in this work.

# 6

# Conclusions

The 511 keV gamma-ray line from the Galactic Center has posed one of the most persistent puzzles in astrophysics for decades[6]. This line arises from the annihilation of electrons and positrons into photons via para-positronium formation, where the positrons are produced by an as-yet unidentified source. The intensity and morphology of this emission continue to elude conventional astrophysical explanations, motivating the exploration of exotic mechanisms, including those involving dark matter.

In Chapter 2 we went through the astrophysical evidence for dark matter, followed by a review of its properties and an in-depth study of the theoretical foundation required to compute relic abundances via the Boltzmann equation.
Moreover, we discussed the experimental constraints on dark matter, including those from collider searches, direct and indirect detection experiments, as well as cosmological and astrophysical observations.

In Chapter 3 we focused on analyzing the 511 keV line signal and its spatial morphology. We showed that while positrons from decays of radioactive isotopes like $^{26}$Al can account for part of the emission in the Galactic disk, they fail to explain consistently the intense signal observed in the Galactic bulge[3, 162]. This opens the door to dark matter explanations of the 511 keV line[11, 171]. The morphology of the signal favours DM annihilations over DM decays, and that limits on the injection energy of the positrons give an upper limit on the dark matter mass that could possibly explain the 511 keV line. Furthermore, using both standard and generalized NFW profiles with dark matter spikes around the supermassive black hole at the Galactic Center, we determined the positron injection rate required to explain the 511 keV signal, and consequently derived the best-fit values of the thermally-averaged DM annihilation cross section[11].

In Chapter 4, we investigated a $p$-wave annihilation dark matter model as a potential explanation for the 511 keV gamma-ray line from the Galactic Center. The model features a velocity-suppressed annihilation cross section, consistently explaining the 511 keV line, while matching the observed DM relic abundance.
We showed that for suitable choices of model parameters, such as the dark matter mass, mediator mass, and couplings, the model can simultaneously fit the 511 keV signal and satisfy

current cosmological, astrophysical, and experimental constraints. These include bounds from supernova cooling, dark matter self-interactions, direct detection experiments like SENSEI and DAMIC-M, and collider searches such as NA64. One of the main new results presented here is an in-depth analysis of resonant enhancements in the dark matter annihilation cross section. Based on this scenario, we organized the discussion into distinct regimes (resonant and non-resonant regimes) according to the proximity to the resonance condition.
Overall, the $p$-wave model represents a testable scenario, and upcoming low-threshold direct detection measurements may offer critical tests of its validity.

In Chapters 5, we explored a coannihilation dark matter model capable of simultaneously accounting for the observed dark matter relic abundance and the 511 keV gamma-ray line from the Galactic Center. This model involves two nearly degenerate dark sector states, where the heavier component is depleted at late times by down-scattering processes, naturally suppressing positron production today and satisfying stringent cosmological bounds.
We outlined the cosmological history of the heavier dark matter component $\chi_2$ over the age of the Galaxy, computing its fractional abundance relative to the total dark matter density. In scenarios where $\chi_2$ is not fully depleted by the present day, down-scattering processes, such as $\chi_2\mathrm{N} \to \chi_1\mathrm{N}$ and $\chi_2 e^{\pm} \to \chi_1 e^{\pm}$, can give rise to detectable signals in direct detection experiments, offering promising experimental prospects. In contrast, up-scattering processes were found to be kinematically forbidden across the parameter space considered, due to insufficient kinetic energy to overcome the mass splitting $\delta$.
The analysis showed that the coannihilation model that we have considered is consistent with current experimental, cosmological and astrophysical limits, including those from the Cosmic Microwave Background (CMB), SN 1987A, and direct detection experiments such as XENON1T and CRESST. Overall, the coannihilation model remains a viable and testable explanation for the 511 keV line, with future low-threshold direct detection experiments expected to play a key role in probing its parameter space.

In both Chapters 4 and 5, we extended the previous work presented in Ref. [171] by incorporating updated constraints and applying new best-fit values of the dark matter annihilation cross section, derived in Chapter 3. Most of the results presented in Chapters 4 and 5 are original and I derived them for this thesis work.

A key feature of both scenarios analyzed in Chapters 4 and 5 is that they predict rates of dark matter annihilations that depend on time. In this way, both models can explain the dark matter relic abundance via thermal freeze-out and, at the same time, the 511 keV line, which requires smaller cross sections than the freeze-out one. In addition, in both scenarios the dark matter annihilation rates are suppressed at late cosmological times, which guarantees that the energy injected into the intergalactic medium remains below the thresholds probed by the CMB observations[27], thus satisfying current cosmological bounds.

While the two models present some similiraties, they also significantly differ in both their theoretical structure and in the experimental signatures they offer. The $p$-wave annihilation model, discussed in Chapter 4, features elastic scattering between dark matter and Standard Model particles, allowing it to be probed via standard direct detection experiments, especially as detector thresholds improve. In addition, we showed that observations of the Bullet Cluster can constrain the dark matter self-interacting cross sections, playing a significant role in the phenomenological analysis of the $p$-wave model under consideration.

In contrast, the coannihilation model, discussed in Chapter 5, predicts inelastic interactions between the two nearly-degenerate dark matter components. As a result, these processes offer signals generally not testable by standard direct detection experiments, which are instead designed to probe elastic scattering interactions. However, this model gives rise to down-scattering processes, where the heavier dark matter state $\chi_2$ scatters off electrons or nuclei in a detector, transitioning to the lighter state $\chi_1$ and depositing a measurable amount of energy. These processes fall within the sensitivity range of current and upcoming low-threshold direct detection experiments, thus representing a promising way to test the coannihilation model under consideration.

Furthermore, for sufficiently small mass splitting between the two dark matter components, in overdense regions of the Universe, such as the Milky Way, a virialization process can occur. During this phenomenon, the up-scattering process $\chi_1\chi_1 \to \chi_2\chi_2$ can reenter thermal equilibrium over the age of the Galaxy, effectively repopulating the $\chi_2$ component. This regeneration mechanism allows to enhance down-scattering signals in direct detection experiments. This phenomenon, however, does not affect the $p$-wave annihilation model, where such late-time population dynamics are absent.

In summary, while both models are viable explanations for the 511 keV line, they present some differences both in the theoretical predictions and the experimental signature they offer. As a result, the combined data from direct detection, astrophysical observations, and cosmological measurements will be essential to discriminate between them in the near future.

Some aspects that can be further investigated in the near future include:

- *Improved modeling of galactic dark matter spikes*: the positron injection rate in both $p$-wave and coannihilation scenarios is highly sensitive to the assumed dark matter density profile near the Galactic Center, particularly the structure of the spike induced by the supermassive black hole (See Figs. 4.5 and 5.10). A more refined treatment of dynamical processes, such as baryonic feedback, stellar scattering, and gravitational heating, would allow for more accurate predictions and better understanding of model viability.
- *Future experiments and observations*: the next generation of gamma-ray telescopes, such as e-ASTROGAM[130] and AMEGO[131] could offer new data on the morphology of the 511 keV line and potentially reveal other spectral features indicative of dark matter annihilation in the MeV range. Furthermore, upcoming low-threshold direct detection experiments[97, 189, 209] and CMB spectral distortion measurements[137] may offer complementary tests on the parameter space of light dark matter models.
- *Incorporation of more precise astrophysical modeling*: a key limitation in interpreting the 511 keV signal is the uncertainty in positron propagation. Future work incorporating realistic transport models of positrons in the interstellar medium, potentially using GALPROP or PIC simulations, would reduce modeling uncertainties[6, 210].

- *New models exploration*: new scenarios may be investigated in the future, such as slightly-asymmetric dark matter, whose annihilation is naturally suppressed at late times due to the particle-antiparticle asymmetry. Exploring its potential connection to the 511 keV gamma-ray line from the Galactic Center could offer new insights into both the signal's origin and the dark matter nature.

Although further work is needed to refine the models analyzed in Chapters 4 and 5, our results lend support to the hypothesis that the persistent 511 keV gamma-ray signal observed from the Galactic Center could be linked to dark matter annihilation into $e^-e^+$ pairs, potentially offering valuable insight into the fundamental properties of dark matter particles. To conclude, a key point of this thesis, is that for both the $p$-wave annihilation model discussed in Chapter 4 and the coannihilation model discussed in Chapter 5, we identified new experimental and observational tests of the dark matter explanation of the 511 keV gamma-ray line from the Galactic Center.

# Acknowledgements

I would like to sincerely thank my supervisor, Dr. Filippo Sala, for proposing this project to me and for his constant guidance, encouragement, and insightful discussions throughout the development of this work. His expertise and support have been fundamental at every stage of the research.
I would also like to thank Prof. Silvia Pascoli for her kind support and valuable advice to help me prepare for the PhD interviews.
Finally, I am also grateful for the stimulating environment provided by the theoretical physics group at the University of Bologna, which contributed to the progress of this thesis.

# Appendix A

# Early universe cosmology

In this appendix we provide a brief introduction to early universe cosmology, with a particular focus on the thermal history of the universe.
In its earliest moments the universe was hot and dense and particles were in thermal equilibrium, constantly interacting and exchanging energy within the thermal plasma. As the universe expanded and cooled, these interactions gradually became less efficient, eventually leading to the decoupling of various particle species. This transition is essential in order to understand the relic abundance of particles such as dark matter. Moreover, departures from equilibrium were essential for shaping the universe as we know it today, playing a central role in the formation of the cosmic microwave background and the synthesis of the first light elements during Big Bang nucleosynthesis.

## A.1 The Friedmann equations

The cosmological principle stands as a foundational assumption in modern cosmology, asserting that the universe is homogeneous and isotropic on sufficiently large scales. This principle is not derived from first principles, but rather is a simplifying hypothesis grounded in observational evidence.
The universe can be classified into three different categories:

- flat if it has zero curvature, meaning that $k = 0$;
- closed if it has positive curvature, meaning that $k = 1$;
- open if it has negative curvature, meaning that $k = -1$.

The cosmological metric used to describe the universe is the FLRW metric:

$$ds^2 = dt^2 - a(t)^2 \left[ \frac{dr^2}{1 - kr^2} + r^2 (d\theta^2 + \sin^2\theta d\phi^2) \right], \tag{A.1}$$

where $a(t)$ is the scale factor, which measures how much the universe has expanded or contracted since a given reference time.
By solving the Einstein equations, $G_{\mu\nu} + \Lambda g_{\mu\nu} = 8\pi G T_{\mu\nu}$, by using the FLRW metric in Eq.

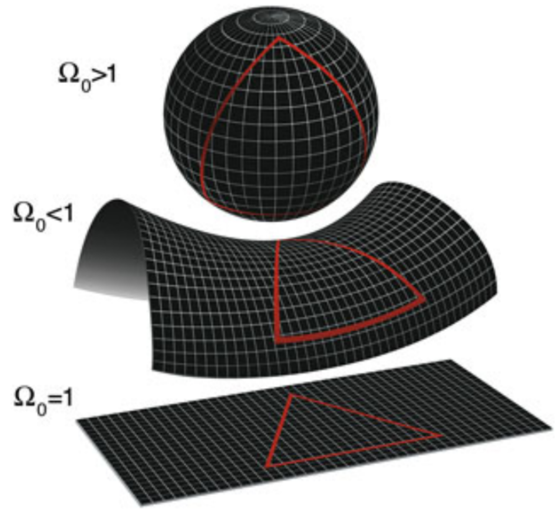


Figure A.1: From top to bottom we have a closed universe, corresponding to a density parameter $\Omega > 1$, a hyperbolic universe, corresponding to $\Omega < 1$ and a flat universe, corresponding to $\Omega = 1$. The density parameter of the universe is defined as $\Omega = \frac{\rho}{\rho_c}$, where $\rho$ is the actual energy density of the universe, including contributions from all components, like matter, radiation and vacuum energy, while $\rho_c$ is the critical density.
***Reprinted from WMAP Science Team work, 2024, NASA. Retrivied from*** **`https://wmap.gsfc.nasa.gov/universe/uni_shape.html`.**

(A.1), we obtain the two Friedmann equations:

$$\begin{cases} \left(\frac{\dot{a}}{a}\right)^2 + \frac{k}{a^2} = \frac{8\pi G}{3}\rho \\ \frac{\ddot{a}}{a} = -\frac{4\pi G}{3}(\rho + 3p) \end{cases} \tag{A.2}$$

Let us now consider a flat universe, which implies that $k = 0$; in this case the first Friedmann equation reduces to $\left(\frac{\dot{a}}{a}\right)^2 = \frac{8\pi G}{3}\rho$. We can now divide the analysis into three different cases:

- for a flat and matter-dominated universe we have that

$$\rho_{\text{dust}} = \frac{\rho_{m,0}}{a^3} \implies \frac{\dot{a}^2}{a^2} = \frac{8\pi G}{3a^3}\rho_{m,0} \implies \sqrt{a}da = \sqrt{\frac{8\pi G\rho_{m,0}}{3}}dt \implies a(t) \propto t^{2/3}, \tag{A.3}$$

  where $H_0 = \frac{\dot{a}}{a}\Big|_{t=t_0}$ is the Hubble constant today, $\rho_{\text{dust}}$ is the energy density of dust, which is pressurless matter and $\rho_{m,0}$ is the matter energy density today.

- For a flat and radiation-dominated universe we have that

$$\rho_{\text{rad}} = \frac{\rho_{r,0}}{a^4} \implies \frac{\dot{a}^2}{a^2} = \frac{8\pi G}{3a^4}\rho_{r,0} \implies ada = \sqrt{\frac{8\pi G\rho_{r,0}}{3}}dt \implies a(t) \propto t^{1/2}, \tag{A.4}$$

  where $\rho_{r,0}$ is the the radiation energy density today.

- For a flat and empty universe, dominated by a positive vacuum energy, we have that

$$\rho_\Lambda = \frac{\Lambda}{8\pi G} \implies \frac{\dot{a}^2}{a^2} = \frac{\Lambda}{3} \implies \frac{da}{a} = \sqrt{\frac{\Lambda}{3}}dt \implies a(t) = e^{\sqrt{\frac{\Lambda}{3}}t}, \tag{A.5}$$

  where $\Lambda$ is the cosmological constant. In particular, we can notice that $\rho_\Lambda$ remains constant as the universe expands.

## A.2 Equilibrium thermodynamics

A system of particles is said to be in kinetic equilibrium if the particles exchange energy and momentum efficiently. In this state of maximum entropy, the distribution functions, depending on the particle's quantum statistics, take the form of the Fermi-Dirac or Bose-Einstein distributions:

$$f(p) = \frac{1}{e^{\frac{E-\mu}{T}} \pm 1}, \tag{A.6}$$

where $E = \sqrt{p^2 + m^2}$ and $\mu$ is the chemical potential[211].
The $+$ sign in Eq. (A.6) refers to fermions, while the $-$ sign refers to bosons. In the non-relativistic limit, where $T \ll m$, both the Fermi-Dirac and the Bose-Einstein distributions in Eq. (A.6) reduce to the Maxwell-Boltzmann distribution. Indeed

$$\frac{1}{e^{\frac{E-\mu}{T}} \pm 1} \simeq e^{-\frac{E-\mu}{T}}. \tag{A.7}$$

We can define the number density, the energy density and the pressure of a particle species respectively as

$$n = \frac{g}{(2\pi)^3} \int d^3p f(p), \tag{A.8}$$

$$\rho = \frac{g}{(2\pi)^3} \int d^3p f(p) E(p), \tag{A.9}$$

$$P = \frac{g}{(2\pi)^3} \int d^3p f(p) \frac{|\vec{p}|^2}{3E}, \tag{A.10}$$

where $g$ is the number of internal degrees of freedom for the particle of interest. In particular:

- for a massless vector boson $g = 2$, which are the two transversal polarizations;
- for a massive vector boson $g = 3$, which are the two transversal polarizations in addition to the longitudinal one;
- for a Dirac fermion $g = 4$;
- for a Majorana fermion $g = 2$;
- for a real scalar $g = 1$;
- for a complex scalar $g = 2$.

We can solve the integrals in Eqs. A.8, A.9 and A.10 both in the relativistic limit, where $T \gg m$ and in the non-relativistic one, where $T \ll m$, and what we find is that

- for $T \gg m$ the number density is given by

$$\begin{cases} n_B = \frac{\xi(3)}{\pi^2} g T^3 & \text{for bosons} \\ n_F = \frac{3}{4} n_B & \text{for fermions} \end{cases}, \tag{A.11}$$

  where $\xi(3)$ is the Riemann zeta function, evaluated as $\xi(n)\big|_{n=3}$.
  The energy density, instead, is given by

$$\begin{cases} \rho_B = \frac{\pi^2}{30} g T^4 & \text{for bosons} \\ \rho_F = \frac{7}{8} \rho_B & \text{for fermions} \end{cases}. \tag{A.12}$$

  Eventually, the pressure is given by $P = \frac{\rho}{3}$.

- For $T \ll m$ we have said that both the Fermi-Dirac and the Bose-Einstein distribution in Eq. (A.6) reduce to the Maxwell-Boltzmann distribution in Eq. (A.7), so the number density, energy density and pressure coincide for bosons and fermions. In particular:

$$n = g\left(\frac{mT}{2\pi}\right)^{3/2} e^{-\frac{m-\mu}{T}}, \tag{A.13}$$

$$\rho = mn, \tag{A.14}$$

$$P = mT \ll mn = \rho. \tag{A.15}$$

### A.2.1 Thermal equilibrium

In the early universe temperatures were extremely high and particles interacted frequently, maintaining thermal equilibrium. The evolution of the universe's thermal state is governed by a competition between two key quantities:

- the interaction rate $\Gamma$, which quantifies how often particles interact with each other and it scales like $\Gamma = n\langle \sigma v\rangle$, where n is the number density of the particle species of interest, while $\langle \sigma v\rangle$ is the thermally averaged cross section;

- the Hubble parameter $H$, which describes the expansion rate of the universe. During the radiation-dominated era it is defined as $H = \sqrt{\frac{8\pi G \rho_r}{3}}$, where $G$ is the Newtonian gravitational constant, while $\rho_r$ is the radiation energy density, as written in Eq. (A.12). Therefore, we can write that in the radiation-dominated era

$$H = \sqrt{\frac{8\pi G}{3}\frac{\pi^2 g_\rho}{30}} T^2 \simeq 1.67 g_\rho^{1/2} \frac{T^2}{M_{\rm pl}}, \tag{A.16}$$

  where $g_\rho$ counts the relativistic energy degrees of freedom and it is defined like

$$g_\rho(T) = \sum_B g_B \left(\frac{T_B}{T_\gamma}\right)^4 + \frac{7}{8}\sum_F g_F \left(\frac{T_F}{T_\gamma}\right)^4. \tag{A.17}$$

Here $g_B$ and $g_F$ quantify respectively the bosonic and fermionic internal degrees of freedom.

A particle species remains in thermal equilibrium as long as its interaction rate satisfies that $\Gamma \gg H$, which implies that the corresponding interaction timescale, $t_c \equiv \frac{1}{\Gamma}$, is much smaller than the Hubble time, $t_H \equiv \frac{1}{H}$. When $\Gamma \sim H$, instead, the interaction rate becomes comparable to the expansion rate and the particle species effectively starts decoupling from the the thermal bath.

### A.2.2 Conservation of entropy

To describe the evolution of the universe, it is helpful to track a conserved quantity. In cosmology, entropy provides more valuable insights than energy and, according to the second law of thermodynamics, the total entropy of the universe either increases or remains constant. Moreover, it can be demonstrated that entropy is conserved when the system is in equilibrium.
Now consider the second law of thermodynamics for a system in equilibrium, meaning that $\mu = 0$:

$$TdS = dU + PdV = \rho dV + V d\rho + PdV \implies V d\rho + \rho dV = TdS - PdV, \tag{A.18}$$

where we have used that $U = \rho V$. Moreover, we can write that $S = sV$, where $s$ is the entropy density, therefore

$$\begin{aligned} &V d\rho + \rho dV = T(V ds + sdV) - PdV \implies dV(Ts - P - \rho) - V d\rho + TV ds = 0 \\ &\implies \frac{dV}{V}\underbrace{(Ts - P - \rho)}_{A} + \underbrace{(Tds - d\rho)}_{B} = 0. \end{aligned} \tag{A.19}$$

We recall that the volume $V$ is an extensive quantity, while the entropy density $s$ and the energy density $\rho$ are intensive quantities. What is the difference?

- An extensive quantity depends on the size and amount of a substance and, therefore, it is additive;
- an intensive quantity does not depend on the size of the substance that we are considering.

This implies that terms $A$ and $B$ are not related with each other and they vanish independently, which means that

$$s = \frac{\rho + P}{T}. \tag{A.20}$$

By using Eqs. A.12, A.13, A.14 and A.15, we recall that the energy density and pressure of dust go respectively as $\rho_m = mn \propto (mT)^{3/2} e^{-\frac{m}{T}}$ and $P_m = nT \ll \rho_m$, while the energy density and pressure of a relativistic particle species go as $\rho_r \propto T^4$ and $P_r = \frac{\rho_r}{3}$.

We can thus rewrite Eq. (A.20) as $s = \frac{(\rho_m+\rho_r)+(P_m+P_r)}{T}$, which is dominated by radiation and, therefore, $s \simeq \frac{\rho_r+P_r}{T} = \frac{4}{3}\frac{\rho_r}{T}$.
We can express everything in terms of the photon temperature $T_\gamma$ and, recalling the expression for $\rho_B$ in Eq. (A.12), we find that

$$s = \frac{4}{3}\frac{\pi^2}{30} g_s T_\gamma^3 = \frac{2\pi^2}{45} g_s T_\gamma^3, \tag{A.21}$$

where $g_s$ takes into account the relativistic entropy degrees of freedom and it is defined as

$$g_s(T) = \sum_B g_B \left(\frac{T_B}{T_\gamma}\right)^3 + \frac{7}{8}\sum_F g_F \left(\frac{T_F}{T_\gamma}\right)^3, \tag{A.22}$$

This implies that from entropy conservation $sa^3 \propto g_s T_\gamma^3 a^3 = \text{const} \implies T_\gamma \propto g_s^{-1/3} a^{-1}$. Therefore, the entropy stored in the relativistic degrees of freedom is transferred to the rest of the plasma, increasing the temperature $T_\gamma$. Indeed, as the universe expands the energies of the particles are redshifted, so some relativistic particles become non-relativistic and thus $g_s$ decreases.
We show in Fig. A.2 the behaviour of $g_s(T)$ with temperature.

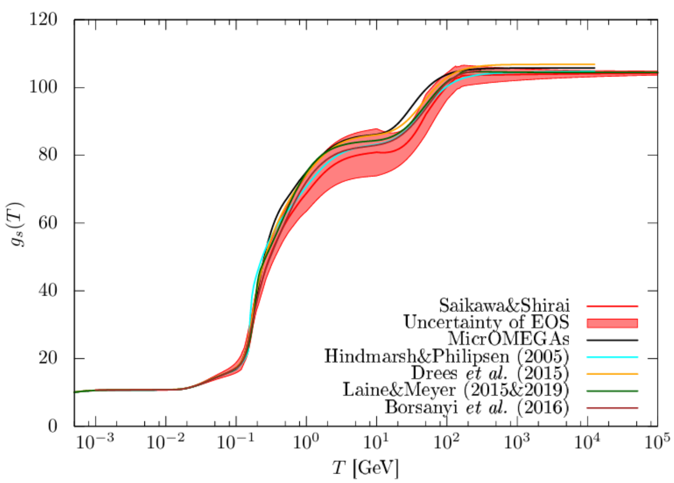


Figure A.2: Evolution of $g_s(T)$ with temperature in the Standard Model.
***Reprinted from "Precise WIMP Dark Matter Abundance and Standard Model Thermodynamics", by Ken'ichi Saikawa and Satoshi Shirai***[54]

.

We notice from Eqs. A.17 and A.22 that if a particle species is in thermal equilibrium, then $T_B = T_F = T_\gamma \implies \left(\frac{T_B}{T_\gamma}\right)^3 = \left(\frac{T_B}{T_\gamma}\right)^4, \left(\frac{T_F}{T_\gamma}\right)^3 = \left(\frac{T_F}{T_\gamma}\right)^4$.
The situation changes instead for neutrinos, because they decoupled when relativistic, so they are still counted in the relativistic degrees of freedom in Eqs. A.17 and A.22, but with a temperature $T_F \neq T_\gamma$, since they are not anymore in thermal equilibrium after decoupling occurs.
At $T \lesssim 0.5$ MeV electrons and positrons are no longer relativistic, so we remain with only photons and neutrinos as relativistic species. Therefore, we can write that

- $g_\rho(T \lesssim 0.5 \text{ MeV}) = 2 + \frac{7}{8} \cdot 3 \cdot 2\left(\frac{T_\nu}{T_\gamma}\right)^4$.

- $g_s(T \lesssim 0.5 \text{ MeV}) = \underbrace{2}_{\text{photons}} + \underbrace{\frac{7}{8} \cdot 3 \cdot 2\left(\frac{T_\nu}{T_\gamma}\right)^3}_{\text{neutrinos}}$.

As we have already said, shortly after neutrino decoupling, temperature drops to around 0.5 MeV, when $e^-$ and $e^+$ annihilate. Their energy and entropy densities are transferred to the photon bath but not to the decoupled neutrinos. Therefore, the photons are heated relative to neutrinos. To quantify this effect, we calculate the change in the effective number of degrees of freedom associated to entropy.
Since entropy is conserved before and after $e^-e^+$ annihilation, then

$$(g_s a^3 T_\gamma^3)_{\rm before} = (g_s a^3 T_\gamma^3)_{\rm after}. \tag{A.23}$$

We can thus write that

$$(aT_\gamma)_{\rm before} = (aT_\gamma)_{\rm after}\left(\frac{g_{s,\rm after}}{g_{s,\rm before}}\right)^{1/3}. \tag{A.24}$$

Before $e^-e^+$ annihilation, in the thermal bath we have electrons, positrons and photons, so $g_{s,\rm before} = 2 + \frac{7}{8}\cdot 4 = \frac{11}{2}$. After $e^-e^+$ annihilation, instead, in the thermal bath we have only photons, so $g_{s,\rm after} = 2$.
We can thus rewrite Eq. (A.25) as

$$(aT_\gamma)_{\rm before} = (aT_\gamma)_{\rm after}\left(\frac{4}{11}\right)^{1/3}. \tag{A.25}$$

Eq. (A.24) shows us that $aT_\gamma$ increases after $e^-e^+$ annihilation, while $aT_\nu$ remains the same[26], since neutrinos have already decoupled. This implies that the photon bath is heated with respect to neutrinos, meaning that

$$T_\nu = \left(\frac{4}{11}\right)^{1/3} T_\gamma. \tag{A.26}$$

This is also shown diagramatically in Fig. A.3.
We can now compute

- $g_\rho(T \lesssim 0.5 \text{ MeV}) = 2 + \frac{7}{8}\cdot 3\cdot 2\cdot \left(\frac{4}{11}\right)^{4/3} = 3.36.$
- $g_s(T \lesssim 0.5 \text{ MeV}) = 2 + \frac{7}{8}\cdot 3\cdot 2\cdot \frac{4}{11} = 3.91.$

Eventually, by using the results of Refs. [54, 92], we can define

$$g_*^{1/2}(T) = \frac{g_s(T)}{g_\rho^{1/2}(T)}\left(1 + \frac{1}{3}\frac{d\,\ln(g_s(T))}{d\,\ln(T)}\right). \tag{A.27}$$

We show in Fig. A.4 the behaviour of $g_*^{1/2}(T)$ with temperature.

[26] Actually, in the instantaneous freeze-out approximation, after neutrino decoupling, occuring at a temperature $T \simeq 1$ MeV, neutrino temperature $T_\nu$ starts diverging from the temperature of the photon bath, as we can also see from Fig. A.3. However, neutrinos do not really freeze-out instantaneously at $T \simeq 1$ MeV; therefore the photon bath is effectively heaten with respect to neutrinos after $e^-e^+$ annihilation.

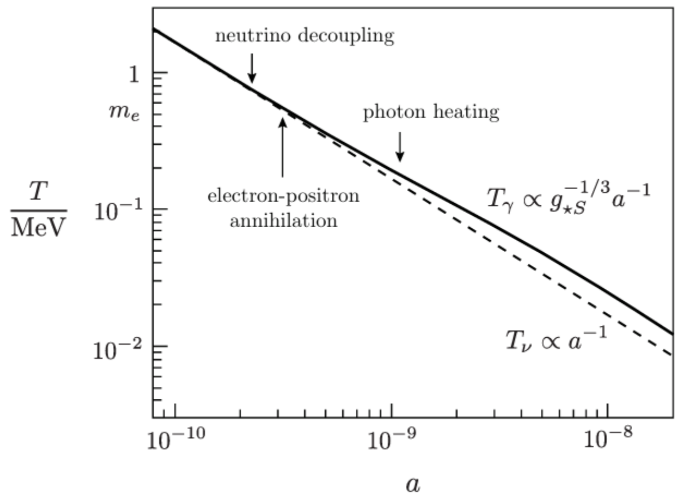


Figure A.3: Heating of the photon bath with respect to netrinos after $e^-e^+$ annihilation.
***Reprinted from "Cosmology", by Daniel Baumann, Insititute of Theoretical Physics, University of Amsterdam***[211]

.

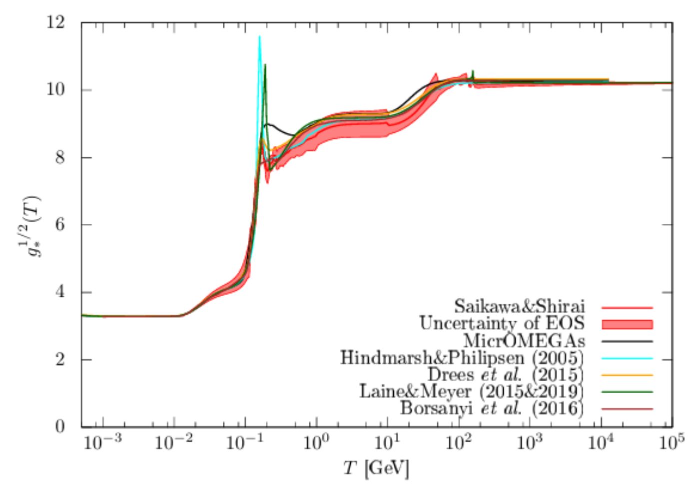


Figure A.4: Evolution of $g_*^{1/2}(T)$ with temperature in the Standard Model.
***Reprinted from "Precise WIMP Dark Matter Abundance and Standard Model Thermodynamics", by Ken'ichi Saikawa and Satoshi Shirai***[54]

.

## A.3 The Boltzmann equation

As already seen in App. A.2.1, a particle species is coupled to the SM plasma if $\Gamma \gtrsim H$, while it is decoupled from it when $\Gamma \lesssim H$, where we recall that $\Gamma = n\langle\sigma v\rangle$ is the interaction rate of the particle we are considering and $H$ is the Hubble parameter. Although this reasoning is usually very accurate in determining the freeze-out temperature of the particle, a more precise way to proceed is to track microscopically the particle's phase space distribution function $f(p^\mu, x^\mu)$, through the Boltzmann equation[212]

$$\hat{\mathbf{L}}[f] = \hat{\mathbf{C}}[f], \tag{A.28}$$

where $\hat{\mathbf{C}}$ is the collision operator and $\hat{\mathbf{L}}$ is the Liouville operator, defined as

$$\hat{\mathbf{L}} = p^\alpha \frac{\partial}{\partial x^\alpha} - \Gamma^\alpha_{\beta\gamma} p^\beta p^\gamma \frac{\partial}{\partial p^\alpha}. \tag{A.29}$$

We notice that the gravitational effects are taken into account inside the affine connection $\Gamma^\alpha_{\beta\gamma}$, in particular in the FLRW spacetime the phase space density is spatially homogeneous and isotropic, meaning that $f = f(|\vec{p}|, t) \equiv f(E, t)$.
Therefore, we can compute the Liouville operator in Eq. (A.29) for the FLRW metric in Eq. (A.1), finding that

$$\hat{\mathbf{L}}[f(E,t)] = E\frac{\partial f}{\partial t} - \frac{\dot{a}}{a}|\vec{p}|^2 \frac{\partial f}{\partial E}, \tag{A.30}$$

where $\frac{\dot{a}}{a}$ takes into account the expansion of the universe.
Using now Eq. (A.8), we can write the time dependent number density as

$$n(t) = \frac{g}{(2\pi)^3} \int d^3p \; f(E,t) \tag{A.31}$$

and, integrating by parts, we can rewrite the Boltzmann equation as

$$\dot{n} + 3\frac{\dot{a}}{a} n = \frac{g}{(2\pi)^3} \int \hat{\mathbf{C}}[f] \frac{d^3p}{E}, \tag{A.32}$$

where the dot operator indicates a total derivate with respect to time and therefore $\dot{n} \equiv \frac{dn}{dt}$.
Let us now consider a generic scattering process $\psi_1 + \psi_2 + \cdots \to \psi_a + \psi_b + \cdots$. The right-hand side of Eq. (A.32) can thus be written as

$$\begin{aligned} \frac{g_\psi}{(2\pi)^3} \int \hat{\mathbf{C}}[f] \frac{d^3p_\psi}{E_\psi} = - \int & d\Pi_1 d\Pi_2 \cdots d\Pi_a d\Pi_b \cdots (2\pi)^4 \delta^{(4)}(p_1 + p_2 + \cdots - p_a - p_b - \cdots) \\ & \times [|M|^2_{\psi_1+\psi_2+\cdots\to\psi_a+\psi_b+\cdots} f_1 f_2 \cdots (1 \pm f_a)(1 \pm f_b) \cdots - \\ & - |M|^2_{\psi_a+\psi_b+\cdots\to\psi_1+\psi_2+\cdots} f_a f_b \cdots (1 \pm f_1)(1 \pm f_2) \cdots ], \end{aligned} \tag{A.33}$$

where $f_i$ is the phase space density of $\psi_i$ and in $(1 \pm f_i)$ we choose the plus sign if we are dealing with bosons, whereas the minus sign applies to fermions. Moreover, $d\Pi_i$ is defined as

$$d\Pi_i \equiv \frac{g_i}{(2\pi)^3} \frac{d^3p_i}{2E_i}, \tag{A.34}$$

where $g_i$ takes into account the internal degrees of freedom of the $i^{\text{th}}$ particle that we are considering.
We can also notice that $\delta^{(4)}(p_1 + p_2 + \cdots - p_a - p_b - \cdots)$ imposes energy and momentum

conservation.
Moreover, assuming T or equivalently CP conservation, we can write that

$$|M|^2_{\psi_1+\psi_2+\cdots\to\psi_a+\psi_b+\cdots} = |M|^2_{\psi_a+\psi_b+\cdots\to\psi_1+\psi_2+\cdots} \equiv |M|^2, \tag{A.35}$$

where $|M|^2$ is averaged over the initial spins and summed over the final ones.
This assumption is almost always valid apart from some specific cases, such as when we deal with baryon asimmetry, where CP-symmetry violation is one of the three Sakharov conditions, which need to be satisfied in order to generate dynamically a matter-antimatter asymmetry in the universe.
In the limit that particles follow a Maxwell-Boltzmann statistics, then we can write that

$$1 \pm f_\alpha = 1 \pm e^{-\frac{E_\alpha - \mu_\alpha}{T}} \approx 1, \tag{A.36}$$

where $E_\alpha \approx m_\alpha \gg T$, since we are in the non-relativistic limit and $m_\alpha$ is the mass of the $\alpha^{\text{th}}$ particle we are considering.
Exploiting those approximations, we can rewrite the Boltzmann equation A.32 as

$$\begin{aligned}\dot{n}_1 + 3Hn_1 = &-\int d\Pi_1 d\Pi_2 \cdots d\Pi_a d\Pi_b \cdots (2\pi)^4 |M|^2 \delta^{(4)}(p_1 + p_2 + \cdots - p_a - p_b - \cdots) \\ &\times [f_1 f_2 \cdots - f_a f_b \cdots],\end{aligned} \tag{A.37}$$

where $H \equiv \frac{\dot{a}}{a}$.
We notice that if we do not have collisions between particles and thus $\hat{\mathbf{C}} = 0$, then $\dot{n}_1 + 3Hn_1 = 0 \implies n_1 \propto a^{-3}$. Indeed

$$\frac{\dot{n}_1}{n_1} = -3H \equiv -3\frac{\dot{a}}{a} \implies \int \frac{dn_1}{n_1} = -3\int \frac{da}{a} \implies \ln(n_1) \propto -3\ln(a) \implies n_1 \propto a^{-3}. \tag{A.38}$$

This shows that, in absence of collisions, the number of particles $N_1 = n_1 a^3 = \text{const}$.
Let us now consider for simplicity a $2 \to 2$ scattering process, for which the Boltzmann equation A.37 can be rewritten as

$$\dot{n}_1 + 3Hn_1 = \int d\Pi_1 d\Pi_2 d\Pi_3 d\Pi_4 (2\pi)^4 |M|^2 \delta^{(4)}(p_1 + p_2 - p_3 - p_4)[f_3 f_4 - f_1 f_2] \tag{A.39}$$

and let us massage a little bit the terms appearing in the equation. Indeed, assuming that all the particles involved are in kinetic equilibrium[27] with each other, we can write that

$$f_3 f_4 - f_1 f_2 = e^{\frac{(\mu_3+\mu_4)-(E_3+E_4)}{T}} - e^{\frac{(\mu_1+\mu_2)-(E_1+E_2)}{T}}. \tag{A.40}$$

Since energy is conserved, as imposed by $\delta^{(4)}(p_1 + p_2 - p_3 - p_4)$, then we can rewrite Eq. (A.40) as

$$f_3 f_4 - f_1 f_2 = e^{-\frac{E_1+E_2}{T}} \left[ e^{\frac{\mu_3+\mu_4}{T}} - e^{\frac{\mu_1+\mu_2}{T}} \right]. \tag{A.41}$$

We can now define the equilibrium number density as

$$n_1^{\text{eq}} = \frac{g_1}{(2\pi)^3} \int d^3 p_1 \; e^{-\frac{E_1}{T}} \implies n_1 = n_1^{\text{eq}} e^{\frac{\mu_1}{T}}, \tag{A.42}$$

[27] Kinetic equilibrium between particles ensure that they mantain the same temperature $T$.

while the thermally-averaged annihilation cross section times velocity is given by

$$\langle\sigma v\rangle_{\psi_1+\psi_2\to\psi_3+\psi_4} = \frac{1}{n_1^{\rm eq} n_2^{\rm eq}} \int d\Pi_1 \cdots d\Pi_4 e^{-\frac{E_1+E_2}{T}} (2\pi)^4 \delta^{(4)}(p_1+p_2-p_3-p_4)|M|^2, \quad \text{(A.43)}$$

where $v \equiv v_{\rm rel}$ is the relative velocity between the two incoming particles $\psi_1$ and $\psi_2$. It is now easy to see that we can rewrite the Maxwell-Boltzmann equation A.39 as

$$\dot{n}_1 + 3Hn_1 = n_1^{\rm eq} n_2^{\rm eq} \langle\sigma v\rangle \left( \frac{n_3 n_4}{n_3^{\rm eq} n_4^{\rm eq}} - \frac{n_1 n_2}{n_1^{\rm eq} n_2^{\rm eq}} \right), \quad \text{(A.44)}$$

where, indeed, $\frac{n_i n_j}{n_i^{\rm eq} n_j^{\rm eq}} = e^{\frac{\mu_i+\mu_j}{T}}$, because of what is written in Eq. (A.42).
We also assume that $\psi_3$ and $\psi_4$ have thermal distributions with zero chemical potential, which is a good assumption, since $\psi_3$ and $\psi_4$ will usually have additional interactions which are stronger than the ones with $\psi_1$ and $\psi_2$. Under the assumption that $\mu_3 = \mu_4 = 0$, then Eq. (A.44) becomes

$$\dot{n}_1 + 3Hn_1 = -\langle\sigma v\rangle \Big( n_1 n_2 - n_1^{\rm eq} n_2^{\rm eq} \Big). \quad \text{(A.45)}$$

An alternative way to rewrite the Boltzmann equation A.45 is to introduce the yield $Y_1 = \frac{n_1}{s}$, where $s$ is the entropy density, in a such a way that

$$s\dot{Y}_1 = s\frac{\dot{n}_1 s - n_1 \dot{s}}{s^2} = \dot{n}_1 - n_1 \frac{\dot{s}}{s}. \quad \text{(A.46)}$$

Using the conservation of entropy, then we have that

$$\frac{d(sa^3)}{dt} = 0 \implies sa^3 = \text{const} \implies s = a^{-3}\text{const} \implies \frac{\dot{s}}{s} = \frac{-3\dot{a}a^{-4}\text{const}}{a^{-3}\text{const}} = -3H. \quad \text{(A.47)}$$

Therefore, we can rewrite the left-hand side of the Boltzmann equation A.45 as $\dot{n}_1 + 3Hn_1 = s\dot{Y}_1$. Furthermore, since the interaction term will usually depend explicitely upon temperature, rather than time, it is useful to introduce the variable $x \equiv \frac{m}{T}$, where $m$ is any convenient mass scale, usually taken as the mass of the particle of interest.
During the radiation-dominated epoch $x$ and $t$ are related by

$$t \simeq 0.3 g_\rho^{-\frac{1}{2}} \frac{M_{\rm pl}}{T^2} \simeq 0.3 g_\rho^{-\frac{1}{2}} \frac{M_{\rm pl}}{m^2} x^2. \quad \text{(A.48)}$$

Indeed, the first Friedmann equation in A.2, for a flat and radiation-dominated universe, can be rewritten as

$$\left(\frac{\dot{a}}{a}\right)^2 = \frac{8\pi G}{3}\rho_r, \quad \text{(A.49)}$$

where $\rho_r$ is the radiation energy density, defined as in Eq. (A.12).
We can thus solve Eq. (A.49) as

$$\left(\frac{\dot{a}}{a}\right)^2 = \frac{8\pi G}{3}\frac{\pi^2}{30} g_\rho(T) T^4 \propto \frac{8\pi G}{3}\frac{\pi^2}{30}\frac{g_\rho(T)}{g_s^{4/3}(T) a^4} \propto a^{-4}, \quad \text{(A.50)}$$

where we have used that, from conservation of entropy, the standard model temperature goes as $T \propto g_s(T)^{-1/3}a^{-1}$. Developing the calculations of Eq. (A.50), we can find that

$$\dot{a}a \propto 1 \implies ada \propto dt \implies a \propto \sqrt{t}. \tag{A.51}$$

Having derived this, we can find a relation between time $t$ and the Hubble constant $H$, indeed we have that

$$H \equiv \frac{\dot{a}}{a} = \frac{1}{2(\sqrt{t})^2} = \frac{1}{2t}. \tag{A.52}$$

On the other hand, using that in natural units the gravitational constant can be written as $G = \frac{1}{M_{\text{pl}}^2}$, we can find from Eq. (A.49) that

$$\frac{1}{2t} = H = \frac{\sqrt{\frac{8\pi}{3}\rho_r}}{M_{\text{pl}}} = \sqrt{\frac{8\pi^3}{90}g_\rho}\frac{T^2}{M_{\text{pl}}} \simeq 1.67 g_\rho^{1/2}\frac{T^2}{M_{\text{pl}}}, \tag{A.53}$$

where we have used the bosonic relativistic energy density expression in Eq. (A.12). We thus recover the relation in Eq. (A.48), using that $x \equiv \frac{m}{T}$.
Considering an annihilation process of the form $\bar{\psi}\psi \to \bar{X}X$, we can rewrite the Boltzmann equation A.45 as

$$s\dot{Y}_\psi = -\langle\sigma v\rangle[\underbrace{n_\psi^2}_{s^2Y_\psi^2} - \underbrace{(n_\psi^{\text{eq}})^2}_{s^2(Y_\psi^{\text{eq}})^2}] \implies \dot{Y}_\psi = -\langle\sigma v\rangle[Y_\psi^2 - (Y_\psi^{\text{eq}})^2]s. \tag{A.54}$$

Next, we can also write that

$$\frac{dY_\psi}{dx} = \frac{dY_\psi}{dt}\frac{dt}{dx} \simeq \dot{Y}_\psi 0.6 g_\rho^{-1/2}\frac{M_{\text{pl}}}{m_\psi^2}x, \tag{A.55}$$

where we have used Eq. (A.48). Manipulating a little bit the terms and exploting Eq. (A.53), we find that

$$\dot{Y}_\psi = \frac{dY_\psi}{dx}\frac{1}{x}\underbrace{1.67 g_\rho^{1/2}\frac{m_\psi^2}{M_{\text{pl}}}}_{\equiv H(m_\psi)} = \frac{dY_\psi}{dx}\frac{H(m_\psi)}{x}. \tag{A.56}$$

The Boltzmann equation, written in terms of the temperature, thus becomes

$$\frac{dY_\psi}{dx} = -\frac{x\langle\sigma v\rangle}{H(m_\psi)}[Y_\psi^2 - (Y_\psi^{\text{eq}})^2]s. \tag{A.57}$$

We can now use this Boltzmann equation to compute the freeze-out temperature $T_{\text{fo}}$ and the relic yield $Y_\infty$ of a massive particle, as illustrated schematically in Fig. A.5.

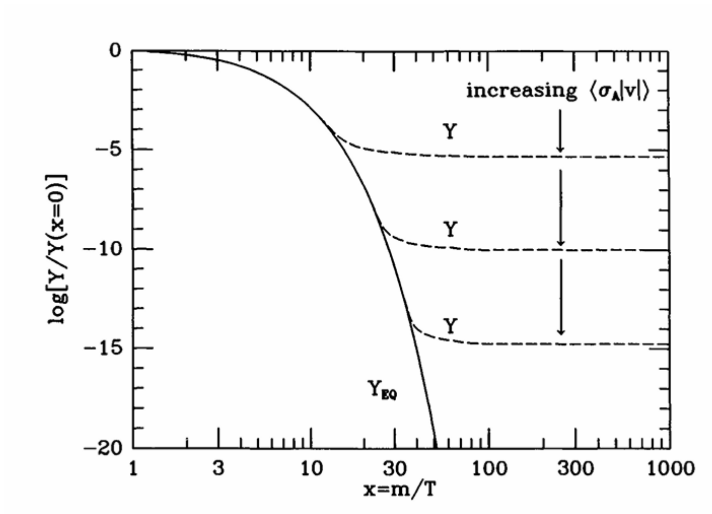


Figure A.5: Freeze-out scenario of a massive particle. The dashed line is the actual abundance, while the solid line is the equilibrium abundance. Moreover, $\langle \sigma_A |v| \rangle$ indicates the thermal average of the annihilation cross section times velocity.
***Reprinted from "The Early Universe", by E. W. Kolb & M. S. Turner, 1990, Taylor & Francis***[212]

.

# Appendix B

# Cross sections and decay rates computations

A four-component Dirac spinor field, indicated as $\psi(x)$, can be seen as made up of two mass-degenerate two-component spinor fields, $\chi_\alpha(x)$ and $\eta_\alpha(x)$, which possess opposite $U(1)$-charge and it is defined as:

$$\psi(x) \equiv \begin{pmatrix} \chi_\alpha(x) \\ \eta^{\dagger\dot{\alpha}}(x) \end{pmatrix}, \tag{B.1}$$

where $\alpha$ and $\dot{\alpha}$ are spinorial indices, used respectively to indicate a left-handed spinor, which transforms according to the $\left(\frac{1}{2}, 0\right)$ representation, and a right-handed spinor, which transforms according to the $\left(0, \frac{1}{2}\right)$ representation[213].
Therefore, it is useful to introduce the chiral spinors but first of all we need to define the chiral projection operators:

$$\begin{cases} P_L \equiv \frac{1}{2}(\mathbb{1} - \gamma_5) = \begin{pmatrix} \delta_\alpha^{\ \beta} & 0 \\ 0 & 0 \end{pmatrix} \\ \\ P_R \equiv \frac{1}{2}(\mathbb{1} + \gamma_5) = \begin{pmatrix} 0 & 0 \\ 0 & \delta^{\dot{\alpha}}_{\ \dot{\beta}} \end{pmatrix} \end{cases}. \tag{B.2}$$

The left and right-handed Weyl spinors are thus defined as:

$$\begin{cases} \psi_L(x) \equiv P_L\psi(x) = \begin{pmatrix} \chi_\alpha(x) \\ 0 \end{pmatrix} \\ \\ \psi_R(x) \equiv P_R\psi(x) = \begin{pmatrix} 0 \\ \eta^{\dagger\dot{\alpha}}(x) \end{pmatrix} \end{cases}. \tag{B.3}$$

We can then defined the Dirac conjugate fields $\bar{\psi}(x)$ and the charge conjugate field $\psi^C(x)$ as:

$$\begin{aligned} \bar{\psi}(x) &\equiv \psi^\dagger(x)\gamma^0 = \begin{pmatrix} \eta^\alpha(x) & \chi^\dagger_{\dot{\alpha}}(x) \end{pmatrix} \\ \psi^C(x) &\equiv C\bar{\psi}^T(x) = \begin{pmatrix} \eta_\alpha(x) \\ \chi^{\dagger\dot{\alpha}}(x) \end{pmatrix} \end{aligned}. \tag{B.4}$$

A fermion is said to be a Majorana fermion if it satisfies the Majorana condition, namely $\psi(x) = \psi^C(x)$, which implies that

$$\psi_M(x) = \begin{pmatrix} \chi_\alpha(x) \\ \chi^{\dagger\dot{\alpha}}(x) \end{pmatrix}. \tag{B.5}$$

We can thus make some conversions between the 2-component spinor notation and the 4-component spinor notation, in particular:

- for a Dirac fermion we can write that $\bar{\psi}^i\psi_j = \eta^i\chi_j + \chi^{\dagger i}\eta_j^\dagger$;

- for a Majorana fermion we can write that $\bar{\psi}_M^i\psi_{Mj} = \xi^i\xi_j + \xi^{\dagger i}\xi_j^\dagger$.

## B.1 Compute cross sections and decay rates with Mathematica

Mathematica is a widely used computational software in particle physics, providing powerful tools for symbolic and numerical calculations. In particular, it allows to use packages like FeynCalc [214, 215], FeynArts [216, 217], and FeynRules[218], which help to calculate cross sections and decay rates.
These packages can be used to efficiently handle complex calculations, automate the generation of Feynman rules, and perform loop-level computations, making them indispensable in high-energy physics research and phenomenology.
FeynArts is an independent package from FeynCalc, but the output generated by the former can be used by the latter to evaluate the corresponding amplitudes. However, since many of the functions in FeynArts have the same names as those in FeynCalc, loading both packages in the same Mathematica session typically results in a large number of warnings. One workaround is to first generate the amplitudes with FeynArts, save them in a notebook, then restart Mathematica, reopen the notebook, and only then load FeynCalc to evaluate the amplitudes. While this solution works, there is a quicker way to operate. It is reccomended, indeed, to modify FeynArts by renaming its functions, preventing any conflicts and allowing both FeynArts and FeynCalc to be used together in the same session.
FeynRules is another essential package in Mathematica, which allows to define theoretical models in terms of the interaction Lagrangian, and then automatically derives the corresponding Feynman rules, including vertices, propagators, and coupling constants. FeynRules supports both the Standard Model and beyond, making it versatile for a wide range of particle physics calculations. It integrates with other packages like FeynCalc and FeynArts, enabling a smooth workflow for generating Feynman diagrams, computing amplitudes, and evaluating cross sections and decay rates.
Having said that, FeynRules can thus be used to define and create new Beyond-the-Standard-Model (BSM) theories by specifying a Lagrangian for the new interactions and particles. To create a BSM model, we can define the fields, the interactions involved, and the coupling constants in the Mathematica environment. Once the model is specified, FeynRules automatically generates the Feynman rules for the interactions, including vertices and propagators, which can then be used to compute scattering amplitudes, cross sections, and decay rates. Once we have finished with FeynRules, we can export these generated Feynman rules to other programs, such

as FeynCalc or MadGraph, for further analysis and simulation. This makes it a powerful tool for model-building and phenomenological studies in high-energy physics.

### B.1.1 Definition of new BSM models in Mathematica

We can start creating a new model by writing all the information characterizing it, such as the model's name and the contact details of the authors. We can also define the particle content of the new theory and the corresponding Lagragian.
We can consider as simple example the $p$-wave Lagrangian in Eq. (4.4), in order to understand how to implement a new model in the Mathematica envinronment. Below we report the definition of all the model's parameters:

```
M$ModelName = "pWave";

M$Information = {
  Authors      -> {"Michael Mancini"},
  Institutions -> {"Unibo"},
  Emails       -> {"michael.mancini2@studio.unibo.it"},
  Date         -> "October 29, 2024"
};

M$Parameters = {

  yD == {
    ParameterType    -> External,
    ParameterName    -> yD,
    Description      -> "DM Yukawa coupling constant"
  },

  ge == {
    ParameterType    -> External,
    ParameterName    -> ge,
    Description      -> "electron Yukawa coupling constant"
  }
};

M$ClassesDescription = {

  F[1] == {
      ClassName -> chi,
      ParticleName -> "\[Chi]",
      PropagatorLabel -> "\[Chi]",
      SelfConjugate -> True,
      Mass -> m\[Chi]
  },
```

```
   F[2] == {
      ClassName -> e,
      ParticleName -> "e",
      PropagatorLabel -> "e",
      SelfConjugate -> False,
      Spin -> 1/2,
      Mass -> me
  },

  S[1] == {
      ClassName     -> S,
      ParticleName    -> "S",
      PropagatorLabel -> "S",
      SelfConjugate -> True,
      Spin -> 0,
      Mass -> mS
  }
};

LP = i*chibar.Ga[mu].DC[chi, mu] + i*ebar.Ga[mu].DC[e, mu]
+ 1/2 del[S, mu] del[S, mu] + 1/2*yD*chibar.chi*S + ge*ebar.e*S
- me*ebar.e - m\[Chi]*chibar.chi - 1/2*mS*S^2;
```

We can now use this new model, written in a "pWave.fr" file to generate Feynman rules and compute the cross sections or decay rates of the proccesses of interest.
We now report below how to work with FeynCalc, FeynArts and FeynRules, avoiding shadowing problems, in order to compute the cross section relative to $\chi\chi \to e^- e^+$ as a useful example.

```
Quit[];
FR$Parallel = False;
$FeynRulesPath = SetDirectory["Directory of the FeynRule package"];
<< FeynRules`;
SetDirectory["Directory of the p-wave model generated with FeynRules"];
LoadModel["pWave.fr"];
WriteFeynArtsOutput[LP, Output -> "pWave"];

$ContextPath = DeleteCases[$ContextPath, "FeynRules`"];

$LoadAddOns = {"FeynArts"};
<< FeynCalc`
$FAVerbose = 0;

top2To2 = CreateTopologies[0, 2 -> 2, ExcludeTopologies -> {WFCorrections}];
diags2To2 = InsertFields[top2To2, {F[1], F[1]} -> {F[2], -F[2]},
InsertionLevel -> {Classes}, Model -> FileNameJoin[{"pWave", "pWave"}]];
Paint[diags2To2, ColumnsXRows -> {3, 1}, Numbering -> None, SheetHeader -> None,
```

```
ImageSize -> {768, 256}];
amp = FCFAConvert[CreateFeynAmp[diags2To2], IncomingMomenta -> {p1, p2},
OutgoingMomenta -> {p3, p4}, ChangeDimension -> 4, List -> False, Contract -> True]
// Simplify

amp = DiracSimplify[%]

ampSq = amp ComplexConjugate[amp];
FermionSpinSum[ampSq]/4;
ampSq = DiracSimplify[%]
```

This code written in Mathematica will first generate the Feynnman diagram relative to the process we are considering, in this case $\chi\chi \to e^-e^+$ and then it will compute the amplitude squared.
In the following we will show computations, which have been in the first instance performed by hand and then checked exploiting Mathematica and the packages mentioned above.

## B.2 Cross sections compuations

In this appendices' section we will report the computation for some scattering processes, in particular the ones relative to the $p$-wave model discussed in App. B.2.1 and the ones relative to the coannihilation model discusses in App. B.2.2[171].
In doing so, we will use apposite Feynman rules for fermion-number-violating interactions, since we deal with Majorana fermions, which violate the lepton number[219].

### B.2.1 $p$-wave model

#### Computation of $\chi e^- \to \chi e^-$ cross section

By using the lagrangian in Eq. (4.4), we can compute the cross section for DM-e elastic scattering; the process to consider is thus $\chi(p_1)e^-(p_2) \to \chi(p_3)e^-(p_4)$.
First of all, we can depict in Fig. B.1 the Feynman rules to use in order to compute the cross section.

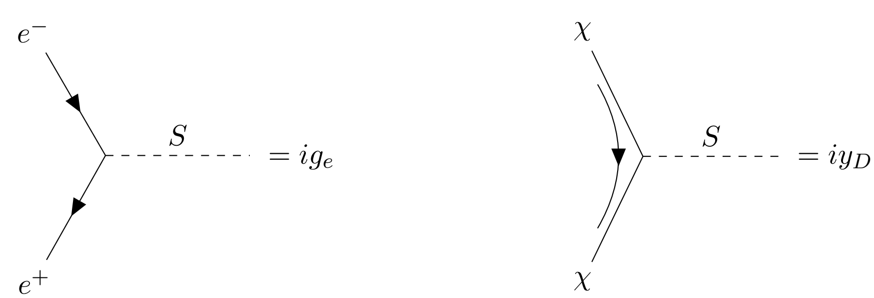


Figure B.1: Feynman rules for the $p$-wave model.

We can then draw the Feynman diagram relative to the process we are considering as illustrated in Fig. B.2.

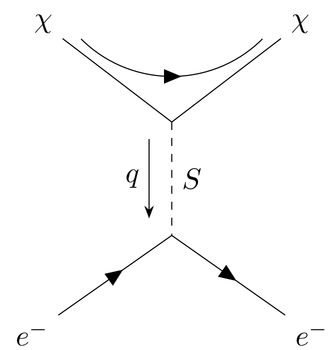


Figure B.2: DM-e elastic scattering

The corresponding scattering amplitude can be written as:

$$iM = i^2 y_D g_e \bar{u}_4 u_2 \frac{i}{q^2 - m_S^2} \bar{u}_3 u_1 = -i \frac{y_D g_e}{q^2 - m_S^2} \bar{u}_4 u_2 \bar{u}_3 u_1, \tag{B.6}$$

where $u_i \equiv u(s_i, p_i)$, with $s_i$ and $p_i$ which are respectively the spin and the four-momentum of the i-th particle.
Given two generic spinors $\psi_1$ and $\psi_2$, we can infer that $\bar{\psi}_1\psi_2$ is a Lorentz scalar and therefore we can write that:

$$(\bar{\psi}_1\psi_2)^* = (\bar{\psi}_1\psi_2)^\dagger = (\psi_1^\dagger\gamma^0\psi_2)^\dagger = \psi_2^\dagger \underbrace{\gamma^{0\dagger}}_{\gamma^0} \psi_1 = \bar{\psi}_2\psi_1, \tag{B.7}$$

where $(\bar{\psi}_1\psi_2)^* = (\bar{\psi}_1\psi_2)^\dagger$, because the transpose of a number coincides with the number itself.
Having said that, we can write that:

$$-iM^* = i \frac{y_D g_e}{q^2 - m_S^2} \bar{u}_2 u_4 \bar{u}_1 u_3, \tag{B.8}$$

from which follows that

$$|M|^2 = \frac{(y_D g_e)^2}{(q^2 - m_S^2)^2} (\bar{u}_4 u_2 \bar{u}_2 u_4)(\bar{u}_3 u_1 \bar{u}_1 u_3). \tag{B.9}$$

In computing the $\chi e^- \to \chi e^-$ cross section, we assume that both the dark matter particle $\chi$ and the electron $e^-$ are unpolarized in their initial states. This is a standard and physically well-justified assumption, since both particles are expected to be non-relativistic and randomly oriented in the GC environment.
Using the following relation:

$$\sum_s u_i \bar{u}_i = \not{p}_i + m_i, \tag{B.10}$$

the unpolarized scattering amplitude reduces to

$$|M|^2_{\text{unp}} = \frac{1}{4} \sum_s |M|^2 = \frac{(y_D g_e)^2}{4(q^2 - m_S^2)^2} \text{Tr}[(\not{p}_4 + m_e)(\not{p}_2 + m_e)] \text{Tr}[(\not{p}_1 + m_\chi)(\not{p}_3 + m_\chi)]. \tag{B.11}$$

Traces are a direct consequence of the use of spinorial indices; for the sake of clarity we will explicit all the spinorial indices for each spinor, so that we can rewrite $\bar{u}u$ in spinorial notation as $\bar{u}_\alpha u_\alpha$, being $\bar{u}u$ a scalar.
As an example, we can write

$$\begin{aligned}&\sum_{s_2,s_4}(\bar{u}_{4\alpha}u_{2\alpha}\bar{u}_{2\beta}u_{4\beta}) = \sum_{s_2,s_4}(u_{4\beta}\bar{u}_{4\alpha}u_{2\alpha}\bar{u}_{2\beta}) = (\not{p}_4 + m_e)_{\beta\alpha}(\not{p}_2 + m_e)_{\alpha\beta} = \\ &= [(\not{p}_4 + m_e)(\not{p}_2 + m_e)]_{\beta\beta} = \mathrm{Tr}[(\not{p}_4 + m_e)(\not{p}_2 + m_e)].\end{aligned} \tag{B.12}$$

We now want to calculate the two traces:

- $\mathrm{Tr}[(\not{p}_4 + m_e)(\not{p}_2 + m_e)] = p_{4\alpha}p_{2\beta}\underbrace{\mathrm{Tr}[\gamma^\alpha\gamma^\beta]}_{4g^{\alpha\beta}} + m_e^2\underbrace{\mathrm{Tr}[\mathbb{1}]}_{4} = 4(p_2 \cdot p_4 + m_e^2)$;
- $\mathrm{Tr}[(\not{p}_1 + m_\chi)(\not{p}_3 + m_\chi)] = 4(p_1 \cdot p_3 + m_\chi^2)$.

We can thus rewrite the unpolarized scattering amplitude, exploiting what we have obtained, as:

$$|M|^2_{\text{unp}} = \frac{4(y_D g_e)^2}{(q^2 - m_S^2)^2}(p_2 \cdot p_4 + m_e^2)(p_1 \cdot p_3 + m_\chi^2). \tag{B.13}$$

We can study the scattering in the center of mass frame and, supposing that the particles move in the y-z plane, the four-momenta can be written as:

$$p_1 = \begin{pmatrix} E_\chi \\ 0 \\ 0 \\ |\vec{p}| \end{pmatrix}, \quad p_2 = \begin{pmatrix} E_e \\ 0 \\ 0 \\ -|\vec{p}| \end{pmatrix}, \quad p_3 = \begin{pmatrix} E_\chi \\ 0 \\ |\vec{k}|\sin\theta \\ |\vec{k}|\cos\theta \end{pmatrix}, \quad p_4 = \begin{pmatrix} E_e \\ 0 \\ -|\vec{k}|\sin\theta \\ -|\vec{k}|\cos\theta \end{pmatrix} \tag{B.14}$$

where $|\vec{k}| \equiv k = p \equiv |\vec{p}|$ because we are dealing with an elastic scattering.
We can now rewrite the unpolarized scattering amplitude in terms of the Mandelstam variable $t$ as

$$|M|^2_{\text{unp}} = \frac{y_D^2 g_e^2 (t - 4m_e^2)(t - 4m_\chi^2)}{(t - m_S^2)^2}. \tag{B.15}$$

We recall that the Mandelstam variable $t$ is defined as $t \equiv (p_1 - p_3)^2$, where

$$p_1 - p_3 = \begin{pmatrix} 0 \\ 0 \\ -p\sin\theta \\ p - p\cos\theta \end{pmatrix}. \tag{B.16}$$

This implies that

$$(p_1 - p_3)^2 = -p^2\sin^2\theta - (p - p\cos\theta)^2 = -p^2\sin^2\theta - p^2 - p^2\cos^2\theta + 2p^2\cos\theta = 2p^2(\cos\theta - 1). \tag{B.17}$$

For a $2 \to 2$ scattering process in the center of mass we can write the differential cross section as

$$\left.\frac{d\sigma}{d\Omega}\right|_{\text{CM}} = \frac{|M|^2_{\text{unp}}}{64\pi^2 E_{\text{CM}}^2}\underbrace{\frac{p_f}{p_i}}_{1}, \tag{B.18}$$

where $\frac{p_f}{p_i} = 1$ again because we are dealing with an elastic scattering, while $E_{\text{CM}}^2 = s$, where $s$ is another Mandelstam variable defined as $s \equiv (p_1 + p_2)^2$.
The differential cross section thus becomes

$$\left.\frac{d\sigma}{d\Omega}\right|_{\text{CM}} = \frac{y_D^2 g_e^2 (t - 4m_e^2)(t - 4m_\chi^2)}{64\pi^2 s (t - m_S^2)^2}. \tag{B.19}$$

Moreover, we can also write that

$$s \equiv (p_1 + p_2)^2 = (E_\chi + E_e)^2 = m_e^2 + m_\chi^2 + 2p^2 + 2\sqrt{(m_e^2 + p^2)(m_\chi^2 + p^2)}. \tag{B.20}$$

If we then integrate over the solid angle and we expand around $p \approx 0$, we get as final result for the cross section in the center of mass frame

$$\sigma_e = \frac{(y_D g_e)^2}{\pi} \frac{\mu_{\text{eDM}}^2}{m_S^4}, \tag{B.21}$$

where $\mu_{\text{eDM}} = \frac{m_e m_\chi}{m_e + m_\chi}$ is the reduces mass.

**Computation of $\chi\chi \to e^- e^+$ cross section**

We now consider DM particles annihilating into electron and positron through a decaying real scalar $S$, namely $\chi(p_1)\chi(p_2) \to e^-(p_3)e^+(p_4)$.
The Feynman rules to use are the same of Fig. B.1, while the scattering process can be depicted as in Fig. B.3.

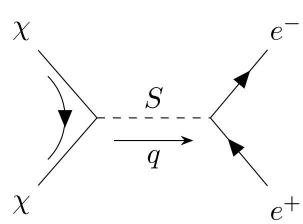


Figure B.3: DM annihilation process.

The corresponding scattering amplitude can be written as

$$iM = i^2 y_D g_e \bar{u}_3 v_4 \frac{i}{q^2 - m_S^2 + i m_S \Gamma_S} \bar{v}_2 u_1 = -\frac{i y_D g_e}{q^2 - m_S^2 + i m_S \Gamma_S} \bar{u}_3 v_4 \bar{v}_2 u_1, \tag{B.22}$$

where $\Gamma_S$ is the width relative to decaying scalar $S$ and $\frac{i}{q^2 - m_S^2 + i m_S \Gamma_S}$ is the full Breit-Wigner propagator for an unstable particle.
As before, we can compute the unpolarized scattering amplitude averaging over the initial spins and summing over the final ones, getting as result

$$|M|^2_{\text{unp}} = \frac{(y_D g_e)^2}{4(q^2 - m_S^2)^2 + m_S^2 \Gamma_S^2} \underbrace{\text{Tr}[(\not{p}_3 + m_e)(\not{p}_4 - m_e)]}_{4(p_3 \cdot p_4 - m_e^2)} \underbrace{\text{Tr}[(\not{p}_1 + m_\chi)(\not{p}_2 - m_\chi)]}_{4(p_1 \cdot p_2 - m_\chi^2)}. \tag{B.23}$$

Computing the traces, and checking the results in Mathematica, we get as result

$$|M|^2_{\text{unp}} = \frac{4(y_D g_e)^2}{(q^2 - m_S^2)^2 + m_S^2\Gamma_S^2}(p_3 \cdot p_4 - m_e^2)(p_1 \cdot p_2 - m_\chi^2). \tag{B.24}$$

I can rewrite everything in terms of the Mandelstam variable $s = (p_1 + p_2)^2 = (p_3 + p_4)^2$ as

$$|M|^2_{\text{unp}} = \frac{(y_D g_e)^2}{(s - m_S)^2 + m_S^2\Gamma_S^2}(s - 4m_e^2)(s - 4m_\chi^2). \tag{B.25}$$

We can now proceed to compute the differential cross section, which as befor, is defined in the center of mass frame as

$$\left.\frac{d\sigma}{d\Omega}\right|_{\text{CM}} = \frac{|M|^2_{\text{unp}}}{64\pi^2 s}\frac{p_f}{p_i}, \tag{B.26}$$

where in this case $\frac{p_f}{p_i} \neq 1$.
We can study the scattering in the center of mass frame and, supposing that particles move in the y-z plane, the four-momenta can be written as:

$$p_1 = \begin{pmatrix} E_\chi \\ 0 \\ 0 \\ |\vec{p}| \end{pmatrix}, \quad p_2 = \begin{pmatrix} E_\chi \\ 0 \\ 0 \\ -|\vec{p}| \end{pmatrix}, \quad p_3 = \begin{pmatrix} E_e \\ 0 \\ |\vec{k}|\sin\theta \\ |\vec{k}|\cos\theta \end{pmatrix}, \quad p_4 = \begin{pmatrix} E_e \\ 0 \\ -|\vec{k}|\sin\theta \\ -|\vec{k}|\cos\theta \end{pmatrix}, \tag{B.27}$$

where, by imposing the on-shell conditions $p_i^2 = m_i^2$, we get

$$\begin{cases} |\vec{p}| \equiv p = \sqrt{E_\chi^2 - m_\chi^2} \\ |\vec{k}| \equiv k = \sqrt{E_e^2 - m_e^2} \end{cases} . \tag{B.28}$$

We can massage a little bit these terms noticing that the total energy in the center of mass frame is given by $E_{\text{CM}} = 2E_\chi = 2E_e \implies E_\chi^2 = E_e^2 = \frac{E_{\text{CM}}^2}{4} = \frac{s}{4}$. This allows to rewrite the momenta in Eq. (B.28) as

$$\begin{cases} p = \frac{1}{2}\sqrt{s - 4m_\chi^2} \\ k = \frac{1}{2}\sqrt{s - 4m_e^2} \end{cases} . \tag{B.29}$$

The differential cross section thus becomes

$$\left.\frac{d\sigma}{d\Omega}\right|_{\text{CM}} = \frac{(y_D g_e)^2}{64\pi^2 s}\frac{(s - 4m_e^2)^{3/2}\sqrt{s - 4m_\chi^2}}{(s - m_S)^2 + m_S^2\Gamma_S^2}. \tag{B.30}$$

Integrating over the solid angle, we can obtain the cross section in the center of mass frame which is given by

$$\sigma\big|_{\text{CM}} = \int d\Omega \left.\frac{d\sigma}{d\Omega}\right|_{\text{CM}} = \frac{(y_D g_e)^2}{16\pi s}\frac{(s - 4m_e^2)^{3/2}\sqrt{s - 4m_\chi^2}}{(s - m_S)^2 + m_S^2\Gamma_S^2}. \tag{B.31}$$

We can now express everything in terms of the relative velocity between the colliding DM particles. In general, the relative velocity between two particles is defined as

$$v_{ij} = \frac{\sqrt{(p_i \cdot p_j)^2 - m_i^2 m_j^2}}{E_i E_j}. \tag{B.32}$$

In our case, the relative velocity is

$$v_{\rm rel} = \frac{\sqrt{(p_1 \cdot p_2)^2 - m_\chi^4}}{E_\chi^2}, \tag{B.33}$$

which, exploiting the four-momenta as defined in Eq. (B.27), becomes

$$v_{\rm rel} = \frac{\sqrt{(E_\chi^2 + p^2)^2 - m_\chi^4}}{E_\chi^2} = \frac{\sqrt{m_\chi^4 + 4p^4 + 4p^2 m_\chi^2 - m_\chi^4}}{m_\chi^2 + p^2} = \frac{2p\sqrt{m_\chi^2 + p^2}}{m_\chi^2 + p^2} = \frac{2p}{\sqrt{m_\chi^2 + p^2}}. \tag{B.34}$$

Taylor expanding the relative velocity around $p \approx 0$, we get

$$v_{\rm rel} = \frac{2p}{m_\chi} + \mathcal{O}(p^2) \implies p \simeq \frac{m_\chi v_{\rm rel}}{2}. \tag{B.35}$$

Exploiting this result, we can rewrite the Mandelstam variable $s$ in terms of the relative velocity as

$$s = (p_1 + p_2)^2 = E_{\rm CM}^2 = 4E_\chi^2 = 4m_\chi^2 + 4p^2 \simeq 4m_\chi^2 + m_\chi^2 v_{\rm rel}^2. \tag{B.36}$$

Therefore, we can rewrite the cross section in Eq. (B.31) in terms of the relative velocity and expanding around $v_{\rm rel} \approx 0$, we get

$$\sigma v_{\rm rel} = v_{\rm rel}^2 \frac{(y_D g_e)^2}{8\pi} \frac{m_\chi^2 \left(1 - \frac{m_e^2}{m_\chi^2}\right)^{3/2}}{(m_S - 4m_\chi^2)^2 + m_S^2 \Gamma_S^2}. \tag{B.37}$$

The decay rate of the scalar particle S , denoted as $\Gamma_S$, is computed explicitly in Sec. B.3.1

**Computation of $\chi\chi \to \chi\chi$ cross section**

In this paragraph we consider DM self-interacting processes that may occur in the $p$-wave model, namely $\chi(p_1)\chi(p_2) \to \chi(p_3)\chi(p_4)$. We exploit the Feynman rules depicted in Fig. B.1 in order to compute the cross section. We can draw instead the Feynman diagrams relative to the process we are considering as illustrated in Fig. B.4.

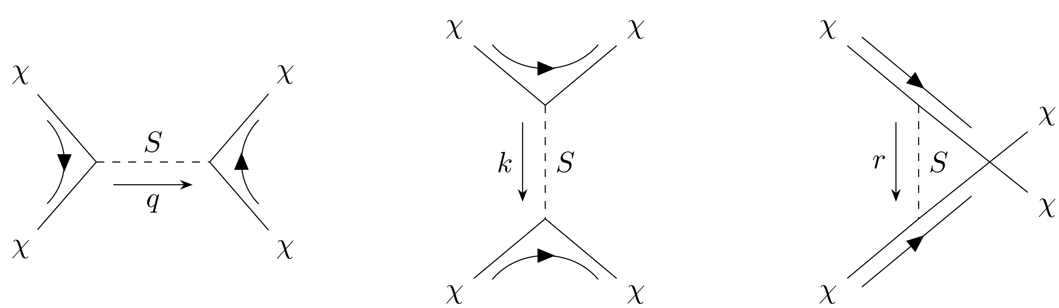


Figure B.4: DM self-interacting processes.

The corresponding scattering amplitude can be written as

$$iM = -\frac{iy_D^2}{q^2 - m_S^2 + im_S\Gamma_S}\bar{v}_2 u_1 \bar{u}_3 v_4 - \frac{iy_D^2}{k^2 - m_S^2}\bar{u}_3 u_1 \bar{u}_4 u_2 + \frac{iy_D^2}{r^2 - m_S^2}\bar{u}_4 u_1 \bar{u}_3 u_2, \tag{B.38}$$

where the plus sign in the last term is due to the fact that in the u-channel we are exchanging two fermion lines with respect to the t-channel and $im_S\Gamma_S$ in the s-channel is added in order to study the process close to the resonance regime. Moreover we can write that

$$\begin{cases} q = p_1 + p_2 \\ k = p_1 - p_3 \\ r = p_1 - p_4 \end{cases} . \tag{B.39}$$

We can study the scattering in the center of mass frame and, supposing that the particles move in the y-z plane, the four-momenta can be written as:

$$p_1 = \begin{pmatrix} E_\chi \\ 0 \\ 0 \\ |\vec{p}| \end{pmatrix}, \quad p_2 = \begin{pmatrix} E_\chi \\ 0 \\ 0 \\ -|\vec{p}| \end{pmatrix}, \quad p_3 = \begin{pmatrix} E_\chi \\ 0 \\ |\vec{k}|\sin\theta \\ |\vec{k}|\cos\theta \end{pmatrix}, \quad p_4 = \begin{pmatrix} E_\chi \\ 0 \\ -|\vec{k}|\sin\theta \\ -|\vec{k}|\cos\theta \end{pmatrix}, \tag{B.40}$$

where $p \equiv |\vec{p}| = \sqrt{E_\chi^2 - m_\chi^2} = \vec{k} \equiv k$.
Therefore, we can write that

- $s = (p_1 + p_2)^2 = 4E_\chi^2 = 4m_\chi^2 + 4p^2$;

- $t = (p_1 - p_3)^2 = -p^2\sin^2\theta - p^2 - p^2\cos^2\theta + 2p^2\cos\theta = 2p^2(\cos\theta - 1)$;

- $u = (p_1 - p_4)^2 = -p^2\sin^2\theta - p^2 - p^2\cos^2\theta - 2p^2\cos\theta = -2p^2(\cos\theta + 1)$.

We want to work in the non-relativistic limit, therefore, integrating over the solid angle and then expanding around $p \simeq 0$, we get as result

$$\sigma_{\text{self}} = \frac{y_D^4 m_\chi^2}{4\pi m_S^4}. \tag{B.41}$$

Moreover, we have two identical particles in the final state, so we should divide Eq. (B.41) by 2, obtaining as final result

$$\sigma_{\text{self}} = \frac{y_D^4 m_\chi^2}{8\pi m_S^4}. \tag{B.42}$$

### B.2.2 Coannihilation model

#### Computation of $\chi_1\chi_2 \to e^+e^-$ cross section

Let us now compute the cross section relative to the $\chi_1(p_1)\chi_2(p_2) \to e^-(p_3)e^+(p_4)$ coannihilation process, by using the lagrangian in Eq. (5.1)
First of all, we can depict in Fig. B.5 the Feynman rules to use in order to compute the cross section.
We can then draw the Feynman diagram relative to the process we are considering as illustrated in Fig. B.6.

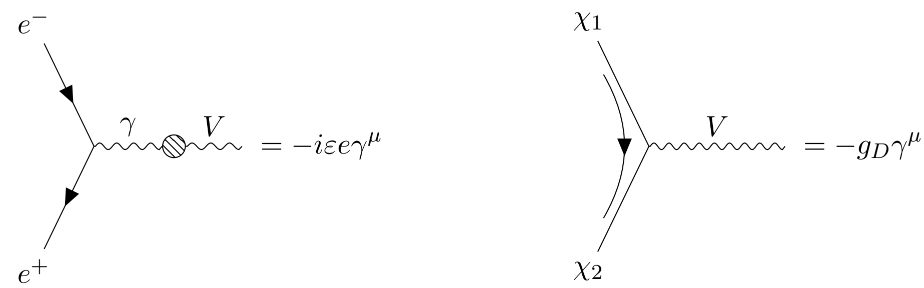


Figure B.5: Feynman rules for the coannihilation model.

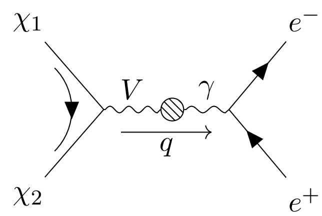


Figure B.6: $e^-e^+$ production in the coannihilation model.

The corresponding scattering amplitude can be written as

$$iM = -\varepsilon e g_D \bar{u}_3\gamma^\nu v_4 \frac{1}{q^2 - m_V^2}\Big( - g_{\mu\nu} + \frac{q_\mu q_\nu}{m_V^2}\Big)\bar{v}_2\gamma^\mu u_1, \tag{B.43}$$

where $q^\mu = p_1^\mu + p_2^\mu$.
From the Dirac equation $(i\gamma^\mu\partial_\mu - m)\psi(x) = 0$ we get that

$$\begin{cases} (\underbrace{\gamma^\mu p_\mu}_{\not{p}} - m)u_s(p) = 0 & \text{if } \psi(x) = u_s(p)e^{-ip\cdot x} \\ (\not{p} + m)v_s(p) = 0 & \text{if } \psi(x) = v_s(p)e^{ip\cdot x} \end{cases}. \tag{B.44}$$

Equivalently, introducing the Dirac conjugate spinor $\bar{\psi}(x) = \psi^\dagger(x)\gamma^0$, from the Dirac equation $\bar{\psi}(x)(i\gamma^\mu\overleftarrow{\partial}_\mu + m) = 0$ we get that

$$\begin{cases} \bar{u}_s(p)(-\not{p} + m) = 0 & \text{if } \bar{\psi}(x) = \bar{u}_s(p)e^{ip\cdot x} \\ \bar{v}_s(p)(\not{p} + m) = 0 & \text{if } \bar{\psi}(x) = \bar{v}_s(p)e^{-ip\cdot x} \end{cases}. \tag{B.45}$$

Summarizing, we thus have that

$$\begin{cases} (\not{p} - m)u_s(p) = \bar{u}_s(p)(-\not{p} + m) = 0 \\ (\not{p} + m)v_s(p) = \bar{v}_s(p)(\not{p} + m) = 0 \end{cases}. \tag{B.46}$$

We can notice that in the scattering amplitude in Eq. (B.43) we have something similar, indeed:

$$q_\mu\bar{v}_2\gamma^\mu u_1 = \bar{v}_2(\not{p}_1 + \not{p}_2)u_1 = \bar{v}_2 \underbrace{\not{p}_1 u_1}_{m_{\chi_1}u_1} + \underbrace{\bar{v}_2\not{p}_2}_{-m_{\chi_2}\bar{v}_2} u_1 = \bar{v}_2 u_1(m_{\chi_1} - m_{\chi_2}) = \bar{v}_2 u_1\delta \simeq 0 \tag{B.47}$$

since $\delta \ll m_{\chi 1}, m_{\chi 2}$. Therefore the $q_\mu q_\nu$ term in the scattering amplitude in Eq. (B.43) gives zero contribution and therefore we remain with

$$iM = \frac{\varepsilon e g_D}{q^2 - m_V^2} \bar{u}_3 \gamma^\mu v_4 \bar{v}_2 \gamma_\mu u_1. \tag{B.48}$$

As usual, we can compute the unpolarized scattering amplitude averaging over the initial spins and summing over the final ones, getting as result

$$|M|^2_{\text{unp}} = \frac{\varepsilon^2 e^2 g_D^2}{4(q^2 - m_V^2)^2} \text{Tr}[(\not{p}_4 - m_e)\gamma^\nu(\not{p}_3 + m_e)\gamma^\mu] \text{Tr}[(\not{p}_2 - M_{\text{DM}})\gamma_\mu(\not{p}_1 + M_{\text{DM}})\gamma_\nu], \tag{B.49}$$

where we have used that $m_{\chi 1} \simeq m_{\chi 2} \equiv M_{\text{DM}}$.
Computing the traces with the use of Mathematica, we get

$$|M|^2_{\text{unp}} = \frac{8\varepsilon^2 e^2 g_D^2}{(q^2 - m_V^2)^2} [m_e^2\, p_1 \cdot p_2 + M_{\text{DM}}^2\, p_3 \cdot p_4 + p_1 \cdot p_4 p_2 \cdot p_3 + p_1 \cdot p_3 p_2 \cdot p_4 + 2 m_e^2 M_{\text{DM}}^2]. \tag{B.50}$$

We now want to rewrite the unpolarized scattering amplitude in Eq. (B.50) in terms of the Mandelstam variables, therefore we recall that

- $(p_1 + p_2)^2 = (p_3 + p_4)^2 \equiv s$
  $\implies s = \underbrace{p_1^2 + p_2^2}_{2M_{\text{DM}}^2} + 2 p_1 \cdot p_2 \implies \begin{cases} p_1 \cdot p_2 = \frac{s - 2M_{\text{DM}}^2}{2} \\ p_3 \cdot p_4 = \frac{s - 2m_e^2}{2} \end{cases}.$
- $(p_1 - p_3)^2 = (p_2 - p_4)^2 \equiv t$
  $\implies t = \underbrace{p_1^2 + p_3^2}_{M_{\text{DM}}^2 + m_e^2} - 2 p_1 \cdot p_3 \implies p_1 \cdot p_3 = p_2 \cdot p_4 = \frac{-t + M_{\text{DM}}^2 + m_e^2}{2}.$
- $(p_1 - p_4)^2 = (p_2 - p_3)^2 \equiv u$
  $\implies u = \underbrace{p_1^2 + p_4^2}_{M_{\text{DM}}^2 + m_e^2} - 2 p_1 \cdot p_4 \implies p_1 \cdot p_4 = p_2 \cdot p_3 = \frac{-u + M_{\text{DM}}^2 + m_e^2}{2}.$

We can rewrite the unpolarized scattering amplitude in Eq. (B.50) as:

$$|M|^2_{\text{unp}} = [2m_e^4 + 2M_{\text{DM}}^4 + 2m_e^2(2M_{\text{DM}}^2 + s - t - u) + 2M_{\text{DM}}^2(s - t - u) + t^2 + u^2] \frac{2\epsilon^2 e^2 g_D^2}{(s - m_V^2)^2}. \tag{B.51}$$

We can study the scattering in the center of mass frame and, supposing that the particles move in the y-z plane, the four-momenta can be written as:

$$p_1 = \begin{pmatrix} E_{\text{DM}} \\ 0 \\ 0 \\ |\vec{p}| \end{pmatrix}, \quad p_2 = \begin{pmatrix} E_{\text{DM}} \\ 0 \\ 0 \\ -|\vec{p}| \end{pmatrix}, \quad p_3 = \begin{pmatrix} E_e \\ 0 \\ |\vec{k}|\sin\theta \\ |\vec{k}|\cos\theta \end{pmatrix}, \quad p_4 = \begin{pmatrix} E_e \\ 0 \\ -|\vec{k}|\sin\theta \\ -|\vec{k}|\cos\theta \end{pmatrix}, \tag{B.52}$$

where we have used again that $m_{\chi 1} \simeq m_{\chi 2} \equiv M_{\text{DM}}$.
Therefore, we can write that

$$t = (p_1 - p_3)^2 = m_e^2 + M_{\text{DM}}^2 - 2E_{\text{DM}} E_e + 2pk\cos\theta, \tag{B.53}$$

where

$$\begin{cases} |\vec{p}| \equiv p = \sqrt{E_{\text{DM}}^2 - M_{\text{DM}}^2} \\ |\vec{k}| \equiv k = \sqrt{E_e^2 - m_e^2} \end{cases} . \tag{B.54}$$

Moreover, using that $E_{\text{CM}} = 2E_{\text{DM}} = 2E_e = \sqrt{s}$, we can write that

$$t = m_e^2 + M_{\text{DM}}^2 - \frac{s}{2} + 2\sqrt{\frac{s^2}{16} - \frac{sm_e^2}{4} - \frac{sM_{\text{DM}}^2}{4} + m_e^2 M_{\text{DM}}^2}\, \cos\theta. \tag{B.55}$$

As for $u$ instead, we can write that

$$\begin{aligned} u = (p_1 - p_4)^2 &= m_e^2 + M_{\text{DM}}^2 - 2E_{\text{DM}}E_e - 2pk\cos\theta \\ &= m_e^2 + M_{\text{DM}}^2 - \frac{s}{2} - 2\sqrt{\frac{s^2}{16} - \frac{sm_e^2}{4} - \frac{sM_{\text{DM}}^2}{4} + m_e^2 M_{\text{DM}}^2}\, \cos\theta. \end{aligned} \tag{B.56}$$

Therefore, the unpolarized scattering amplitude becomes

$$|M|_{\text{unp}}^2 = \frac{\varepsilon^2 g_D^2 e^2}{s - m_V^2}[4m_e^2(4M_{\text{DM}}^2 \cos^2\theta + s\sin^2\theta) + s(4M_{\text{DM}}^2 \sin^2\theta + s\cos^2\theta + s)]. \tag{B.57}$$

We now recall that the differential cross section for a $2 \to 2$ scattering process is calculated as in Eq. (B.26), where now $\frac{p_f}{p_i} = \frac{k}{p}$. Moreover, we can rewrite $k$ and $p$ in terms of the Mandelstam variable $s$ as

$$\begin{cases} k = \sqrt{E_e^2 - m_e^2} = \sqrt{\frac{s}{4} - m_e^2} = \frac{1}{2}\sqrt{s - 4m_e^2} \\ p = \sqrt{E_{\text{DM}}^2 - M_{\text{DM}}^2} = \sqrt{\frac{s}{4} - M_{\text{DM}}^2} = \frac{1}{2}\sqrt{s - 4M_{DM}^2} \end{cases} . \tag{B.58}$$

Using Eqs. B.57 and B.58, we can write the differential cross section as

$$\begin{aligned} \frac{d\sigma}{d\Omega}\bigg|_{\text{CM}} &= \frac{\varepsilon^2 e^2 g_D^2}{64\pi^2 s(s - m_V^2)} \frac{\sqrt{s - 4m_e^2}}{\sqrt{s - 4M_{\text{DM}}}^2} \cdot \\ &\cdot [4m_e^2(4M_{\text{DM}}^2 \cos^2\theta + s\sin^2\theta) + s(4M_{\text{DM}}^2 \sin^2\theta + s\cos^2\theta + s)]. \end{aligned} \tag{B.59}$$

Integrating over the solid angle, we get

$$\sigma\big|_{\text{CM}} = \int \frac{d\sigma}{d\Omega}\bigg|_{\text{CM}} d\Omega = \frac{\varepsilon^2 e^2 g_D^2}{12\pi s(s - m_V^2)^2}\sqrt{\frac{s - 4m_e^2}{s - 4M_{\text{DM}}^2}}(2M_{\text{DM}}^2 + s)(2m_e^2 + s). \tag{B.60}$$

Recalling the expression for the relative velocity in Eq. (B.36), we can rewrite Eq. (B.60) in term of the $v_{\text{rel}}$ and expand everything around $v_{\text{rel}} \simeq 0$, obtaining as result

$$\sigma\big|_{\text{CM}} = 4\varepsilon^2 \alpha_e g_D^2 \frac{M_{\text{DM}}^2 + m_e^2/2}{(m_V^2 - 4M_{\text{DM}}^2)^2}\sqrt{1 - \frac{m_e^2}{M_{\text{DM}}^2}}, \tag{B.61}$$

where we have introduced the fine structure constant $\alpha_e = \frac{e^2}{4\pi}$.

### Computation of $\chi_i\chi_i \to \varphi\varphi$ cross section

Let us now compute the cross section relative to the $\chi(p_1)\chi_2(p_2) \to \varphi(p_3)\varphi(p_4)$ process.
In addition to the Feynman rules illustrated in Fig. B.5, we can depict other Feynman rules useful for the process in Fig. B.7.

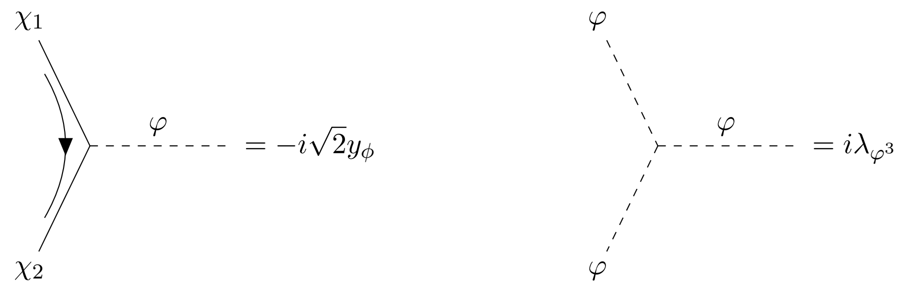


Figure B.7: DM-scalar coupling.

We can then draw the Feynman diagram relative to the process we are considering as illustrated in Fig. B.8.

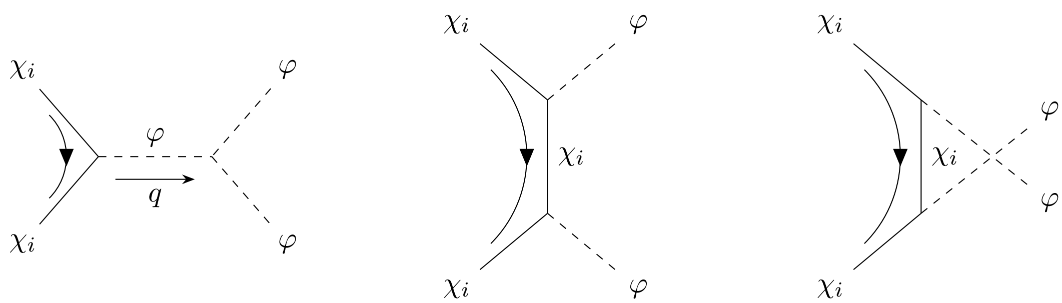


Figure B.8: Inelastic scattering in the coannihilation model.

In the limit that $\frac{y_\phi v_\phi}{\lambda_{\varphi^3}} \ll 1$, the last two Feynman diagrams in Fig. B.8 are subdominant with respect to the first one.
The corresponding scattering amplitude can thus be written as

$$iM = \sqrt{2}y_\phi\lambda_{\varphi^3}\bar{v}_2 u_1 \frac{i}{q^2 - m_\varphi^2}. \tag{B.62}$$

We can now find the unpolarized scattering amplitude averaging over the initial spins, finding that

$$|M|^2_{\text{unp}} = \frac{(y_\phi\lambda_{\varphi^3})^2}{2(q^2 - m_\varphi^2)^2} \underbrace{\text{Tr}[(\not{p}_1 + M_{\text{DM}})(\not{p}_2 - M_{\text{DM}})]}_{4(p_1\cdot p_2 - M^2_{\text{DM}})} = 2\frac{(y_\phi\lambda_{\varphi^3})^2}{(q^2 - m_\varphi^2)^2}(p_1 \cdot p_2 - M^2_{\text{DM}}), \tag{B.63}$$

where we have used that $m_{\chi_1} \simeq m_{\chi_2} \simeq M_{\text{DM}}$.
We can study the scattering in the center of mass frame and, supposing that the particles move

in the y-z plane, the four-momenta can be written as:

$$p_1 = \begin{pmatrix} E_{\rm DM} \\ 0 \\ 0 \\ |\vec{p}| \end{pmatrix}, \quad p_2 = \begin{pmatrix} E_{\rm DM} \\ 0 \\ 0 \\ -|\vec{p}| \end{pmatrix}, \quad p_3 = \begin{pmatrix} E_\varphi \\ 0 \\ |\vec{k}|\sin\theta \\ |\vec{k}|\cos\theta \end{pmatrix}, \quad p_4 = \begin{pmatrix} E_\varphi \\ 0 \\ -|\vec{k}|\sin\theta \\ -|\vec{k}|\cos\theta \end{pmatrix}, \tag{B.64}$$

where we can write that

$$\begin{cases} |\vec{p}| \equiv p = \sqrt{E_{\rm DM}^2 - M_{\rm DM}^2} = \sqrt{\frac{s}{4} - M_{\rm DM}^2} = \frac{1}{2}\sqrt{s - 4M_{\rm DM}^2} \\ |\vec{k}| \equiv k = \sqrt{E_\varphi^2 - m_\varphi^2} = \sqrt{\frac{s}{4} - m_\varphi^2} = \frac{1}{2}\sqrt{s - 4m_\varphi^2} \end{cases}. \tag{B.65}$$

Using the four-momenta in Eq. (B.64), we can write that

$$p_1 \cdot p_2 = E_{\rm DM}^2 + p^2 = M_{\rm DM}^2 + 2p^2 \tag{B.66}$$

and thus the unpolarized scattering amplitude becomes

$$|M|^2_{\rm unp} = 4\frac{(y_\phi \lambda_{\varphi^3})^2}{(s - m_\varphi^2)^2} p^2, \tag{B.67}$$

where we have used that $(p_1 + p_2)^2 = q^2 = 4E_{\rm DM}^2 \equiv s$.
We now use Eq. (B.26) to compute the differential cross section, where $\frac{p_f}{p_i} = \frac{k}{p}$, so that we get

$$\left.\frac{d\sigma}{d\Omega}\right|_{\rm CM} = \frac{(y_\phi \lambda_{\varphi^3})^2}{16\pi^2 s(s - m_\varphi^2)^2} kp \tag{B.68}$$

and integrating over the solid angle, we remain with

$$\sigma\big|_{\rm CM} = \frac{(y_\phi \lambda_{\varphi^3})^2}{4\pi s(s - m_\varphi^2)^2} kp. \tag{B.69}$$

We can now use Eq. (B.65) to rewrite the cross section in Eq. (B.69) as

$$\sigma\big|_{\rm CM} = \frac{(y_\phi \lambda_{\varphi^3})^2}{16\pi s(s - m_\varphi^2)^2} \sqrt{s - 4M_{\rm DM}^2}\sqrt{s - 4m_\varphi^2}. \tag{B.70}$$

Now, using Eq. (B.36) and expanding around $v_{\rm rel} \simeq 0$, we can write that

$$\sigma v_{\rm rel} = v_{\rm rel}^2 \frac{(y_\phi \lambda_{\varphi^3})^2}{32\pi(4M_{\rm DM}^2 - m_\varphi^2)^2} \sqrt{1 - \frac{m_\varphi^2}{M_{\rm DM}^2}}. \tag{B.71}$$

Moreover, we can notice that in the final state we have two indistinguishable particles $\varphi$, so we multiply the cross section times velocity in Eq. (B.71) by $\frac{1}{2}$, obtaining as final result

$$\sigma v_{\rm rel} = v_{\rm rel}^2 \frac{(y_\phi \lambda_{\varphi^3})^2}{64\pi(4M_{\rm DM}^2 - m_\varphi^2)^2} \sqrt{1 - \frac{m_\varphi^2}{M_{\rm DM}^2}}. \tag{B.72}$$

### Computation of $\chi_2\chi_2 \to \chi_1\chi_1$ cross section

Let us now compute the cross section relative to the $\chi_2(p_1)\chi_2(p_2) \to \chi_1(p_3)\chi_1(p_4)$ process. We can use the Feyman rules depicted in Fig. B.5 in order to perform computations. We can also draw the Feynman diagrams relative to the process we are considering, as illustrated in Fig. B.9.

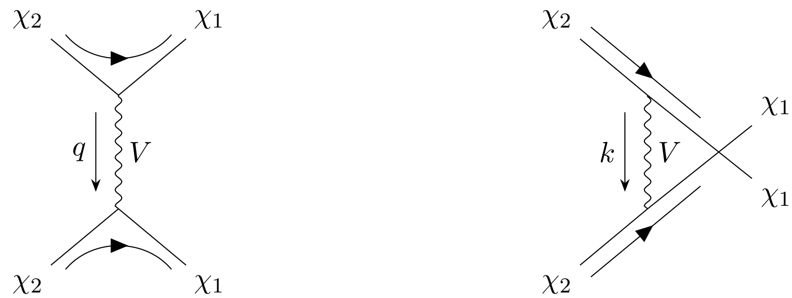


Figure B.9: Feynman diagrams relative to the $\chi_2\chi_2 \to \chi_1\chi_1$ scattering process.

The corresponding scattering amplitude can thus be written as

$$iM = ig_D^2 \bar{u}_3 \gamma^\mu u_1 \frac{\left( - g_{\mu\nu} + \frac{q_\mu q_\nu}{m_V^2} \right)}{q^2 - m_V^2} \bar{u}_4 \gamma^\nu u_2 - ig_D^2 \bar{u}_3 \gamma^\nu u_2 \frac{\left( - g_{\mu\nu} + \frac{k_\mu k_\nu}{m_V^2} \right)}{k^2 - m_V^2} \bar{u}_4 \gamma^\mu u_1, \tag{B.73}$$

where the minus sign in the second term is due to the fact that the exchange of two fermionic lines introduces a minus sign.
Exploting again the Dirac equations as we did in App. B.2.2, we can write that

$$\begin{aligned} \bar{u}_3 \gamma^\mu u_1 q_\mu &= \bar{u}_3 \not{q} u_1 = \bar{u}_3 (\not{p}_1 - \not{p}_3) u_1 = \bar{u}_3 m_{\chi_2} u_1 - \bar{u}_3 m_{\chi_1} u_1 = \bar{u}_3 \underbrace{(m_{\chi_2} - m_{\chi_1})}_{\delta} u_1 \\ &= \delta \bar{u}_3 u_1. \end{aligned} \tag{B.74}$$

In the same way

$$\bar{u}_4 \gamma^\mu u_1 k_\mu = \delta \bar{u}_4 u_1. \tag{B.75}$$

Since $\delta \ll m_V$, we can neglect both the $\frac{q_\mu q_\nu}{m_V^2}$ and the $\frac{k_\mu k_\nu}{m_V^2}$ term in Eq. (B.73), which thus becomes

$$iM = \underbrace{-\frac{ig_D^2}{t - m_V^2} \bar{u}_3 \gamma^\mu u_1 \bar{u}_4 \gamma_\mu u_2}_{iM_t} + \underbrace{\frac{ig_D^2}{u - m_V^2} \bar{u}_3 \gamma^\mu u_2 \bar{u}_4 \gamma_\mu u_1}_{iM_u}. \tag{B.76}$$

Therefore, we can write that

$$|M|^2 = |M_t|^2 + |M_u|^2 + 2\Re\mathfrak{e}(M_t^* M_u), \tag{B.77}$$

from which follows the unpolarized scattering amplitude, averaging over the initial spins and summing over the final ones:

$$
\begin{aligned}
|M|^2_{\text{unp}} = &\frac{g_D^4}{4(t-m_V^2)^2}\text{Tr}[(\not{p}_3+m_{\chi_1})\gamma^\mu(\not{p}_1+m_{\chi_2})\gamma^\alpha]\text{Tr}[(\not{p}_4+m_{\chi_1})\gamma_\mu(\not{p}_2+m_{\chi_2})\gamma_\alpha] \\
&+\frac{g_D^4}{4(u-m_V^2)^2}\text{Tr}[(\not{p}_3+m_{\chi_1})\gamma^\mu(\not{p}_2+m_{\chi_2})\gamma^\alpha]\text{Tr}[(\not{p}_4+m_{\chi_1})\gamma_\mu(\not{p}_1+m_{\chi_2})\gamma_\alpha] \\
&-\frac{g_D^4}{2(t-m_V^2)(u-m_V^2)}\text{Tr}[(\not{p}_1+m_{\chi_2})\gamma^\mu(\not{p}_3+m_{\chi_1})\gamma^\alpha(\not{p}_2+m_{\chi_2})\gamma_\mu(\not{p}_4+m_{\chi_1})\gamma_\alpha]
\end{aligned}
\tag{B.78}
$$

We can study the scattering in the center of mass frame and, supposing that the particles move in the y-z plane, the four-momenta can be written as:

$$
p_1=\begin{pmatrix}E_{\chi_2}\\0\\0\\|\vec{p}|\end{pmatrix},\quad p_2=\begin{pmatrix}E_{\chi_2}\\0\\0\\-|\vec{p}|\end{pmatrix},\quad p_3=\begin{pmatrix}E_{\chi_1}\\0\\|\vec{k}|\sin\theta\\|\vec{k}|\cos\theta\end{pmatrix},\quad p_4=\begin{pmatrix}E_{\chi_1}\\0\\-|\vec{k}|\sin\theta\\-|\vec{k}|\cos\theta\end{pmatrix},
\tag{B.79}
$$

where we can write that

$$
\begin{cases}
|\vec{p}|\equiv p=\sqrt{E_{\chi_2}^2-m_{\chi_2}^2}=\sqrt{\frac{s}{4}-m_{\chi_2}^2}=\frac{1}{2}\sqrt{s-4m_{\chi_2}^2}\\
|\vec{k}|\equiv k=\sqrt{E_{\chi_1}^2-m_{\chi_1}^2}=\sqrt{\frac{s}{4}-m_{\chi_1}^2}=\frac{1}{2}\sqrt{s-4m_{\chi_1}^2}
\end{cases}.
\tag{B.80}
$$

Indeed, the center of mass energy is $\sqrt{s}=E_{\text{CM}}=2E_{\chi_2}=2E_{\chi_1}$.
As always, we can compute the differential cross section as defined in Eq. (B.26). Moreover, we can write that

- $t=(p_1-p_3)^2=m_{\chi_1}^2+m_{\chi_2}^2-2E_{\chi_1}E_{\chi_2}+2pk\cos\theta$
  $=m_{\chi_1}^2+m_{\chi_2}^2-\dfrac{s}{2}+\dfrac{1}{2}\sqrt{(s-4m_{\chi_1}^2)(s-4m_{\chi_2}^2)}\cos\theta$
- $u=(p_1-p_4)^2=m_{\chi_1}^2+m_{\chi_2}^2-2E_{\chi_1}E_{\chi_2}-2pk\cos\theta\quad.$
  $=m_{\chi_1}^2+m_{\chi_2}^2-\dfrac{s}{2}-\dfrac{1}{2}\sqrt{(s-4m_{\chi_1}^2)(s-4m_{\chi_2}^2)}\cos\theta$

In the limit that $m_{\chi_1}\simeq m_{\chi_2}\simeq M_{\text{DM}}$ and using that $s\simeq 4M_{\text{DM}}^2+M_{\text{DM}}^2v_{\text{rel}}^2$, if we expand around $v_{\text{rel}}\simeq 0$, we get as final result that

$$
\sigma\big|_{\text{CM}}=\frac{g_D^4M_{\text{DM}}^2}{4\pi m_V^4}.
\tag{B.81}
$$

Moreover, since in the final state we have two identical particles, we should divide by 2 the cross section in Eq. (B.81), obtaining

$$
\sigma\big|_{\text{CM}}=\frac{g_D^4M_{\text{DM}}^2}{8\pi m_V^4}.
\tag{B.82}
$$

This result coincides at first order with Eq. B1 of Ref. [191] in the limit that $m_1\simeq m_2$ and expanding around $v_{\text{rel}}\simeq 0$.

## B.3 Decay rates computation

### B.3.1 Computation of $\Gamma_S$

In this appendices' section we compute the decay rate for the scalar $S$, indicated as $\Gamma_S$, for the $p$-wave model discussed in Sec. 4.1.
Since we assume that $m_S > m_\chi > m_e$, then $S$ has two decay channels:

- $S \to e^- e^+$.
- $S \to \chi\chi$.

#### Computation of $S \to e^- e^+$ decay rate

Let's start by computing $S(p_1) \to e^-(p_2)e^+(p_3)$, whose Feynman diagram is the one depicted in Fig. B.10.

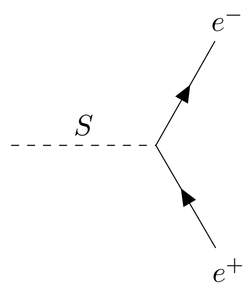


Figure B.10: Feynman diagram relative to $\Gamma_S \to e^- e^+$

The corresponding scattering amplitude is

$$iM = ig_e \bar{u}_2 v_3. \tag{B.83}$$

Summing over the final spin states we can find the unpolarized scattering amplitude:

$$|M|^2_{\text{unp}} = \sum_s |M|^2 = g_e^2 \text{Tr}[(\not{p}_2 + m_e)(\not{p}_3 - m_e)] = 4g_e^2(p_2 \cdot p_3 - m_e^2). \tag{B.84}$$

In the center of mass reference frame the decaying particle is at rest and, assuming that the particles are moving in the $y - z$ plane, we can write the corresponding four-momenta as

$$p_1 = \begin{pmatrix} m_S \\ 0 \\ 0 \\ 0 \end{pmatrix}, \quad p_2 = \begin{pmatrix} E_e \\ 0 \\ |\vec{k}| \sin\theta \\ |\vec{k}| \cos\theta \end{pmatrix}, \quad p_3 = \begin{pmatrix} E_e \\ 0 \\ -|\vec{k}| \sin\theta \\ -|\vec{k}| \cos\theta \end{pmatrix}, \tag{B.85}$$

where $k \equiv |\vec{k}| = \sqrt{E_e^2 - m_e^2}$.
Moreover, we can write that

$$p_1^2 = m_S^2 = (p_2 + p_3)^2 = 2m_e^2 + 2p_2 \cdot p_3 \implies p_2 \cdot p_3 = \frac{m_S^2}{2} - m_e^2, \tag{B.86}$$

from which follows the unpolarized scattering amplitude

$$|M|^2_{\text{unp}} = 4g_e^2\left(\frac{m_S^2}{2} - 2m_e^2\right) = 2g_e^2 m_S^2\left(1 - \frac{4m_e^2}{m_S^2}\right). \tag{B.87}$$

The differential decay rate is defined as

$$d\Gamma = \frac{|M|^2_{\text{unp}}}{2m_S} d\Pi_2, \tag{B.88}$$

where

$$d\Pi_2 = \frac{d\Omega}{16\pi^2}\frac{|\vec{p}_f|}{E_{\text{CM}}}, \quad |\vec{p}_f| \equiv k = \sqrt{E_e^2 - m_e^2}. \tag{B.89}$$

We can now write that

$$\begin{aligned} p_1 \cdot p_2 = m_S E_e \implies E_e &= \frac{p_1 \cdot p_2}{m_S} = \frac{(p_2 + p_3) \cdot p_2}{m_S} = \frac{m_e^2 + p_2 \cdot p_3}{m_S} = \frac{\cancel{m_e^2} + \frac{m_S^2}{2} - \cancel{m_e^2}}{m_S} \\ &= \frac{m_S}{2}. \end{aligned} \tag{B.90}$$

At this point, we can write that

$$k = \sqrt{\frac{m_S^2}{4} - m_e^2} = \frac{m_S}{2}\sqrt{1 - \frac{4m_e^2}{m_S^2}}. \tag{B.91}$$

Moreover, $E_{\text{CM}}^2 = (p_2 + p_3)^2 = p_1^2 = m_S^2$ and thus we can write that

$$\frac{d\Gamma}{d\Omega} = \frac{|M|^2_{\text{unp}}}{32\pi^2 m_S}\frac{\cancel{m_S}}{2\cancel{m_S}}\sqrt{1 - \frac{4m_e^2}{m_S^2}} = \frac{g_e^2}{32\pi^2 \cancel{m_S}} m_S^{\cancel{2}}\left(1 - \frac{4m_e^2}{m_S^2}\right)^{\frac{3}{2}} = \frac{g_e^2}{32\pi^2} m_S\left(1 - \frac{4m_e^2}{m_S^2}\right)^{\frac{3}{2}}. \tag{B.92}$$

Integrating over the solid angle, we get as result

$$\Gamma_{S \to e^- e^+} = \int \frac{d\Gamma}{d\Omega} d\Omega = \frac{g_e^2}{8\pi} m_S\left(1 - \frac{4m_e^2}{m_S^2}\right)^{\frac{3}{2}}. \tag{B.93}$$

**Computation of $S \to \chi\chi$ decay rate**

We now compute the decay rate for $S(p_1) \to \chi(p_2)\chi(p_3)$, whose Feynman diagram is the one depicted in Fig. B.11.
Here the computation is really similar to the one in Sec. B.3.1, so we will go fast through it.
We can write the unpolarized scattering amplitude as

$$|M|^2_{\text{unp}} = y_D^2(p_2 \cdot p_3 - m_\chi^2). \tag{B.94}$$

We can now compute the differential decay rate as in Eq. (B.88), finding

$$\frac{d\Gamma}{d\Omega} = \frac{y_D^2}{32\pi^2} m_S\left(1 - \frac{4m_\chi^2}{m_S^2}\right)^{\frac{3}{2}}. \tag{B.95}$$

Integrating over the solid angle and dividing by 2 the result due to the fact that we have two identical particles in the final state, we find

$$\Gamma_{S \to \chi\chi} = \frac{y_D^2}{16\pi} m_S\left(1 - \frac{4m_\chi^2}{m_S^2}\right)^{\frac{3}{2}}. \tag{B.96}$$

We can now find the total decay rate for the new scalar $S$ as $\Gamma_S = \Gamma_{S \to e^+ e^+} + \Gamma_{S \to \chi\chi}$, using Eqs. B.93 and B.96. Consequently the lifetime of $S$ is given by $\tau_S = \frac{1}{\Gamma_S}$.

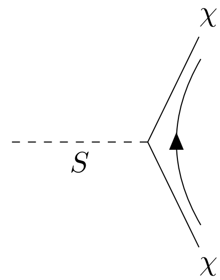


Figure B.11: Feynman diagram relative to $\Gamma_{S\to\chi\chi}$

## B.4 Masses and couplings

In this section we want to derive the masses for all the particles involved in the coannihilation model discussed in Sec. 5.1.1, whose Lagrangian in the one written in Eq. (5.1).

We recall that we can write $\phi$ in polar coordinates as $\phi = |\phi| e^{i\frac{\theta}{v_\phi}}$, where $\theta$ is a Goldstone bosons and $|\phi| = \frac{\varphi+v_\phi}{\sqrt{2}}$. In the unitary gauge the Goldstone boson disappears and we remain with $\phi = \phi^* = \frac{\varphi+v_\phi}{\sqrt{2}}$.
In particular, in the unitary gauge we can write:

$$\mathscr{L} \supset -\frac{y_\phi}{\sqrt{2}}(\varphi + v_\phi)(\chi_2^2 - \chi_1^2) - \frac{\bar{m}}{2}(\chi_1^2 + \chi_2^2) \tag{B.97}$$

The mass terms are the ones proportional to the VEV $v_\phi$, therefore

$$\mathscr{L} \supset -\frac{y_\phi}{\sqrt{2}} v_\phi(\chi_2^2 - \chi_1^2) - \frac{\bar{m}}{2}(\chi_1^2 + \chi_2^2) \equiv -\frac{m_i}{2}(\chi_2^2 + \chi_1^2). \tag{B.98}$$

By manipulating a little bit the terms in the Lagrangian we get

$$\mathscr{L} \supset \frac{\chi_1^2}{2}\underbrace{\left(-\bar{m} + \frac{2y_\phi}{\sqrt{2}} v_\phi\right)}_{-\bar{m}+\frac{\delta}{2}} + \frac{\chi_2^2}{2}\underbrace{\left(-\bar{m} - \frac{2y_\phi}{\sqrt{2}} v_\phi\right)}_{-\bar{m}-\frac{\delta}{2}} \equiv -\frac{m_i}{2}(\chi_2^2 + \chi_1^2), \tag{B.99}$$

where $\delta = 2\sqrt{2} y_\phi v_\phi$. Therefore, we obtain $m_{1,2} = \bar{m} \mp \frac{\delta}{2}$.
The mass of $\varphi$ comes from the term inside the potential $V(|\phi|)$ in Eq. (5.2) proportional to $v_\phi \varphi^2$, namely

$$\lambda_\phi v_\phi^2 \varphi^2 \equiv \frac{m_\varphi^2}{2}\varphi^2 \implies m_\varphi^2 = 2\lambda_\phi v_\phi^2. \tag{B.100}$$

Eventually, we can also find the mass of the dark photon $V^\mu$, through the Higgs mechanism mediated by the scalar $\phi$.
The dark kinetic term takes the form:

$$(D_\mu \phi)^* D^\mu \phi = (\partial_\mu - i g_D q_\phi V_\mu)\phi^*(\partial^\mu + i g_D q_\phi V^\mu)\phi, \tag{B.101}$$

where $g_D$ is the $U(1)'$ coupling constant and $q_\phi$ is the charge of the scalar $\phi = \frac{1}{\sqrt{2}}(\varphi + v_\phi)$.
Therefore, we get:

$$(D_\mu \phi)^* D^\mu \phi \supset \frac{v_\phi^2}{2} g_D^2 q_\phi^2 V_\mu V^\mu \equiv \frac{m_V^2}{2} V_\mu V^\mu \implies m_V = g_D q_\phi v_\phi. \tag{B.102}$$

Since from Ref. [171] we know that $\phi$ has charge $q_\phi = 2$, we can write the mass of the dark photon as $m_V = 2 g_D v_\phi$.

# Appendix C

# Resonant dark matter

The expression *resonant dark matter* refers to a particular class of models where the DM annihilation is significantly enhanced due to a resonance condition, which occurs when the mediator's mass approaches twice the DM's mass, namely $m_{\rm med} \simeq 2M_{\rm DM}$. In this limit, we should write the DM annihilation cross section as proportional to the Breit-Wigner propagator, namely

$$\sigma v \propto \frac{1}{(s - m_{\rm med}^2)^2 + m_{\rm med}^2 \Gamma_{\rm med}^2}, \tag{C.1}$$

where $\Gamma_{\rm med}$ is the mediator's width and $s$ is the usual Mandelstam variable.

In the following we investigate the resonance regime of the $p$-wave model discussed in Chapter 4.

## C.1 Resonance regime analysis for $p$-wave models

The $p$-wave model discussed in Sec. 4.1 gives better results in the limit that $m_S \to 2m_\chi$, since in the non-resonant regime, where $m_S \gg 2m_\chi$, the $m_S - g_e$ parameter space is significantly contrained by experiments.
The cross section relative to the $\chi\chi \to e^-e^+$ annihilation process in Eq. (4.5) is derived by Taylor expanding the original cross section around $v_{\rm rel} \simeq 0$. However, as already mentioned in Sec. 2.3.2, in the vicinity of a resonance, the usual expansion in powers of $v_{\rm rel}$ fails, since the annihilation cross section changes sharply with energy and cannot be well approximated by a low-velocity series[92]. We thus need to find a more precise expression for $\chi\chi \to e^-e^+$ cross section, which can be written as

$$\sigma v_{\chi\chi\to e^-e^+} = \frac{A f(v_{\rm rel})}{(s - m_S)^2 + m_S^2 \Gamma_S^2}, \tag{C.2}$$

where $A$ is a constant, independent of $v_{\rm rel}$, while $f(v_{\rm rel})$, on the contrary, is a generic function of the relative velocity. Recalling Eq. (B.36), we can write that

$$\sigma v_{\chi\chi\to e^-e^+} = \frac{A f(v_{\rm rel})}{(4m_\chi^2 + m_\chi^2 v_{\rm rel}^2 - m_S^2)^2 + m_S^2 \Gamma_S^2}. \tag{C.3}$$

To parametrize deviations from unity in the ratio $\frac{m_S}{2m_\chi}$, we can introduce a small quantity $\epsilon \ll 1$, such that $\frac{m_S}{2m_\chi} = 1 + \epsilon$. In this way, we can rewrite the cross section in Eq. (C.2) as

$$\sigma v = \frac{Af(v_{\rm rel})}{16m_\chi^4\left(1 + \frac{v_{\rm rel}^2}{4} - \underbrace{\frac{m_S^2}{4m_\chi}}_{(1+\epsilon)^2}\right)^2 + \underbrace{\frac{m_S^2}{4m_\chi}}_{(1+\epsilon)^2} 4m_\chi^2\Gamma_S^2} \tag{C.4}$$

and developing all the computations, we obtain

$$\sigma v = \frac{Af(v_{\rm rel})}{m_\chi^4(-4\epsilon^2 - 8\epsilon + v_{\rm rel}^2)^2 + (1+\epsilon)^2 4m_\chi^2\Gamma_S^2}, \tag{C.5}$$

where, from Eq. (B.96), we have that

$$\Gamma_S = \Gamma_{S\to\chi\chi} + \Gamma_{S\to e^-e^+} \simeq \Gamma_{S\to\chi\chi} \simeq \frac{y_D^2}{16\pi} m_S\left(1 - \frac{4m_\chi^2}{m_S^2}\right)^{3/2} = \frac{y_D^2}{16\pi} m_S\left[1 - \frac{1}{(1+\epsilon)^2}\right]^2, \tag{C.6}$$

since $y_D \gg g_e$ and therefore $S$ decays quickly into a $\chi - \chi$ pair.
We can now rewrite $(1+\epsilon)^2 4m_\chi^2\Gamma_S^2$ as

$$\begin{aligned}
&(1+\epsilon)^2 4m_\chi^2 \frac{y_D^4}{256\pi^2} m_S^2\left[1 - \frac{1}{(1+\epsilon)^2}\right]^3 = \\
&\frac{y_D^4}{256\pi^2} 16m_\chi^4(1+\epsilon)^2 \underbrace{\frac{m_S^2}{4m_\chi^2}}_{(1+\epsilon)^2}\left[1 - \frac{1}{(1+\epsilon)^2}\right]^3 = \\
&\frac{y_D^4 m_\chi^4}{16\pi^2}\left[(1+\epsilon)^{4/3} - \frac{1}{(1+\epsilon)^{2/3}}\right]^3 = \\
&\frac{y_D^4 m_\chi^4}{16\pi^2}\left[\frac{\epsilon^2 + 2\epsilon}{(1+\epsilon)^{2/3}}\right]^3
\end{aligned} \tag{C.7}$$

Using Eq. (C.7), we can rewrite Eq. (C.5) as

$$\sigma v = \frac{Af(v_{\rm rel})}{m_\chi^4} \frac{1}{(-4\epsilon^2 - 8\epsilon + v_{\rm rel}^2)^2 + \frac{y_D^4}{16\pi^2}\left[\frac{\epsilon^2+2\epsilon}{(1+\epsilon)^{2/3}}\right]^3} \tag{C.8}$$

and, expanding $\left[\frac{\epsilon^2+2\epsilon}{(1+\epsilon)^{2/3}}\right]^3$ around $\epsilon \simeq 0$, we get

$$\left[\frac{\epsilon^2 + 2\epsilon}{(1+\epsilon)^{2/3}}\right]^3 = 8\epsilon^3 - 4\epsilon^4 + \mathcal{O}(\epsilon^5). \tag{C.9}$$

Moreover, since $\epsilon \ll 1$ and, if we want to ensure perturbativity, $y_D < \sqrt{4\pi}$, we can ignore higher terms in $\epsilon$, obtaining

$$\sigma v \simeq \frac{Af(v_{\rm rel})}{m_\chi^4} \frac{1}{(v_{\rm rel}^2 - 8\epsilon)^2}. \tag{C.10}$$

### C.1.1 Thermal average computation

Given that the cross section in Eq. (C.10) depends on $v_{\rm rel}^2$, we evaluate the thermal average $\langle v_{\rm rel}^2\rangle$, which is distinct from the square of the average relative velocity, that is $\langle v_{\rm rel}\rangle^2$, and correctly accounts for the distribution of velocities in Eq. (C.10).
Specifically, given a generic quantity $g(\vec{v}_1,\vec{v}_2)$, we can define its thermal average as

$$\langle g(\vec{v}_1,\vec{v}_2)\rangle = \frac{1}{\mathcal{N}}\int d^3v_1 d^3v_2 g(\vec{v}_1,\vec{v}_2) f(\vec{v}_1) f(\vec{v}_2), \tag{C.11}$$

where $f(\vec{v}_i) = \left(\frac{m}{2\pi T}\right)^{3/2} e^{-\frac{m\vec{v}_i^2}{2T}}$ with $i=1,2$ are the distribution velocities of the incoming particles, while $\mathcal{N}$ is a normalization constant defined in such a way that

$$\langle 1\rangle = 1 = \frac{1}{\mathcal{N}}\int d^3v_1 d^3v_2 f(\vec{v}_1) f(\vec{v}_2) \implies \mathcal{N} = \int d^3v_1 d^3v_2 f(\vec{v}_1) f(\vec{v}_2). \tag{C.12}$$

Therefore, we are assuming that the incoming particles follow a Maxwell-Boltzmann distribution and that $m_1 = m_2 \equiv m$, which is our case.
Let us now rewrite everything in terms of the relative velocity, which is defined as in Eq. (B.33), from which in the non-relativistic limit we obtain that

$$v_{\rm rel} \simeq \frac{2p}{m_\chi}, \tag{C.13}$$

where, in the center of mass (COM) frame and in the non-relativistic limit, $p\equiv|\vec{p}| = m|\vec{v}_1| = m|\vec{v}_2|$ is the modulus of the incoming particles. In the non-relativistic limit we can thus write that $\vec{v}_{\rm rel} = \vec{v}_1 - \vec{v}_2$. Furthermore, we recall that the COM velocity for a system of $N$ particles is defined as

$$\vec{v}_{\rm CM} = \frac{m_1\vec{v}_1 + m_2\vec{v}_2 + \cdots + m_N\vec{v}_N}{m_1+m_2+\cdots+m_N}. \tag{C.14}$$

In our case we have two incoming particles with masses $m_1 = m_2 \equiv m$ and, therefore, the COM velocity is defined as $\vec{v}_{\rm CM} = \frac{\vec{v}_1+\vec{v}_2}{2}$.
We can thus perform the change of coordinates $\{\vec{v}_1,\vec{v}_2\}\to\{\vec{v}_{\rm rel},\vec{v}_{\rm CM}\}$, whose Jacobian is equal to 1 and this allows to rewrite the thermal average in Eq. (C.11) as

$$\langle g(\vec{v}_{\rm rel},\vec{v}_{\rm CM})\rangle = \frac{\int d^3v_{\rm rel} d^3v_{\rm CM} h(\vec{v}_{\rm rel},\vec{v}_{\rm CM}) g(\vec{v}_{\rm rel},\vec{v}_{\rm CM})}{\int d^3v_{\rm rel} d^3v_{\rm CM} h(\vec{v}_{\rm rel},\vec{v}_{\rm CM})}, \tag{C.15}$$

where, using that

$$\begin{cases} \vec{v}_1 = \dfrac{2\vec{v}_{\rm CM}+\vec{v}_{\rm rel}}{2} \\ \vec{v}_2 = \dfrac{2\vec{v}_{\rm CM}-\vec{v}_{\rm rel}}{2} \end{cases}, \tag{C.16}$$

we obtain

$$h(\vec{v}_{\rm rel},\vec{v}_{\rm CM}) = \left(\frac{m}{2\pi T}\right)^3 e^{-\frac{m}{T}\left(v_{\rm CM}^2+\frac{v_{\rm rel}^2}{4}\right)}. \tag{C.17}$$

It is possibe to notice that, if the function to be thermally-averaged is a function of $v_{\rm rel}$ only, the integral over $d^3v_{\rm CM}$ is a 3D Gaussian integral of the form

$$\int dxdydz e^{-\alpha(x^2+y^2+z^2)} = \left(\int dx e^{-\alpha x^2}\right)^3 = \left(\frac{\pi}{\alpha}\right)^{3/2}. \tag{C.18}$$

Hence, we can write that

$$\int d^3v_{\rm rel} d^3v_{\rm CM} \left(\frac{m}{2\pi T}\right)^3 e^{-\frac{m}{T}\left(v_{\rm CM}^2+\frac{v_{\rm rel}^2}{4}\right)} = \int d^3v_{\rm rel}\left(\frac{x}{2\pi}\right)^3 e^{-\frac{xv_{\rm rel}^2}{4}} \underbrace{\left(\int d^3v_{\rm CM} e^{-xv_{\rm CM}^2}\right)}_{\left(\frac{\pi}{x}\right)^{3/2}} \tag{C.19}$$
$$= \left(\frac{x}{2\pi}\right)^3 \left(\frac{\pi}{x}\right)^{3/2} \int d^3v_{\rm rel} e^{-\frac{xv_{\rm rel}^2}{4}},$$ [28]

where we have defined $x \equiv \frac{m}{T}$, as usual.
Furthermore, to compute the integral over $d^3v_{\rm rel}$, we can perform a change of spherical coordinates, obtaining

$$\int d^3v_{\rm rel} e^{-\frac{xv_{\rm rel}^2}{4}} = 4\pi \int_0^\infty dv_{\rm rel} v_{\rm rel}^2 e^{-\frac{xv_{\rm rel}^2}{4}}. \tag{C.20}$$

For instance, at FO, using Eqs. C.15, C.19 and C.20, we can write that

$$\langle v_{\rm rel}^2 \rangle = \frac{\int_0^\infty dv_{\rm rel} v_{\rm rel}^4 e^{-\frac{x_{\rm fo} v_{\rm rel}^2}{4}}}{\int_0^\infty dv_{\rm rel} v_{\rm rel}^2 e^{-\frac{x_{\rm fo} v_{\rm rel}^2}{4}}} = \frac{6}{x_{\rm fo}}. \tag{C.21}$$

In first approximation we can thus write that at FO $v_{\rm rel}^2 \simeq \langle v_{\rm rel}^2 \rangle = \frac{6}{x_{\rm fo}}$.

### C.1.2 Relic abundance and 511 keV line in the resonant regime

At this point, we can determine the range of $\epsilon$ for which expanding the cross section in Eq. (C.8) around $v_{\rm rel} \simeq 0$ provides a sufficiently accurate approximation. Specifically, we find that for $\epsilon \geq 0.27$, the relative error introduced by the expansion remains below 33%. Therefore, within this range, the velocity-averaged cross sections given in Eqs. (4.5) and (4.7) can be reliably used. While the accuracy of the expansion improves with larger values of $\epsilon$, we adopt the conservative threshold of $\epsilon \geq 0.27$ for simplicity and clarity. This choice ensures that the parameter space displayed in Fig. 4.2 remains sufficiently open and interpretable.

For sufficiently small values of $\epsilon$ , the cross section in Eq. (C.10) can be approximated as

$$\sigma v \simeq \frac{A f(v_{\rm rel})}{m_\chi^4} \frac{1}{v_{\rm rel}^4}. \tag{C.22}$$

[28] In general the distribution of velocities depend on temperature and, therefore, on $x = m/T$. However, we can treat $x$ as a constant within the integral in Eq. (C.19), since the thermal average is computed instantaneously at a fixed cosmological time. The result of the integral can then be used in the Boltzmann equation, where $x$ evolves with the expansion of the universe.

In particular, we find that for $\epsilon \lesssim 0.0064$, the relative error introduced by this approximation remains below 33%, justifying its validity.
However, $\epsilon$ cannot be taken too small, as the physical treatment of the problem requires that the thermally-averaged annihilation cross section responsible for the 511 keV line signal, namely $\langle \sigma v \rangle_{511}$, remains much smaller than the freeze-out cross section, that is $\langle \sigma v \rangle_{\text{fo}}$. In particular, to ensure consistency with the observed dark matter relic abundance and avoid overproduction of positrons, we require $\langle \sigma v \rangle_{511} \lesssim \langle \sigma v \rangle_{\text{fo}}$, which implies a lower bound of approximately $\epsilon \gtrsim 5.3 \cdot 10^{-5}$, even though we never reach such small values of $\epsilon$.

In summary, we can state that for $\epsilon \geq 0.27$, it is a good approximation to use the cross sections given in Eqs. (4.5) and (4.7), which are derived by expanding around $v_{\text{rel}} \simeq 0$. However, in the range $5.3 \cdot 10^{-5} \lesssim \epsilon \lesssim 0.0064$, we are too close to the resonance regime, where the low-velocity expansion breaks down and no longer provides an accurate description of the annihilation process.
In this region, a more appropriate treatment is required, and the corresponding thermally-averaged cross sections can be approximated as:

$$\begin{aligned} \langle \sigma v \rangle_{511} &\simeq \frac{y_D^2 g_e^2}{2\pi m_\chi^2}\left(1 - \frac{m_e^2}{m_\chi^2}\right)^{3/2} \frac{\langle v_{\text{rel}}^2 \rangle}{64\epsilon^2}, \qquad \langle v_{\text{rel}}^2 \rangle \simeq (1.1 \cdot 10^{-3})^2; \\ \langle \sigma v \rangle_{\text{fo}} &\simeq \frac{y_D^2 g_e^2}{2\pi m_\chi^2}\left(1 - \frac{m_e^2}{m_\chi^2}\right)^{3/2} \left\langle \frac{1}{v_{\text{rel}}^2} \right\rangle, \quad \left\langle \frac{1}{v_{\text{rel}}^2} \right\rangle = \frac{x_{\text{fo}}}{2}. \end{aligned} \tag{C.23}$$

These expressions are obtained using the thermal average definition in Eq. (C.15), together with the Maxwell-Boltzmann velocity distribution in Eq. (C.19) and the change to spherical coordinates as described in Eq. (C.20). Specifically, one finds:

$$\left\langle \frac{1}{v_{\text{rel}}^2} \right\rangle = \frac{\int_0^\infty dv_{\text{rel}} e^{-\frac{x_{\text{fo}} v_{\text{rel}}^2}{4}}}{\int_0^\infty dv_{\text{rel}} v_{\text{rel}}^2 e^{-\frac{x_{\text{fo}} v_{\text{rel}}^2}{4}}} = \frac{x_{\text{fo}}}{2}. \tag{C.24}$$

This result highlights the different behavior of the thermal average depending on the velocity regime and justifies the separation into distinct $\epsilon$ intervals.

In the intermediate $\epsilon$ regime, specifically for $0.0064 \lesssim \epsilon < 0.27$, neither of the previously discussed approximations is fully reliable. In this range, the system is too close to the resonance for the low-velocity expansion around $v_{\text{rel}} \simeq 0$ to remain valid, yet not sufficiently resonant to apply the approximation discussed in the $5.3 \cdot 10^{-5} \lesssim \epsilon \lesssim 0.0064$ regime. Therefore, in order to obtain precise predictions for the annihilation rate, it becomes necessary to compute the full thermally-averaged cross sections without relying to the procedure already discussed.
In this thesis we focus on the $p$-wave phenomelogy within the ranges $5.3 \cdot 10^{-5} \lesssim \epsilon \lesssim 0.0064$ and $\epsilon \geq 0.27$, where the presented theoretical approximations still yield quite accurate results.

# Bibliography


[1] Marco Cirelli, Alessandro Strumia, and Jure Zupan. "Dark Matter". In: (June 2024). arXiv: 2406.01705 [hep-ph].

[2] III Johnson W. N., Jr. Harnden F. R., and R. C. Haymes. "The Spectrum of Low-Energy Gamma Radiation from the Galactic-Center Region". In: *Astrophysical Journal* 172 (1972), pp. L1–L7. DOI: 10.1086/180878.

[3] J. Knodlseder et al. "The All-sky distribution of 511 keV electron-positron annihilation emission". In: *Astron. Astrophys.* 441 (2005), pp. 513–532. DOI: 10.1051/0004-6361:20042063. arXiv: astro-ph/0506026.

[4] Georg Weidenspointner et al. "An asymmetric distribution of positrons in the Galactic disk revealed by gamma-rays". In: *Nature* 451 (2008), pp. 159–162. DOI: 10.1038/nature06490.

[5] L. Bouchet. "A complete all-sky survey with INTEGRAL/SPI: sources census, hard X-ray diffuse emission and annihilation line". In: *Proceedings of The Extreme Sky: Sampling the Universe above 10 keV*. Vol. 096. SISSA, 2009, p. 016. DOI: 10.22323/1.096.0016. URL: https://pos.sissa.it/096/016/.

[6] N. Prantzos et al. "The 511 keV emission from positron annihilation in the Galaxy". In: *Rev. Mod. Phys.* 83 (2011), pp. 1001–1056. DOI: 10.1103/RevModPhys.83.1001. arXiv: 1009.4620 [astro-ph.HE].

[7] Yago Ascasibar et al. "Constraints on dark matter and the shape of the Milky Way dark halo from the 511-keV line". In: *Mon. Not. Roy. Astron. Soc.* 368 (2006), pp. 1695–1705. DOI: 10.1111/j.1365-2966.2006.10226.x. arXiv: astro-ph/0507142.

[8] John F. Beacom, Nicole F. Bell, and Gianfranco Bertone. "Gamma-ray constraint on Galactic positron production by MeV dark matter". In: *Phys. Rev. Lett.* 94 (2005), p. 171301. DOI: 10.1103/PhysRevLett.94.171301. arXiv: astro-ph/0409403.

[9] John F. Beacom and Hasan Yuksel. "Stringent constraint on galactic positron production". In: *Phys. Rev. Lett.* 97 (2006), p. 071102. DOI: 10.1103/PhysRevLett.97.071102. arXiv: astro-ph/0512411.

[10] Ryan J. Wilkinson et al. "Ruling out the light weakly interacting massive particle explanation of the Galactic 511 keV line". In: *Phys. Rev. D* 94.10 (2016), p. 103525. DOI: 10.1103/PhysRevD.94.103525. arXiv: 1602.01114 [astro-ph.CO].

[11] Pedro De la Torre Luque et al. "511 keV Galactic Photons from a Dark Matter Spike". In: (Oct. 2024). arXiv: 2410.16379 [astro-ph.HE].

[12] Souradeep Das et al. "Relaxation of Energy Constraints for Positrons Generating the Galactic Annihilation Signal". In: (June 2025). arXiv: 2506.00847 [astro-ph.HE].

[13] Ciaran A. J. O'Hare. "Cosmology of axion dark matter". In: *PoS* COSMICWISPers (2024), p. 040. DOI: 10.22323/1.454.0040. arXiv: 2403.17697 [hep-ph].

[14] Scott Dodelson and Lawrence M. Widrow. "Sterile-neutrinos as dark matter". In: *Phys. Rev. Lett.* 72 (1994), pp. 17–20. DOI: 10.1103/PhysRevLett.72.17. arXiv: hep-ph/9303287.

[15] Rouven Essig et al. "Working Group Report: New Light Weakly Coupled Particles". In: *Snowmass 2013: Snowmass on the Mississippi.* Oct. 2013. arXiv: 1311.0029 [hep-ph].

[16] Leszek Roszkowski, Enrico Maria Sessolo, and Sebastian Trojanowski. "WIMP dark matter candidates and searches—current status and future prospects". In: *Rept. Prog. Phys.* 81.6 (2018), p. 066201. DOI: 10.1088/1361-6633/aab913. arXiv: 1707.06277 [hep-ph].

[17] Bernard Carr, Florian Kuhnel, and Marit Sandstad. "Primordial Black Holes as Dark Matter". In: *Phys. Rev. D* 94.8 (2016), p. 083504. DOI: 10.1103/PhysRevD.94.083504. arXiv: 1607.06077 [astro-ph.CO].

[18] Vera C. Rubin and W. Kent Ford Jr. "Rotation of the Andromeda Nebula from a Spectroscopic Survey of Emission Regions". In: *Astrophys. J.* 159 (1970), pp. 379–403. DOI: 10.1086/150317.

[19] V. C. Rubin, N. Thonnard, and W. K. Ford Jr. "Rotational properties of 21 SC galaxies with a large range of luminosities and radii, from NGC 4605 /R = 4kpc/ to UGC 2885 /R = 122 kpc/". In: *Astrophys. J.* 238 (1980), p. 471. DOI: 10.1086/158003.

[20] Yoshiaki Sofue and Vera Rubin. "Rotation curves of spiral galaxies". In: *Ann. Rev. Astron. Astrophys.* 39 (2001), pp. 137–174. DOI: 10.1146/annurev.astro.39.1.137. arXiv: astro-ph/0010594.

[21] Katherine Freese. "Review of Observational Evidence for Dark Matter in the Universe and in upcoming searches for Dark Stars". In: *EAS Publ. Ser.* 36 (2009). Ed. by E. Pécontal et al., pp. 113–126. DOI: 10.1051/eas/0936016. arXiv: 0812.4005 [astro-ph].

[22] Russell Kirk. "Dark Matter Genesis". PhD thesis. Royal Holloway, U. of London, Royal Holloway, U. of London, 2017.

[23] Douglas Clowe et al. "A direct empirical proof of the existence of dark matter". In: *Astrophys. J. Lett.* 648 (2006), pp. L109–L113. DOI: 10.1086/508162. arXiv: astro-ph/0608407.

[24] Marusa Bradac et al. "Revealing the properties of dark matter in the merging cluster MACSJ0025.4-1222". In: *Astrophys. J.* 687 (2008), p. 959. DOI: 10.1086/591246. arXiv: 0806.2320 [astro-ph].

[25] M. J. Jee et al. "A Study of the Dark Core in A520 with Hubble Space Telescope: The Mystery Deepens". In: *Astrophys. J.* 747 (2012), p. 96. DOI: 10.1088/0004-637X/747/2/96. arXiv: 1202.6368 [astro-ph.CO].

[26] F. Zwicky. "Die Rotverschiebung von extragalaktischen Nebeln". In: *Helv. Phys. Acta* 6 (1933), pp. 110–127. DOI: 10.1007/s10714-008-0707-4.

[27] N. Aghanim et al. "Planck 2018 results. VI. Cosmological parameters". In: *Astron. Astrophys.* 641 (2020). [Erratum: Astron.Astrophys. 652, C4 (2021)], A6. DOI: `10.1051/0004-6361/201833910`. arXiv: `1807.06209 [astro-ph.CO]`.

[28] G. Hinshaw et al. "Nine-Year Wilkinson Microwave Anisotropy Probe (WMAP) Observations: Cosmological Parameter Results". In: *Astrophys. J. Suppl.* 208 (2013), p. 19. DOI: `10.1088/0067-0049/208/2/19`. arXiv: `1212.5226 [astro-ph.CO]`.

[29] Max Tegmark et al. "Cosmological parameters from SDSS and WMAP". In: *Phys. Rev. D* 69 (2004), p. 103501. DOI: `10.1103/PhysRevD.69.103501`. arXiv: `astro-ph/0310723`.

[30] Daniel J. Eisenstein et al. "Detection of the Baryon Acoustic Peak in the Large-Scale Correlation Function of SDSS Luminous Red Galaxies". In: *Astrophys. J.* 633 (2005), pp. 560–574. DOI: `10.1086/466512`. arXiv: `astro-ph/0501171`.

[31] Wayne Hu and Scott Dodelson. "Cosmic Microwave Background Anisotropies". In: *Ann. Rev. Astron. Astrophys.* 40 (2002), pp. 171–216. DOI: `10.1146/annurev.astro.40.060401.093926`. arXiv: `astro-ph/0110414`.

[32] M. Milgrom. "A Modification of the Newtonian dynamics as a possible alternative to the hidden mass hypothesis". In: *Astrophys. J.* 270 (1983), pp. 365–370. DOI: `10.1086/161130`.

[33] M. Milgrom. "A Modification of the Newtonian dynamics: Implications for galaxies". In: *Astrophys. J.* 270 (1983), pp. 371–383. DOI: `10.1086/161131`.

[34] Jacob D. Bekenstein. "Relativistic gravitation theory for the MOND paradigm". In: *Phys. Rev. D* 70 (2004). [Erratum: Phys.Rev.D 71, 069901 (2005)], p. 083509. DOI: `10.1103/PhysRevD.70.083509`. arXiv: `astro-ph/0403694`.

[35] Constantinos Skordis and Tom Zlosnik. "New Relativistic Theory for Modified Newtonian Dynamics". In: *Phys. Rev. Lett.* 127.16 (2021), p. 161302. DOI: `10.1103/PhysRevLett.127.161302`. arXiv: `2007.00082 [astro-ph.CO]`.

[36] Anthony Aguirre, Joop Schaye, and Eliot Quataert. "Problems for MOND in clusters and the Ly-alpha forest". In: *Astrophys. J.* 561 (2001), p. 550. DOI: `10.1086/323376`. arXiv: `astro-ph/0105184`.

[37] Benoit Famaey and Stacy McGaugh. "Modified Newtonian Dynamics (MOND): Observational Phenomenology and Relativistic Extensions". In: *Living Rev. Rel.* 15 (2012), p. 10. DOI: `10.12942/lrr-2012-10`. arXiv: `1112.3960 [astro-ph.CO]`.

[38] Paul Bode, Jeremiah P. Ostriker, and Neil Turok. "Halo formation in warm dark matter models". In: *Astrophys. J.* 556 (2001), pp. 93–107. DOI: `10.1086/321541`. arXiv: `astro-ph/0010389`.

[39] Matteo Viel et al. "Constraining warm dark matter candidates including sterile neutrinos and light gravitinos with WMAP and the Lyman-alpha forest". In: *Phys. Rev. D* 71 (2005), p. 063534. DOI: `10.1103/PhysRevD.71.063534`. arXiv: `astro-ph/0501562`.

[40] Kevork Abazajian. "Linear cosmological structure limits on warm dark matter". In: *Phys. Rev. D* 73 (2006), p. 063513. DOI: `10.1103/PhysRevD.73.063513`. arXiv: `astro-ph/0512631`.

[41] Volker Springel et al. “Simulating the joint evolution of quasars, galaxies and their large-scale distribution”. In: *Nature* 435 (2005), pp. 629–636. DOI: 10.1038/nature03597. arXiv: astro-ph/0504097.

[42] S. L. Dubovsky, D. S. Gorbunov, and G. I. Rubtsov. “Narrowing the window for millicharged particles by CMB anisotropy”. In: *JETP Lett.* 79 (2004), pp. 1–5. DOI: 10.1134/1.1675909. arXiv: hep-ph/0311189.

[43] Rouven Essig et al. “Constraining Light Dark Matter with Diffuse X-Ray and Gamma-Ray Observations”. In: *JHEP* 11 (2013), p. 193. DOI: 10.1007/JHEP11(2013)193. arXiv: 1309.4091 [hep-ph].

[44] Tracy R. Slatyer and Chih-Liang Wu. “General Constraints on Dark Matter Decay from the Cosmic Microwave Background”. In: *Phys. Rev. D* 95.2 (2017), p. 023010. DOI: 10.1103/PhysRevD.95.023010. arXiv: 1610.06933 [astro-ph.CO].

[45] Brian D. Fields et al. “Big-Bang Nucleosynthesis after Planck”. In: *JCAP* 03 (2020). [Erratum: JCAP 11, E02 (2020)], p. 010. DOI: 10.1088/1475-7516/2020/03/010. arXiv: 1912.01132 [astro-ph.CO].

[46] C. Alcock et al. “The MACHO project: Microlensing results from 5.7 years of LMC observations”. In: *Astrophys. J.* 542 (2000), pp. 281–307. DOI: 10.1086/309512. arXiv: astro-ph/0001272.

[47] Giorgio Arcadi et al. “The waning of the WIMP? A review of models, searches, and constraints”. In: *Eur. Phys. J. C* 78.3 (2018), p. 203. DOI: 10.1140/epjc/s10052-018-5662-y. arXiv: 1703.07364 [hep-ph].

[48] Matteo Viel et al. “Warm dark matter as a solution to the small scale crisis: New constraints from high redshift Lyman-$\alpha$ forest data”. In: *Phys. Rev. D* 88 (2013), p. 043502. DOI: 10.1103/PhysRevD.88.043502. arXiv: 1306.2314 [astro-ph.CO].

[49] Kim Griest and Marc Kamionkowski. “Unitarity Limits on the Mass and Radius of Dark Matter Particles”. In: *Phys. Rev. Lett.* 64 (1990), p. 615. DOI: 10.1103/PhysRevLett.64.615.

[50] David N. Spergel and Paul J. Steinhardt. “Observational evidence for selfinteracting cold dark matter”. In: *Phys. Rev. Lett.* 84 (2000), pp. 3760–3763. DOI: 10.1103/PhysRevLett.84.3760. arXiv: astro-ph/9909386.

[51] Scott W. Randall et al. “Constraints on the Self-Interaction Cross-Section of Dark Matter from Numerical Simulations of the Merging Galaxy Cluster 1E 0657-56”. In: *Astrophys. J.* 679 (2008), pp. 1173–1180. DOI: 10.1086/587859. arXiv: 0704.0261 [astro-ph].

[52] Matthew G. Walker et al. “A Universal Mass Profile for Dwarf Spheroidal Galaxies”. In: *Astrophys. J.* 704 (2009). [Erratum: Astrophys.J. 710, 886–890 (2010)], pp. 1274–1287. DOI: 10.1088/0004-637X/704/2/1274. arXiv: 0906.0341 [astro-ph.CO].

[53] Giuseppina Battaglia, Amina Helmi, and Maarten Breddels. “Internal kinematics and dynamical models of dwarf spheroidal galaxies around the Milky Way”. In: *New Astron. Rev.* 57 (2013), pp. 52–79. DOI: 10.1016/j.newar.2013.05.003. arXiv: 1305.5965 [astro-ph.CO].

[54] Ken'ichi Saikawa and Satoshi Shirai. "Precise WIMP Dark Matter Abundance and Standard Model Thermodynamics". In: *JCAP* 08 (2020), p. 011. DOI: `10.1088/1475-7516/2020/08/011`. arXiv: `2005.03544 [hep-ph]`.

[55] Seyed Yaser Ayazi and Mojtaba Hosseini. "Beyond Freeze-Out: A Novel Freeze-in Mechanism for Dark Matter via Supercooled Phase Transitions". In: (Feb. 2025). arXiv: `2502.14526 [hep-ph]`.

[56] Sean Tulin and Hai-Bo Yu. "Dark Matter Self-interactions and Small Scale Structure". In: *Phys. Rept.* 730 (2018), pp. 1–57. DOI: `10.1016/j.physrep.2017.11.004`. arXiv: `1705.02358 [hep-ph]`.

[57] John Dubinski and R. G. Carlberg. "The Structure of cold dark matter halos". In: *Astrophys. J.* 378 (1991), p. 496. DOI: `10.1086/170451`.

[58] Julio F. Navarro, Carlos S. Frenk, and Simon D. M. White. "The Structure of cold dark matter halos". In: *Astrophys. J.* 462 (1996), pp. 563–575. DOI: `10.1086/177173`. arXiv: `astro-ph/9508025`.

[59] Julio F. Navarro, Carlos S. Frenk, and Simon D. M. White. "A Universal density profile from hierarchical clustering". In: *Astrophys. J.* 490 (1997), pp. 493–508. DOI: `10.1086/304888`. arXiv: `astro-ph/9611107`.

[60] Ricardo A. Flores and Joel R. Primack. "Observational and theoretical constraints on singular dark matter halos". In: *Astrophys. J. Lett.* 427 (1994), pp. L1–4. DOI: `10.1086/187350`. arXiv: `astro-ph/9402004`.

[61] Ben Moore. "Evidence against dissipationless dark matter from observations of galaxy haloes". In: *Nature* 370 (1994), p. 629. DOI: `10.1038/370629a0`.

[62] Ben Moore et al. "Cold collapse and the core catastrophe". In: *Mon. Not. Roy. Astron. Soc.* 310 (1999), pp. 1147–1152. DOI: `10.1046/j.1365-8711.1999.03039.x`. arXiv: `astro-ph/9903164`.

[63] James S. Bullock et al. "Profiles of dark haloes. Evolution, scatter, and environment". In: *Mon. Not. Roy. Astron. Soc.* 321 (2001), pp. 559–575. DOI: `10.1046/j.1365-8711.2001.04068.x`. arXiv: `astro-ph/9908159`.

[64] Kyle A. Oman et al. "The unexpected diversity of dwarf galaxy rotation curves". In: *Mon. Not. Roy. Astron. Soc.* 452.4 (2015), pp. 3650–3665. DOI: `10.1093/mnras/stv1504`. arXiv: `1504.01437 [astro-ph.GA]`.

[65] G. Kauffmann, S. D. M. White, and B. Guiderdoni. "The formation and evolution of galaxies within merging dark matter haloes". In: *Mon. Not. Roy. Astron. Soc.* 264.1 (1993), pp. 201–218. DOI: `10.1093/mnras/264.1.201`.

[66] Michael Boylan-Kolchin, James S. Bullock, and Manoj Kaplinghat. "Too big to fail? The puzzling darkness of massive Milky Way subhaloes". In: *Mon. Not. Roy. Astron. Soc.* 415 (2011), p. L40. DOI: `10.1111/j.1745-3933.2011.01074.x`. arXiv: `1103.0007 [astro-ph.CO]`.

[67] Michael Boylan-Kolchin, James S. Bullock, and Manoj Kaplinghat. "The Milky Way's bright satellites as an apparent failure of LCDM". In: *Mon. Not. Roy. Astron. Soc.* 422 (2012), pp. 1203–1218. DOI: `10.1111/j.1365-2966.2012.20695.x`. arXiv: `1111.2048 [astro-ph.CO]`.

[68] Erik J. Tollerud, Michael Boylan-Kolchin, and James S. Bullock. “M31 Satellite Masses Compared to LCDM Subhaloes”. In: *Mon. Not. Roy. Astron. Soc.* 440.4 (2014), pp. 3511–3519. DOI: 10.1093/mnras/stu474. arXiv: 1403.6469 [astro-ph.GA].

[69] Shea Garrison-Kimmel et al. “Too Big to Fail in the Local Group”. In: *Mon. Not. Roy. Astron. Soc.* 444.1 (2014), pp. 222–236. DOI: 10.1093/mnras/stu1477. arXiv: 1404.5313 [astro-ph.GA].

[70] Julio F. Navarro, Vincent R. Eke, and Carlos S. Frenk. “The cores of dwarf galaxy halos”. In: *Mon. Not. Roy. Astron. Soc.* 283 (1996), pp. L72–L78. DOI: 10.1093/mnras/283.3.L72. arXiv: astro-ph/9610187.

[71] Fabio Governato et al. “At the heart of the matter: the origin of bulgeless dwarf galaxies and Dark Matter cores”. In: *Nature* 463 (2010), pp. 203–206. DOI: 10.1038/nature08640. arXiv: 0911.2237 [astro-ph.CO].

[72] Stephane Colombi, Scott Dodelson, and Lawrence M. Widrow. “Large scale structure tests of warm dark matter”. In: *Astrophys. J.* 458 (1996), p. 1. DOI: 10.1086/176788. arXiv: astro-ph/9505029.

[73] Mark R. Lovell et al. “The Haloes of Bright Satellite Galaxies in a Warm Dark Matter Universe”. In: *Mon. Not. Roy. Astron. Soc.* 420 (2012), pp. 2318–2324. DOI: 10.1111/j.1365-2966.2011.20200.x. arXiv: 1104.2929 [astro-ph.CO].

[74] Mark R. Lovell et al. “The properties of warm dark matter haloes”. In: *Mon. Not. Roy. Astron. Soc.* 439 (2014), pp. 300–317. DOI: 10.1093/mnras/stt2431. arXiv: 1308.1399 [astro-ph.CO].

[75] Shunsaku Horiuchi et al. “Properties of resonantly produced sterile neutrino dark matter subhaloes”. In: *Mon. Not. Roy. Astron. Soc.* 456.4 (2016), pp. 4346–4353. DOI: 10.1093/mnras/stv2922. arXiv: 1512.04548 [astro-ph.CO].

[76] Vid Irsic et al. “New Constraints on the free-streaming of warm dark matter from intermediate and small scale Lyman-$\alpha$ forest data”. In: *Phys. Rev. D* 96.2 (2017), p. 023522. DOI: 10.1103/PhysRevD.96.023522. arXiv: 1702.01764 [astro-ph.CO].

[77] Andrea V. Maccio et al. “Cores in warm dark matter haloes: a Catch 22 problem”. In: *Mon. Not. Roy. Astron. Soc.* 424 (2012), pp. 1105–1112. DOI: 10.1111/j.1365-2966.2012.21284.x. arXiv: 1202.1282 [astro-ph.CO].

[78] Mark Vogelsberger and Jesus Zavala. “Direct detection of self-interacting dark matter”. In: *Mon. Not. Roy. Astron. Soc.* 430 (2013), pp. 1722–1735. DOI: 10.1093/mnras/sts712. arXiv: 1211.1377 [astro-ph.CO].

[79] Filippo Sala. *Dark Matter notes*. Unpublished lecture notes, University of Bologna. 2024.

[80] Marco Fabbrichesi, Emidio Gabrielli, and Gaia Lanfranchi. “The Dark Photon”. In: (May 2020). DOI: 10.1007/978-3-030-62519-1. arXiv: 2005.01515 [hep-ph].

[81] Jonathan L. Feng. “The WIMP paradigm: Theme and variations”. In: *SciPost Phys. Lect. Notes* 71 (2023), p. 1. DOI: 10.21468/SciPostPhysLectNotes.71. arXiv: 2212.02479 [hep-ph].

[82] Gary Steigman. “Equivalent Neutrinos, Light WIMPs, and the Chimera of Dark Radiation”. In: *Phys. Rev. D* 87.10 (2013), p. 103517. DOI: 10.1103/PhysRevD.87.103517. arXiv: 1303.0049 [astro-ph.CO].

[83] Kenneth M. Nollett and Gary Steigman. "BBN And The CMB Constrain Light, Electromagnetically Coupled WIMPs". In: *Phys. Rev. D* 89.8 (2014), p. 083508. DOI: 10.1103/PhysRevD.89.083508. arXiv: 1312.5725 [astro-ph.CO].

[84] Miguel Escudero. "Neutrino decoupling beyond the Standard Model: CMB constraints on the Dark Matter mass with a fast and precise $N_{\text{eff}}$ evaluation". In: *JCAP* 02 (2019), p. 007. DOI: 10.1088/1475-7516/2019/02/007. arXiv: 1812.05605 [hep-ph].

[85] Nashwan Sabti et al. "Refined Bounds on MeV-scale Thermal Dark Sectors from BBN and the CMB". In: *JCAP* 01 (2020), p. 004. DOI: 10.1088/1475-7516/2020/01/004. arXiv: 1910.01649 [hep-ph].

[86] Geneviève Bélanger et al. "micrOMEGAs5.0 : Freeze-in". In: *Comput. Phys. Commun.* 231 (2018), pp. 173–186. DOI: 10.1016/j.cpc.2018.04.027. arXiv: 1801.03509 [hep-ph].

[87] Mark Hindmarsh and Owe Philipsen. "WIMP dark matter and the QCD equation of state". In: *Phys. Rev. D* 71 (2005), p. 087302. DOI: 10.1103/PhysRevD.71.087302. arXiv: hep-ph/0501232.

[88] Manuel Drees, Fazlollah Hajkarim, and Ernany Rossi Schmitz. "The Effects of QCD Equation of State on the Relic Density of WIMP Dark Matter". In: *JCAP* 06 (2015), p. 025. DOI: 10.1088/1475-7516/2015/06/025. arXiv: 1503.03513 [hep-ph].

[89] M. Laine and M. Meyer. "Standard Model thermodynamics across the electroweak crossover". In: *JCAP* 07 (2015), p. 035. DOI: 10.1088/1475-7516/2015/07/035. arXiv: 1503.04935 [hep-ph].

[90] Sz. Borsanyi et al. "Calculation of the axion mass based on high-temperature lattice quantum chromodynamics". In: *Nature* 539.7627 (2016), pp. 69–71. DOI: 10.1038/nature20115. arXiv: 1606.07494 [hep-lat].

[91] Gary Steigman, Basudeb Dasgupta, and John F. Beacom. "Precise Relic WIMP Abundance and its Impact on Searches for Dark Matter Annihilation". In: *Phys. Rev. D* 86 (2012), p. 023506. DOI: 10.1103/PhysRevD.86.023506. arXiv: 1204.3622 [hep-ph].

[92] Paolo Gondolo and Graciela Gelmini. "Cosmic abundances of stable particles: Improved analysis". In: *Nucl. Phys. B* 360 (1991), pp. 145–179. DOI: 10.1016/0550-3213(91)90438-4.

[93] E. Aprile et al. "Light Dark Matter Search with Ionization Signals in XENON1T". In: *Phys. Rev. Lett.* 123.25 (2019), p. 251801. DOI: 10.1103/PhysRevLett.123.251801. arXiv: 1907.11485 [hep-ex].

[94] E. Aprile et al. "Constraining the spin-dependent WIMP-nucleon cross sections with XENON1T". In: *Phys. Rev. Lett.* 122.14 (2019), p. 141301. DOI: 10.1103/PhysRevLett.122.141301. arXiv: 1902.03234 [astro-ph.CO].

[95] Orr Abramoff et al. "SENSEI: Direct-Detection Constraints on Sub-GeV Dark Matter from a Shallow Underground Run Using a Prototype Skipper-CCD". In: *Phys. Rev. Lett.* 122.16 (2019), p. 161801. DOI: 10.1103/PhysRevLett.122.161801. arXiv: 1901.10478 [hep-ex].

[96] Prakruth Adari et al. "First Direct-Detection Results on Sub-GeV Dark Matter Using the SENSEI Detector at SNOLAB". In: *Phys. Rev. Lett.* 134.1 (2025), p. 011804. DOI: 10.1103/PhysRevLett.134.011804. arXiv: 2312.13342 [astro-ph.CO].

[97] Gordan Krnjaic. "Testing Thermal-Relic Dark Matter with a Dark Photon Mediator". In: (May 2025). arXiv: 2505.04626 [hep-ph].

[98] Anya Paopiamsap et al. "Constraints on dark matter and astrophysics from tomographic $\gamma$-ray cross-correlations". In: *Phys. Rev. D* 109.10 (2024), p. 103517. DOI: 10.1103/PhysRevD.109.103517. arXiv: 2307.14881 [astro-ph.CO].

[99] M. G. Aartsen et al. "Search for Neutrinos from Dark Matter Self-Annihilations in the center of the Milky Way with 3 years of IceCube/DeepCore". In: *Eur. Phys. J. C* 77.9 (2017), p. 627. DOI: 10.1140/epjc/s10052-017-5213-y. arXiv: 1705.08103 [hep-ex].

[100] K. Choi et al. "Search for neutrinos from annihilation of captured low-mass dark matter particles in the Sun by Super-Kamiokande". In: *Phys. Rev. Lett.* 114.14 (2015), p. 141301. DOI: 10.1103/PhysRevLett.114.141301. arXiv: 1503.04858 [hep-ex].

[101] Guansen Wang et al. "Exploring sub-GeV Dark Matter Physics with Cosmic Ray and Future Telescopes". In: (Mar. 2025). arXiv: 2503.22148 [astro-ph.HE].

[102] Yu. M. Andreev et al. "Search for Light Dark Matter with NA64 at CERN". In: *Phys. Rev. Lett.* 131.16 (2023), p. 161801. DOI: 10.1103/PhysRevLett.131.161801. arXiv: 2307.02404 [hep-ex].

[103] Yu. M. Andreev et al. "Searching for Light Dark Matter and Dark Sectors with the NA64 experiment at the CERN SPS". In: (May 2025). arXiv: 2505.14291 [hep-ex].

[104] Torsten Åkesson et al. "Current Status and Future Prospects for the Light Dark Matter eXperiment". In: *Snowmass 2021*. Mar. 2022. arXiv: 2203.08192 [hep-ex].

[105] Paul Frederik Depta et al. "BBN constraints on the annihilation of MeV-scale dark matter". In: *JCAP* 04 (2019), p. 029. DOI: 10.1088/1475-7516/2019/04/029. arXiv: 1901.06944 [hep-ph].

[106] Cara Giovanetti et al. "Joint Cosmic Microwave Background and Big Bang Nucleosynthesis Constraints on Light Dark Sectors with Dark Radiation". In: *Phys. Rev. Lett.* 129.2 (2022), p. 021302. DOI: 10.1103/PhysRevLett.129.021302. arXiv: 2109.03246 [hep-ph].

[107] Keir K. Rogers, Cora Dvorkin, and Hiranya V. Peiris. "Limits on the Light Dark Matter–Proton Cross Section from Cosmic Large-Scale Structure". In: *Phys. Rev. Lett.* 128.17 (2022), p. 171301. DOI: 10.1103/PhysRevLett.128.171301. arXiv: 2111.10386 [astro-ph.CO].

[108] Edward Hardy and Robert Lasenby. "Stellar cooling bounds on new light particles: plasma mixing effects". In: *JHEP* 02 (2017), p. 033. DOI: 10.1007/JHEP02(2017)033. arXiv: 1611.05852 [hep-ph].

[109] Edward Hardy, Anton Sokolov, and Henry Stubbs. "Supernova bounds on new scalars from resonant and soft emission". In: *JHEP* 04 (2025), p. 013. DOI: 10.1007/JHEP04(2025)013. arXiv: 2410.17347 [hep-ph].

[110] E. Aprile et al. “Dark Matter Search Results from a One Ton-Year Exposure of XENON1T”. In: *Phys. Rev. Lett.* 121.11 (2018), p. 111302. DOI: 10.1103/PhysRevLett.121.111302. arXiv: 1805.12562 [astro-ph.CO].

[111] D. S. Akerib et al. “Results from a search for dark matter in the complete LUX exposure”. In: *Phys. Rev. Lett.* 118.2 (2017), p. 021303. DOI: 10.1103/PhysRevLett.118.021303. arXiv: 1608.07648 [astro-ph.CO].

[112] Xiangyi Cui et al. “Dark Matter Results From 54-Ton-Day Exposure of PandaX-II Experiment”. In: *Phys. Rev. Lett.* 119.18 (2017), p. 181302. DOI: 10.1103/PhysRevLett.119.181302. arXiv: 1708.06917 [astro-ph.CO].

[113] I. Arnquist et al. “First Constraints from DAMIC-M on Sub-GeV Dark-Matter Particles Interacting with Electrons”. In: *Phys. Rev. Lett.* 130.17 (2023), p. 171003. DOI: 10.1103/PhysRevLett.130.171003. arXiv: 2302.02372 [hep-ex].

[114] Rouven Essig et al. “First Direct Detection Limits on sub-GeV Dark Matter from XENON10”. In: *Phys. Rev. Lett.* 109 (2012), p. 021301. DOI: 10.1103/PhysRevLett.109.021301. arXiv: 1206.2644 [astro-ph.CO].

[115] E. Armengaud et al. “Searching for low-mass dark matter particles with a massive Ge bolometer operated above-ground”. In: *Phys. Rev. D* 99.8 (2019), p. 082003. DOI: 10.1103/PhysRevD.99.082003. arXiv: 1901.03588 [astro-ph.GA].

[116] Troy A. Porter, Robert P. Johnson, and Peter W. Graham. “Dark Matter Searches with Astroparticle Data”. In: *Ann. Rev. Astron. Astrophys.* 49 (2011), pp. 155–194. DOI: 10.1146/annurev-astro-081710-102528. arXiv: 1104.2836 [astro-ph.HE].

[117] Rebecca K. Leane. “Indirect Detection of Dark Matter in the Galaxy”. In: *3rd World Summit on Exploring the Dark Side of the Universe*. 2020, pp. 203–228. arXiv: 2006.00513 [hep-ph].

[118] Kimberly K. Boddy et al. “New dark matter analysis of milky way dwarf satellite galaxies with madhatv2”. In: *Phys. Rev. D* 109.10 (2024), p. 103007. DOI: 10.1103/PhysRevD.109.103007. arXiv: 2401.05327 [hep-ph].

[119] M. Ackermann et al. “Searching for Dark Matter Annihilation from Milky Way Dwarf Spheroidal Galaxies with Six Years of Fermi Large Area Telescope Data”. In: *Phys. Rev. Lett.* 115.23 (2015), p. 231301. DOI: 10.1103/PhysRevLett.115.231301. arXiv: 1503.02641 [astro-ph.HE].

[120] Thong T. Q. Nguyen et al. “Strong Constraints on Dark Photon and Scalar Dark Matter Decay from INTEGRAL and AMS-02”. In: (Nov. 2024). arXiv: 2412.00180 [hep-ph].

[121] Pedro De la Torre Luque, Martin Wolfgang Winkler, and Tim Linden. “Antiproton bounds on dark matter annihilation from a combined analysis using the DRAGON2 code”. In: *JCAP* 05 (2024), p. 104. DOI: 10.1088/1475-7516/2024/05/104. arXiv: 2401.10329 [astro-ph.HE].

[122] H. Abdallah et al. “Search for dark matter annihilations towards the inner Galactic halo from 10 years of observations with H.E.S.S”. In: *Phys. Rev. Lett.* 117.11 (2016), p. 111301. DOI: 10.1103/PhysRevLett.117.111301. arXiv: 1607.08142 [astro-ph.HE].

[123] H. Abdalla et al. "Search for Dark Matter Annihilation Signals in the H.E.S.S. Inner Galaxy Survey". In: *Phys. Rev. Lett.* 129.11 (2022), p. 111101. DOI: 10.1103/PhysRevLett.129.111101. arXiv: 2207.10471 [astro-ph.HE].

[124] R. Abbasi et al. "Search for dark matter from the center of the Earth with 10 years of IceCube data". In: *Eur. Phys. J. C* 85.5 (2025), p. 490. DOI: 10.1140/epjc/s10052-025-14144-7. arXiv: 2412.12972 [astro-ph.HE].

[125] Thomas Siegert, Francesca Calore, and Pasquale Dario Serpico. "Sub-GeV Dark Matter Annihilation: Limits from Milky Way observations with INTEGRAL". In: *Mon. Not. Roy. Astron. Soc.* 528.2 (2024), pp. 3433–3440. DOI: 10.1093/mnras/stae104. arXiv: 2401.03795 [astro-ph.HE].

[126] Marco Cirelli et al. "Integral X-ray constraints on sub-GeV Dark Matter". In: *Phys. Rev. D* 103.6 (2021), p. 063022. DOI: 10.1103/PhysRevD.103.063022. arXiv: 2007.11493 [hep-ph].

[127] Marco Cirelli. "Sub-GeV Dark Matter and X-rays". In: *PoS* CORFU2021 (2022), p. 096. DOI: 10.1016/j.nuclphysb.2024.116479.

[128] Christopher V. Cappiello, Kenny C. Y. Ng, and John F. Beacom. "Reverse Direct Detection: Cosmic Ray Scattering With Light Dark Matter". In: *Phys. Rev. D* 99.6 (2019), p. 063004. DOI: 10.1103/PhysRevD.99.063004. arXiv: 1810.07705 [hep-ph].

[129] Zhan-Hong Lei, Jian Tang, and Bing-Long Zhang. "Constraints on cosmic-ray boosted dark matter in CDEX-10 *". In: *Chin. Phys. C* 46.8 (2022), p. 085103. DOI: 10.1088/1674-1137/ac68da. arXiv: 2008.07116 [hep-ph].

[130] A. De Angelis et al. "The e-ASTROGAM mission". In: *Exper. Astron.* 44.1 (2017), pp. 25–82. DOI: 10.1007/s10686-017-9533-6. arXiv: 1611.02232 [astro-ph.HE].

[131] Regina Caputo et al. "All-sky Medium Energy Gamma-ray Observatory: Exploring the Extreme Multimessenger Universe". In: (July 2019). arXiv: 1907.07558 [astro-ph.IM].

[132] Adam Coogan, Logan Morrison, and Stefano Profumo. "Precision gamma-ray constraints for sub-GeV dark matter models". In: *JCAP* 08 (2021), p. 044. DOI: 10.1088/1475-7516/2021/08/044. arXiv: 2104.06168 [hep-ph].

[133] J. P. Lees et al. "Search for Invisible Decays of a Dark Photon Produced in $e^+e^-$ Collisions at BaBar". In: *Phys. Rev. Lett.* 119.13 (2017), p. 131804. DOI: 10.1103/PhysRevLett.119.131804. arXiv: 1702.03327 [hep-ex].

[134] Luigi Corona. "Searches for Invisible New Particles at Belle II". In: *Moscow Univ. Phys. Bull.* 79.Suppl 1 (2024), pp. 418–423. DOI: 10.3103/S0027134924701169. arXiv: 2401.07845 [hep-ex].

[135] Jinhan Liang, Zuowei Liu, and Lan Yang. "Probing sub-GeV leptophilic dark matter at Belle II and NA64". In: *JHEP* 05 (2022), p. 184. DOI: 10.1007/JHEP05(2022)184. arXiv: 2111.15533 [hep-ph].

[136] P. Crivelli. "Status and prospects of the NA64 experiment at the CERN SPS". In: *Workshop on Feebly-Interacting Particles.* Jan. 2023. arXiv: 2301.09905 [hep-ex].

[137] Tracy R. Slatyer. “Indirect dark matter signatures in the cosmic dark ages. I. Generalizing the bound on s-wave dark matter annihilation from Planck results”. In: *Phys. Rev. D* 93.2 (2016), p. 023527. DOI: 10.1103/PhysRevD.93.023527. arXiv: 1506.03811 [hep-ph].

[138] Masahiro Kawasaki et al. “Revisiting Big-Bang Nucleosynthesis Constraints on Long-Lived Decaying Particles”. In: *Phys. Rev. D* 97.2 (2018), p. 023502. DOI: 10.1103/PhysRevD.97.023502. arXiv: 1709.01211 [hep-ph].

[139] Miguel Escudero et al. “A fresh look into the interacting dark matter scenario”. In: *JCAP* 06 (2018), p. 007. DOI: 10.1088/1475-7516/2018/06/007. arXiv: 1803.08427 [astro-ph.CO].

[140] Gianpiero Mangano et al. “Cosmological bounds on dark matter-neutrino interactions”. In: *Phys. Rev. D* 74 (2006), p. 043517. DOI: 10.1103/PhysRevD.74.043517. arXiv: astro-ph/0606190.

[141] Ali Kurmus et al. “The feasibility of constraining DM interactions with high-redshift observations by JWST”. In: *Mon. Not. Roy. Astron. Soc.* 516.1 (2022), pp. 1524–1538. DOI: 10.1093/mnras/stac2195. arXiv: 2203.04985 [astro-ph.GA].

[142] Jae Hyeok Chang, Rouven Essig, and Samuel D. McDermott. “Supernova 1987A Constraints on Sub-GeV Dark Sectors, Millicharged Particles, the QCD Axion, and an Axion-like Particle”. In: *JHEP* 09 (2018), p. 051. DOI: 10.1007/JHEP09(2018)051. arXiv: 1803.00993 [hep-ph].

[143] Andrea Caputo et al. “Dark photon limits: A handbook”. In: *Phys. Rev. D* 104.9 (2021), p. 095029. DOI: 10.1103/PhysRevD.104.095029. arXiv: 2105.04565 [hep-ph].

[144] Gordan Krnjaic. “Probing Light Thermal Dark-Matter With a Higgs Portal Mediator”. In: *Phys. Rev. D* 94.7 (2016), p. 073009. DOI: 10.1103/PhysRevD.94.073009. arXiv: 1512.04119 [hep-ph].

[145] Simon Knapen, Tongyan Lin, and Kathryn M. Zurek. “Light Dark Matter: Models and Constraints”. In: *Phys. Rev. D* 96.11 (2017), p. 115021. DOI: 10.1103/PhysRevD.96.115021. arXiv: 1709.07882 [hep-ph].

[146] Vanda Silveira and A. Zee. “SCALAR PHANTOMS”. In: *Phys. Lett. B* 161 (1985), pp. 136–140. DOI: 10.1016/0370-2693(85)90624-0.

[147] John McDonald. “Gauge singlet scalars as cold dark matter”. In: *Phys. Rev. D* 50 (1994), pp. 3637–3649. DOI: 10.1103/PhysRevD.50.3637. arXiv: hep-ph/0702143.

[148] P. S. Bhupal Dev, Rabindra N. Mohapatra, and Yongchao Zhang. “Long Lived Light Scalars as Probe of Low Scale Seesaw Models”. In: *Nucl. Phys. B* 923 (2017), pp. 179–221. DOI: 10.1016/j.nuclphysb.2017.07.021. arXiv: 1703.02471 [hep-ph].

[149] Peter W. Graham, David E. Kaplan, and Surjeet Rajendran. “Cosmological Relaxation of the Electroweak Scale”. In: *Phys. Rev. Lett.* 115.22 (2015), p. 221801. DOI: 10.1103/PhysRevLett.115.221801. arXiv: 1504.07551 [hep-ph].

[150] Thomas Flacke et al. “Phenomenology of relaxion-Higgs mixing”. In: *JHEP* 06 (2017), p. 050. DOI: 10.1007/JHEP06(2017)050. arXiv: 1610.02025 [hep-ph].

[151] Hans A. Bethe and James R. Wilson. “Revival of a stalled supernova shock by neutrino heating”. In: *Astrophys. J.* 295 (1985), pp. 14–23. DOI: 10.1086/163343.

[152] G. G. Raffelt. *Stars as laboratories for fundamental physics: The astrophysics of neutrinos, axions, and other weakly interacting particles.* May 1996. ISBN: 978-0-226-70272-8.

[153] Eric Braaten. "Neutrino emissivity of an ultrarelativistic plasma from positron and plasmino annihilation". In: (Nov. 1991).

[154] Thomas Siegert. "The Positron Puzzle". In: Mar. 2023. DOI: 10.1007/s10509-023-04184-4. arXiv: 2303.15582 [astro-ph.HE].

[155] Celine Boehm et al. "MeV dark matter: Has it been detected?" In: *Phys. Rev. Lett.* 92 (2004), p. 101301. DOI: 10.1103/PhysRevLett.92.101301. arXiv: astro-ph/0309686.

[156] Thomas Siegert et al. "Gamma-ray spectroscopy of positron annihilation in the Milky Way". In: *Astronomy & Astrophysics* 586 (2016), A84. DOI: 10.1051/0004-6361/201527510. arXiv: 1512.00325 [astro-ph.HE].

[157] F. Frontera et al. "Understanding the origin of the positron annihilation line and the physics of supernova explosions". In: *Experimental Astronomy* 51.6 (2021), pp. 1175–1202. DOI: 10.1007/s10686-021-09727-7.

[158] Eugene Churazov et al. "Positron annihilation spectrum from the Galactic Center region observed by SPI/INTEGRAL". In: *Mon. Not. Roy. Astron. Soc.* 357 (2005), pp. 1377–1386. DOI: 10.1111/j.1365-2966.2005.08757.x. arXiv: astro-ph/0411351.

[159] Pierre Jean et al. "Spectral analysis of the galactic e+ e- annihilation emission". In: *Astron. Astrophys.* 445 (2006), pp. 579–589. DOI: 10.1051/0004-6361:20053765. arXiv: astro-ph/0509298.

[160] A. Ore and J. L. Powell. "Three-Photon Annihilation of an Electron-Positron Pair". In: *Physical Review* 75 (1949), pp. 1696–1699. DOI: 10.1103/PhysRev.75.1696.

[161] F. W. Stecker. "Cosmic gamma rays". In: *Astrophysics and Space Science* 3 (1969), pp. 579–596. DOI: 10.1007/BF00704862.

[162] Laurent Bouchet, Jean-Pierre Roques, and Elisabeth Jourdain. "On the morphology of the electron-positron annihilation emission as seen by SPI/INTEGRAL". In: *Astrophys. J.* 720 (2010), pp. 1772–1780. DOI: 10.1088/0004-637X/720/2/1772. arXiv: 1007.4753 [astro-ph.HE].

[163] Carolyn A. Kierans et al. "Positron Annihilation in the Galaxy". In: (Mar. 2019). arXiv: 1903.05569 [astro-ph.HE].

[164] Roland Diehl et al. "26al in the inner galaxy". In: *Astron. Astrophys.* 449 (2006), pp. 1025–1031. DOI: 10.1051/0004-6361:20054301. arXiv: astro-ph/0512334.

[165] Georg Weidenspointner et al. "The sky distribution of positronium annihilation continuum emission measured with spi/integral". In: *Astron. Astrophys.* 450 (2006), p. 1012. DOI: 10.1051/0004-6361:20054046. arXiv: astro-ph/0601673.

[166] Celeste Keith and Dan Hooper. "511 keV excess and primordial black holes". In: *Phys. Rev. D* 104.6 (2021), p. 063033. DOI: 10.1103/PhysRevD.104.063033. arXiv: 2103.08611 [astro-ph.CO].

[167] Aaron C. Vincent, Pierrick Martin, and James M. Cline. "Interacting dark matter contribution to the Galactic 511 keV gamma ray emission: constraining the morphology with INTEGRAL/SPI observations". In: *JCAP* 04 (2012), p. 022. DOI: 10.1088/1475-7516/2012/04/022. arXiv: 1201.0997 [hep-ph].

[168] Abdelaziz Hussein et al. "Theoretical Predictions for the Inner Dark Matter Distribution in the Milky Way Informed by Simulations". In: (Jan. 2025). arXiv: `2501.14868 [hep-ph]`.

[169] Douglas P. Finkbeiner and Neal Weiner. "Exciting Dark Matter and the INTEGRAL/SPI 511 keV signal". In: *Phys. Rev. D* 76 (2007), p. 083519. DOI: `10.1103/PhysRevD.76.083519`. arXiv: `astro-ph/0702587`.

[170] Maxim Pospelov and Adam Ritz. "The galactic 511 keV line from electroweak scale WIMPs". In: *Phys. Lett. B* 651 (2007), pp. 208–215. DOI: `10.1016/j.physletb.2007.06.027`. arXiv: `hep-ph/0703128`.

[171] Yohei Ema, Filippo Sala, and Ryosuke Sato. "Dark matter models for the 511 keV galactic line predict keV electron recoils on Earth". In: *Eur. Phys. J. C* 81.2 (2021), p. 129. DOI: `10.1140/epjc/s10052-021-08899-y`. arXiv: `2007.09105 [hep-ph]`.

[172] Eugene Vasiliev. "Dark matter annihilation near a black hole: Plateau vs. weak cusp". In: *Phys. Rev. D* 76 (2007), p. 103532. DOI: `10.1103/PhysRevD.76.103532`. arXiv: `0707.3334 [astro-ph]`.

[173] Stuart L. Shapiro and Jessie Shelton. "Weak annihilation cusp inside the dark matter spike about a black hole". In: *Phys. Rev. D* 93.12 (2016), p. 123510. DOI: `10.1103/PhysRevD.93.123510`. arXiv: `1606.01248 [astro-ph.HE]`.

[174] Miguel Pato, Fabio Iocco, and Gianfranco Bertone. "Dynamical constraints on the dark matter distribution in the Milky Way". In: *JCAP* 12 (2015), p. 001. DOI: `10.1088/1475-7516/2015/12/001`. arXiv: `1504.06324 [astro-ph.GA]`.

[175] Paolo Gondolo and Joseph Silk. "Dark matter annihilation at the galactic center". In: *Phys. Rev. Lett.* 83 (1999), pp. 1719–1722. DOI: `10.1103/PhysRevLett.83.1719`. arXiv: `astro-ph/9906391`.

[176] Oleg Y. Gnedin and Joel R. Primack. "Dark Matter Profile in the Galactic Center". In: *Phys. Rev. Lett.* 93 (2004), p. 061302. DOI: `10.1103/PhysRevLett.93.061302`. arXiv: `astro-ph/0308385`.

[177] David Merritt. "Single and binary black holes and their influence on nuclear structure". In: *Carnegie Observatories Centennial Symposium. 1. Coevolution of Black Holes and Galaxies*. Jan. 2003. arXiv: `astro-ph/0301257`.

[178] R. Abuter et al. "Mass distribution in the Galactic Center based on interferometric astrometry of multiple stellar orbits". In: *Astron. Astrophys.* 657 (2022), p. L12. DOI: `10.1051/0004-6361/202142465`. arXiv: `2112.07478 [astro-ph.GA]`.

[179] Kayhan Gultekin et al. "The M-sigma and M-L Relations in Galactic Bulges and Determinations of their Intrinsic Scatter". In: *Astrophys. J.* 698 (2009), pp. 198–221. DOI: `10.1088/0004-637X/698/1/198`. arXiv: `0903.4897 [astro-ph.GA]`.

[180] Piero Ullio, HongSheng Zhao, and Marc Kamionkowski. "A Dark matter spike at the galactic center?" In: *Phys. Rev. D* 64 (2001), p. 043504. DOI: `10.1103/PhysRevD.64.043504`. arXiv: `astro-ph/0101481`.

[181] David Merritt, Stefan Harfst, and Gianfranco Bertone. "Collisionally Regenerated Dark Matter Structures in Galactic Nuclei". In: *Phys. Rev. D* 75 (2007), p. 043517. DOI: `10.1103/PhysRevD.75.043517`. arXiv: `astro-ph/0610425`.

[182] Stuart L. Shapiro and Douglas C. Heggie. “Effect of stars on the dark matter spike around a black hole: A tale of two treatments”. In: *Phys. Rev. D* 106.4 (2022), p. 043018. DOI: 10.1103/PhysRevD.106.043018. arXiv: 2209.08105 [astro-ph.GA].

[183] E. Gallego-Cano et al. “New constraints on the structure of the nuclear stellar cluster of the Milky Way from star counts and MIR imaging”. In: *Astronomy and Astrophysics* 634 (2020), A71. DOI: 10.1051/0004-6361/201935303.

[184] M. Habibi et al. “Spectroscopic Detection of a Cusp of Late-type Stars around the Central Black Hole in the Milky Way”. In: *The Astrophysical Journal Letters* 872.1 (2019), p. L15. DOI: 10.3847/2041-8213/ab03cf. URL: https://doi.org/10.3847/2041-8213/ab03cf.

[185] Pedro De la Torre Luque, Shyam Balaji, and Jordan Koechler. “Importance of Cosmic-Ray Propagation on Sub-GeV Dark Matter Constraints”. In: *Astrophys. J.* 968.1 (2024), p. 46. DOI: 10.3847/1538-4357/ad41e0. arXiv: 2311.04979 [hep-ph].

[186] Mohammad Aghaie et al. “(H)ALPing the 511 keV line: A thermal DM interpretation of the 511 keV emission”. In: (Jan. 2025). arXiv: 2501.10504 [hep-ph].

[187] N. Castelló-Mor. “DAMIC-M Experiment: Thick, Silicon CCDs to search for Light Dark Matter”. In: *Nucl. Instrum. Meth. A* 958 (2020). Ed. by Manfred Krammer et al., p. 162933. DOI: 10.1016/j.nima.2019.162933. arXiv: 2001.01476 [physics.ins-det].

[188] Alexis Aguilar-Arevalo et al. “The Oscura Experiment”. In: (Feb. 2022). arXiv: 2202.10518 [astro-ph.IM].

[189] Rebecca K. Leane and John F. Beacom. “Sub-GeV Dark Matter Direct Detection with Neutrino Observatories”. In: (Mar. 2025). arXiv: 2503.09685 [hep-ph].

[190] E. Valenti et al. “The central velocity dispersion of the Milky Way bulge”. In: *Astronomy & amp; Astrophysics* 616 (2018), A83. ISSN: 1432-0746. DOI: 10.1051/0004-6361/201832905. URL: http://dx.doi.org/10.1051/0004-6361/201832905.

[191] Asher Berlin, Gordan Krnjaic, and Elena Pinetti. “Reviving MeV-GeV indirect detection with inelastic dark matter”. In: *Phys. Rev. D* 110.3 (2024), p. 035015. DOI: 10.1103/PhysRevD.110.035015. arXiv: 2311.00032 [hep-ph].

[192] Eder Izaguirre, Gordan Krnjaic, and Brian Shuve. “Discovering Inelastic Thermal-Relic Dark Matter at Colliders”. In: *Phys. Rev. D* 93.6 (2016), p. 063523. DOI: 10.1103/PhysRevD.93.063523. arXiv: 1508.03050 [hep-ph].

[193] Asher Berlin and Felix Kling. “Inelastic Dark Matter at the LHC Lifetime Frontier: ATLAS, CMS, LHCb, CODEX-b, FASER, and MATHUSLA”. In: *Phys. Rev. D* 99.1 (2019), p. 015021. DOI: 10.1103/PhysRevD.99.015021. arXiv: 1810.01879 [hep-ph].

[194] Mariana Carrillo González and Natalia Toro. “Cosmology and signals of light pseudo-Dirac dark matter”. In: *JHEP* 04 (2022), p. 060. DOI: 10.1007/JHEP04(2022)060. arXiv: 2108.13422 [hep-ph].

[195] Peter W. Graham et al. “Exothermic Dark Matter”. In: *Phys. Rev. D* 82 (2010), p. 063512. DOI: 10.1103/PhysRevD.82.063512. arXiv: 1004.0937 [hep-ph].

[196] Rouven Essig et al. “On the Origin of Light Dark Matter Species”. In: (Apr. 2010). arXiv: 1004.0691 [hep-ph].

[197] David Curtin et al. "Illuminating Dark Photons with High-Energy Colliders". In: *JHEP* 02 (2015), p. 157. DOI: 10.1007/JHEP02(2015)157. arXiv: 1412.0018 [hep-ph].

[198] Patrick J. Fitzpatrick et al. "New thermal relic targets for inelastic vector-portal dark matter". In: *Phys. Rev. D* 106.8 (2022), p. 083507. DOI: 10.1103/PhysRevD.106.083507. arXiv: 2105.05255 [hep-ph].

[199] Brian Batell, Maxim Pospelov, and Adam Ritz. "Direct Detection of Multi-component Secluded WIMPs". In: *Phys. Rev. D* 79 (2009), p. 115019. DOI: 10.1103/PhysRevD.79.115019. arXiv: 0903.3396 [hep-ph].

[200] Paolo Gondolo, Junji Hisano, and Kenji Kadota. "The Effect of quark interactions on dark matter kinetic decoupling and the mass of the smallest dark halos". In: *Phys. Rev. D* 86 (2012), p. 083523. DOI: 10.1103/PhysRevD.86.083523. arXiv: 1205.1914 [hep-ph].

[201] Bridget Bertoni et al. "Constraints and consequences of reducing small scale structure via large dark matter-neutrino interactions". In: *JHEP* 04 (2015), p. 170. DOI: 10.1007/JHEP04(2015)170. arXiv: 1412.3113 [hep-ph].

[202] Asher Berlin et al. "Dark Matter, Millicharges, Axion and Scalar Particles, Gauge Bosons, and Other New Physics with LDMX". In: *Phys. Rev. D* 99.7 (2019), p. 075001. DOI: 10.1103/PhysRevD.99.075001. arXiv: 1807.01730 [hep-ph].

[203] Paul J. McMillan. "Mass models of the Milky Way". In: *Mon. Not. Roy. Astron. Soc.* 414 (2011), pp. 2446–2457. DOI: 10.1111/j.1365-2966.2011.18564.x. arXiv: 1102.4340 [astro-ph.GA].

[204] Manoj Kaplinghat et al. "Tying Dark Matter to Baryons with Self-interactions". In: *Phys. Rev. Lett.* 113 (2014), p. 021302. DOI: 10.1103/PhysRevLett.113.021302. arXiv: 1311.6524 [astro-ph.CO].

[205] E. Aprile et al. "Excess electronic recoil events in XENON1T". In: *Phys. Rev. D* 102.7 (2020), p. 072004. DOI: 10.1103/PhysRevD.102.072004. arXiv: 2006.09721 [hep-ex].

[206] Torsten Bringmann and Maxim Pospelov. "Novel direct detection constraints on light dark matter". In: *Phys. Rev. Lett.* 122.17 (2019), p. 171801. DOI: 10.1103/PhysRevLett.122.171801. arXiv: 1810.10543 [hep-ph].

[207] Yohei Ema, Filippo Sala, and Ryosuke Sato. "Light Dark Matter at Neutrino Experiments". In: *Phys. Rev. Lett.* 122.18 (2019), p. 181802. DOI: 10.1103/PhysRevLett.122.181802. arXiv: 1811.00520 [hep-ph].

[208] James Alvey et al. "Detecting Light Dark Matter via Inelastic Cosmic Ray Collisions". In: *Phys. Rev. Lett.* 123 (2019), p. 261802. DOI: 10.1103/PhysRevLett.123.261802. arXiv: 1905.05776 [hep-ph].

[209] Marco Battaglieri et al. "US Cosmic Visions: New Ideas in Dark Matter 2017: Community Report". In: *U.S. Cosmic Visions: New Ideas in Dark Matter*. July 2017. arXiv: 1707.04591 [hep-ph].

[210] Fiona H. Panther. "Positron Transport and Annihilation in the Galactic Bulge". In: *Galaxies* 6.2 (2018), p. 39. DOI: 10.3390/galaxies6020039. arXiv: 1801.09365 [astro-ph.HE].

[211] Daniel Baumann. *Cosmology Lecture Notes*. Institute of Theoretical Physics, University of Amsterdam. URL: https://physics.bu.edu/~schmaltz/PY555/baumann_notes.pdf.

[212] Edward W. Kolb and Michael S. Turner. *The Early Universe*. Vol. 69. Taylor and Francis, May 2019. ISBN: 978-0-429-49286-0, 978-0-201-62674-2. DOI: 10.1201/9780429492860.

[213] Herbi K. Dreiner, Howard E. Haber, and Stephen P. Martin. "Two-component spinor techniques and Feynman rules for quantum field theory and supersymmetry". In: *Phys. Rept.* 494 (2010), pp. 1–196. DOI: 10.1016/j.physrep.2010.05.002. arXiv: 0812.1594 [hep-ph].

[214] R. Mertig, M. Bohm, and Ansgar Denner. "FEYN CALC: Computer algebraic calculation of Feynman amplitudes". In: *Comput. Phys. Commun.* 64 (1991), pp. 345–359. DOI: 10.1016/0010-4655(91)90130-D.

[215] Rolf Shtabovenko Vladyslav Shtabovenko and Frederik Orellana. *Guide to FeynCalc*. Available online: https://feyncalc.github.io. 2024.

[216] J. Kublbeck, M. Bohm, and Ansgar Denner. "Feyn Arts: Computer Algebraic Generation of Feynman Graphs and Amplitudes". In: *Comput. Phys. Commun.* 60 (1990), pp. 165–180. DOI: 10.1016/0010-4655(90)90001-H.

[217] Thomas Hahn. *FeynArts User Guide*. Available online: https://feynarts.de. 2019.

[218] Adam Alloul et al. "FeynRules 2.0 - A complete toolbox for tree-level phenomenology". In: *Comput. Phys. Commun.* 185 (2014), pp. 2250–2300. DOI: 10.1016/j.cpc.2014.04.012. arXiv: 1310.1921 [hep-ph].

[219] Ansgar Denner et al. "Feynman rules for fermion number violating interactions". In: *Nucl. Phys. B* 387 (1992), pp. 467–481. DOI: 10.1016/0550-3213(92)90169-C.